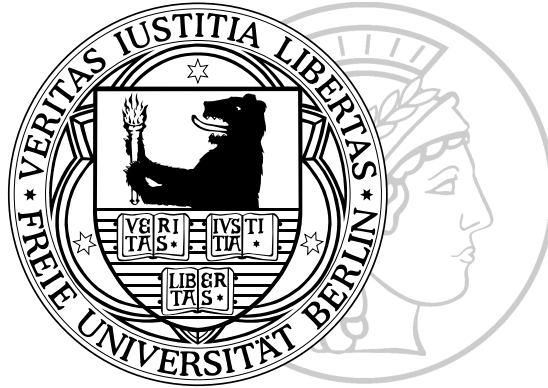


Self-consistent GW approach for the unified description of ground and excited states of finite systems



Dissertation

zur Erlangung des Grades

Doktor der Naturwissenschaften (Dr. rer. nat.)

eingereicht im Fachbereich Physik
der Freie Universität Berlin

vorgelegt in Juli 2013 von

Fabio Caruso

Diese Arbeit wurde von Juni 2009 bis Juni 2013 am Fritz-Haber-Institut der Max-Planck-Gesellschaft in der Abteilung Theorie unter Anleitung von Prof. Dr. Matthias Scheffler angefertigt.

1. Gutachter: Prof. Dr. Matthias Scheffler
2. Gutachter: Prof. Dr. Felix von Oppen

Tag der Disputation: 21. Oktober 2013

Hierdurch versichere ich, dass ich in meiner Dissertation alle Hilfsmittel und Hilfen angegeben habe und versichere gleichfalls auf dieser Grundlage die Arbeit selbstständig verfasst zu haben.

Die Arbeit habe ich nicht schon einmal in einem früheren Promotionsverfahren verwendet und ist nicht als ungenügend beurteilt worden.

Berlin, 31. Juli 2013

per Maria Rosa, Alberto, e Silvia

ABSTRACT

Ab initio methods provide useful tools for the prediction and characterization of material properties, as they allow to obtain information complementary to purely experimental investigations. The *GW* approach to many-body perturbation theory (MBPT) has recently emerged as the method of choice for the evaluation of single-particle excitations in molecules and extended systems. Its application to the characterization of the electronic properties of technologically relevant materials – such as, e.g., dyes for photovoltaic applications or transparent conducting oxides – is steadily increasing over the last years. The *GW* approximation is typically introduced as a first-order perturbative correction (G_0W_0) to density-functional theory (DFT) or Hartree-Fock (HF). However, this also introduces a severe initial-state dependence that affects the G_0W_0 solution. Due to its non-perturbative nature, self-consistent *GW* (sc-*GW*) ameliorates several shortcomings of the G_0W_0 scheme, such as the violation of the particle-number conservation and the dependence on the initial reference ground state. Nevertheless, the suitability and overall accuracy of sc-*GW* has often been questioned, mostly because of numerical problems with previous implementations and the lack of systematic studies for a wide range of systems.

In this doctoral work, the sc-*GW* approach for total energies and spectroscopic properties has been implemented in the Fritz Haber Institute *ab initio* molecular simulations code (FHI-aims) in an all-electron numeric atom-centered orbital framework. With this implementation I then performed a systematic assessment of ground- and excited-state properties of atoms and molecules.

In this work, sc-*GW* has been employed to study the excitation spectra of organic molecules, molecules of interest for photovoltaic applications, and prototypical donor-acceptor systems. At self-consistency, the quasi-particle energies are in good agreement with experiment and, on average, more accurate than G_0W_0 based on HF or semi-local DFT. For covalently bonded dimers, the capability of DFT- and MBPT-based approaches to describe the correlated electronic ground state at dissociation was investigated. Static and local approximations of exchange-correlation potentials – as opposed to non-local, frequency dependent self-energy approximations – are shown to be more effective in describing the dissociation regime. sc-*GW* calculations for ground-state properties (as, e.g., binding energies, bond lengths, vibrational frequencies, and dipole moments) are presented. For ground-state properties, I show that sc-*GW* achieves a comparable performance to exact-exchange plus correlation in the random-phase approximation (EX+cRPA) which is, however, not as good as that of renormalized second-order perturbation theory (rPT2). Finally, the correct distribution of the electron density in prototypical donor-acceptor compounds suggests that sc-*GW* is a promising method for the description of electronic excitations in charge-transfer systems.

ZUSAMMENFASSUNG

Im Vergleich zu einer rein experimentellen Vorgehensweise bieten *ab initio* Methoden die Möglichkeit Ergebnisse auf fundamental anderem Weg zu erlangen. Eine vielversprechende Wahl für die Bestimmung von Ein-Teilchen Anregungen in Molekülen und in ausgedehnten Systemen ist der *GW*-Ansatz in der Vielteilchenstörungstheorie. Seine Verwendung bei der Analyse technologisch interessanter Materialien nimmt stetig zu, z.B. bei halbleitenden Farbstoffen für die Anwendung in der Photovoltaik oder bei transparenten leitenden Oxiden. Üblicherweise wird die *GW*-Näherung als eine Korrektur in erster Ordnung (G_0W_0) auf die Ergebnisse der Dichtefunktionaltheorie (DFT) oder Hartree-Fock-Theorie (HF) angewandt. Dies wiederum führt zu einer starken Abhängig vom Startzustand der G_0W_0 -Lösung. Dank seines nicht-störungstheoretischen Charakters vermag es der selbstkonsistente *GW*-Ansatz (*sc-GW*) einige der Nachteile von G_0W_0 , z.B. die Nichterhaltung der Teilchenzahl oder die Abhängig vom Referenzzustand, aufzuheben. Auf Grund von numerischen Problemen in existierenden Implementationen und der fehlenden systematischen Analyse einer Vielzahl von Systemen wurde die Eignung und Genauigkeit von *sc-GW* allerdings oft in Frage gestellt.

In der vorliegenden Doktorarbeit wurde die *sc-GW* Methode für Gesamtenergien und spektroskopische Eigenschaften im Rahmen eines alle Elektronen umfassenden numerischen, atom-zentrierten Basis Ansatzes in das Fritz Haber Institute *ab initio* molecular simulations package (FHI-aims) implementiert. Mittels dieser Implementation wurde eine systematische Untersuchung der Grund- und Anregungszustände von Atomen und Molekülen durchgeführt.

Anschliessend wurde die *sc-GW*-Methode für die Untersuchung von Anregungsspektren organischer Moleküle, Moleküle für die Verwendung in der Photovoltaik und prototypische Donor/Akzeptor System angewandt. Bei erreichter Selbstkonsistenz stimmen die Quasiteilchen Energien gut mit experimentellen Ergebnissen überein und sind im Durchschnitt deutlich genauer als bei G_0W_0 -Rechnungen, die auf HF oder semi-lokaler DFT basieren. Weiterhin wurde der korrelierten elektronischen Grundzustandes bei der Dissoziation von kovalent gebundenen Dimeren auf seine Beschreibung durch DFT und Störungstheoretischen Methoden untersucht. Im Vergleich zu nicht-lokalen, frequenzabhängigen Selbstenergienäherungen wie z.B. *GW* beschreibt die statische und lokale Näherung des Austausch-Korrelationspotentials in DFT die Dissoziation besser,

vorausgesetzt man verwendet moderne Funktionale wie z.B. exakter Austausch plus Korrelation in der Random Phase Approximation (Ex+cRPA). Abschliessend werden die Grundzustandseigenschaften (Bindungsenergien, Bindungslängen, Schwingungsfrequenzen und Dipolmomente) untersucht. *sc-GW* ist ähnlich leistungsfähig wie Ex+cRPA, aber weniger leistungsfähig als renormalized second-order perturbation theory (rPT2). Aus der korrekten Verteilung der Elektronendichte in prototypischen Donor-Akzeptor Systemen lässt sich schließen, dass *sc-GW* eine viel versprechende Methode zur Beschreibung dieser Systeme ist.

CONTENTS

1	Introduction	1
I	Theoretical Background	5
2	The Many-Body Problem	7
2.1	The Many-Body Hamiltonian	7
2.2	The Born-Oppenheimer approximation	8
2.3	Ab-initio electronic-structure approaches	9
2.4	Wave-function-based methods	10
2.5	Density-functional theory	13
3	Green-Function Methods	23
3.1	Definition of the Green function	23
3.2	Connection to DFT: The Sham-Schlüter equation	28
3.3	Relation to physical properties	29
4	Hedin's equations: the GW approximation	37
4.1	Hedin's equations	37
4.2	The GW approximation	41
4.3	Perturbative G_0W_0	42
4.4	Partially self-consistent GW	46
4.5	Fully self-consistent GW	47
4.6	Connection of GW and RPA	49
II	Implementation	53
5	Self-consistent GW equations in a numeric orbital basis	55
5.1	Numeric atom-centered orbitals	55
5.2	The resolution of the identity	59
5.3	Working equations for self-consistent GW	60

6	Frequency and time dependence in self-consistent <i>GW</i>	69
6.1	Imaginary time and frequency formalism	69
6.2	Evaluation of Fourier integrals	71
7	Numerical evaluation of physical quantities	77
7.1	Spectral function	77
7.2	Galitskii-Migdal total energy	81
III	Applications to atoms and molecules	85
8	Unified description of ground and excited states	87
8.1	Independence of the starting point and conservation laws	87
8.2	Total energies	90
8.3	Electron density and dipole moment	95
8.4	Summary	99
9	The bond-breaking puzzle: many-body versus density-functional theory	101
9.1	Evaluation of the sc-RPA total energy	102
9.2	Potential-energy curve of H ₂ : sc-RPA and sc-GW	103
9.3	Natural occupations and the role of spin-symmetry	106
9.4	Summary	108
10	Assessment of <i>GW</i> methods for photoemission processes in molecules	111
10.1	A hierarchy of theoretical consistency	111
10.2	The azabenzenes	113
10.3	Ionization energies of closed-shell molecules	123
10.4	Summary	128
11	Conclusions and outlook	131
IV	Backmatter	135
	Appendices	137
A	Functional identities	139
B	Convergence with the grid parameters	141
C	Ionization energies of closed-shell molecules	143
D	Total energy of atoms	147
E	Spectra of benzene, pyrazine, pyridazine, and pyrimidine	149
F	Derivation of the Klein and Luttinger-Ward functionals	163

Curriculum Vitæ	167
Publications	169
Bibliography	173
Acknowledgements	193

1 INTRODUCTION

In the XV century, the driving force of the first chemical and physical discoveries was the belief that base metals, such as plumb and iron, could be transformed into gold by bringing them in touch with the *lapis philosophicus*, the philosopher's stone. This belief led to many efforts towards the synthesis of the *lapis philosophicus* perpetrated by several scholars over the centuries, including Isaac Newton. Nowadays, material science has moved towards less-esoteric goals but, in a certain sense, is still addressing the problem of turning "iron" into "gold", i.e., through the transformation of sun light into more controllable forms of energy.

Solar cells based on the photovoltaic effect, whereby electricity can be generated through exposure of the cell to sunlight, constitute one out of many examples of solar-energy conversion techniques. In all solar-energy conversion devices, the light harvesting is triggered by the absorption of a photon in a light absorbing material. The photon energy is thus transferred to the material and transformed, e.g., in electronic excitations and/or nuclear vibrations. Providing the theoretical tools for *predicting* (not just reproducing) these processes in complex materials is one of the roles of atomistic modeling in the quest for new materials for energy conversion. The achievement of this goal is the key to go beyond conventional "trial and error" approaches to material research – as recently recognized and endorsed by large scale projects, such as the Material Genome Initiative.¹ However, despite the omnipresence of electronic excitations in energy-conversion and energy-storage devices, the methods at hand for their theoretical description are at an earlier stage of development as compared to approaches that address ground-state properties.

Density-functional theory (DFT) is the method of choice for the *ab initio* description (i.e., based on the fundamental equations of quantum mechanics) of the ground-state properties of atoms, molecules, and periodic solids. DFT is in principle exact for the ground-state energy, and the electron density – although in practice approximations become necessary. On the whole, DFT contributed enormously to the development of condensed-matter physics and quantum chemistry, and is by far the most diffuse electronic structure approach. However, when it comes to excited states, DFT – and our present techniques to deal with it – falls short. For instance, it is well known that even exact Kohn-Sham DFT would not correctly reproduce the fundamental band gap of a

¹<http://www.whitehouse.gov/mgi>

semiconductor. To describe direct and inverse photoemission processes (i.e., processes involving the loss or gain of an electron), DFT is generally coupled to many-body perturbation theory (MBPT). One advantage of this synergy is the possibility to treat ground- and excited-states at different levels of theory: The ground-state properties can be determined at the DFT level, whereas MBPT-based methods – which are often computationally more demanding than conventional density-functional approximations – can be employed just for the evaluation of excited-state properties. Two common frameworks for the evaluation of spectral properties are dynamical mean-field theory (DMFT) and the *GW* approximation. DMFT has gained popularity due to its capability to reproduce spectral features of materials generally classified as strongly correlated. The applicability of DMFT is restricted to systems with strongly localized frontier orbitals as, for instance, *3d*- and *4f*-electron systems. The *GW* approximation, on the other hand, is more versatile and it can be in principle applied to any compound.

The popularity of the *GW* approach has steadily increased over the last years. In principle, the *GW* approximation (as DFT and Hartree-Fock) requires the satisfaction of a self-consistency condition based on the solution of the Dyson equation. However in most cases, *GW* calculations rely on first-order perturbation theory and additional technical approximations aimed to reduce the computational cost. These approximations make *GW* calculations applicable to molecules up to hundred(s) atoms, and periodic solids with large unit cells that would not be treatable otherwise. On the other hand, perturbation theory limits the predictive power of the *GW* approximation, e.g., by making the results dependent on the arbitrary reference ground state. These aspects motivate this doctoral work, in which the *non-perturbative* (i.e. self-consistent) *GW* approximation is considered for finite systems.

In the past, self-consistent *GW* (sc-*GW*) has been recognized as a good candidate for ameliorating the pathologies of the perturbative *GW* approximation. However, sc-*GW* calculations are scarce due to their numerical complexity and an overall assessment of their accuracy is still missing. Based on previous works on model systems, several authors argued that self-consistency in the *GW* approach deteriorates the agreement with experiment and it was therefore considered counter productive and non-necessary. However, the present work started from the assessment that the scarce numerical evidence is not sufficient to corroborate this belief. In this doctoral work, sc-*GW* has been implemented in the Fritz-Haber-Institut *ab initio* molecular simulation (FHI-aims) code, and applied to the description of the ground-state and excited-state properties of atoms and molecules. It is shown that sc-*GW* has several properties that make it a good candidate for a versatile, general purpose electronic-structure approach – within the limitations imposed by its numerical cost. The first advancement is the independence of the results of the initial reference state; the second, the description of ground and excited states at the same level of theory.

Part I of this thesis is devoted to an overview of basic aspects of electronic structure and many-body perturbation theory: (i) the many-body problem of interacting electrons and nuclei, and density-functional theory; (ii) Green-function theory and its connection

to physical quantities; (iii) Hedin's equations and the GW approximation. In Part II, I present the implementation of sc- GW in the FHI-aims package and discuss: (i) the reformulation of the Hedin's equation in a form suitable for practical calculations; (ii) an alternative representation of the time- and frequency-dependent quantities in sc- GW , that facilitates the evaluation of Fourier integrals; (iii) the reformulation of spectral properties and of the total-energy expression in a basis representation, and numerical convergence tests. Finally, in Part III – which is concerned with the application of the sc- GW approach to real systems – I will report: (i) an overall assessment of sc- GW for ground-state properties of atoms and molecules; (ii) a comparison of the density-functional and many-body description of the dissociation limit for covalently-bonded diatomic molecules; (iii) the definition of a hierarchy of theoretical consistency for GW methods at different level of self-consistency, and the investigation of the accuracy of sc- GW for excited states.

Part I

Theoretical Background

2 THE MANY-BODY PROBLEM

2.1 THE MANY-BODY HAMILTONIAN

A system of non-relativistic interacting quantum particles in a static time-independent potential is described by the time-independent Schrödinger equation [1]:

$$\hat{H} |\Phi_n\rangle = E_n |\Phi_n\rangle \quad . \quad (2.1)$$

Here, $|\Phi_n\rangle$ is the wave function of the quantum system in its n -th excited state, and E_n the corresponding energy. The eigenvalues and eigenvectors of Eq. 2.1 grant access to all time-independent properties of the system. In the absence of external electro-magnetic fields, the Hamilton operator \hat{H} is:

$$\hat{H} = \hat{T}_e + \hat{T}_n + \hat{V}_{e-e} + \hat{V}_{e-n} + \hat{V}_{n-n} \quad , \quad (2.2)$$

where \hat{T}_e and \hat{T}_n are the electronic and nuclear kinetic-energy operators, \hat{V}_{e-e} and \hat{V}_{n-n} account for electron-electron and nuclear-nuclear Coulomb repulsions, and \hat{V}_{e-n} is the electron-nuclear Coulomb interaction. The kinetic operators are given by:

$$\hat{T}_e = \sum_{i=1}^{N_e} -\frac{\hat{\nabla}_i^2}{2} \quad , \quad \hat{T}_n = \sum_{I=1}^{N_n} -\frac{\hat{\nabla}_I^2}{2M_I} \quad , \quad (2.3)$$

whereas the interaction terms can be expressed as:

$$\hat{V}_{e-e} = \sum_{ij}^{N_e} \frac{1}{|\hat{r}_i - \hat{r}_j|} \quad , \quad \hat{V}_{e-n} = \sum_i^{N_e} \sum_I^{N_n} \frac{-Z_I}{|\hat{r}_i - \hat{R}_I|} \quad , \quad \hat{V}_{n-n} = \sum_{IJ}^{N_n} \frac{Z_I Z_J}{|\hat{R}_I - \hat{R}_J|} \quad . \quad (2.4)$$

Here, N_e and N_n are the number of electrons and nuclei, respectively. Z_I is the electric charge of the I -th atom and M_I its mass. Here and through the rest of this thesis Hartree atomic units ($\hbar = m_e = e^2 = 1$) are used.

2.2 THE BORN-OPPENHEIMER APPROXIMATION

The Born-Oppenheimer (BO) approximation reduces the complexity of the Schrödinger Eq. 2.1 by separating nuclear and electronic degrees of freedom in the many-body wave function. The assumption at the basis of this approximation is that electrons follow “adiabatically” the movement of the nuclei, and it is based on the different time scale characteristic of the electronic and nuclear motion. This leads to a factorization of the wave function into a nuclear part χ and an electronic part Ψ :

$$|\Phi\rangle = |\Psi\rangle \otimes |\chi\rangle \quad . \quad (2.5)$$

The BO approximation is exact in the limit of infinite nuclear masses, and it is often a well justified approximation for systems composed by elements with large atomic numbers. On the other hand, compounds containing light elements, such as hydrogen and lithium, may be characterized by non-adiabatic coupling of electronic and nuclear degrees of freedom, and therefore the BO approximation may no longer be adequate. In the field of spectroscopy, a known effect arising from non-adiabatic couplings is, for instance, the zero-temperature electron-phonon renormalization of band-gaps in semiconductors [2, 3] and, more generally, all effects arising from electron-vibration interactions as, e.g., vibrational replicas in the photo-emission spectra of molecules [4]. For semiconductors, the impact of electron-phonon coupling on band gaps is of the order of 20-50 meV [5]. For molecules, nuclear vibrations might lead to shifts of the order of 5 to 20 meV in the ionization energies of aromatic molecules [6]. However, for simplicity non-adiabatic electron-vibration couplings will not be considered here, and these effects will be neglected in the theory-experiment comparisons reported in later Chapters unless otherwise stated. All of the work presented in the following will focus on electronic degrees of freedom in the BO approximation, with the nuclei fixed at their equilibrium configuration.

THE ELECTRONIC HAMILTONIAN

If electrons and nuclei are treated independently, the Schrödinger equation reduces to an eigenvalue problem, similar to Eq. 2.1, for the electronic degrees of freedom only. The solution of the electronic problem requires the solution of the electronic Schrödinger equation:

$$\hat{H}_e |\Psi_n\rangle = E_n^e |\Psi_n\rangle \quad , \quad (2.6)$$

where the electronic Hamiltonian \hat{H}_e is defined by:

$$\hat{H}_e = \hat{T}_e + \hat{V}_{e-e} + \hat{V}_{e-n} \quad , \quad (2.7)$$

or in second-quantized form:

$$\hat{H}_e = \sum_{ij} h_{0,ij} \hat{c}_i^\dagger \hat{c}_j + \sum_{ijklm} v_{ijklm} \hat{c}_i^\dagger \hat{c}_j^\dagger \hat{c}_m \hat{c}_l \quad , \quad (2.8)$$

where $v_{ijklm} = \langle \phi_i \phi_j | \hat{V}_{e-n} | \phi_l \phi_m \rangle$ and $h_{0,ij} = \langle \phi_i | \hat{T}_e + \hat{V}_{e-n} | \phi_j \rangle$. \hat{c}_i^\dagger and \hat{c}_i are the creation and annihilation operators of the single-particle state ϕ_i .

Here the electron-nuclei interaction \hat{V}_{e-n} depends parametrically on the nuclear coordinates, i.e., the \hat{R} operators become real numbers. Then, \hat{V}_{e-n} can be expressed as a single-particle operator, since

$$\hat{V}_{e-n} = \sum_i^{N_e} \hat{v}_{\text{ext}}(\hat{\mathbf{r}}_i) \equiv \sum_i^{N_e} \left(\sum_I^{N_n} \frac{-Z_I}{|\hat{\mathbf{r}}_i - R_I|} \right) \quad , \quad (2.9)$$

where I defined the external potential as $\hat{v}_{\text{ext}}(\hat{\mathbf{r}}_i) \equiv \sum_I \frac{-Z_I}{|\hat{\mathbf{r}}_i - R_I|}$. Similarly, V_{n-n} and T_n in Eq. 2.2 become real additive constants that do not alter the electronic eigenstates, but just introduce a rigid shift of the entire eigenvalue spectrum.

2.3 AB-INITIO ELECTRONIC-STRUCTURE APPROACHES

Even within the Born-Oppenheimer approximation, the electronic Schrödinger equation (Eq. 2.6) is tractable analytically only for a few cases. Three simple examples are the free particle, the hydrogen atom, and the harmonic oscillator – all cases for which there is no electron-electron interaction in the electronic Hamiltonian, i.e., $V_{e-e} = 0$ in Eq. 2.7. For real systems involving two electrons or more, however, the eigenvalue problem in Eq. 2.6 cannot be solved analytically due to the presence of the electron-electron Coulomb-interaction term, which introduces correlation of the electronic motion.

For a considerably small number of electrons ($N_e < 10 - 15$), Eq. 2.7 may be tackled by means of numerical techniques as full configuration interaction (full-CI) [7] or quantum Monte Carlo methods [8, 9]. However, the computational load required by the exact solution of Eq. 2.7 increases exponentially with the number of degrees of freedom of the many-body wave function. Therefore, for a broad class of physically interesting systems the Schrödinger equation must be approximated.

Within the class of *ab initio* (or first-principles) electronic-structure approaches, approximations are developed starting from the fundamental laws of quantum mechanics. Different approximate *ab-initio* approaches have been developed over the years. The most prominent are density-functional theory (DFT) [10–12], many-body perturbation theory (MBPT) [7, 13, 14], coupled-cluster theory [15] and quantum Monte-Carlo methods [8, 9]. Each approach has its strengths and weaknesses in terms of accuracy, applicability, and computational efficiency. The framework of choice here is MBPT, for which a concise account will be given in Chap. 3.

Wave-function-based methods, such as coupled cluster and full configuration in-

teraction, are the most accurate methods at hand for small molecules, and therefore will be used as references in the following Chapters. An introduction to Hartree-Fock, coupled-cluster methods, and full configuration interaction is given in Sec. 2.4. DFT methods will also be employed in this work – mostly as starting point for MBPT-based first-order perturbation theory – and a short review of the theory will be presented in Sec. 2.5.

2.4 WAVE-FUNCTION-BASED METHODS

The family of wave-function-based methods addresses the electronic problem by introducing an *ansatz* for the form of the many-body wave function, and solving the electronic Schrödinger equation within the sub-space defined by the chosen wave-function form. Methods belonging to this family are, for instance, Hartree-Fock, coupled cluster, and full configuration interaction, that will shortly be introduced below.

In later Chapters, Hartree-Fock will mostly be used as initial reference state for many-body perturbation-theory calculations, whereas coupled cluster and full configuration interaction will be employed as reference methods for quantities not available experimentally, such as total energies and electron densities.

HARTREE-FOCK

In the Hartree-Fock approximation (HF), the ground-state electronic wave function Ψ takes the form of a Slater determinant [16], that for an N -electron system can be expressed as:

$$\Psi_0(\mathbf{r}_1, \dots, \mathbf{r}_N) = \frac{1}{N!} \begin{vmatrix} \psi_1(\mathbf{r}_1) & \dots & \psi_1(\mathbf{r}_N) \\ \vdots & \ddots & \vdots \\ \psi_N(\mathbf{r}_1) & \dots & \psi_N(\mathbf{r}_N) \end{vmatrix} . \quad (2.10)$$

Here, $\psi_n(\mathbf{r}_j)$ denotes the n -th single-particle orbital occupied by the j -th electron. The wave function expressed by Eq. 2.10 is the simplest wave-function form that properly accounts for the indistinguishable nature of electrons and for their fermionic character.

In HF, the structure of the wave function in Eq. 2.10 implies that electrons interact with each other only through the Hartree mean field and through the exact-exchange potential. The many-body correlations arising from Coulomb interactions are completely neglected: this makes HF the reference method for the definition of Coulomb correlation in quantum chemistry. In practice, the Coulomb correlation is quantitatively defined as the difference between the non-relativistic energy of a system and its total energy in the HF approximation.

By restricting the Hilbert space to wave functions of the form given in Eq. 2.10, the Schrödinger equation can be solved by seeking – through a Lagrange multiplier method [7] – the set of single-particle orbitals that minimizes the total energy. This procedure

leads to the HF equations:

$$[h_0(\mathbf{r}) + v_H(\mathbf{r})]\psi_n^\sigma(\mathbf{r}) + \int d\mathbf{r}' \Sigma_x^\sigma(\mathbf{r}, \mathbf{r}') \psi_n^\sigma(\mathbf{r}') = \epsilon_n^\sigma \psi_n^\sigma(\mathbf{r}) \quad , \quad (2.11)$$

where h_0 is the sum of the kinetic-energy operator and the external potential. Σ_x^σ is the exact-exchange operator, defined by:

$$\Sigma_x^\sigma(\mathbf{r}, \mathbf{r}') = - \sum_n^{\text{occ}} \int d\mathbf{r}'' \frac{\psi_n^{\sigma*}(\mathbf{r}'') \psi_n^\sigma(\mathbf{r}'')}{|\mathbf{r} - \mathbf{r}''|} \quad , \quad (2.12)$$

and v_H is the Hartree potential:

$$v_H(\mathbf{r}) = \sum_\sigma \sum_n^{\text{occ}} \int d\mathbf{r}' \frac{\psi_n^{\sigma*}(\mathbf{r}') \psi_n^\sigma(\mathbf{r}')}{|\mathbf{r} - \mathbf{r}'|} = \int d\mathbf{r}' \frac{n(\mathbf{r}')}{|\mathbf{r} - \mathbf{r}'|} \quad . \quad (2.13)$$

Here, the electron density n is defined as $n(\mathbf{r}) = \sum_\sigma \sum_n^{\text{occ}} \psi_n^{\sigma*}(\mathbf{r}) \psi_n^\sigma(\mathbf{r})$. Equations 2.11-2.13 define a closed set of integro-differential equations that must be solved self-consistently, to obtain the single-particle orbitals ψ_n^σ and eigenvalues ϵ_n^σ .

In HF, the single-particle eigenvalues may be approximately related to ionization energies and electron affinities. For a N -electron system, the s -th ionization energy I is defined as:

$$I_s = E(N) - E_s(N-1) \quad , \quad (2.14)$$

where $E(N)$ is the ground-state total energy and $E_s(N-1)$ the total energy of the $(N-1)$ -particle system in its s -th excited state. The electron affinity A is defined analogously as:

$$A_s = E_s(N+1) - E(N) \quad . \quad (2.15)$$

Koopmans' theorem provides an approximate recipe to relate ionization energies and the single-particle eigenvalues in the HF approximation:

$$-\epsilon_s \simeq E(N) - E_s(N-1) = I_s \quad . \quad (2.16)$$

A similar relation holds for the electron affinities. In the context of Hartree-Fock, Eq. 2.16 is valid in the *frozen-orbital* approximations, i.e., under the assumption that – after the removal of the s -th electron from an N -electron system – the remaining $N-1$ single-particle orbitals do not relax. The agreement of Koopmans' ionization energies in HF with the experimental ones is in most cases only qualitative: For atoms and molecules, ionization energies are generally found within 2 – 5 eV from the experimental reference [7]. This and other shortcomings arise from the lack of Coulomb correlation in HF and from the frozen-orbital approximation.

FULL CONFIGURATION INTERACTION

To properly account for Coulomb correlation in wave-function-based methods, it is necessary to go beyond the Hartree-Fock approximation for the wave function. In full configuration interaction, the wave function is expanded in a basis of Slater determinants, as:

$$|\Psi\rangle = c_0|\Psi_0\rangle + \sum_{ar} c_a^r |\Psi_a^r\rangle + \left(\frac{1}{2!}\right)^2 \sum_{\substack{ab \\ rs}} c_{ab}^{rs} |\Psi_{ab}^{rs}\rangle + \left(\frac{1}{3!}\right)^2 \sum_{\substack{abc \\ rst}} c_{abc}^{rst} |\Psi_{abc}^{rst}\rangle + \dots \quad (2.17)$$

Here, $|\Psi_0\rangle$ denotes the Slater determinant of the HF ground state. $|\Psi_a^r\rangle$ is a singly-excited Slater determinant, which is defined as in Eq. 2.10, but where the a -th occupied single-particle orbital is replaced by the r -th unoccupied orbital. Similarly, $|\Psi_{ab}^{rs}\rangle$ denotes doubly-excited Slater determinants, and so on. In Eq. 2.17, the sums over a, b, c, \dots run over the occupied states of a preliminary HF calculation, whereas the sums over r, s, t, \dots run over unoccupied HF orbitals. The coefficients $c_0, c_a^r, c_{ab}^{rs}, \dots$ are determined by diagonalization of the Hamiltonian matrix [7].

The wave function in Eq. 2.17 is referred to as full configuration-interaction (full-CI) wave function, and is exact within a given basis set. In the complete-basis-set limit, full-CI is an exact solution of the Schrödinger equation in the Born-Oppenheimer approximation. It is evident however, that the rank of the full-CI Hamiltonian matrix grows exponentially with the system size, due to all possible combinations of excited determinants that must be accounted for. Therefore, full-CI calculations are prohibitive for systems with more than 10-15 electrons, although the combination of full-CI with quantum Monte-Carlo allows to treat systems up to 30-50 electrons with comparable accuracy [17, 18]. Approximated CI expansions may be obtained by truncating the sum in Eq. 2.17 to a certain order, e.g. including only singly and doubly excited Slater determinants. Approximated wave functions based on the truncation of Eq. 2.17, however, are affected by the *size-consistency* problem: the total energy of a polyatomic system does not scale correctly (i.e., linearly) with the number of electrons.

COUPLED CLUSTER

Coupled-cluster methods [15, 19, 20] approximate the wave function in the form:

$$|\Psi_{cc}\rangle = e^{\hat{T}}|\Psi_0\rangle = (1 + \hat{T} + \frac{1}{2!}\hat{T}^2 + \frac{1}{3!}\hat{T}^3 + \dots)|\Psi_0\rangle \quad . \quad (2.18)$$

The operator \hat{T} is defined as $\hat{T} = \hat{T}_1 + \hat{T}_2 + \dots + \hat{T}_N$, where N is the total number of electrons and:

$$\hat{T}_1|\Psi_0\rangle = \sum_{ar} c_a^r |\Psi_a^r\rangle \quad (2.19)$$

$$\hat{T}_2|\Psi_0\rangle = \sum_{\substack{ab \\ rs}} c_{ab}^{rs} |\Psi_{ab}^{rs}\rangle \quad (2.20)$$

⋮

Based on the above definitions the exponential operator can be rewritten by grouping the terms corresponding to the same excitation order:

$$e^{\hat{T}} = 1 + \hat{T}_1 + \left(\hat{T}_2 + \frac{\hat{T}_1^2}{2!}\right) + \left(\hat{T}_3 + \hat{T}_1\hat{T}_2 + \frac{\hat{T}_1^3}{3!}\right) + \dots \quad (2.21)$$

If the full operator $e^{\hat{T}}$ is considered, then Eq. 2.18 coincides with the full-CI wave function. As in full-CI, once the structure of the coupled-cluster wave function is defined, the electronic problem is solved by diagonalization of the Hamiltonian matrix [7].

As compared to the full-CI *ansatz* of Eq. 2.17, the advantage of the coupled-cluster wave-function form is that one may obtain accurate approximations to Ψ through the truncation of the \hat{T} operator expansion to the second (coupled-cluster singles doubles, or CCSD) or third order (CCSDT). Coupled cluster singles, doubles, with the perturbative inclusion of triples – in short, CCSD(T) – is considered the “gold standard” of quantum chemistry because it yields an accuracy of approximately 40 meV (1 Kcal/mol) for the ground-state properties of molecules, at a much lower computational cost than full-CI [21]. Approximations based on the truncation of coupled-cluster expansion for the wave function are not affected by the size-consistency problem and are therefore preferable to methods based on the truncation of the CI expansion.

2.5 DENSITY-FUNCTIONAL THEORY

Since the early years of quantum mechanics, approaches that recast the Schrödinger equation into a simplified form involving only the electron density have been popular. In contrast to the many-body wave function – which depends on $3N$ coordinates, N being the number of electrons – the electron density has only 3 degrees of freedom and is a simpler and more manageable object. The first progress in this context was due to Thomas [22] and Fermi [23], which in 1927 proposed independently an approximate model – known as the Thomas-Fermi model – for electrons in an external potential, which used the electron density as central variable. An additional approach is due to Slater: The X_α method [24].

The question whether the density (and functionals of the density) uniquely deter-

mines the wave function – and, therefore, the physical properties – of a quantum-mechanical system was eventually answered by Hohenberg and Kohn (HK) in 1964 [10]. Hohenberg and Kohn proved two theorems, which may be summarized as follows.

1. Given an inhomogeneous electron system moving in a time-independent external potential \hat{V}_{e-n} ¹ there is a one-to-one correspondence between the external potential \hat{V}_{e-n} and the ground-state electron density. As the potential \hat{V}_{e-n} determines the many-body Hamiltonian, the ground-state wave function of the system follows uniquely from the ground-state density. Thus, there exists a one-to-one correspondence between the many-body ground state of a system and its density.
2. Because of point 1. one can express the total energy as a (in principle unknown) universal (i.e., system independent) functional of the density. A variational principle demonstrates that this universal functional has an absolute minimum that is reached for the exact density of the system.

These two theorems indicate that the total energy of a system in its ground state can be expressed as a functional of the density, i.e., $E_{\text{tot}} = E_{\text{tot}}[n]$, although the functional dependence of E_{tot} on n is (and probably will remain) unknown. Several extensions of the HK theorem have been proposed over the years to account for systems with a degenerate ground state [25], spin-dependent interactions and interactions with magnetic fields [26], finite temperature [27], and time-dependent potentials [28]. A detailed overview is given, for instance, in Refs. [12, 25, 29, 30]. The HK theorems can be generalized to encompass excitations [31, 32]. However, the applicability of the theorem for excited states is considerably more limited, since no one-to-one correspondence between the density and excited eigenstates of the Hamiltonian exists [32]. Nevertheless, there exists a one-to-one correspondence between the Green function and the electron density and, therefore, the Green function G may also be expressed as a unique functional of the density [31]. In other words, the electron density uniquely determines also single-particle excitations, but since the functional dependence of G on the density is not known this relation is not directly applicable to the computation of single-particle excitations.

KOHN-SHAM FORMULATION OF DFT

To translate the Hohenberg-Kohn theorems into a concrete recipe for electronic-structure calculations, Kohn and Sham (KS) introduced a fictitious non-interacting-particle system (also referred to as KS system), with the same spatial density as the *real* interacting system [11]. The density of the non-interacting reference system would then yield the exact total energy of the interacting system, if the functional dependence of the total energy on the electron density were known, and if the effective single-particle potential v_{eff} that defines the KS system exists. The mapping of the many-body problem into a

¹As an example, the external potential can be of the form given in Eq. 2.9, although the HK theorem is more general.

system of non-interacting particles does not constitute an approximation. Therefore, as discussed below, the KS method allows one to tackle the many-body problem – in principle exactly, although approximations become necessary in practice – by solving the following set of single-particle-like Schrödinger equations:

$$\left[-\frac{\nabla^2}{2} + v_{\text{eff}}[n](\mathbf{r}) \right] \psi_n(\mathbf{r}) = \epsilon_n \psi_n(\mathbf{r}) \quad , \quad (2.22)$$

where the density is constructed by means of the single-particle orbitals as

$$n(\mathbf{r}) = \sum_{i=1}^{\text{occ}} \psi_i^*(\mathbf{r}) \psi_i(\mathbf{r}) \quad , \quad (2.23)$$

and $v_{\text{eff}}[n]$ is an effective single-particle potential defined as:

$$v_{\text{eff}}[n](\mathbf{r}) \equiv v_{\text{H}}[n](\mathbf{r}) + v_{\text{ext}}(\mathbf{r}) + v_{\text{xc}}[n](\mathbf{r}) \quad . \quad (2.24)$$

The Hartree potential v_{H} and the external potential v_{ext} are defined as in Eqs. 2.13 and 2.9, respectively. Here, v_{xc} is the exchange-correlation potential, which accounts for all electron-electron interactions beyond the classical Hartree potential and for the kinetic correlation energy, i.e., the difference between the full kinetic energy and the kinetic energy of the KS non-interacting system. v_{xc} is related to the exchange-correlation energy E_{xc} by the equality:

$$v_{\text{xc}}[n](\mathbf{r}) = \frac{\delta E_{\text{xc}}[n]}{\delta n(\mathbf{r})} \quad . \quad (2.25)$$

The self-consistent solution of Eqs. 2.22-2.24 would yield the exact ground-state density and total energy, if $v_{\text{xc}}[n]$ were known. Unfortunately, the dependence of v_{xc} on the electron density is unknown and must be approximated.

DENSITY-FUNCTIONAL APPROXIMATIONS

Since the performance of density-functional calculations is contingent to the approximation for the exchange-correlation functional, several hundreds of approximations to v_{xc} were proposed over the years. A comprehensive list of the most widely used approximations has been reported by Marques *et al.* [33]. The most relevant are generally classified in the following sorting categories:

- Local-density approximations (LDA) [11, 34].
- Generalized gradient approximations (GGA) [35].
- Meta-generalized gradient approximations (meta-GGA) [36].
- Hybrid functionals [37].²

²These class of functionals involve a generalization of the KS approach to spatially non-local exchange-

- Self-interaction corrected functionals [38].
- Optimized effective potentials (OEP) [30].

In the LDA, the exchange-correlation functional is expressed in terms of the electron density (and not, for instance, its derivatives). More flexibility is given in GGA-type approximations, where $E_{xc}[n]$ is expressed in terms of the density and gradients of the density. Meta-GGA approximations, on the other hand, also introduce a dependence of the exchange-correlation functional on the second derivatives (i.e., the Laplacians) of the density. Hybrid functionals, as discussed below in more detail, can be obtained from any of the above through the replacement of a fraction α of (local) exchange with HF exact exchange. In self-interaction corrected functionals, the exchange-correlation functional is obtained by introducing non-local corrections that eliminate the self-interaction error characteristic of local functionals. Finally, OEP-based exchange correlation potentials denote a class of local potentials derived from non-local, orbital-dependent expressions for the exchange-correlation energy.

DFT calculations based on the LDA often give good agreement with experimental ground-state properties for systems in which the electron density varies slowly in space, such as metals and *sp*-bonded semiconductors [39]. On the other hand, for atoms and small molecules, where the density is rapidly varying, the LDA systematically overestimates binding energies and bond lengths. As compared to the LDA, GGA functionals are in better agreement with experimental atomization energies and structural parameters, in particular for atoms and small molecules [40]. One of the most popular GGA functionals, is the one proposed by Perdew, Burke, and Ernzerhof [41], denoted PBE in the following. The PBE functional describes well the structural properties of molecules and the cohesive properties of solids, although it exhibits a tendency to underestimate binding and cohesive energies. Moreover, PBE largely underestimates dispersive (e.g., van der Waals) interactions, which are generally accounted for in a post-processing fashion, as discussed for instance in Ref. [42].

One of the main shortcomings of semi-local density functionals of the GGA or LDA type is the presence of a spurious interaction of an electron with itself – denoted as *self-interaction* error. This problem arises from the approximate treatment of the exchange interaction and is at the origin of several pathologies of semi-local DFT, such as the delocalization error [43–45]. Hybrid density functionals ameliorate this problem by replacing a fraction of the local exchange functional with the non-local Hartree-Fock exact-exchange operator. For a given semi-local exchange-correlation potential v_{xc} , a hybrid functional v_{xc}^H can be generated as follows:

$$v_{xc}^H(\mathbf{r}, \mathbf{r}') = v_c(\mathbf{r}) + (1 - \alpha)v_x(\mathbf{r}) + \alpha\Sigma_x(\mathbf{r}, \mathbf{r}') \quad , \quad (2.26)$$

correlation potentials. This extension of the basic KS formalism is often referred to as generalized Kohn-Sham (GKS) DFT.

where $v_{c(x)}$ is the correlation (exchange) part of v_{xc} , and Σ_x is the exact-exchange operator of Hartree-Fock theory (defined in Eq. 2.12). Here, α is a parameter that regulates the admixture of Hartree-Fock and GGA exchange. Through Eq. 2.26 the self-interaction error may be removed completely by setting $\alpha = 1$. However, the self-interaction error is in part responsible for fortunate error cancellations that ultimately improve the performance of semi-local density functionals [46, 47]. Hence, the full elimination of the self-interaction error is counter-productive and deteriorates the agreement with experiment. In practice, most hybrid functionals employ values of α that range between 0 and 0.5. In the present work, most DFT calculations are based on the PBE exchange-correlation potential, its hybrid variant PBE0 obtained from Eq. 2.26 with $\alpha = 0.25$ (where the fraction of exact exchange is derived *ab initio* based on perturbation theory [48]), and PBE-based hybrids with different values of α [49].

To construct the exchange-correlation potential from Eq. 2.25, the dependence of the exchange-correlation energy E_{xc} on the electron density must be known. In several instances, however, approximations to E_{xc} depend explicitly on single-particle orbitals (i.e., $E_{xc} = E_{xc}[\{\psi_n\}]$) as, for instance, the just mentioned hybrid functionals and the random-phase approximation introduced below. Since the explicit dependence of the single-particle orbitals on the electron density is not known, the functional derivative $\delta E_{xc}[\{\psi_n\}]/\delta n(\mathbf{r})$ – required for the determination of the corresponding KS potential – cannot be evaluated straightforwardly. The optimized effective potential (OEP) method denotes a class of approaches that allow one to derive a closed expression for v_{xc} from an orbital-dependent exchange-correlation energy functional $E_{xc}[\{\psi_n\}]$ [30, 50, 51]. Most approaches to the OEP problem are based on the Sham-Schlüter equation [30, 50, 52], on the chain rule [30, 50], or on the direct-minimization scheme proposed by Yang and Wu [53]. The Sham-Schlüter equation will be introduced in Chap. 3, whereas the direct minimization approach will be discussed in Chap. 9.

As an example, I will summarize here the application of the chain-rule method to the evaluation of the local exact-exchange KS potential $v_x(\mathbf{r})$ – one of the OEP potentials that found the broadest application in electronic-structure theory [30]. The exact-exchange KS potential is the local potential corresponding to the Hartree-Fock exchange energy:

$$E_x[\{\psi_n\}] = \frac{1}{2} \sum_{n,m}^{\text{occ}} \int d\mathbf{r} d\mathbf{r}' \frac{\psi_n(\mathbf{r})\psi_n^*(\mathbf{r}')\psi_m(\mathbf{r})\psi_m^*(\mathbf{r}')}{|\mathbf{r} - \mathbf{r}'|}, \quad (2.27)$$

that depends explicitly on the occupied single-particle orbitals $\{\psi_n\}$. Making use of the chain rule (Eq. A.6 in Appendix A), the exact-exchange KS potential can be rewritten as (see, e.g., Ref. [54]):

$$v_x(\mathbf{r}) \equiv \frac{\delta E_x[\{\psi_n\}]}{\delta n(\mathbf{r})} = \sum_n \int d\mathbf{r}' d\mathbf{r}'' \left[\frac{\delta E_x[\{\psi_n\}]}{\delta \psi_n(\mathbf{r}')} \frac{\delta \psi_n(\mathbf{r}')}{\delta v_{\text{eff}}(\mathbf{r}'')} + c.c. \right] \frac{\delta v_{\text{eff}}(\mathbf{r}'')}{\delta n(\mathbf{r})}, \quad (2.28)$$

where v_{eff} is the total effective KS potential. As discussed in detail in Ref. [54], the first functional derivative in the right-hand side of Eq. 2.28 can be evaluated explicitly from

Eq. 2.27, the last one yields the inverse (non-interacting) KS response function (Eq. 2.30), whereas $\delta\psi_n(\mathbf{r}')/\delta v_{\text{eff}}(\mathbf{r}'')$ may be evaluated by resorting to perturbation theory. In practice, with some manipulation it is possible to derive a closed expression for the local exact-exchange KS potential. This strategy may be applied also to orbital-dependent functionals for the correlation energy, such as the RPA correlation energy introduced below [55]. However, the complexity and the applicability of the resulting local potential depend crucially on the initial form for the energy functional.

PHYSICAL INTERPRETATION OF THE DFT ORBITALS AND EIGENVALUES

The orbitals and orbital energies derived from a Kohn-Sham (KS) DFT calculation are single-particle quantities that characterize the non-interacting KS reference system. The electron density derived from the occupied KS orbitals coincides with that of the real system, but the energy hierarchy of the KS orbitals does not necessarily reflect the band structure of a solid, or the energy levels of a molecule. Generally, some care is needed when interpreting the KS eigenvalues as excitation energies. In practice, the agreement of experimental IEs and KS orbital energies is often poor. For instance for semi-local functionals, the average percentage error between the KS HOMO and the first IE is of the order of 40-50% (see e.g. Refs. [56–58]), although some improvement may be obtained – at the cost of introducing empirical parameters in the exchange-correlation potentials – for hybrid and range-separated functionals [59]. On the whole, the physical interpretation of the (generalized) KS orbitals and orbital energies has been a controversial matter of debate.

Janak [60] demonstrated that the highest occupied molecular orbital (HOMO) of exact KS-DFT equals the chemical potential of the system [60–64], and therefore it might be related to the first ionization energy defined in Eq. 2.14. Analogous to Koopmans' theorem of HF theory, the Janak's theorem shows that first KS eigenvalue can be approximately interpreted as the ionization energy. If combined with Slater's transition-state concept (STS) [65, 66] – where the ionization energies are approximated by (minus) the KS eigenvalue at half occupations, i.e., $-I_s^{\text{STS}} = \epsilon_s^{\text{KS}}(N - 1/2)$ – this is even an excellent approximation. On the other hand, no such theorem exists to relate the electron affinity – defined in Eq. 2.15 – and the lowest unoccupied molecular orbital (LUMO) of KS theory, or for any other single-particle excitation of the system. However, even for the first ionization energy the agreement with experiment is often only qualitative, mostly due to the impact of the self-interaction error on the single-particle eigenvalues. Non-local functionals – such as hybrids and range-separated hybrids – permit one to alleviate the self-interaction error of semi-local functionals, and generally yield a better agreement between the HOMO and the ionization energy. In fact, as demonstrated by Atalla *et al.* in Ref. [67] it is generally possible to determine a fraction of exact exchange α that yields a first ionization energy in agreement with quasi-particle calculations based on the *GW* approximation. This is not surprising since one may argue that non-local exchange-correlation potentials can be interpreted as approximate many-body self-energies with

static screening and, consequently, the single-particle eigenvalues can be approximately related to quasi-particle excitations.

A more rigorous approach for determining single-particle excitation energies from DFT calculations is the Δ self-consistent field method (Δ -SCF). Based on definition of the ionization energy and the electron affinity in Eqs. 2.14-2.15, in the Δ -SCF approach the excitation energies are evaluated as total energy differences from distinct DFT calculations. A first calculation for an N -electron system yields the total energy $E(N)$; a second DFT calculation for the system with $N - 1$ (or $N + 1$) electrons provide $E(N - 1)$ (or $E(N + 1)$). Then, the ionization energy and electron affinity can be straightforwardly derived from the definitions in Eqs. 2.14-2.15. Since DFT is in principle exact for the total energy, the Δ -SCF approach would yield the correct ionization energies and electron affinities if evaluated with the exact exchange-correlation functional. For the first ionization energy of closed-shell molecules, Δ -SCF yields good quantitative agreement with experiment (see e.g. [56]), and, therefore, it provides an inexpensive alternative to Green-function-based calculations.

RANDOM-PHASE APPROXIMATION (RPA)

The random-phase approximation (RPA) was originally proposed by Bohm and Pines [68–70] for the electron gas, but recently it has also been applied to periodic [71–73] and finite systems [74–76]. The RPA is an orbital-dependent functional for the correlation energy, and is given by:

$$E_c^{\text{RPA}} = \int_0^\infty \frac{d\omega}{2\pi} \text{Tr} [\ln(1 - \chi_s(i\omega)v) + \chi_s(i\omega)v] \quad , \quad (2.29)$$

where $\chi_s(i\omega)$ is the non-interacting KS density-density response function, which can be expressed through the Adler-Wiser formula:

$$\chi_s(\mathbf{r}, \mathbf{r}', \omega) = \sum_\sigma \sum_n^{\text{occ}} \sum_m^{\text{empty}} \frac{\psi_n^{\sigma*}(\mathbf{r})\psi_m^\sigma(\mathbf{r})\psi_n^\sigma(\mathbf{r}')\psi_m^{\sigma*}(\mathbf{r}')}{\omega - (\epsilon_n^\sigma - \epsilon_m^\sigma) + i\eta} + c.c. \quad . \quad (2.30)$$

The Goldstone diagrams for the RPA correlation energy are depicted in Fig. 2.1.

The RPA correlation energy is often evaluated perturbatively on top of a DFT calculation – i.e., Eqs. 2.29 and 2.30 are evaluated using DFT orbitals and orbital energies – and combined with exact-exchange (denoted in the following EX+cRPA). EX+cRPA ameliorates several deficiencies of conventional approximations to DFT, such as the self-interaction error and the poor description of van der Waals interactions [77]. The performance of the EX+cRPA method for molecules and *sp*-bonded solids has been well benchmarked in the literature (see e.g. Refs. [77–79] for a review). As compared to semi-local and hybrid DFT, EX+cRPA noticeably improves the binding and cohesive energies of weakly-bonded molecules and solids, respectively, due to the seamless inclusion of van der Waals forces. For covalently-bonded systems on the other hand, the performance of EX+cRPA is disappointing since it does not improve over PBE, and is

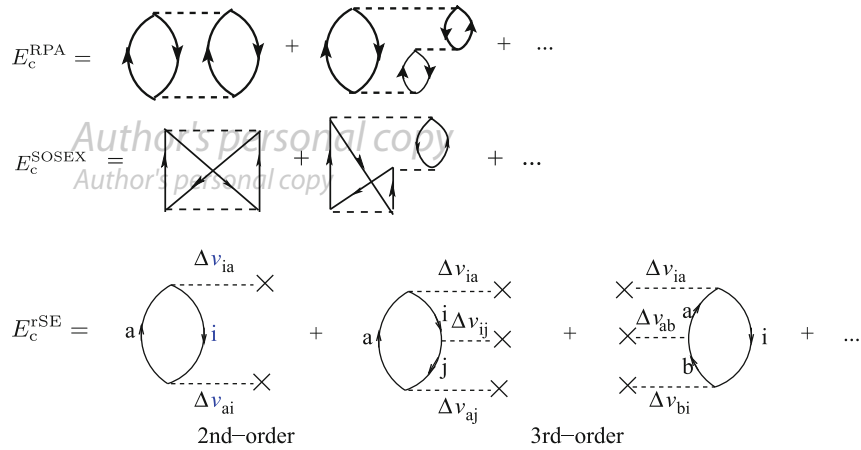


Figure 2.1: Representation of the RPA, SOSEX, and rSE contribution to the correlation energy in terms of Goldstone diagrams [7]. Adapted from Ref. [77]. Upgoing (downgoing) solid lines represent particles (holes) associated with unoccupied (occupied) orbital energies, whereas dashed lines denote the bare Coulomb interaction. Dashed lines ending with a cross denote matrix elements of the form $\langle \psi_n | -\hat{\nabla}^2/2 + \hat{v}_{\text{ext}} + \hat{v}^{\text{HF}} | \psi_m \rangle$, \hat{v}^{HF} being the self-consistent Hartree-Fock single-particle potential (see Ref. [77] for more details).

not as good as hybrid DFT [77]. The reader is referred to Ref. [77] and references therein for a comprehensive overview of the performance of perturbative EX+cRPA.

The relevance of the RPA for the present work stems mostly from its analogy with the *GW* approximation, that will be addressed in detail in Chap. 9.

BEYOND RPA: RENORMALIZED SECOND-ORDER PERTURBATION THEORY

A prominent shortcoming of EX+cRPA is the spurious *self-correlation* error that affects the RPA correlation energy functional. The self-correlation – defined in analogy to the well known self-interaction error – emerges in Eq. 2.29 due to the self-screening of an electron. The effects of this error are exemplified by the non-zero correlation energy of one-electron systems. The self-correlation error (and the missing higher-order diagrams) are responsible for the systematic overestimation of total energies, for the underestimation of binding energies, and for the failure to describe stretched radicals.

The inclusion of second-order screened exchange (SOSEX) to EX+cRPA mitigates the self-correlation error [80, 81] by adding higher-order (screened-) exchange diagrams – represented in Fig. 2.1 – to the RPA series of ring diagrams. EX+cRPA+SOSEX is self-correlation free in the one electron case, however some self-correlation error is still present for more electron systems. The performance of the SOSEX correction for finite systems has been investigated by Paier and coworkers [82, 83]. In certain cases, EX+cRPA+SOSEX performs better than the simpler EX+cRPA, however the improvements are not systematic. The reason for this is that the self-correlation error often mimics the effects of higher-order energy diagrams neglected in EX+cRPA. Therefore, it may occur that EX+cRPA+SOSEX deteriorates the results of EX+cRPA, as it happens for

the dissociation of covalently-bonded systems [77].

To further improve total and binding energies of finite systems, an additional beyond-RPA scheme has recently been proposed by Ren and coworkers [80], based on the inclusion of single-excitation (SE) terms in the total energy. For perturbative calculations based on Hartree-Fock, the SE contribution to the total energy is zero due to the Brillouin theorem [7]. However, for other (e.g., DFT-based) starting points the SE contribution to the total energy cannot be neglected. As compared to conventional EX+cRPA calculations, the combination of EX+cRPA and SE considerably improves the binding energy of weakly bounded systems, as exemplified [80] by the lower average error for the binding energies of the S22 set of weakly bounded compounds [84]. In the same spirit of RPA, the SE correction can also be “renormalized” by summing up a series of (infinitely many) higher-order SE corrections. This leads to the renormalized SE correction (rSE), for which the diagrammatic series is depicted in Fig. 2.1.

Renormalized second-order perturbation theory (rPT2), recently proposed in Refs. [77, 82], combines the elements introduced above: EX+cRPA, SOSEX, and rSE. All the exchange- and correlation-energy diagrams depicted in Fig. 2.1 are included in the rPT2 total energy. The rPT2 nomenclature follows from the consideration that the “unscreened” rPT2 diagrammatic series accounts for all second-order Rayleigh-Schrödinger perturbation-theory (RSPT) diagrams. Second-order Møller-Plesset perturbation theory (MP2), for instance, is straightforwardly recovered by keeping only the leading terms (i.e., the first diagram in Fig. 2.1) in the diagrammatic expansion of the RPA and SOSEX series. In rPT2, the renormalization of the second-order diagrams allows to avoid the divergence of the total energy for small values of the HOMO-LUMO gap, that affects conventional RSPT. rPT2 is a powerful perturbative approach for the evaluation of correlation energies in finite systems and, according to recent benchmark data, it yields atomization energies with an average accuracy of 0.1 eV [77, 85].

3 GREEN-FUNCTION METHODS

Green functions are central in the development of MBPT [13, 86]. The single-particle Green function is a mathematical object which may be associated with the probability amplitude of the propagation processes of a particle (or a hole) in an N -particles system. Owing to its connections to ground- and excited-state properties, the electronic single-particle Green function is particularly useful in electronic-structure theory, and its calculation is the primary goal of the theoretical and numerical methods presented in Parts I and II of this thesis, respectively.

In this Chapter, I will briefly review the zero-temperature Green function formalism that is relevant for the development of the subsequent parts of this work.

3.1 DEFINITION OF THE GREEN FUNCTION

The single-particle Green function is defined as:

$$G(1, 2) = -i \langle \Psi | \hat{T} [\hat{\psi}(1) \hat{\psi}^\dagger(2)] | \Psi \rangle \quad , \quad (3.1)$$

where the collective index for space-time-spin variables $1 \equiv \{\mathbf{r}_1, t_1, \sigma_1\}$ was introduced. The ket $|\Psi\rangle$ labels the normalized many-body wave function of the N -electron ground state, and is related to the electronic Hamiltonian (Eq. 2.7) through the Schrödinger equation. $\hat{\psi}(1)$ and $\hat{\psi}^\dagger(2)$ are annihilation and creation operators in the Heisenberg picture, which obey fermionic anti-commutation relations:

$$[\hat{\psi}_\sigma(\mathbf{r}), \hat{\psi}_{\sigma'}^\dagger(\mathbf{r}')]_+ = \delta(\mathbf{r}, \mathbf{r}') \delta_{\sigma\sigma'} \quad (3.2a)$$

$$[\hat{\psi}_\sigma(\mathbf{r}), \hat{\psi}_{\sigma'}(\mathbf{r}')]_+ = [\hat{\psi}_\sigma^\dagger(\mathbf{r}), \hat{\psi}_{\sigma'}^\dagger(\mathbf{r}')]_+ = 0 \quad . \quad (3.2b)$$

Finally, \hat{T} is Wick's time-ordering operator:

$$\hat{T} [\hat{\psi}(1) \hat{\psi}^\dagger(2)] = \begin{cases} \hat{\psi}(1) \hat{\psi}^\dagger(2) & \text{if } t_1 > t_2 \\ -\hat{\psi}^\dagger(2) \hat{\psi}(1) & \text{if } t_2 < t_1 \end{cases} \quad . \quad (3.3)$$

More generally, the N -particle Green function is defined analogous to Eq. 3.1:

$$G^N(1, \dots, N; 1', \dots, N') = (-i)^N \langle \Psi | \hat{T} [\hat{\psi}(1) \dots \hat{\psi}(N) \hat{\psi}^\dagger(N') \dots \hat{\psi}^\dagger(1')] | \Psi \rangle \quad . \quad (3.4)$$

G^N is linked to $G^{(N+1)}$ and $G^{(N-1)}$ through the so-called Bogoliubov-Born-Green-Kirkwood-Yvon (BBGKY) hierarchy of integro-differential equations, that completely determine the N -particle Green function, if G^{N+1} is known. The first of element ($N = 1$) of the BBGKY chain follows straightforwardly from the commutation relations in Eqs. 3.2a and 3.2b and from the definitions of the one- and two-particle Green functions given in Eqs. 3.1 and 3.4 (see, e.g., Ref. [87] for a derivation):

$$\left[i \frac{\partial}{\partial t_1} - h_0(1) \right] G(1, 2) + i \int d3 v(1, 3) G_2(1, 3^+; 2, 3^{++}) = \delta(1, 2) \quad . \quad (3.5)$$

Here, $h(1) \equiv h_0(\mathbf{r}_1)\delta(t_1)$ is the single-particle term of the electronic Hamiltonian, $v(1, 2) \equiv v(\mathbf{r}_1, \mathbf{r}_2)\delta(t_1 - t_2) = \delta(t_1 - t_2)/|\mathbf{r}_1 - \mathbf{r}_2|$ is the repulsive Coulomb interaction between electrons, and I used the notation $1^+ \equiv \{\mathbf{r}_1, t_1 + \eta, \sigma_1\}$, η being a positive infinitesimal. Equation 3.5 is not directly helpful for the development of approximations, since it expresses the Green function in terms of a more complex object, G_2 . However, Eq. 3.5 may be simplified and rewritten without the two-particle Green function by introducing an auxiliary quantity, the self-energy, which closes the BBGKY hierarchy.

The self-energy Σ is formally defined by the following identity:

$$\int d3 [v_H(3)\delta(3, 1) + \Sigma(1, 3)]G(3, 2) = -i \int d3 v(1, 3)G_2(1, 3^+; 1, 3^{++}) \quad , \quad (3.6)$$

where $v_H(1) \equiv v_H(\mathbf{r}_1)\delta(t_1)$ is the Hartree potential defined in Eq. 2.13. The replacement of Eq. 3.6 into the left-hand side of Eq. 3.5 yields the Dyson equation in differential form:¹

$$\left[i \frac{\partial}{\partial t_1} - h_0(1) - v_H(1) \right] G(1, 2) - \int d3 \Sigma(1, 3)G(3, 2) = \delta(1, 2) \quad . \quad (3.7)$$

The self-energy is in general a complex, non-local, and non-Hermitian operator. Its real part can be related to the exchange and correlation contributions to the quasi-particle energies, whereas its imaginary part contains information about the excitation lifetime [88]. In principle, Σ accounts for all possible events that a particle (be it an electron or a hole) may experience in its propagation in a many-electron system in the Born-Oppenheimer approximation. These processes include for instance the formation of one, or more (potentially infinite) electron-hole pairs which interact with the propagating particle. All these events give rise to an infinite series of virtual processes that may affect the propagation of a particle, and therefore determine its Green function. Some lowest-order processes are reported in Fig. 3.1 in terms of Feynman diagrams [89], where arrows represent the free propagation of the particle, and wiggly lines the bare Coulomb interaction.

¹Equation 3.7 is also often referred to as equation of motion of the interacting Green function.

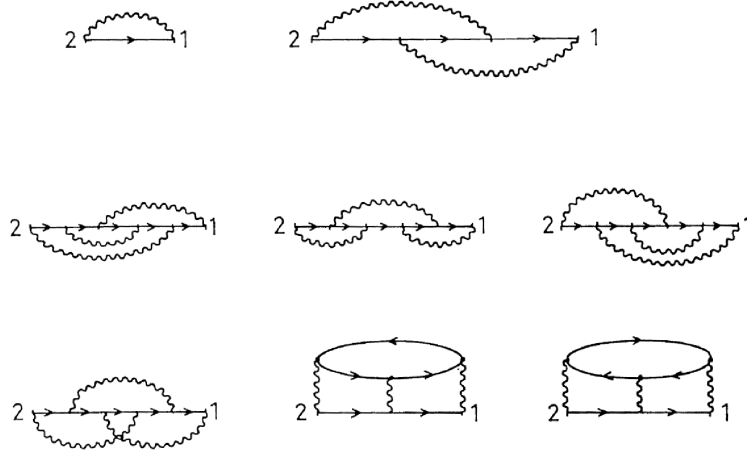


Figure 3.1: Some first-, second- and third-order diagrams of the self-energy expanded in series of the (bare) Coulomb interaction v . Arrows are non-interacting Green functions, wiggly lines represent the Coulomb interaction. Adapted from Ref. [88].

LEHMANN REPRESENTATION

A useful representation of the Green function may be obtained by introducing the explicit time-dependence of the field operators in the Heisenberg picture ($\hat{\psi}_\sigma(\mathbf{r}, t) = e^{i\hat{H}t}\hat{\psi}_\sigma(\mathbf{r})e^{-i\hat{H}t}$) into Eq. 3.1.2:

$$\begin{aligned}
 G^\sigma(\mathbf{r}t, \mathbf{r}'t') &= -i\langle\Psi|e^{i\hat{H}t}\hat{\psi}_\sigma(\mathbf{r})e^{-i\hat{H}(t-t')}\hat{\psi}_\sigma^\dagger(\mathbf{r}')e^{-i\hat{H}t'}|\Psi\rangle\theta(t-t') \\
 &= -i\sum_s e^{i(E_0-E_s^{N+1})(t-t')}\langle\Psi|\hat{\psi}_\sigma(\mathbf{r})|\Psi_s^{N+1}\rangle\langle\Psi_s^{N+1}|\hat{\psi}_\sigma^\dagger(\mathbf{r}')|\Psi\rangle\theta(t-t') \\
 &= -i\sum_s e^{-i\varepsilon_s(t-t')}f_s^\sigma(\mathbf{r})f_s^{\sigma*}(\mathbf{r}')\theta(t-t') \quad , \quad (3.8)
 \end{aligned}$$

where I introduced the completeness relation $\sum_s |\Psi_s^{N+1}\rangle\langle\Psi_s^{N+1}| = 1$, Ψ_s^{N+1} being the s -th excited state of the $N + 1$ -particle system, and E_s^{N+1} the corresponding energy. The following definitions have been introduced:

$$\varepsilon_s \equiv E_s^{N+1} - E_0 \quad , \quad (3.9a)$$

$$f_s^\sigma(\mathbf{r}) \equiv \langle\Psi|\hat{\psi}_\sigma(\mathbf{r})|\Psi_s^{N+1}\rangle \quad , \quad (3.9b)$$

$$f_s^{\sigma*}(\mathbf{r}') \equiv \langle\Psi_s^{N+1}|\hat{\psi}_\sigma^\dagger(\mathbf{r}')|\Psi\rangle \quad . \quad (3.9c)$$

f_s^σ and $f_s^{\sigma*}$ are often referred to as Lehmann amplitudes and describe the overlap between the ground state and an excited state of the system with an extra electron. In other words, the f_s may be interpreted as the probability amplitudes for electron-addition

²I will consider here and until the end of this Section only the case $t > t'$, i.e., the upper case of Eqs. 3.3. Then, the time ordering operator can be dropped and the Green function describes the propagation of an additional electron in the system. The $t' > t$ case follows by analogy.

(or -ionization, if $t' > t$) processes. Equation 3.8 shows that for a time-independent Hamiltonian the Green function depends only on the differences $t - t'$, therefore I will set $\tau \equiv t - t'$.

Using the integral representation of the step-function:

$$\theta(\tau) = - \int_{-\infty}^{+\infty} \frac{d\omega}{2\pi i} \frac{e^{-i\omega\tau}}{\omega + i\eta} \quad , \quad (3.10)$$

and Fourier transforming Eq. 3.8 to frequency one obtains the Lehmann representation [90] of the Green function:

$$G^\sigma(\mathbf{r}, \mathbf{r}', \omega) = \sum_s \frac{f_s^\sigma(\mathbf{r}) f_s^{*\sigma}(\mathbf{r}')}{\omega - \varepsilon_s + i\eta} \quad . \quad (3.11)$$

This representation is general, as no restrictions have been imposed so far beside the time-independence of the Hamiltonian \hat{H} . It indicates that G has poles at $\varepsilon_s = E_s^{N+1} - E_0$, i.e., the single-particle excitation energies. Similarly, it follows for $t < t'$ that the Green function is peaked at the energies $\varepsilon_s = E_0 - E_s^{N-1}$. This makes the Green function the ideal quantity for the theoretical description of direct- and inverse-photoemission processes, i.e., events in which the system is driven out of its ground state upon removal (addition) of an electron.

From the Lehmann representation (replacing Eq. 3.8 into Eq. 3.7), one may derive an alternative expression of the Dyson equation, known as the quasi-particle equation:

$$[h_0(\mathbf{r}) + v_H(\mathbf{r})]f_s(\mathbf{r}) + \int d\mathbf{r}' \Sigma(\mathbf{r}, \mathbf{r}', \varepsilon_s) f_s(\mathbf{r}') = \varepsilon_s f_s(\mathbf{r}) \quad . \quad (3.12)$$

The expression above recasts the Dyson equation into a single-particle eigenvalue problem. The solution of Eq. 3.12 with the exact self-energy would – in principle – give access to all single-particle excitation energies of the system (ε_s) and the probability amplitudes of the ionization processes (f_s). The solution of Eq. 3.12 is however more complicated than a conventional eigenvalue problem because the self-energy is non-Hermitian and frequency-dependent.

NON-INTERACTING LIMIT

To sketch a connection with Hartree-Fock and density-functional theory, I introduce below the Green function for a non-interacting electron system.

The ideal case of the non-interacting inhomogeneous electron gas not only provides valuable insight into the properties of the Green function, but is also of interest for practical calculations. In most cases, *ab initio* electronic-structure approaches rely on a (effective) non-interacting-particle picture for the simplification of the many-body problem.

In a non-interacting system of N particles, the many-body Hamiltonian reduces to a sum over single-particle Hamilton operators. The corresponding Schrödinger

equation can be mapped to N single-particle Schrödinger equations, which can be solved numerically exactly to yield a set of single-particle eigenvalues $\{\epsilon_n^\sigma\}$ and eigenfunctions $\{\psi_n^\sigma\}$. The ground-state wave function Ψ_0 is then obtained by constructing a Slater determinant (Eq. 2.10) with the single-particle eigenfunctions.

The Green function of a non-interacting system then assumes a particularly simple expression, as the Lehmann amplitudes can be identified with the single-particle orbitals (see e.g. [88]):

$$f_s^\sigma(\mathbf{r}) = \langle \Psi_0 | \hat{\psi}_\sigma(\mathbf{r}) | \Psi_s^{N+1} \rangle = \sum_n \psi_n^\sigma(\mathbf{r}) \langle \Psi_0 | \hat{c}_n^\sigma | \Psi_s^{N+1} \rangle = \sum_n \psi_n^\sigma(\mathbf{r}) \delta_{n,s} = \psi_s^\sigma(\mathbf{r}) \quad . \quad (3.13)$$

To derive this expression, I used the expansion of the field operators in the basis of the eigenstates of the single-particle Hamiltonian: $\hat{\psi}_\sigma(\mathbf{r}) = \sum_n \psi_n^\sigma(\mathbf{r}) \hat{c}_n^\sigma$. Similarly, the single-particle excitation energies correspond to the single-particle eigenvalues, i.e., $\epsilon_s = E_s^{N+1} - E_0 = \epsilon_s^\sigma$.

Thus, one can rewrite the Lehmann representation (Eq. 3.11) of the Green function (allowing now also for $t' > t$) in terms of single-particle orbitals and eigenvalues as:

$$G_0^\sigma(\mathbf{r}, \mathbf{r}', \omega) = \sum_n \frac{\psi_n^\sigma(\mathbf{r}) \psi_n^{\sigma*}(\mathbf{r}')}{\omega - (\epsilon_n^\sigma - \mu) - i\eta \text{sgn}(\epsilon_n^\sigma - \mu)} \quad , \quad (3.14)$$

where μ is the Fermi energy. The same applies to its Fourier transform:

$$G_0^\sigma(\mathbf{r}, \mathbf{r}', \tau) = -i \sum_n e^{-i(\epsilon_n^\sigma - \mu)\tau} \psi_n^{\sigma*}(\mathbf{r}) \psi_n^\sigma(\mathbf{r}') \times \\ \times [\theta(\tau)\theta(\epsilon_n^\sigma - \mu) - \theta(-\tau)\theta(\mu - \epsilon_n^\sigma)] \quad . \quad (3.15)$$

By differentiating Eq. 3.15 with respect to t and remembering that $h_0^\sigma \psi_i^\sigma = \epsilon_i^\sigma \psi_i^\sigma$, it is straightforward to derive the equation of motion for the non-interacting Green function:

$$\left[i \frac{\partial}{\partial t_1} - h_0(1) \right] G_0(1, 2) = \delta(1, 2) \quad , \quad (3.16)$$

which relates the non-interacting Green function to the single-particle term of the many-body Hamiltonian h_0 .

The Dyson equation in its conventional form can be derived by replacing the δ -function in Eq. 3.7 by means of the left-hand side of Eq. 3.16:

$$\left[i \frac{\partial}{\partial t_1} - h_0(1) \right] [G(1, 2) - G_0(1, 2)] = \int d3 [v_H(1)\delta(1, 3) + \Sigma(1, 3)] G(3, 2) \quad . \quad (3.17)$$

Making use of Eq. 3.16, the right-hand side can be rewritten as follows:

$$\int d3[v_{\text{H}}(1)\delta(1,3) + \Sigma(1,3)]G(3,2) = \left[i\frac{\partial}{\partial t_1} - h_0(1) \right] \int d34G_0(1,3)[v_{\text{H}}(3)\delta(3,4) + \Sigma(3,4)]G(4,2) \quad . \quad (3.18)$$

Combining Eqs. 3.17 and 3.18 yields the Dyson equation:

$$G(1,2) = G_0(1,2) + \int d34G_0(1,3)[v_{\text{H}}(3)\delta(3,4) + \Sigma(3,4)]G(4,2) \quad , \quad (3.19)$$

or, using the definition of the inverse of an operator (Eq. A.1 in Appendix A):

$$G^{-1}(1,2) = G_0^{-1}(1,2) - v_{\text{H}}(1)\delta(1,2) - \Sigma(1,2) \quad . \quad (3.20)$$

3.2 CONNECTION TO DFT: THE SHAM-SCHLÜTER EQUATION

The formal connection of many-body perturbation and density-functional theory is provided through the Sham-Schlüter equation (SSE) [52]:

$$\int d\mathbf{r}_1 v_{\text{xc}}(\mathbf{r}_1) \int \frac{d\omega}{2\pi} G_s(\mathbf{r}, \mathbf{r}_1, \omega) G(\mathbf{r}_1, \mathbf{r}, \omega) = \int d\mathbf{r}_1 d\mathbf{r}_2 \int \frac{d\omega}{2\pi} G_s(\mathbf{r}, \mathbf{r}_1, \omega) \Sigma(\mathbf{r}_1, \mathbf{r}_2, \omega) G(\mathbf{r}_2, \mathbf{r}, \omega) \quad , \quad (3.21)$$

where G_s is the Green function of the Kohn-Sham system and reproduces the same density as the fully interacting system.

The SSE is an exact condition that links the exchange-correlation potential v_{xc} and the self-energy Σ . In practice, Eq. 3.21 may be employed in its linearized form, i.e., replacing G by G_s :

$$\int d\mathbf{r}_1 v_{\text{xc}}(\mathbf{r}_1) \int \frac{d\omega}{2\pi} G_s(\mathbf{r}, \mathbf{r}_1, \omega) G_s(\mathbf{r}_1, \mathbf{r}, \omega) = \int d\mathbf{r}_1 d\mathbf{r}_2 \int \frac{d\omega}{2\pi} G_s(\mathbf{r}, \mathbf{r}_1, \omega) \Sigma(\mathbf{r}_1, \mathbf{r}_2, \omega) G_s(\mathbf{r}_2, \mathbf{r}, \omega) \quad . \quad (3.22)$$

The expression above allows one to derive approximations to v_{xc} from a given expression for Σ , avoiding the solution of the Dyson equation to determine G . This is of interest for the development of systematic approximations to the exchange-correlation potential in DFT. In fact, the SSE formally links many-body perturbation theory and density-functional theory, and provides, in principle, a way to derive a local KS potential starting from a given approximation to the many-body self-energy.

As an example, if Σ is in the Hartree-Fock approximation, the solution of the linearized SSE provides the local exact-exchange potential [91]. In the GW approximation

for Σ , v_{xc} would give the so-called the self-consistent RPA potential $v_c^{\text{RPA}}(\mathbf{r}) = \frac{\delta E_c^{\text{RPA}}}{\delta n(\mathbf{r})}$ [55, 92, 93], where E_c^{RPA} is given by Eq. 2.30. The SSE has been solved numerically only in a few isolated cases, such as spherical atoms [94] and simple solids [95, 96]. In most cases however, the problem presented by Eq. 3.22 is too complex to be tackled numerically.

3.3 RELATION TO PHYSICAL PROPERTIES

The single-particle Green function gives access to less information on a given quantum system than the full many-body wave function Ψ . This evidently arises because most of the degrees of freedom of Ψ are integrated out by the expectation values of Eq. 3.1. Nonetheless, the Green function still provides a relatively simple access to the expectation values of single-particle operators, ground-state total energies and excitation spectra. In the following, I will shortly recall how does the Green function relates to these quantities.

ONE- AND TWO-PARTICLE OPERATORS

Consider a non-local single-particle operator \hat{O}_1 in its second-quantized form:

$$\hat{O}_1 = \int d\mathbf{r}d\mathbf{r}' \hat{\psi}^\dagger(\mathbf{r}) O_1(\mathbf{r}, \mathbf{r}') \hat{\psi}(\mathbf{r}') \quad , \quad (3.23)$$

where the spin degrees of freedom are omitted for simplicity. The expectation value of this operator can be expressed in terms of the single-particle Green function, just by making use of the definition in Eq. 3.1:

$$\begin{aligned} \langle \Psi | \hat{O}_1 | \Psi \rangle &= \int d\mathbf{r}d\mathbf{r}' O_1(\mathbf{r}, \mathbf{r}') \langle \Psi | \hat{\psi}^\dagger(\mathbf{r}) \hat{\psi}(\mathbf{r}') | \Psi \rangle \\ &= -i \int d\mathbf{r}d\mathbf{r}' O_1(\mathbf{r}, \mathbf{r}') G(\mathbf{r}t, \mathbf{r}'t^+) \quad . \end{aligned} \quad (3.24)$$

Similarly, the second-quantized form of a two-particle operator \hat{O}_2 is:

$$\hat{O}_2 = \int d\mathbf{r}d\mathbf{r}' \hat{\psi}^\dagger(\mathbf{r}) \hat{\psi}^\dagger(\mathbf{r}') O_2(\mathbf{r}, \mathbf{r}') \hat{\psi}(\mathbf{r}') \hat{\psi}(\mathbf{r}) \quad . \quad (3.25)$$

Correspondingly, the ground-state expectation value of Eq. 3.25 yields:

$$\begin{aligned} \langle \Psi | \hat{O}_2 | \Psi \rangle &= \int d\mathbf{r}d\mathbf{r}' O_2(\mathbf{r}, \mathbf{r}') \langle \Psi | \hat{\psi}^\dagger(\mathbf{r}) \hat{\psi}^\dagger(\mathbf{r}') \hat{\psi}(\mathbf{r}') \hat{\psi}(\mathbf{r}) | \Psi \rangle \\ &= - \int d\mathbf{r}d\mathbf{r}' O_2(\mathbf{r}, \mathbf{r}') G_2(\mathbf{r}t^-, \mathbf{r}'t; \mathbf{r}t^{++}, \mathbf{r}'t^+) \quad , \end{aligned} \quad (3.26)$$

where I introduced the definition of the two-particle Green function (Eq. 3.4 with $N = 2$).

TOTAL-ENERGY FUNCTIONALS

The total energy is obtained from the ground-state expectation value of the electronic Hamiltonian, defined in Eq. 2.8. The Hamiltonian is a sum of a single-particle operator (h_0 , that includes the kinetic energy and the external potential) and a two-particle operator (the Coulomb interaction). The expectation value of the single-particle term h_0 can be evaluated straightforwardly from Eq. 3.24. The expectation value of the Coulomb operator, on the other hand, would require the two-particle Green function, according to Eq. 3.26. However, with some manipulation it is possible to express the total energy in terms of the single-particle Green function only:

$$E_{\text{tot}}^{\text{GM}}[G] = -i \int d1 \lim_{2 \rightarrow 1^+} \left[i \frac{\partial}{\partial t_1} + h_0(1) \right] G(1, 2) + E_{\text{ion}} \quad , \quad (3.27)$$

where E_{ion} is a positive shift due to the internuclear interactions. The reader is referred to Ref. [13, 97] for a detailed derivation. Equation 3.27 is the Galitskii-Migdal (GM) formula for the total energy. The GM formula will be used in later Chapters of this thesis for total-energy calculations for atoms and molecules.

In Eq. 3.27, the total energy has an explicit functional dependence on the Green function. This functional dependence however is not unique. In fact, MBPT provides a way to define total-energy functionals in various (potentially infinite) forms [98]. Other examples are the Luttinger-Ward [99] and the Klein functionals [100]:

$$E_{\text{tot}}^{\text{LW}}[G] = -E_{\text{H}}[G] + \Phi[G] - \text{Tr}[\Sigma[G]G] - \text{Tr}[\ln(G_0^{-1} - v_{\text{H}} - \Sigma[G])] \quad , \quad (3.28)$$

$$E_{\text{tot}}^{\text{K}}[G] = -E_{\text{H}}[G] + \Phi[G] - \text{Tr}[(G_0^{-1} - v_{\text{H}})G - 1] - \text{Tr}[\ln G^{-1}] \quad , \quad (3.29)$$

where $E_{\text{H}}[G] \equiv -i \int d\mathbf{r} v_{\text{H}}(\mathbf{r})G(\mathbf{r}t, \mathbf{r}t^+)$ is the Hartree energy. A derivation of these two functionals is reported in Appendix F. Here I used the short-hand notation:

$$\text{Tr}[AB] = \int_{-\infty}^{\infty} \frac{d\omega}{2\pi} e^{i\omega\eta} \int d\mathbf{r} d\mathbf{r}' A(\mathbf{r}, \mathbf{r}', i\omega) B(\mathbf{r}', \mathbf{r}, i\omega) \quad , \quad (3.30)$$

and I introduced the so-called Φ -functional, defined as:

$$\Phi[G] = \sum_{n=1}^{\infty} \frac{1}{2n} \text{Tr}[\Sigma^{(n)}[G]G] \quad , \quad (3.31)$$

where $\Sigma^{(n)}$ is the sum of the n -th order terms of the self-energy expanded in terms of the Coulomb interaction. In terms of Feynman diagrams, $\Sigma^{(n)}$ only includes graphs that contain n explicit Coulomb lines.

A useful property of the total-energy functionals introduced above can be easily derived differentiating both functionals with respect to G . Considering the Klein functional

for definiteness, one obtains:

$$\begin{aligned} \frac{\delta E_{\text{tot}}^{\text{K}}[G]}{\delta G} &= \frac{\delta}{\delta G} [-E_{\text{H}}[G] + \Phi[G] - \text{Tr}[(G_0^{-1} - v_{\text{H}})G - 1] - \text{Tr}[\ln G^{-1}]] \\ &= -v_{\text{H}} + \Sigma[G] - G_0^{-1} + G^{-1} \quad , \end{aligned} \quad (3.32)$$

where I used the identity $\Sigma = \frac{\delta \Phi[G]}{\delta G}$. From Eq. 3.32 follows that the Klein functional is stationary (i.e., $\frac{\delta E_{\text{tot}}^{\text{K}}[G]}{\delta G} = 0$) at the Green function that solves the Dyson equation. The same property is derived in a similar way also for the Luttinger-Ward functional. Due to this condition, these functionals are often referred to as variational. Equation 3.32 suggests that for a variational functional, the total energy $E[\bar{G}]$ (evaluated with a trial Green function \bar{G}) will be close to the real total energy $E[G]$ (where G is solution of the Dyson equation) if \bar{G} is a good approximation to G . Therefore, variational total-energy functionals should be more appropriate for the perturbative evaluation of total energies. It is worth emphasizing that this condition does not guarantee that the Green function obtained from the Dyson equation minimizes the total energy ($\frac{\delta E_{\text{tot}}^2}{\delta G} > 0$) – as one would expect by analogy with the variational principle in ordinary quantum mechanics. On the contrary, the total energy assumes a maximum at its stationary point [99].

The existence of different total-energy functionals raises the problem of the uniqueness of the total energy. However, if the Green function and the self-energy are related by the Dyson equation, the Luttinger-Ward and Klein functionals yield the same total energy. This can be easily verified by substituting the relation $G^{-1} + \Sigma = G_0^{-1} - v_{\text{H}}$ in Eq. 3.28. Similarly, it has been shown that the Klein functional is equivalent to the GM formula if the Green function satisfies the Dyson equation [101–103]. Moreover, by replacing the inverted Dyson equation (Eq. 3.20) in the Luttinger-Ward and Klein functionals, one obtains:

$$E_{\text{tot}}^{\text{K}}[G] = -E_{\text{H}} + \Phi[G] - \text{Tr}[\Sigma G] - \text{Tr}[\ln G^{-1}] \quad , \quad (3.33)$$

which demonstrates that the total energy does not depend on the non-interacting Green function G_0 . Summarizing, if the Green function satisfies the Dyson equation the total energy is independent of the non-interacting Green function G_0 , and most importantly it is independent of the form of the total-energy functional. On the other hand, if the Green function does not satisfy the Dyson equation, the total energy is expected to depend on the total-energy functional [101, 103, 104].

CONNECTION TO SPECTROSCOPY

The Lehmann representation of the Green function introduced in Sec. 3.1 illustrates the relevance of the single-particle Green function for the theoretical description of photo-emission processes: Equation 3.11 shows that the Green function has poles at the ionization energies and electron affinities. A quantity that facilitates the extraction of the single-particle excitation energies from the Green function is the (integrated) spectral

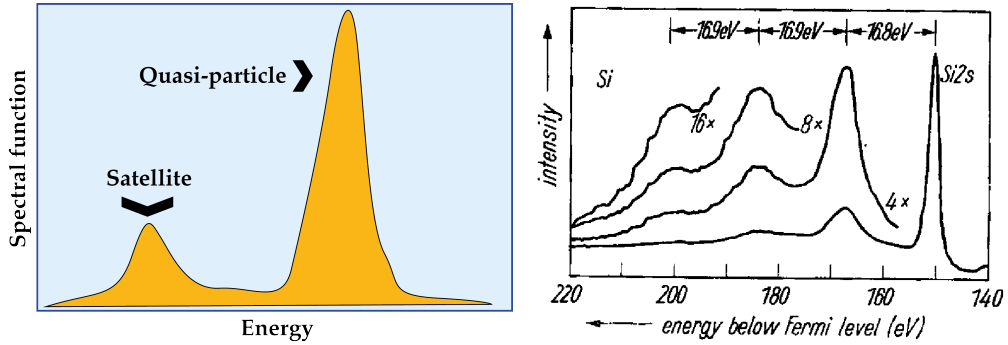


Figure 3.2: Left: pictorial representation of quasi-particle peaks and plasmon satellites in the spectral function. Right: Experimental photoemission spectrum of Silicon. Reproduced from Ref. [105].

function $A(\omega)$, defined as

$$A(\omega) = \frac{1}{\pi} \left| \int d\mathbf{r} \lim_{\mathbf{r}' \rightarrow \mathbf{r}} \text{Im} G(\mathbf{r}, \mathbf{r}', \omega) \right| = \frac{1}{\pi} |\text{Tr}[\text{Im}G(\omega)]| \quad (3.34)$$

From $A(\omega)$ one can derive information related to electron addition and removal processes, the lifetime of quasi-particle excitations and the energy of (non-neutral) collective excitations.

In the *sudden approximation*, the spectral function can be interpreted as a photo-emission current. In this approximation, the emitted electron is assumed to travel directly to the detector without interacting with the systems, after it has been excited. Mathematically, it means that the outgoing-electron wave function is a plane wave. This is a simplified picture that does not account for the following processes: First, electrons in different orbitals (or bands) often have different probabilities (or cross sections) to interact with an incoming photon, which leads to a renormalization of the peak intensity and selection rules. Second, the electron emitted in a photo-emission process may interact with the sample before reaching the detector, exchanging energy with ionic vibrations or with other electrons. As an example, final-state effects in core-electron photo emission – which arise from the interaction of the emitted electron with the screened hole left behind in the photo-emission process – might contribute up to 0.1 eV to the kinetic energy of the emitted electron and are not accounted for by the sudden approximation [106, 107].

Within the sudden approximation, the spectral function provides a connection to measurements in photo-emission spectroscopy (PES) and, correspondingly, structures in $A(\omega)$ may be associated to excitations of the system. In an over-simplified picture, one can distinguish between two different types of structures in a photo-emission spectrum: sharp peaks which arise from single-particle-like excitations, and satellite structures which generally involve the excitation of several (quasi-)particles. The structures of the first type are named “quasi-particle” peaks, and are exemplified by the right peak in the

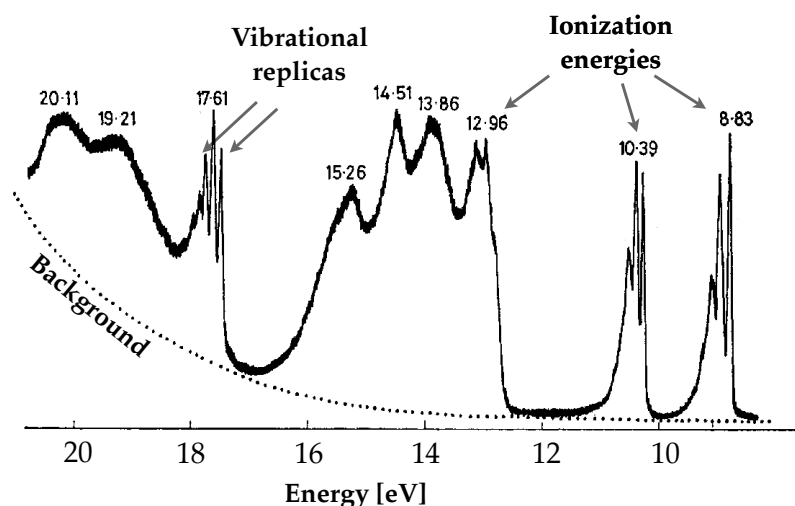


Figure 3.3: Experimental photo-emission spectrum of furan (C_4H_4O). Adapted from Ref. [108].

left panel of Fig. 3.2. The second type of structures, the satellites, are more broadened and show up within a given energy (corresponding to the energy of a collective excitation) from a quasi-particle peak, as sketched in the left panel of Fig. 3.2. In *sp*-semiconductors, the origin of satellites is to be ascribed mostly to electron-hole excitations (i.e., plasmons) induced by the photo-electron. The corresponding structures for a real material are illustrated in Fig. 3.2 on the right, where the experimental photoemission spectrum of silicon is reported. More exotic processes, such as multiple plasmon generation, are also commonly observed in photo-emission experiments, and generally show up as lower energy replica of the plasmon peak (Fig. 3.2, right). These events can also be characterized by means of the single-particle Green function [109–111]. In many materials however – such as transition metal oxides [112] – the origin of satellites is still a matter of debate.

Satellites are common features in the PES spectra of metals and semiconductors [113]. In finite systems, they are observed experimentally in metal clusters of several thousands of atoms (see, e.g., Ref. [114]). For isolated atoms and molecules up to several tens of atoms, however, satellites generally do not appear in photo-emission spectra due to the very short lifetime of this kind of excitation. As illustrated in Fig. 3.3 for furan (C_4H_4O), the photo-emission spectrum of molecules is characterized mostly by quasi-particle peaks, and by vibrational replica generated by the interaction of electrons and nuclear vibrations. In this work, I am primarily interested in the electronic degree of freedom of finite systems. Therefore, in the following I will focus mostly on quasi-particle excitations and disregard satellites.

LIFETIME OF EXCITATIONS

The lifetime of excited states manifests itself as broadening of quasi-particle peaks in the spectral function, and hence can also be inferred in Green function theory. In finite

systems, finite lifetimes of electronic excitations are a well known aspect that has been extensively discussed in the literature. For single atoms, for which vibrational decay channels are not available, electronic lifetimes of holes have been measured with photo-emission[115] and pump-probe techniques[116]. The most likely process that leads to the decay of holes is Auger recombination.

Green's function theory is in principle exact, and is therefore expected to correctly account for the lifetime (i.e., the broadening) of quasi-particle excitations, if the exact self-energy were used. The origin of peak broadening can easily be understood from the structure of the Lehmann representation:

$$G^\sigma(\mathbf{r}, \mathbf{r}', \omega) = \sum_s \frac{f_s^\sigma(\mathbf{r}) f_s^{*\sigma}(\mathbf{r}')}{\omega - \varepsilon_s - i\eta} \quad ,$$

where I considered only holes for simplicity and, therefore, $\varepsilon_s \equiv E_s^{N-1} - E_0^N$, where E_0^N denotes the ground-state energy of the N -particle system. E_s^{N-1} are the excited-state energies of the $N-1$ particle system (i.e., they solve $\hat{H}\Psi_s^{N-1} = E_s^{N-1}\Psi_s^{N-1}$, where \hat{H} is the many-body Hamiltonian). Typically, such a neutral excitation spectrum exhibits a few discrete peaks, if the $N-1$ particle system has bound states, followed by a continuum as electrons are excited above the vacuum level. Therefore, if the hole left behind by the photo-emission process is close to the Fermi energy, the energies E_s^{N-1} (and subsequently also ε_s) are discrete. The spectral function therefore exhibits a series of δ -functions. However, if the holes are low enough in energy, E_s^{N-1} lies in the continuum of the $N-1$ particle systems. This is typically when $E_s^{N-1} - E_0^{N-1}$ is larger than the next ionization energy $E_0^{N-2} - E_0^{N-1}$, where E_0^{N-2} and E_0^{N-1} are the ground-state energies of the $N-2$ and $N-1$ particle systems, respectively. Correspondingly, ε_s varies continuously and gives rise to a series of delta peaks that are infinitely closely spaced and merge into a single quasiparticle peak with a finite broadening.

As a simple example,³ consider a non-stationary quasi-particle state (for instance, a hole in the core). Since the quasi-particle state may decay, one may assume that the probability amplitude for its propagation (i.e., its Green function) decreases exponentially as $e^{-\frac{t}{\tau}}$, $\Gamma \equiv \tau^{-1}$ being the inverse lifetime. The Green function of such particle can be expressed as [13]:

$$G_i(t) = -ie^{-i\varepsilon_i t} e^{-\frac{t}{\tau}} \quad , \quad (3.35)$$

and its Fourier transform:

$$G_i(\omega) = \frac{1}{\omega - \varepsilon_i + i\Gamma} \quad . \quad (3.36)$$

³The reader is referred to Refs. [13, 88] for a more rigorous account.

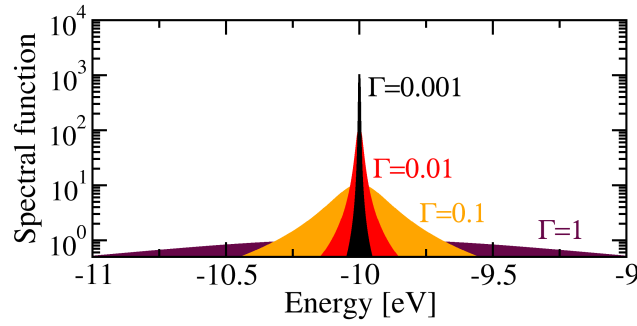


Figure 3.4: Spectral function (on a logarithmic scale) corresponding the Green function in Eq. 3.36 at different values of the inverse lifetime Γ .

According to Eq. 3.34, the spectral function is given by a Lorentzian of the form:

$$A(\omega) = \frac{1}{\pi} \frac{\Gamma}{(\omega - \epsilon_i)^2 + \Gamma^2} \quad . \quad (3.37)$$

This simple spectral function is depicted in Fig. 3.4 for several values of Γ . The inverse proportionality between τ and Γ demonstrates that short lifetimes induce large broadenings of the quasi-particle peaks. Conversely, long lifetimes are associated with a small broadening and, in the limit $\tau \rightarrow \infty$ (or $\Gamma \rightarrow 0$), Eq. 3.37 reduces to a δ -function.

DENSITY, DENSITY MATRIX, AND NATURAL OCCUPATIONS

For a system of N particles, the single-particle density matrix is defined as:

$$\gamma(\mathbf{r}, \mathbf{r}') = \int d\mathbf{r}_2 \dots d\mathbf{r}_N \Psi^*(\mathbf{r}, \mathbf{r}_2, \dots, \mathbf{r}_N) \Psi(\mathbf{r}', \mathbf{r}_2, \dots, \mathbf{r}_N) \quad , \quad (3.38)$$

where Ψ denotes the ground-state many-body wave function. The diagonal of the density matrix γ coincides with the electron density, i.e., $\gamma(\mathbf{r}, \mathbf{r}) = n(\mathbf{r})$. The density matrix can be obtained directly from the single-particle Green function:

$$\gamma(\mathbf{r}, \mathbf{r}') = -2iG(\mathbf{r}, \mathbf{r}', \tau = 0^-) \quad . \quad (3.39)$$

Similarly, the density can be derived from G by setting $\mathbf{r} = \mathbf{r}'$ in Eq. 3.39. The density matrix can also be expressed as:

$$\gamma(\mathbf{r}, \mathbf{r}') = \sum_i n_i \phi_i(\mathbf{r}) \phi_i(\mathbf{r}') \quad , \quad (3.40)$$

where ϕ_i and n_i denote the natural orbitals and the natural occupation numbers, respectively, that can be obtained from the diagonalization of γ . The density matrix is a useful instrument to characterize the nature of interactions in a quantum system. For instance, the density matrix is idempotent (i.e., $\gamma^2 = \gamma$) in a non-interacting system, whereas in the presence of two-body interactions $\text{Tr}[\gamma^2] \geq \text{Tr}[\gamma]$. A direct consequence of this

property is that the natural occupation numbers n_i are either 1 or 0, in a non-interacting system, whereas in an interacting system they are fractional. Deviations from unity of n_i can therefore be ascribed to a deviation from a single Slater determinant picture. The more n_i deviate from integer occupation, the stronger is the multi-reference character of the wave function.

4 HEDIN'S EQUATIONS: THE GW APPROXIMATION

In 1965 Lars Hedin proposed a self-consistent set of equations – today known as Hedin's equations – that provides a formally exact recipe for the evaluation of the Green function and the self-energy [14]. Hedin's equations rephrase the many-body problem in terms of a set of auxiliary quantities of direct physical meaning – such as, e.g., the screened Coulomb interaction W , first introduced by Hubbard [117]. This work had profound consequences in modern electronic-structure theory as it provided a first practical approach for calculations of electronic excitations in solids. Hedin's equations are central in the work presented in the following parts of this thesis, therefore the basic equations and their derivation will be reviewed in this Chapter.

4.1 HEDIN'S EQUATIONS

The goal of the following derivation is to recast the problem of determining the Green function (Eqs. 3.19) into a closed set of integro-differential equations. Without loss of generality, one can assume the electronic system to be perturbed by a small time-independent potential φ , which can be set to zero at the end of the derivation. Following Ref. [14] a set of auxiliary quantities may be introduced to simplify the notation. For simplicity, all definitions are listed in Table 4.1. Since our ultimate goal is the calculation of G and Σ , the quantities defined in Table 4.1 might be regarded as bare mathematical tools. However, most quantities (the screened Coulomb interaction W , the inverse dielectric matrix ϵ^{-1} , the reducible and irreducible polarizability χ and χ_0), are defined in analogy with their classical counterparts in the classical electrostatic theory of dielectrics.

The starting point of this derivation is the definition of the self-energy Σ given in Eq. 3.6:

$$\int d3[v_{\text{H}}(3)\delta(3,1) + \Sigma(1,3)]G(3,2) = -i \int d3v(1,3)G_2(1,3^+; 2,3^{++}) \quad , \quad (4.1)$$

which depends explicitly on the two-particle Green function. The following operatorial

Table 4.1: Definition of the quantities involved in the derivation of Hedin's equations.

total classical potential	$V(1) \equiv \varphi(1) - i \int d2v(1, 2)G(2, 2^+)$
3-point vertex	$\Gamma(1, 2; 3) \equiv -\frac{\delta G^{-1}(1, 2)}{\delta V(3)}$
dielectric matrix	$\epsilon^{-1}(1, 2) \equiv \frac{\delta V(1)}{\delta \varphi(2)}$
screened Coulomb interaction	$W(1, 2) \equiv \int d3v(1, 3)\epsilon^{-1}(3, 2)$
irreducible polarizability	$\chi_0(1, 2) \equiv -i\frac{\delta G(1, 1^+)}{\delta V(2)} = \frac{\delta n(1)}{\delta V(2)}$
reducible polarizability	$\chi(1, 2) \equiv -i\frac{\delta G(1, 1^+)}{\delta \varphi(2)} = \frac{\delta n(1)}{\delta \varphi(2)}$

identity, due to Schwinger [118]:

$$G_2(1, 3; 2, 3^+) = G(1, 2)G(3, 3^+) - \frac{\delta G(1, 2)}{\delta \varphi(3)} \quad (4.2)$$

holds for the Green function defined in the presence of a small perturbing local potential φ , and permits one to recast Eq. 4.1 without the two-particle Green function:

$$\int d3\bar{\Sigma}(1, 3)G(3, 2) = iG(1, 2) \int d3v(1, 3)G(3, 3^+) - i \int d3v(1, 3) \left. \frac{\delta G(1, 2)}{\delta \varphi(3)} \right|_{\varphi=0} . \quad (4.3)$$

Here I introduced the short-hand notation $\bar{\Sigma}(1, 2) = \Sigma(1, 2) + v_H(1)\delta(1, 2)$. A close expression for $\bar{\Sigma}$ is finally obtained by multiplying Eq. 4.3 on the right by G^{-1} and integrating:

$$\bar{\Sigma}(1, 2) = \delta(1, 2) \int d3v(1, 3)G(3, 3^+) + i \int d34v(1, 3) \frac{\delta G(1, 4)}{\delta \varphi(3)} G^{-1}(4, 2) \quad (4.4a)$$

$$= \delta(1, 2) \int d3v(1, 3)G(3, 3^+) - i \int d34v(1, 3)G(1, 4) \frac{\delta G^{-1}(4, 2)}{\delta \varphi(3)} , \quad (4.4b)$$

where in the last step I made use of the operator identity reported in Eq. A.2 in Appendix A. Noting that the Green function is related the electron density n by the identity $n(1) = -iG(1, 1^+)$, one may promptly recognize in the first term of Eq. 4.4b the Hartree

potential:

$$v_H(1) = \int d2v(1,2)n(2) \quad . \quad (4.5)$$

Making use of the chain rule (Eq. A.6 in Appendix A), one can immediately simplify the expression for the self-energy in Eq. 4.4b, by introducing some of the definitions of Table 4.1:

$$\begin{aligned} \Sigma(1,2) &= -i \int d345v(1,3)G(1,4) \frac{\delta G^{-1}(4,2)}{\delta V(5)} \frac{\delta V(5)}{\delta \varphi(3)} G^{-1}(4,2) \\ &= +i \int d45G(1,4)W(5,1)\Gamma(4,2;5) \quad . \end{aligned} \quad (4.6)$$

Starting from the definition of Γ in Table 4.1, and introducing the Dyson Eq. 3.20 in the presence of the perturbing field φ , one obtains:

$$\begin{aligned} \Gamma(1,2;3) &= -\frac{\delta}{\delta V(3)} [G_0^{-1}(1,2) - v_H(1,2)\delta(1,2) - \Sigma(1,2) - \varphi(1)\delta(1,2)] \\ &= \delta(1,2)\delta(1,3) + \int d45 \frac{\delta \Sigma(1,2)}{\delta G(4,5)} \frac{\delta G(4,5)}{\delta V(3)} \\ &= \delta(1,2)\delta(1,3) + \int d4567 \frac{\delta \Sigma(1,2)}{\delta G(4,5)} G(4,6)G(7,5)\Gamma(6,7;3) \quad , \end{aligned} \quad (4.7)$$

where in the last step I introduced the identity Eq. A.3 of Appendix A and used the definition of Γ .

Using the definitions of W , ϵ^{-1} , χ_0 , and χ , one obtains the following expression for W :

$$\begin{aligned} W(1,2) &= \int d3v(1,3) \frac{\delta}{\delta \varphi(2)} [\varphi(3) - iG(4,4^+)v(4,3)] \\ &= v(1,2) + \int d34v(1,3)\chi(4,2)v(4,3) \\ &= v(1,2) + \int d34v(1,3)\chi_0(3,4)W(4,2) \quad , \end{aligned} \quad (4.8)$$

where the last line was obtained making use of the relation $\chi(1,2) = \int d3\chi_0(1,3)\epsilon^{-1}(3,2)$. The irreducible polarizability χ_0 can be expressed in terms of known quantities as:

$$\begin{aligned} \chi_0(1,2) &= i \int d34G(1,3) \frac{\delta G^{-1}(3,4)}{\delta V(2)} G(4,2) \\ &= -i \int d34G(1,3)G(4,2)\Gamma(3,4;2) \end{aligned} \quad (4.9)$$

Equations 4.6-4.8 constitute a closed set of integro-differential equations, known as

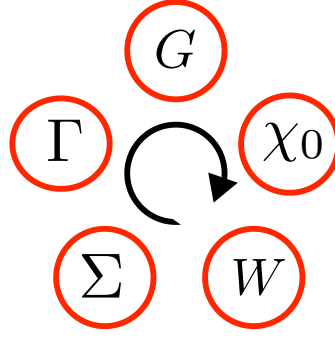


Figure 4.1: Hedin's pentagon. Schematic representation of iterative approach to the solution of Eqs. 4.10a-4.10e.

Hedin's equations:

$$G(1, 2) = G_0(1, 2) + \int d^3 4 G_0(1, 3) [v_H(3) \delta(3, 4) + \Sigma(3, 4)] G(4, 2) \quad (4.10a)$$

$$\chi_0(1, 2) = -i \int d^3 4 G(2, 3) G(4, 2) \Gamma(3, 4; 1) \quad (4.10b)$$

$$W(1, 2) = v(1, 2) + \int d^3 4 v(1, 3) \chi_0(3, 4) W(4, 2) \quad (4.10c)$$

$$\Sigma(1, 2) = i \int d^3 4 G(1, 4) W(3, 1^+) \Gamma(4, 2; 3) \quad (4.10d)$$

$$\Gamma(1, 2; 3) = \delta(1, 2) \delta(1, 3) + \int d^4 5 6 7 \frac{\delta \Sigma(1, 2)}{\delta G(4, 5)} G(4, 6) G(7, 5) \Gamma(6, 7; 3) \quad (4.10e)$$

Thus, the problem of the calculation of the single-particle Green function is reformulated as a self-consistent problem. The self-consistent nature of Eqs. 4.10a-4.10e arises from the interdependence of the each one of Hedin's equations on the other four. The solution of the problem formulated above should be approached by the following iterative scheme: i) Initialization of a first self-consistent field (SCF) calculation with a non-interacting Green function G_0 . ii) Evaluation of Eqs. 4.10b-4.10d, taking $\Gamma(1, 2; 3) = \delta(1, 2) \delta(1, 3)$. iii) Construction the vertex from Eq. 4.10e. iv) Update of the Green function from Eqs. 4.10a. v) Iteration of Eqs. 4.10a-4.10e until the satisfaction of a convergence criterion, such as, for instance, the stability of the ground-state energy. The structure of this SCF loop is sketched in Fig. 4.1.

HARTREE APPROXIMATION

A first approximation to Hedin's equations is obtained by setting $\Sigma = 0$. This approximation corresponds to the Hartree approximation [119]. The Hartree equations for the single-particle orbitals and eigenvalues are trivially recovered by substitution of $\bar{\Sigma}(1, 2) = v_H(1) \delta(1, 2)$ in Eq. 3.12 and by identifying the Lehmann amplitudes with

single-particle wave-functions:

$$[h_0(\mathbf{r}) + v_H(\mathbf{r})]\psi_n^\sigma(\mathbf{r}) = \epsilon_n^\sigma \psi_n^\sigma(\mathbf{r}) \quad (4.11a)$$

$$v_H(\mathbf{r}) = \sum_{\sigma} \sum_n^{\text{occ}} \int d\mathbf{r}' \frac{\psi_n^{\sigma*}(\mathbf{r}')\psi_n^\sigma(\mathbf{r}')}{|\mathbf{r} - \mathbf{r}'|} \quad . \quad (4.11b)$$

In the Hartree approximation, the Hartree particles move independently and interact only with the mean electrostatic field generated by the remaining $N - 1$ electrons. This is a rather poor approximation, because Eqs. 4.11a do not account for the indistinguishable nature of electrons and for the Pauli exclusion principle, that is, for exchange interactions. Due to these shortcomings, the Hartree approximation fails in reproducing even simple experimental facts, such as the formation of chemical bonds.

HARTREE-FOCK APPROXIMATION

For a higher level of theory one has to include in the evaluation of the Green function, in some approximate way, the self-energy Σ . The Hartree-Fock approximation to the self-energy, is retrieved from Hedin's equations by neglecting polarization effects ($\chi_0 = 0$) and restricting the vertex to its zero-th order component ($\Gamma(1, 2; 3) = \delta(1, 2)\delta(1, 3)$). The screened Coulomb interaction reduces to the bare interaction, i.e., $W(1, 2) = v(1, 2)$, reflecting the observation that in absence of polarization there is no screening to renormalize the Coulomb interaction. Thus, Hedin's equations reduce to:

$$G^\sigma(1, 2) = G_0^\sigma(1, 2) + \int d34 G_0^\sigma(1, 3)[v_H(3)\delta(3, 4) + \Sigma^\sigma(3, 4)]G^\sigma(4, 2) \quad (4.12a)$$

$$\Sigma^\sigma(1, 2) = iG^\sigma(1, 2)v(1, 2) \quad . \quad (4.12b)$$

By means of Eq. 3.8 and after a Fourier transform from time to frequency, one can easily show that the self-energy in Eq. 4.12b coincides with the non-local exact-exchange operator defined in Eq. 2.12. Once again, the Hartree-Fock eigenvalue problem in its conventional form is retrieved combining Eq. 2.12 with the reformulation of Dyson equation provided in Eq. 3.12, yielding:

$$[h_0(\mathbf{r}) + v_H(\mathbf{r})]\psi_n^\sigma(\mathbf{r}) + \int d\mathbf{r}' \Sigma_x^\sigma(\mathbf{r}, \mathbf{r}')\psi_n^\sigma(\mathbf{r}') = \epsilon_n^\sigma \psi_n^\sigma(\mathbf{r}) \quad . \quad (4.13)$$

4.2 THE GW APPROXIMATION

Screening between electrons can be accounted for by replacing the bare interaction v in Hartree-Fock theory with the screened Coulomb interaction W . As shown by Hedin [14], one may define a perturbative expansion of the self-energy Σ in terms of W (instead of the usual perturbative expansion around the *bare* Coulomb interaction v). The zero-th order of this expansion coincides with the Hartree-Fock approximation. At first order, the self-energy is obtained as a product of G and W , and it is therefore referred to as the

GW approximation.

The GW approximation, originally proposed by Hedin in Ref. [14], may equivalently be obtained by setting $\Gamma(1, 2; 3) = \delta(1, 2)\delta(1, 3)$ in Eqs. 4.10b, 4.10d, and 4.10e, and yields:

$$G(1, 2) = G_0(1, 2) + \int d^34 G_0(1, 3)[v_H(3)\delta(3, 4) + \Sigma(3, 4)]G(4, 2) \quad (4.14a)$$

$$\chi_0(1, 2) = -iG(1, 2)G(2, 1) \quad (4.14b)$$

$$W(1, 2) = v(1, 2) + \int d^34 v(1, 3)\chi_0(3, 4)W(4, 2) \quad (4.14c)$$

$$\Sigma(1, 2) = iG(1, 2)W(1, 2) \quad (4.14d)$$

As compared to Hartree-Fock, the structure of the self-energy becomes considerably more complex. In the GW approximation the self-energy is a non-local, non-Hermitian, and frequency dependent potential. A direct consequence of these properties, is that the eigenvalue problem formulated in Eq. 3.12 admits left and right eigenvalues, and has in principle to be solved for every frequency. It is therefore unpractical to approach GW calculations as an eigenvalue problem.

4.3 PERTURBATIVE G_0W_0

Due to the complexity of Eqs. 4.14a-4.14d, most numerical implementations of the GW approximation rely on first-order perturbation theory and treat the self-energy and the Green function in a non-self-consistent way. This constitutes a considerable simplification of the problem, that is necessary to extend the applicability of the GW method to solids and molecules up to hundreds of atoms. The G_0W_0 method was first applied to the electron gas by Hedin and coworkers in the late 1960s (see, e.g., Ref. [88] and references therein for a review). The extension of G_0W_0 to quasi-particle calculations in real semiconductors is due to Hybertsen and Louie [57, 120]. Over the years, G_0W_0 became the reference method for the computation of band gaps and band structures for solids [121–123] and more recently also for molecules [58, 124].

The basic idea of the G_0W_0 method is to avoid the self-consistent procedure implied by Eqs. 4.14a-4.14d by resorting to perturbation theory. In this scheme, one can evaluate Eqs. 4.14b-4.14d by replacing G with a Green function obtained from a preliminary density-functional or Hartree-Fock calculation. In such case, the Green function can be expressed in its non-interacting form (Eq. 3.14) and correspondingly, the polarizability in Eq. 4.14b can be evaluated in terms of the single-particle orbitals ψ_n and eigenvalues ϵ_n of the preliminary calculation. By substitution of Eq. 3.14 into Eq. 4.14b, one obtains the Adler-Wiser form [125, 126] for the polarizability reported in Eq. 2.30. No further simplification are involved in the calculation of W . The self-energy, is then expressed as:

$$\Sigma^\sigma(1, 2) = iG_0^\sigma(1, 2)W_0(1, 2) \quad (4.15)$$

where W_0 denotes the screened interaction evaluated from the non-interacting response function χ_0 given in Eq. 2.30. In G_0W_0 , it is common practice to evaluate quasi-particle energies from first-order perturbation theory as corrections to a set of single-particle eigenvalues according to the following scheme. Consider, for instance, a Kohn-Sham system (the generalization to non-local Hartree-Fock-like potentials is straightforward) with exchange-correlation potential v_{xc}^σ and satisfying the single-particle Schrödinger equation:

$$h_0(\mathbf{r})\psi_n^\sigma(\mathbf{r}) + v_{xc}^\sigma\psi_n^\sigma(\mathbf{r}) = \epsilon_{0,n}^\sigma\psi_n^\sigma(\mathbf{r}) \quad . \quad (4.16)$$

If the perturbing potential $\hat{V}(\omega) \equiv \hat{\Sigma}(\omega) - \hat{v}_{xc}$ is small, the Lehmann amplitudes $f_s(\mathbf{r})$ can be approximated by the single-particle orbitals $\psi_n^\sigma(\mathbf{r})$ of the Kohn-Sham calculation [57]. Therefore, replacing $f_s(\mathbf{r})$ by $\psi_n^\sigma(\mathbf{r})$ in Eq. 3.12 and subtracting Eqs. 3.12 and 4.16 leads to:

$$v_{xc}^\sigma\psi_n^\sigma(\mathbf{r}) - \int d\mathbf{r}' \Sigma^\sigma(\mathbf{r}, \mathbf{r}', \epsilon_{n,\sigma}^{\text{QP}})\psi_n^\sigma(\mathbf{r}') = (\epsilon_{0,n}^\sigma - \epsilon_{n,\sigma}^{\text{QP}})\psi_n^\sigma(\mathbf{r}) \quad . \quad (4.17)$$

Multiplying from the left Eq. 4.17 by $\psi_n^\sigma(\mathbf{r})$ and integrating over \mathbf{r} , yields the quasi-particle equation:

$$\epsilon_{n,\sigma}^{\text{QP}} = \epsilon_{0,n}^\sigma + \Sigma_n^\sigma(\epsilon_{n,\sigma}^{\text{QP}}) - v_{xc,n}^\sigma \quad , \quad (4.18)$$

where $\Sigma_n^\sigma(\omega) \equiv \int d\mathbf{r}d\mathbf{r}' \psi_n^\sigma(\mathbf{r})\Sigma^\sigma(\mathbf{r}, \mathbf{r}', \omega)\psi_n^\sigma(\mathbf{r}')$ and similarly for $v_{xc,n}^\sigma$. Equation 4.18 provides the first-order perturbative correction to the unperturbed eigenvalues ϵ_0^σ due to the perturbing potential $\hat{\Sigma} - \hat{v}_{xc}$. The term $\Sigma_n^\sigma(\epsilon_{n,\sigma}^{\text{QP}}) - v_{xc,n}^\sigma$ is the quasi-particle correction.

The G_0W_0 method has had an enormous success for the computations of electronic excitations in solids [121–123]. It has been applied extensively to wide classes of compounds across the entire periodic table including alkaline metals [129, 130], *sp*-bonded semiconductors [57, 120, 131–133], transition metals [134–138], and *f*-electron systems [139, 140]. Moreover, G_0W_0 has been successfully employed in the description and characterization of core-level shifts [141], image-states [142, 143], surfaces [144–146], interfaces [147, 148], and defect formation energies [149–152]. The application to molecules has steadily increased in the last years, and an assessment of G_0W_0 for finite systems is emerging [124, 153–157]. The G_0W_0 method has been implemented in several numerical codes, using different kind of basis functions, such as: numeric atom centered orbitals [158, 159], plane-waves [57, 160–162], linearized augmented-plane-waves [163, 164], and Gaussian orbitals [155, 165]. Throughout this thesis, G_0W_0 calculations have been performed with the Fritz-Haber-Institut *ab initio* molecular simulation package (FHI-aims), with numerically tabulated atom-centered basis functions. The reader is referred to Ref. [158] for a detailed account of the G_0W_0 implementation in the FHI-aims code.

In practice, the evaluation of the quasi-particle energies from Eq. 4.18 often leads

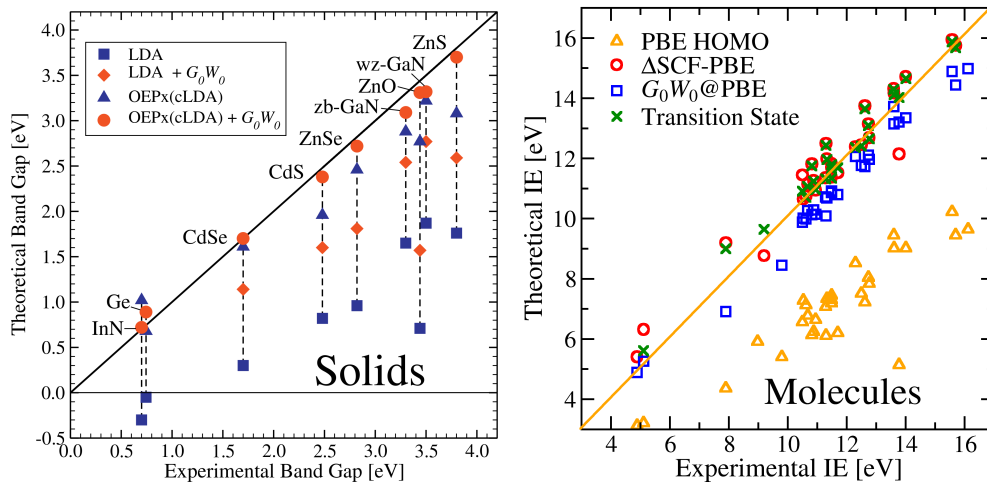


Figure 4.2: Left: Comparison between experimental and theoretical band gaps for a set of semiconductors, based on LDA and the exact-exchange optimized effective potential method with LDA correlation OEPx(cLDA). Adapted from Ref. [127]. Right: Experimental [128] versus theoretical first ionization energy for a set of 30 closed-shell molecules. The PBE eigenvalue corresponding to the highest occupied state is here compared to the G_0W_0 values obtained from Eq. 4.18. Ionization energies from the Δ -SCF and Slater's transition-state theory [65, 66] are included for comparison.

to a good correlation with experimental values for the valence excitation energies and gaps in molecules and semiconductors. This is exemplified in Fig. 4.2, where I report in the left panel a comparison of experimental band gaps and theoretical ones evaluated from LDA, exact-exchange optimized effective potential with LDA correlation (OEPx), and G_0W_0 . Experimental gaps are *not* rescaled by the electron-phonon coupling. This effect might affect the comparison experiment-theory by approximately 20-50 meV (see e.g. Ref. [5]). The right panel of Fig. 4.2 compares the experimental first (vertical) ionization energy of 30 closed-shell molecules with theoretical predictions based on the PBE HOMO, the Δ -SCF method presented in Sec. 2.5, Slater's transition state, and G_0W_0 . For small molecules, vibrational effects contributions to the vertical ionization energies are not expected to exceed 5-10 meV.

SHORTCOMINGS OF G_0W_0

In summary, the approximations implied by Eq. 4.18 (beside the GW form for the self-energy) are (i) the identification of the Lehmann amplitudes $f_s(\mathbf{r})$ with the single-particle eigenstates $\psi_n^\sigma(\mathbf{r})$; (ii) the non-self-consistent calculation of Σ and perturbative evaluation of the quasi-particle energies. Concerning (i), it was reported by Hybertsen and Louie in Ref. [57] that the error introduced by this approximation in the band gap of diamond and silicon should be less than 0.1 eV. However, in several instances it has been argued that quasi-particle orbitals and LDA/PBE orbitals may differ pronouncedly [133, 166, 167]. The approximation (ii) has more profound consequences as it leads to several shortcomings that affect G_0W_0 calculations:

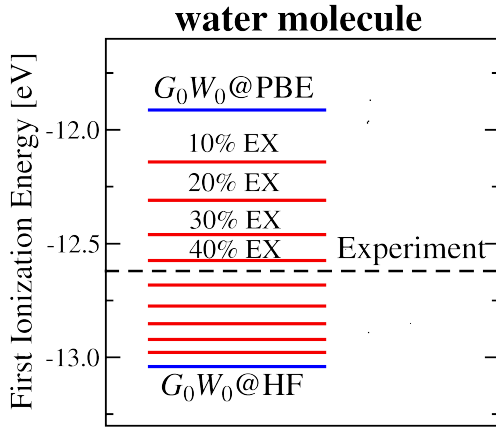


Figure 4.3: First ionization energy of the water molecule, evaluated with G_0W_0 based on HF, PBE, and hybrid PBE using different percentage of exact exchange.

1. **Starting-point dependence:** The most problematic feature of G_0W_0 calculations – as of any approach based on first-order perturbation theory – is the dependence of the results on the preliminary reference calculation, i.e., on the single-particle eigenvalues and eigenvectors employed in Eq. 4.18 (see, e.g., Ref. [168]). To illustrate the strong starting-point dependence in G_0W_0 , I report in Fig. 4.3 the first ionization energy of the water molecule evaluated from G_0W_0 based on several starting points. Quasi-particle energies and band gaps may differ up to several eV, depending on the preliminary calculation (see also the right panel of Fig. 4.2). This deficiency considerably limits the predictive power of the G_0W_0 method, and obstructs a systematic assessment of the GW approximation in electronic-structure calculations.
2. **Violation of conservation laws:** The satisfaction of conservation laws might be irrelevant for the computation of spectral properties, but it is of fundamental importance for systems out of equilibrium and transport phenomena. Conservation laws for number of particles, momentum, and total energy can be reformulated in terms of Green functions, as shown in the work of Baym and Kadanoff [102, 169]. For instance, the particle-number conservation requires the satisfaction of the continuity equation:

$$-\partial_t \langle \hat{n}(\mathbf{r}, t) \rangle = \nabla \cdot \langle \hat{j}(\mathbf{r}, t) \rangle \quad (4.19)$$

that relates the density $n(\mathbf{r}, t) = i \lim_{\mathbf{r}' \rightarrow \mathbf{r}} G(\mathbf{r}t, \mathbf{r}'t^+)$ to the particle current density $\langle \hat{j}(\mathbf{r}, t) \rangle = -\frac{1}{2} \lim_{2 \rightarrow 1^+} (\nabla_1 - \nabla_2) G(1, 2)$. The satisfaction of Eq. 4.19 requires the self-energy to obey certain symmetry conditions. Baym showed that the energy, momentum and particle-number-conservation laws are satisfied *if and only if* the self-energy is Φ -derivable [102, 170], i.e., there exists a functional $\Phi[G]$ such that:

$$\Sigma(1, 2) = \frac{\delta \Phi[G]}{\delta G(1, 2)} \quad (4.20)$$

The G_0W_0 self-energy does not satisfy the condition above, which leads to the violation of the conservation laws.

3. **Ground-state properties:** Due to its perturbative nature, the single-particle orbitals remain unchanged from the preliminary calculation in G_0W_0 , as only the eigenvalues are corrected in Eq. 4.18. This drawback might affect the reliability of the quasi-particle energies of systems for which common DFT approximations or HF provide qualitatively wrong ground-state densities, such as for instance for certain molecular interfaces and hetero-junctions [171, 172]. In these cases, it is desirable to describe excited- and ground-state properties at the same level of theory, and therefore go beyond perturbation theory. As discussed in Chap. 8, this may be particularly relevant when questions pertaining to charge transfer or level alignment become important.

4. **Over- and under-screening:** In perturbative G_0W_0 , the screening properties are determined by the inverse dielectric function $\epsilon^{-1} = 1 - v\chi_0$, where χ_0 is given by Eq. 2.30. Due to the inverse proportionality of χ_0 on the occupied-unoccupied transition energies $\Delta_{nm} = \epsilon_n - \epsilon_m$ (where n refers to occupied and m to empty states) the screening properties are strongly influenced by the quality of the eigenvalue spectrum of the preliminary calculation. As a consequence, G_0W_0 calculations based on KS-DFT tend to overestimate screening, since the lack of the derivative discontinuity in the exchange-correlation functional and the self-interaction error systematically reduce the gap between empty and occupied states. Correspondingly, the quasi-particle corrections from Eq. 4.18 are too large and the resulting excitation spectrum underestimates experimental data (see e.g. Fig. 4.2). Similarly, the Hartree-Fock spectrum overestimates Δ_{nm} due to the lack of the correlation energy. This leads to an underestimation of the screening among electrons and induces systematic errors in the quasi-particle energies, which are generally too large compared to experiment (right panel of Fig. 4.2). The over- and under-screening problems are not exclusively due to the non-self-consistent treatment of the self-energy. It has been suggested that even at self-consistency the GW approximation should under-screen the Coulomb interaction due to missing electron-hole interactions, typically accounted for by vertex corrections [173].

4.4 PARTIALLY SELF-CONSISTENT GW

Due to the high computational requirements of self-consistent GW , several approximate self-consistent GW methods have been proposed to ameliorate some of the pathologies of perturbative G_0W_0 . The most prominent are eigenvalue self-consistent GW (ev-sc GW) and quasi-particle self-consistent GW (QP-sc GW), which are introduced below.

SELF-CONSISTENCY IN THE EIGENVALUE

The ev - $scGW$ scheme is the simplest possible way to go beyond perturbative G_0W_0 . This method was originally proposed by Hybertsen and Louie in Ref. [57] and later explored by several authors [124, 174, 175]. In ev - $scGW$, Eqs. 4.15 and 4.18 are part of a self-consistent loop, whereby at each iteration the input eigenvalues are replaced with the real part of the quasi-particle energies. This procedure reduces the starting-point dependence of G_0W_0 , and for certain systems it improves the description of the first ionization energies [124, 175]. However, as discussed in Chapter 10 an inspection of the entire excitation spectrum reveals that lower lying quasi-particle states often worsen. On average, ev - $scGW$ does not lead to a quantitative improvement in the description of the excitation energies of molecules [176]. Moreover, none of the shortcomings listed above is fixed. An assessment of the ev - $scGW$ method for the azabenzenes is presented in Chapter 10.

QUASI-PARTICLE SELF-CONSISTENT GW

The underlying idea of QP- $scGW$ is to find the ground state that minimizes the G_0W_0 quasi-particle correction [177, 178]. In other words, one seeks that non-local exchange-correlation potential that best represents the G_0W_0 self-energy. Unfortunately, no exact correspondence between a non-local static potential and the frequency-dependent self-energy exists, and one has to resort to approximations.

QP- $scGW$ has been applied to a wide class of materials including d - and f -electron systems [177–191]. As compared to G_0W_0 , the QP- $scGW$ greatly reduces (and often eliminates) the dependence on the preliminary calculation. Nevertheless, in certain cases some dependence on the starting point was still observed [192]. The QP- $scGW$ scheme also allows to include exact-exchange and dynamical correlation effects in the ground state. In summary, QP- $scGW$ ameliorates some of the shortcomings listed above, such as the dependence on the starting point, and in many cases it was reported to be more accurate than G_0W_0 [177, 178]. However, the computational cost of QP- $scGW$ is expected to be comparable to full self-consistency since all non-diagonal matrix elements of the self-energy must be calculated.

4.5 FULLY SELF-CONSISTENT GW

Part of the work of this thesis, has been related to the development and implementation of a numerical approach to the self-consistent problem presented by Eqs. 4.14a-4.14d (sc - GW), and its application to atoms and molecules. A detailed account of numerical techniques developed in this work is given in Part II, whereas Part III is devoted to applications. In this Section, a brief review of previous sc - GW calculations is presented.

Previous sc - GW studies have reported conflicting conclusions on the quality of the spectral properties [58, 104, 193–196]. Consequently, no consensus has so far been

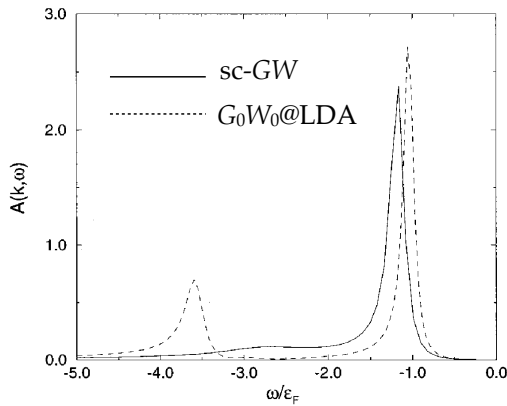


Figure 4.4: Spectral function of the homogeneous electron gas evaluated in the self-consistent GW approximation (solid) and from the perturbative GW method (dashed). Reproduced from Ref. [193].

reached in this respect. The first *sc-GW* calculation was performed for a quasi-one-dimensional model semiconductor [197]. Although this model is of scarce relevance for real systems, it established the importance of self-consistency for eliminating the starting-point dependence of band gaps.

Subsequently, *sc-GW* calculations for the homogeneous electron gas (HEG) were performed. However, they indicated a deterioration of the spectra as compared to perturbative G_0W_0 based on the local-density approximation (LDA) [193]. For the HEG, Holm and von Barth observed a transfer of spectral weight from the plasmon satellite to the quasi-particle peak in self-consistent calculations. This behavior is illustrated in Fig. 4.4, where the *sc-GW* and $G_0W_0@LDA$ spectral functions for the HEG are depicted. This spectral weight transfer results in a weaker plasmon peak and a broader valence band, that worsens the agreement with photo-emission experiments for metallic sodium. It is worthwhile to emphasize that in Ref. [193] no quantitative comparison between experimental and theoretical quasi-particle energies was reported, and the deterioration of spectral properties at self-consistency arises exclusively from the comparison of *sc-GW* band widths and plasmon satellites with experiment on alkali metals.

The first self-consistent calculation for real systems – performed for potassium and silicon in the pseudo-potential approximation – confirmed the picture outlined by Holm and von Barth [194], showing a deterioration of the band width and band gap at self-consistency. In a later work, the authors attributed the origin of this failure to the pseudo-potential approximation, emphasizing the importance of accounting for core-valence interaction [195]. However, these results later turned out to be underconverged with respect to the number of empty states [198]. Recently, *sc-GW* calculations for simple solids and actinides were performed by Kutepov and coworkers [199, 200], who also reported the deterioration of spectral properties at self-consistency. For finite systems, *sc-GW* calculations have been presented for atoms [104, 196], and for molecules [58]. In these works, *sc-GW* ionization energies are found in good agreement with experiment, with a mean absolute error comparable with G_0W_0 based on PBE or HF. Based on these results, several authors had the impression that self-consistency deteriorates the spectral properties compared to perturbative G_0W_0 , and that it is not a good idea to perform

sc-*GW* calculations. However, the scarce numerical evidence for realistic systems is not enough to corroborate this belief.

It was argued that the deterioration of spectra in sc-*GW* might arise due to the iterative construction of the polarizability χ as the product of two Green functions [177]. This would systematically weaken the incoherent part of the Green function, and reduce the intensity of the plasmon satellites. For the small molecules investigated here, however, this mechanism does not apply since quasi-particle peaks carry integer spectral weight, and no plasmon satellites are observed. For extended systems, this mechanism might effectively deteriorate the sc-*GW* spectral function, as for the homogeneous electron gas. Nonetheless, more investigations are needed to judge the performance of sc-*GW* for real solids.

While no agreement has been reached so far about the accuracy of sc-*GW* for the excited-state properties, the discussion of total energies has been less controversial. Self-consistent *GW* total energies have been computed only for a few isolated cases including the HEG [193, 201, 202], closed-shell atoms and small diatomic molecules (H_2 and LiH) [101, 104] and for a few real solids [199, 200]. The total energy is generally found in good agreement with reference values at self-consistency, and in most cases it leads to considerable improvements over non-self-consistent G_0W_0 total energies. Nonetheless, *GW* total-energy calculations are scarce and previous works do not allow a clear evaluation of the real accuracy of the *GW* method for ground-state properties.

In conclusion, the performance of the sc-*GW* method has only been investigated for a limited amount of cases, and no consensus has been reached so far concerning the accuracy and applicability of sc-*GW* in electronic-structure theory. One of the goals of this thesis is therefore to answer these open questions and to provide a systematic assessment of the sc-*GW* method for the description of ground- and excited-state properties.

4.6 CONNECTION OF *GW* AND RPA

In the following Section, I address the relation of the *GW* approximation and RPA, and provide the theoretical background for the study of the dissociation of diatomic molecules presented in Chap. 9. *GW* and RPA approximate correlation and exchange through the same set of Feynman diagrams, illustrated in Fig. 4.5. In other words, they are diagrammatically equivalent. Nonetheless, the terms *GW* and RPA are generally used to denote different types of electronic-structure calculations. The differences and analogies of self-consistent RPA and *GW*, and some of their implications, are reviewed below.

Let us start with the ground-state total-energy expression for an interacting electron

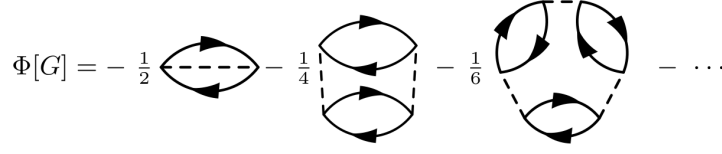


Figure 4.5: Φ functional for RPA and GW correlation energies (Eq. 3.31). The arrowed lines correspond to the interacting Green function G in GW , and the KS Green function G_s in RPA. Dashed lines denote the bare Coulomb interaction, and the minus sign of the prefactor comes from the rules for evaluating Feynman diagrams [99, 169].

system obtained with the adiabatic-connection (AC) technique (see e.g. Ref. [77]):

$$E = E_0 - \frac{1}{2} \int_0^1 d\lambda \int d\mathbf{r}d\mathbf{r}' v(\mathbf{r}, \mathbf{r}') \left[\int_0^\infty \frac{d\omega}{\pi} \chi_\lambda(\mathbf{r}, \mathbf{r}'; i\omega) + n(\mathbf{r})\delta(\mathbf{r} - \mathbf{r}') \right] \quad (4.21)$$

$$= E_0 + \int_0^1 \frac{d\lambda}{\lambda} \int_0^\infty \frac{d\omega}{2\pi} \text{Tr} [\Sigma_\lambda(i\omega)G_\lambda(i\omega)] \quad . \quad (4.22)$$

Here, $v(\mathbf{r}, \mathbf{r}')$ is the Coulomb interaction, $\text{Tr}[AB]$ denotes $\int d\mathbf{r}d\mathbf{r}' A(\mathbf{r}, \mathbf{r}')B(\mathbf{r}', \mathbf{r})$ and $E_0 = T_s + E_H + E_{\text{ext}}$. T_s is the kinetic energy of the KS independent-particle system, E_H the Hartree and E_{ext} the external energy. The parameter λ assumes values between 0 and 1. $\lambda = 0$ ($\lambda = 1$) denotes the non-interacting (interacting) system. Along the AC path (i.e., at each value of λ), the electron density $n(\mathbf{r})$ is assumed to be fixed at its physical value.

The RPA for the total energy can be most conveniently introduced in Eq. 4.21 through the approximation $\chi_\lambda = \chi_s(1 - \lambda v\chi_s)^{-1}$, where $\chi_s = \chi_{\lambda=0} = -iG_sG_s$ is given by the Adler-Wiser formula (Eq. 2.30). Within this approximation, the integrand in Eq. 4.21 is assumed to depend on λ only through the scaled Coulomb interaction λv . Alternatively the RPA total energy can also be obtained through Eq. 4.22 by introducing the (λ -dependent) GW approximation for the proper self-energy Σ_λ [77, 92], where $\Sigma_\lambda^{GW} = \Sigma^{GW}[G_\lambda, W_\lambda]$. The RPA total energy is retrieved by omitting the λ -dependence of G_λ , i.e., replacing G_λ by the KS non-interacting Green function $G_s = G_{\lambda=0}$ and W_λ by $W_s \equiv W_\lambda[G_s]$. Either way, the λ integration in Eqs. 4.21 or 4.22 can now be carried out, yielding the sum of the exact-exchange energy E_x and the RPA correlation energy E_c^{RPA} (Eq. 2.29). The RPA total energy can therefore be expressed as:

$$E^{\text{RPA}}[G_s] = T_s + E_{\text{ext}} + E_H + E_x + E_c^{\text{RPA}} \quad . \quad (4.23)$$

I now come to the differences in the evaluation of the total energy in the context of KS-DFT and MBPT. In MBPT, the Green function G_λ represents an interacting electron system for $\lambda \neq 0$, and has to satisfy the (λ -dependent) Dyson equation:

$$G_\lambda^{-1} = G_s^{-1} - \Sigma_\lambda[G_\lambda] - v_{\text{ext}}^\lambda + v_{\text{ext}} + (1 - \lambda)v_H + v_{\text{xc}} \quad , \quad (4.24)$$

with v_{ext}^λ being the external potential of the λ -dependent system (chosen to keep the

density fixed), and v_{xc} the exchange-correlation potential of the KS non-interacting-particle reference system. Making use of 4.24, the λ -integration in Eq. 4.22 can be carried out and one arrives at the following expression for the total energy

$$E = -E_H[G] + \Phi[G] - \frac{1}{2\pi} \int_{-\infty}^{\infty} d\omega \times \text{Tr} [(G_s^{-1}(i\omega) + v_{xc})G(i\omega) - 1 + \ln(G^{-1}(i\omega))] \quad . \quad (4.25)$$

Details for the derivation of Eq. 4.25 can be found in Appendix F. In Eq. 4.25, $G = G_{\lambda=1}$, and the functional $\Phi[G]$ is defined in Eq. 3.31 [99, 169]. Since $\Sigma = \delta\Phi/\delta G$, an approximation for Φ directly translates into a corresponding approximation for Σ . The diagrammatic representation of Φ in the GW approximation is illustrated in Fig. 4.5. In the KS framework on the other hand, the sc-RPA total energy is obtained by requiring G_s to satisfy the Dyson equation $G_s(i\omega) = (i\omega + \nabla^2/2 - v_{\text{ext}} - v_H - v_{xc}^{\text{RPA}})^{-1}$, where v_{xc}^{RPA} is determined by the linearized Sham-Schlüter equation (Eq. 3.22). Alternatively, the sc-RPA energy can be obtained by minimizing E^{RPA} in Eq. 4.23 with respect to the non-interacting input KS Green functions G_s .

Regarding the energy expression of Eq. 4.25 as a functional of G yields the Klein functional (Eq. 3.29) [100]. It has further been shown [101, 203] that evaluating the Klein functional (using the GW approximation for Φ) with the KS reference Green function G_s one obtains the RPA total energy in Eq. 4.23 (see also Appendix F). This offers a second way to look at the difference between sc-RPA and sc- GW : the sc-RPA energy corresponds to a minimum of the Klein functional within a variational subspace of non-interacting KS Green functions, whereas the sc- GW total energy corresponds to a stationary point of the Klein functional in a larger variational space including both noninteracting and interacting Green functions. However, this stationary point is not necessarily a minimum [99, 100]. In practical calculations, the sc- GW total energy is actually above the sc-RPA energy as it will be shown in Chap. 9.

Finally, another major difference between sc- GW and sc-RPA can be identified in the way the kinetic energy is accounted for in the two approaches. This difference stems from two aspects. First, the sc- GW expression is evaluated with an interacting Green function as opposed to a Kohn-Sham one in sc-RPA. Second, the kinetic correlation energy – i.e., the difference between the full kinetic energy and that of the non-interacting KS system – are included in the RPA correlation energy (Eq. 2.29) through the coupling constant integration. On the other hand, in sc- GW the correlation term is purely Coulombic, and kinetic correlations are already included in the kinetic energy term due to the interacting nature of the sc- GW Green function.

Part II

Implementation

5 SELF-CONSISTENT GW EQUATIONS IN A NUMERIC ORBITAL BASIS

The second part of this thesis is devoted to the numerical implementation of the self-consistent *GW* method in the Fritz-Haber-Institut *ab initio* molecular simulation package (FHI-aims). In this Chapter, I will briefly introduce the numeric atom-centered orbital (NAO) basis sets and the resolution of the identity technique (RI) for the computation of Coulomb-type integrals (see Refs. [158, 204] for a more detailed review of the FHI-aims code). Based on these ingredients, I will derive a reformulation of Hedin’s self-consistent *GW* equations in a matrix representation, suitable for numerical calculations. This paves the way for the application of the sc-*GW* method to the calculation of excited- and ground-state properties of real systems. Technical aspects related to the treatment of the frequency and time dependence of dynamic quantities, and the evaluation of physical properties from the Green function will be addressed in Chapters 6 and 7, respectively.

5.1 NUMERIC ATOM-CENTERED ORBITALS

Basis functions are the central ingredient of most electronic-structure codes. The introduction of a basis allows to rewrite operators as matrices of considerably smaller size as compared to the real-space representation. Most importantly, basis sets enables the reformulation of differential equations as generalized eigenvalue problems. In DFT for example, the basis representation of the Kohn-Sham Eq. 2.22 – a second-order differential equation in Cartesian coordinates – yields the following eigenvalue problem:

$$\sum_j^{N_b} h_{ij}^\sigma c_{jn}^\sigma = \epsilon_n^\sigma \sum_j^{N_b} s_{ij} c_{jn}^\sigma \quad , \quad (5.1)$$

where N_b is the total number of NAO basis functions. In the following, summations over Latin indexes (i, j, l, \dots) are implicitly assumed to run from 1 to N_b . The index n is reserved for the main quantum number. The following quantities were introduced in

Eq. 5.1:

$$h_{ij}^\sigma \equiv \int d\mathbf{r} \varphi_i^*(\mathbf{r}) h^\sigma(\mathbf{r}) \varphi_j(\mathbf{r}) \quad , \quad (5.2)$$

$$s_{ij} \equiv \int d\mathbf{r} \varphi_i^*(\mathbf{r}) \varphi_j(\mathbf{r}) \quad , \quad (5.3)$$

Where $h^\sigma(\mathbf{r})$ is the Kohn-Sham Hamiltonian and s_{ij} the overlap matrix, which for an orthonormal basis set simplifies to $s_{ij} = \delta_{ij}$. The coefficients c_{jn}^σ in turn provide access to the single-particle eigenstates $\psi_n^\sigma(\mathbf{r})$ of the Hamiltonian, through the relation:

$$\psi_n^\sigma(\mathbf{r}) = \sum_j c_{jn}^\sigma \varphi_j(\mathbf{r}) \quad . \quad (5.4)$$

There is in principle no restriction to the shape of the basis functions and different possibilities have been proposed over the years, each one with its own advantages and limitations. Gaussian and plane-wave basis sets, for instance, have been extensively employed in the quantum-chemistry and solid-state physics community, respectively. The main advantage of these type of basis sets is their explicit analytical representation, which facilitates a straightforward evaluation of integrations over the Cartesian coordinates. The drawback is that often a large number of basis functions are required in order to provide sufficient degrees of freedom for describing – for instance – a given set of single-particle orbitals. In other word, the convergence with the number of basis functions is slow. Moreover, due to the rapid oscillations of the one-particle wave functions close to the nucleus, Gaussian and plane-wave basis sets needs the introduction of pseudo-potentials and effective core potentials, respectively, for the description of inner-shell electrons of elements with mass number larger than 20.

From this perspective, numerically tabulated functions are more advantageous. The radial dependence can be chosen freely and permits a systematic optimization of the basis set. In addition, there is no need to treat core and valence separately, since the oscillations of the wave function close to the nucleus may be captured by just a few numerical orbitals with the proper radial dependence. In this case, integrals have to be discretized over real-space meshes, as illustrated in the left panel of Fig. 5.1, and evaluated numerically as sums over a finite number of points.

The numerical approaches presented in this thesis make use of NAO basis sets $\{\varphi(\mathbf{r})\}$, with basis functions of the form:

$$\varphi_i(\mathbf{r}) = \frac{u_i(r)}{r} Y_{lm}(\Omega), \quad (5.5)$$

where $u_i(r)$ are numerically tabulated radial functions and $Y_{lm}(\Omega)$ spherical harmonics. This form guarantees full flexibility for the radial and angular dependence of the basis function. In fact, $\varphi_i(\mathbf{r})$ may also be taken to be numerically tabulated Gaussian functions – which will be used later on for benchmark purpose.

For numerical convenience, one may choose to work with real-valued basis functions

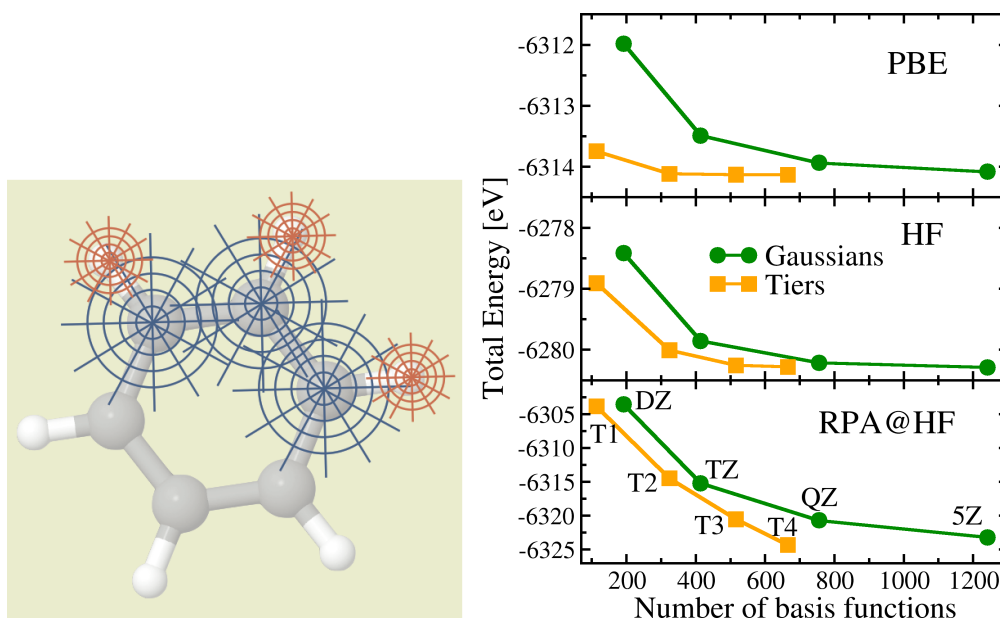


Figure 5.1: Left: Example of atom centered mesh for the computation of real-space integrations for benzene. Intersections between circles and straight lines correspond to integration points. Right: PBE (above), HF (center), and RPA@HF total energy of benzene evaluated with FHI-aims' Tier 1, 2, 3, and 4 and with Dunning's Gaussian augmented correlation-consistent polarized valence N zeta (NZ), with $N = D, T, Q$, and 5 [205].

by requiring – without loss of generality – that $Y_{lm}(\Omega)$ denotes the real part (for $m = 0, \dots, l$) and the imaginary part (for $m = -l, \dots, -1$) of complex spherical harmonics.

The NAOs are suitable to construct basis set hierarchies of increasing accuracy, which in FHI-aims are labeled *Tiers*. In practice, FHI-aims basis sets are constructed by means of the procedure summarized below – a more extended discussion is reported in Ref. [204]. A large pool of NAOs of the form given in Eq. 5.5 is defined. For each element of the periodic table, a corresponding closed-shell optimization target is chosen (typically the simplest closed-shell compound of such element), e.g., a dimer. The basis functions of the pool are added one by one to the optimization target, and only the basis function that induce the largest lowering of total energy is kept. The procedure is iterated until the total energy does not change upon addition of further basis functions.

This strategy is substantially different from the one adopted for the construction of the aug-cc-pVNZ sets: in that case, only the parameters of each Gaussian basis function are optimized, whereas the number of basis functions and the maximum angular momentum are fixed.

Basis sets constructed according to this recipe, have been shown to be transferable (i.e., system independent) and can be employed – with similar benefits – with a wide range on local and non-local DFT exchange-correlation functionals which do not have an explicit dependence on unoccupied states [204]. Most importantly, NAO basis sets permit to systematically converge the calculations by resorting to higher-order Tiers. This is

exemplified in the right panel of Fig. 5.1, where the PBE, HF, and RPA@HF total energy of benzene (C_6H_6) is reported for increasingly larger basis sets. The comparison with Dunning's augmented correlation-consistent polarized valence N zeta (NZ) Gaussian basis functions [205] – with $N = D, T, Q$, and 5 – indicates that fewer NAO basis functions are required to converge the total energy of benzene, and therefore provide an optimal framework for electronic-structure calculation of finite systems. It has been further demonstrated that NAO basis sets may also provide an ideal framework for MBPT-based approaches to electronic correlation that depend explicitly on the empty states such as RPA (see, e.g., the right panel of Fig. 5.1) *GW* calculations [158]. Nonetheless, in this case the convergence with the basis set is slower than in PBE or HF, due to the explicit dependence of the correlation energy (or, the self-energy) on the unoccupied manifold. The origin of this behavior is the explicit dependence of the correlation part of the self-energy on the unoccupied Kohn-Sham or Hartree-Fock eigenstates (see e.g., the sum over empty states in the Adler-Wiser form for the polarizability, Eq. 2.30). In Chapter 7, I will show that in the *GW* approximation, ground- and excited-state properties can be converged systematically by means of FHI-aims Tiers.

In general, for any non-local single-particle operator \hat{O} , the NAO representation O_{ij} and the real-space representation $O(\mathbf{r}, \mathbf{r}')$ are related by:

$$O_{ij} = \int d\mathbf{r}d\mathbf{r}' \varphi_i(\mathbf{r}) O(\mathbf{r}, \mathbf{r}') \varphi_j(\mathbf{r}') \quad (5.6a)$$

$$O(\mathbf{r}, \mathbf{r}') = \sum_{ijklm} \varphi_i(\mathbf{r}) s_{ij}^{-1} O_{jl} s_{lm}^{-1} \varphi_m(\mathbf{r}') \quad (5.6b)$$

Correspondingly, for the single-particle Green function one gets:

$$G_{ij}^\sigma(i\omega) = \int d\mathbf{r}d\mathbf{r}' \varphi_i(\mathbf{r}) G^\sigma(\mathbf{r}, \mathbf{r}', i\omega) \varphi_j(\mathbf{r}') \quad (5.7a)$$

$$G^\sigma(\mathbf{r}, \mathbf{r}', i\omega) = \sum_{ijklm} \varphi_i(\mathbf{r}) s_{ij}^{-1} G_{jm}^\sigma(i\omega) s_{lm}^{-1} \varphi_m(\mathbf{r}') \quad (5.7b)$$

The time representation of $G(\mathbf{r}, \mathbf{r}', \tau)$ follows by replacing ω with τ . Here, the Green function was expressed on the imaginary frequency axis. A discussion about advantages and drawbacks of the imaginary frequency and time formalism is deferred to the next Chapter.

The NAO representation of the non-interacting Green function can be expressed as:

$$\begin{aligned} G_{0,ij}^\sigma(i\omega) &= \sum_n \int d\mathbf{r}d\mathbf{r}' \varphi_i(\mathbf{r}) \frac{\psi_n^\sigma(\mathbf{r}) \psi_n^\sigma(\mathbf{r}')}{i\omega - (\epsilon_n^\sigma - \mu)} \varphi_j(\mathbf{r}') \\ &= \sum_n \sum_{lm} \frac{s_{il} c_{ln}^\sigma c_{mn}^\sigma s_{mj}}{i\omega - (\epsilon_n^\sigma - \mu)} \quad (5.8) \end{aligned}$$

where ψ_n^σ was replaced by its expansion (Eq. 5.4) and the definition of s_{ij} in Eq. 5.3 was

used. Similarly, one obtains:

$$G_{0,ij}^\sigma(i\tau) = i \sum_n \sum_{lm} s_{il} c_{ln}^\sigma c_{mn}^\sigma s_{mj} e^{(\epsilon_n^\sigma - \mu)\tau} \times \\ \times [\theta(\tau)\theta(\mu - \epsilon_n^\sigma) - \theta(-\tau)\theta(\epsilon_n^\sigma - \mu)] \quad . \quad (5.9)$$

For numerical convenience, it is useful to define the generalized Green function \bar{G} that incorporates the inverse overlap matrices:

$$\bar{G}_{ij}^\sigma \equiv \sum_{jl} s_{ij}^{-1} G_{jl}^\sigma s_{jm}^{-1} \quad . \quad (5.10)$$

5.2 THE RESOLUTION OF THE IDENTITY

The expansion of two-particle operators – such as the Coulomb operator \hat{v} – in a single-particle basis requires the evaluation of the following expectation values:

$$(ij|lm) \equiv \langle \varphi_i \varphi_j | \hat{v} | \varphi_l \varphi_m \rangle = \int d\mathbf{r} d\mathbf{r}' \frac{\varphi_i(\mathbf{r}) \varphi_j(\mathbf{r}) \varphi_l(\mathbf{r}') \varphi_m(\mathbf{r}')}{|\mathbf{r} - \mathbf{r}'|} \quad . \quad (5.11)$$

The 4-center integrals $(ij|lm)$ are impractical to handle in an NAO formalism. Numerically, the difficulty arises from the large number of NAO pairs and from the memory requirement for storing the 4-index matrix $(ij|lm)$, which scales with the fourth power of the number of basis functions. The same difficulties are encountered in the evaluation of the polarizability χ and the screened Coulomb interaction W . The computation of the Coulomb integrals in Eq. 5.11 is a problem extensively discussed in the literature [206–208] and efficient techniques have been developed to make this calculation affordable. Here, the method of choice for the calculation of the 4-center integrals is the resolution of the identity technique (RI) [158].

In the RI framework, the integrals in Eq. 5.11 are evaluated efficiently by resorting to an auxiliary basis set $\{P_\mu(\mathbf{r})\}$. The auxiliary basis functions $P_\mu(\mathbf{r})$ have a similar structure as the NAO orbitals defined in Eq. 5.5, and are defined to span the Hilbert space of the product of NAO pairs, so that one can write:

$$\varphi_i(\mathbf{r}) \varphi_j(\mathbf{r}) \simeq \sum_{\mu=1}^{N_{\text{aux}}} C_{ij}^\mu P_\mu(\mathbf{r}) \quad , \quad (5.12)$$

where C_{ij}^μ are the coefficients of the expansion, and N_{aux} is the number of auxiliary basis functions P_μ . In the following, summations over the Greek indexes (μ, ν, \dots) are implicitly assumed to run from 1 to N_{aux} . According to the structure of Eq. 5.12, the set of basis functions P_μ is often referred to as *product basis*.

Due to the high linear dependence of the NAO pairs, the number of product basis functions N_{aux} can be kept considerably smaller than the number of NAO pairs $\sim N_b^2$, making the numerical evaluation of Eq. 5.11 affordable. I refer to Ref. [158] for a detailed

account of the variational approach employed in the determination of the RI expansion coefficients C_{ij}^μ and for a review of the overall accuracy of the RI approach for correlated calculations.

In short, I used the “RI-V” variant of the RI scheme, in which the expansion coefficients are given by:

$$C_{ij}^\mu = \sum_{\nu} (ij|\nu) V_{\nu\mu}^{-1} \quad , \quad (5.13)$$

where $(ij|\nu) \equiv \int d\mathbf{r} \varphi_i(\mathbf{r}) \varphi_j(\mathbf{r}) P_{\nu}(\mathbf{r}') / |\mathbf{r} - \mathbf{r}'|$ and $V_{\nu\mu}$ labels matrix elements of the Coulomb matrix in the auxiliary basis, i.e.:

$$V_{\mu\nu} = \int d\mathbf{r} d\mathbf{r}' \frac{P_{\mu}(\mathbf{r}) P_{\nu}(\mathbf{r}')}{|\mathbf{r} - \mathbf{r}'|} \quad . \quad (5.14)$$

For numerical efficiency, it is convenient to introduce the modified coefficients:

$$M_{ij}^\mu = \sum_{\nu} C_{ij}^\nu V_{\nu\mu}^{1/2} \quad . \quad (5.15)$$

For a generic two-particle operator \hat{O} , the product basis and coordinate representations are connected by the following relations:

$$O(\mathbf{r}, \mathbf{r}') = \sum_{\mu\mu'\nu\nu'} P_{\mu}(\mathbf{r}) S_{\mu\mu'}^{-1} O_{\mu'\nu'} S_{\nu\nu'}^{-1} P_{\nu}(\mathbf{r}') \quad , \quad (5.16a)$$

$$O_{\mu\nu} = \int d\mathbf{r} d\mathbf{r}' P_{\mu}(\mathbf{r}) O(\mathbf{r}, \mathbf{r}') P_{\nu}(\mathbf{r}') \quad , \quad (5.16b)$$

where $S_{\mu\nu} \equiv \int d\mathbf{r} P_{\mu}(\mathbf{r}) P_{\nu}(\mathbf{r})$ is the overlap matrix of the product basis.

5.3 WORKING EQUATIONS FOR SELF-CONSISTENT *GW*

Based on the previous discussion it appears convenient to rewrite the self-consistent *GW* Eqs. 4.14a-4.14d in a mixed NAO-RI framework, where single-particle operators (G , G_0 , Σ , v_H and v_{xc}) are expanded in the NAO basis $\{\varphi_i\}$ and two-particle operators (v , W , and χ) are represented in the auxiliary basis $\{P_{\mu}\}$. How this can be done in practice, will be addressed in the following.

To avoid the numerical evaluation of convolutions on the frequency axis – which would require the redefinition of new frequency grid after each convolution –, χ and Σ are computed in imaginary time. Nonetheless, W and G are expressed in imaginary frequency due to the simpler structure of the Dyson equation, that does not involve integrations. Therefore, all quantities are expressed alternatively in imaginary frequency and time and Fourier transforms are used to switch representation. The alternation of frequency and time across the sc-*GW* loop is illustrated in the flow diagram in Fig. 5.2. Details on the numerical evaluation of Fourier transforms, the advantages and

drawbacks of the representations of dynamical quantities on the imaginary axis are presented in Chap. 6.

Recalling Hedin's equation for W (Eq. 4.14b):

$$W(1, 2) = v(1, 2) + \int d3d4 v(1, 3)\chi(3, 4)W(4, 2) \quad ,$$

one can insert the product basis representation (Eq. 5.16a) for W , v and χ . Simple algebraic manipulations lead to the RI equation for the screened Coulomb interaction:

$$\bar{W}_{\mu\nu}(i\omega) \equiv [v^{-1}W(i\omega)]_{\mu\nu} = [1 - \Pi(i\omega)]_{\mu\nu}^{-1} \quad , \quad (5.17)$$

where I introduced the definition $\Pi_{\mu\nu}(i\omega) \equiv [\chi(i\omega)v]_{\mu\nu}$. The operator Π has to be expressed as an explicit functional of G , and all non-diagonal matrix elements in the Green function have to be included. By virtue of the definition in Eq. 5.15 for the coefficients M_{il}^μ , Π can be expressed as:

$$\Pi_{\mu\nu}(i\tau) = -i \sum_{\sigma} \sum_{ijlm} M_{il}^\mu M_{jm}^\nu \bar{G}_{ij}^\sigma(i\tau) \bar{G}_{lm}^\sigma(-i\tau) \quad . \quad (5.18)$$

The quadruple sum in Eq. 5.18 may be reduced to a sum over just two indexes – with a considerable reduction of computational cost. By introducing the quantity:

$$A_{ij}^{\mu,\sigma}(i\tau) \equiv \sum_i M_{il}^\mu \bar{G}_{ij}^\sigma(i\tau) \quad , \quad (5.19)$$

Eq. 5.18 can be rewritten as:

$$\Pi_{\mu\nu}(i\tau) = -i \sum_{\sigma} \sum_{lj} A_{lj}^{\mu,\sigma}(i\tau) A_{ji}^{\nu,\sigma}(-i\tau) \quad . \quad (5.20)$$

Equations 5.17 and 5.20 constitute the NAO-RI representation of Hedin's equations 4.14b and 4.14c.

An RI-version of Hedin's equation for the GW self-energy:

$$\Sigma^\sigma(1, 2) = i \int d3G^\sigma(1, 3)W(3, 2) \quad , \quad (5.21)$$

can be derived in analogous way:

$$\Sigma_{ij}^\sigma(i\tau) = i \sum_{lm} \sum_{\mu\nu} M_{il}^\mu M_{jm}^\nu \bar{G}_{lm}^\sigma(i\tau) \bar{W}_{\mu\nu}(i\tau) \quad . \quad (5.22)$$

By introducing the auxiliary quantity:

$$B_{jm}^\mu(i\tau) = \sum_{\nu} M_{jm}^\nu \bar{W}_{\mu\nu}(i\tau) \quad , \quad (5.23)$$

the self-energy can be recast in a form in which only double sums appear:

$$\Sigma_{ij}^{\sigma}(i\tau) = i \sum_m \sum_{\mu} A_{im}^{\mu,\sigma}(i\tau) B_{jm}^{\mu}(i\tau) \quad . \quad (5.24)$$

The correlation (exchange) contribution to the self-energy can then be derived straightforwardly from Eq. 5.22 by substituting \bar{W} with $\bar{W}_{\mu\nu}^c \equiv \bar{W}_{\mu\nu} - \delta_{\mu\nu}$ ($\bar{W}_{\mu\nu}^x \equiv \delta_{\mu\nu}$). The Hartree potential v_H is also evaluated as an explicit functional of G according to the equation:

$$v_{H,ij} = \sum_{\sigma} \sum_{lm} \sum_{\mu} M_{ij}^{\mu} M_{lm}^{\mu} \bar{G}_{ij}^{\sigma}(i\tau = 0^-) \quad . \quad (5.25)$$

Finally, the matrix representation of the Dyson equation for the Green function completes the set of Hedin's equations:

$$\bar{G}_{ij}^{\sigma}(i\omega) = \left[\bar{G}_0^{\sigma}(i\omega)^{-1} - \Sigma^{\sigma}(i\omega) + v_{xc}^{\sigma} - \Delta v_H \right]_{ij}^{-1} \quad . \quad (5.26)$$

Here, Δv_H is the difference between the Hartree potential evaluated with the interacting and non-interacting Green function.

Equations 5.17-5.26 provide a matrix representation of Hedin's equations in the self-consistent *GW* approximation (Eqs. 4.14a-4.14d) suitable for numerical calculations. In this formulation i) all electrons are treated on an equal footing, i.e., fully self-consistently; ii) no model screening was used in the calculation of W ; iii) all non-diagonal matrix elements of G and Σ are correctly accounted for. Equations 5.17-5.26 have been implemented in the FHI-aims package and are solved according to the following scheme, also illustrated in Fig. 5.2:

- The Green function $\bar{G}_{0,ij}^{\sigma}(i\tau)$ corresponding to a given set of eigenvalues ϵ_n^{σ} and eigenstates c_{in}^{σ} is obtained through Eqs. 5.9-5.10.
- The coefficients $A_{lj}^{\mu,\sigma}(i\tau)$ are evaluated from Eq. 5.19. The polarizability $\Pi_{\mu\nu}(i\tau)$ is obtained from Eq. 5.20.
- Π is Fourier transformed to imaginary frequency.
- The modified screened Coulomb interaction $\bar{W}_{\mu\nu}(i\omega)$ is evaluated from Eq. 5.17 in imaginary frequency.
- \bar{W} is Fourier transformed to imaginary time.
- The coefficients $B_{ij}^{\mu}(i\tau)$ are evaluated from Eq. 5.23. The self-energy $\Sigma_{ij}^{\sigma}(i\tau)$ is obtained according to Eq. 5.24.
- Σ is Fourier transformed to imaginary frequency.

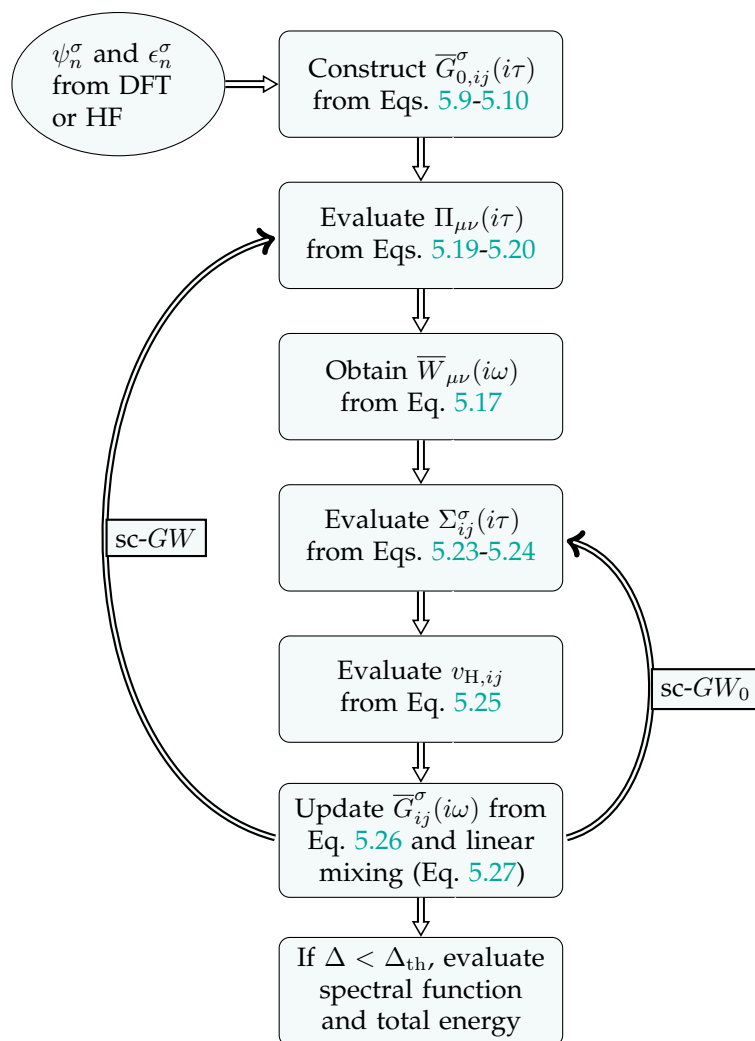


Figure 5.2: Flow diagram of the sc-GW algorithm as implemented in FHI-aims. A Fourier transform is implied whenever frequency and time are alternated.

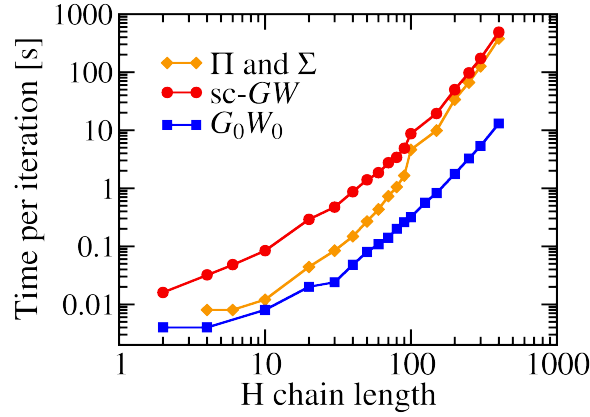


Figure 5.3: Time (in seconds) for a single iteration of the sc-GW loop for linear H-chains of different lengths in a minimal basis. Diamonds indicate the total time required for the evaluation of the polarizability and the self-energy from Eqs. 5.20 and 5.24, respectively. The total time required for the evaluation of the self-energy in G_0W_0 is included for comparison.

- The difference in Hartree potential $\Delta v_{H,ij}$ is obtained evaluating Eq. 5.25 with the non-interacting and the interacting Green function, and taking the difference of the two matrices.
- The modified Green function $\bar{G}_{ij}^\sigma(i\omega)$ is updated by solving the Dyson equation (Eq. 5.26).
- \bar{G} is Fourier transformed to imaginary time and combined with the Green function from the previous iteration through a linear mixing procedure (Eq. 5.27).
- The whole procedure is iterated until the average (absolute) changes of the Green function matrix elements are smaller than 10^{-5} . This convergence criterion is sufficient to guarantee the convergence of excited- and ground-state properties. As discussed below, the convergence is facilitated by a linear mixing of \bar{G}_{ij}^σ at each iteration from Eq. 5.28.

With minor modifications the procedure can be extended to perform partially self-consistent calculation with fixed screened Coulomb interaction (sc- GW_0). In sc- GW_0 , the screened interaction W is evaluated only once from HF or DFT orbitals and only the equations for the self-energy and the Green function are iterated to self-consistency (see Fig. 5.2).

The evaluation of Eqs. 5.18 and 5.22 is the most time-consuming step of this implementation. The scaling of the computational time as a function of the basis set and therefore system size are equal to that of G_0W_0 . To illustrate this, I report in Fig. 5.3 the total computational time spent for a single iteration of Eqs. 5.17-5.26 as a function of the length of a linear hydrogen chain in a minimal basis set. As compared to conventional G_0W_0 implementations, the additional computational cost arises from the non-diagonal matrix elements in the calculation of G and Σ . For systems with a higher degree of

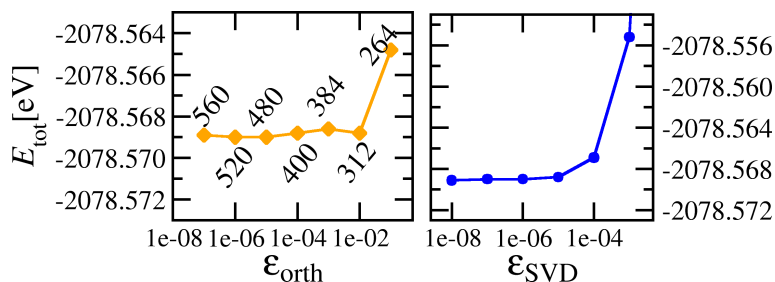


Figure 5.4: sc-GW total energy of H₂O as a function of the convergence parameters ϵ_{orth} (left panel) and ϵ_{SVD} (right panel), evaluated with a Tier 2 basis set. The number of product basis functions corresponding to each value of ϵ_{orth} is also reported.

coordination, the computational-time scaling of G_0W_0 and sc-GW is expected to worsen (in a similar fashion for both approaches) due to the potentially larger auxiliary basis set.

Beside the finite basis set and the discretization of integration grids, the only approximation introduced until this point is the resolution of the identity for the expansion of the product of NAO pairs (Eq. 5.12). As discussed in Ref. [158], the accuracy of the RI can be monitored systematically by means of two control parameters: ϵ_{orth} and ϵ_{SVD} . ϵ_{orth} sets the accuracy threshold for the Gram-Schmidt orthonormalization employed for the reduction of the linear dependence of on-site (i.e., lying on the same atom) product basis functions P_μ . In practice, by choosing smaller values of ϵ_{orth} one may increase the number of product basis functions used in the expansion in Eq. 5.12. Similarly, the parameter ϵ_{SVD} controls the singular value decomposition (SVD) for the orthonormalization of product basis functions on different atoms. A more detail description of the effects of these parameters can be found in Ref. [158]. To show the effect of the RI scheme on the self-consistent Green function, I report in Fig. 5.4 the sc-GW total energy – evaluated from Eq. 7.6 – of the water molecule as a function of ϵ_{orth} (left panel), and ϵ_{SVD} (right panel). For a wide range of values of the control parameters ϵ_{orth} and ϵ_{SVD} , the changes of the total energy are of the order of 10^{-4} eV or less. In all following calculations I used $\epsilon_{\text{orth}} = 10^{-5}$ and $\epsilon_{\text{SVD}} = 10^{-5}$.

At the first iteration of the sc-GW loop, the polarizability Π , screened interaction \overline{W} , and self-energy Σ – evaluated from Eqs. 5.20, 5.17, and 5.24, respectively¹ – have been compared with the corresponding quantities obtained from the G_0W_0 implementation in FHI-aims [158]. This comparison, illustrated in Fig. 5.5, serves as a consistency check. The overlap between the curves obtained from the two different codes demonstrates numerically the correctness of the derivation presented here and of its numerical implementation in FHI-aims.

¹For a comparison of Σ in the G_0W_0 and sc-GW implementations, it is necessary to transform it in the basis of the eigenstates of the initial reference Hamiltonian (in contrast to the NAO basis). Moreover, both calculations must be performed using the same chemical potential μ , which for molecules can be chosen arbitrarily within the HOMO-LUMO gap. Although different values of μ may alter the structure of Σ on the imaginary axis, it does not alter the real-frequency representation of the self-energy.

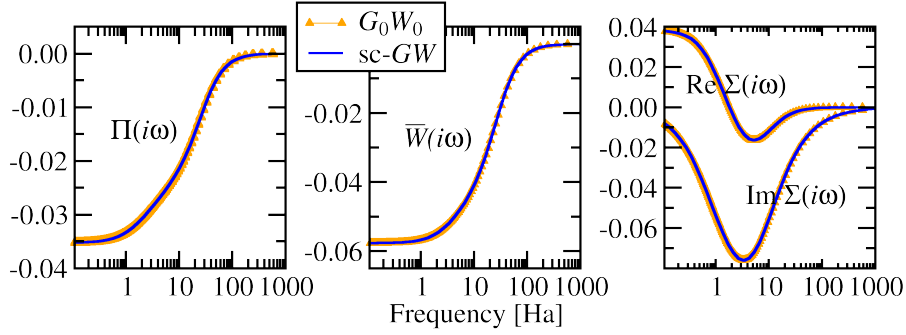


Figure 5.5: Polarizability Π , screened interaction \bar{W} , and self-energy Σ (transformed to the eigenstate basis) evaluated from Eqs. 5.20, 5.17, and 5.24, respectively (solid line) at the first iteration of the sc-GW loop. For comparison, the same quantities from the G_0W_0 implementation in FHI-aims are also reported (see Ref. [158]). For Π and \bar{W} the $\mu = \nu = 1$ matrix element was considered, whereas for Σ_{KS} the curve refer to the highest occupied molecular orbitals. All data refer to H_2O with a Tier 2 basis set.

To facilitate the convergence of the sc-GW loop, the input Green function \bar{G}^{input} of the $(N + 1)$ -th iteration is obtained from a linear mixing scheme:

$$\bar{G}_{ij}^{\text{input}}(i\tau) = (1 - \alpha)\bar{G}_{ij}^N(i\tau) + \alpha\bar{G}_{ij}^{N-1}(i\tau) \quad , \quad (5.27)$$

where \bar{G}^N denotes the Green function obtained from the N -th solution of the Dyson equation, and α is the linear mixing parameter. As illustrated in the right panel of Fig. 5.6, it is found that typically $\alpha = 0.2$ is a good choice, although the optimal value of the mixing parameter is strongly system dependent. The convergence of the self-consistent loop is monitored looking at the average deviation of the Green function at each iteration Δ , defined as:

$$\Delta = \frac{1}{N_b^2} \sum_{i,j} |\bar{G}_{ij}^N(i\tau = 0^-) - \bar{G}_{ij}^{N-1}(i\tau = 0^-)| \quad . \quad (5.28)$$

The sc-GW loop is considered converged when Δ drops below a chosen threshold Δ_{th} . Default settings used in most calculations are $\Delta_{\text{th}} = 10^{-5}$, which suffices to converge both total and quasi-particle energies. For H_2 , H_2O and C_6H_6 , values of Δ as a function of the number of iterations are illustrated in Fig. 5.6 and demonstrate that 5-10 iterations are sufficient to converge the sc-GW Green function within $\Delta_{\text{th}} = 10^{-5}$. For the systems considered in this work, it was not necessary to resort to more elaborate mixing schemes.

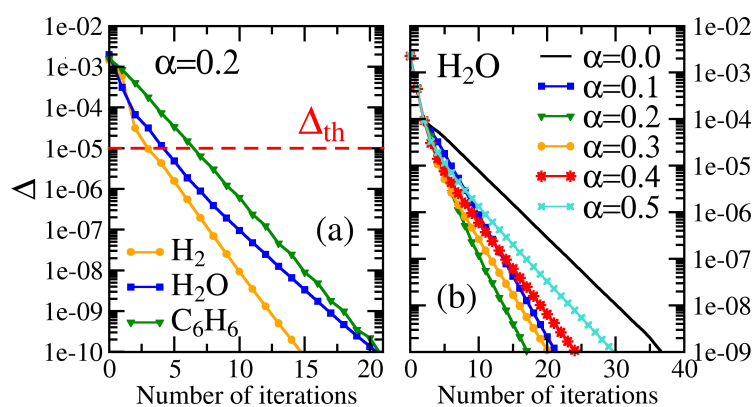


Figure 5.6: Left: Values of Δ – defined in Eq. 5.28 – as a function of the number of iteration of the sc-GW loop for H_2 , H_2O and C_6H_6 in their equilibrium geometry in a Tier 2 basis set. A linear mixing parameter $\alpha = 0.2$ was used in all calculations. Δ_{th} indicates the default value of the convergence threshold. Right: Convergence of Δ for different values of the linear mixing parameter α for the H_2O molecule.

6 FREQUENCY AND TIME DEPENDENCE IN SELF-CONSISTENT GW

In Green function based approaches, most quantities are dynamic – i.e., they have a non-trivial dependence on frequency or time. In a numerical implementation, this may become a major bottleneck, since the number of operations and the computational time are proportional to the number of grid points used to represent the frequency dependence of G and Σ . The grid size necessary for converged GW calculations may depend crucially on the scheme adopted for the treatment of dynamical quantities. A variety of methods has been used in previous GW implementations for dealing with the frequency dependent quantities, including (i) imaginary time/frequency schemes based on Fourier transform [209] or frequency convolution [158]; (ii) real frequency approaches [58]; (iii) spectral functions based schemes [159]; (iv) contour deformation [210]; (v) solution of the Casida equation [165]. As discussed in the following, the approach (i) is particularly suitable for sc- GW calculations and therefore it is the method of choice for the treatment of all dynamical quantities in this implementation.

With the goal of extending the applicability of sc- GW to molecules up to 30-50 atoms, a new method for the numerical evaluation of Fourier transforms in the GW approximation was developed. In the first part of this Chapter, the basics of the imaginary frequency-time framework will be shortly reviewed. The second part is devoted to numerical algorithms developed during this thesis for the evaluation of Fourier type integrals.

6.1 IMAGINARY TIME AND FREQUENCY FORMALISM

The inspection of the analytic expression for the non-interacting Green function:

$$G_0^\sigma(\mathbf{r}, \mathbf{r}', \omega) = \sum_n \frac{\psi_n^\sigma(\mathbf{r})\psi_n^{\sigma*}(\mathbf{r}')}{\omega - (\epsilon_n^\sigma - \mu) - i\eta \text{sgn}(\epsilon_n^\sigma - \mu)} \quad ,$$

indicates that G_0 has sharp δ -function like structures, or *poles*, on the real frequency axis (i.e., for real values of ω). For the non-interacting Green function the poles occur at the frequencies $\omega = \epsilon_n^\sigma - \mu$, but for a Green function G that is obtained from the solution of the Dyson equation, the position of the poles is not known. For this reason,

the description of the Green function on the real frequency axis requires in principle the definition of dense frequency meshes with several thousands of grid points, in order to resolve the poles of G . The same holds for other frequency dependent quantities such as W and Σ .

To circumvent this problem, one can extend the definition of G_0 to the complex frequency plane by allowing for imaginary values of ω in the expression above¹. This procedure is referred to as analytic continuation. On the imaginary axis, G_0 becomes a smooth function of $i\omega$. Numerically, this leads to a considerable reduction of the frequency mesh size, with a corresponding gain in computational efficiency. A more extended discussion of the mathematical foundation of the analytic continuation in Green function theory has been reported by Farid and coworkers in Refs. [211–213].

In the sc-GW implementation discussed here, all dynamic quantities are defined on the imaginary frequency axis. Formally, this can be done by replacing ω by $i\omega$ in the definition of G_0 :

$$G_0^\sigma(\mathbf{r}, \mathbf{r}', i\omega) = \sum_n \frac{\psi_n^\sigma(\mathbf{r})\psi_n^{\sigma*}(\mathbf{r}')}{i\omega - (\epsilon_n^\sigma - \mu)} .$$

which in matrix representation reduces to Eq. 5.8. Similarly, one can define the imaginary time Green function $G(i\tau)$, which should not be confused with the Matsubara Green function. The Matsubara G is also defined in imaginary time, but the ground-state expectation values is replaced by canonical averages at finite temperatures – which lead to the characteristic imaginary-time periodicity [214]. In the zero temperature limit, however, the Matsubara and imaginary-frequency Green functions coincide.

The imaginary time and frequency axes are discretized on exponentially spaced grids composed of N_ω points in the range $\{0, \omega_{\max}\}$, and by $2N_\tau + 1$ points in the range $\{-\tau_{\max}, \tau_{\max}\}$. The grid points ω_k and the integration weights $w(\omega_k)$ are defined as:

$$\begin{aligned} \omega_k &= \omega_0 [e^{(k-1)h} - 1] & w(\omega_k) &= h\omega_0 e^{(k-1)h} \\ \tau_k &= \tau_0 (e^{kh} - 1) & w(\tau_k) &= h\tau_0 e^{kh} . \end{aligned} \tag{6.1}$$

The constant h is obtained from the constraint $\omega_{\max} = \omega_0 [e^{N_\omega h} - 1]$ and the parameter ω_0 sets the initial spacing of the grid. The frequency mesh generated by the grid defined above – illustrated in Fig. 6.1 – is dense close to the origin where $G(i\omega)$ and $G(i\tau)$ show non-trivial analytic features. Moreover, it can be easily extended to high frequencies and therefore it is particularly suitable to capture the slow decaying behaviour ($\sim 1/i\omega$) of $G(i\omega)$. Typical values adopted in numerical calculations are $\omega_{\max} = 5000 \text{ Ha}$, $\tau_{\max} = 1000 \text{ Ha}^{-1}$ and $\omega_0 = \tau_0 = 0.001$.

¹Cauchy's theorem of complex analysis guarantees that there is a one to one correspondence between the real and imaginary frequency Green function, if G is holomorphic – i.e., infinitely differentiable – which is always the case for finite η .

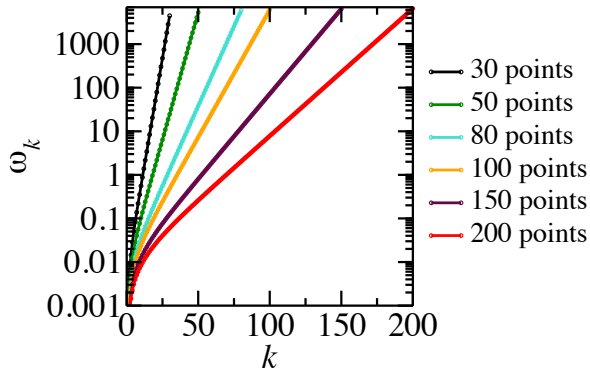


Figure 6.1: Distribution of the frequency points in the logarithmic mesh used in the sc-GW implementation.

6.2 EVALUATION OF FOURIER INTEGRALS

For an efficient and scalable sc-GW implementation, it is convenient to work in a mixed imaginary time-frequency framework. The computation of frequency convolutions can be replaced by products in imaginary time by virtue of the convolution theorem – which are numerically more efficient –, whereas the Dyson equations for G and W may be solved on the imaginary frequency domain, avoiding the evaluation of time integrals. Therefore, Fourier transforms (FT) are necessary to switch between the time and frequency representations of G , Π , \bar{W} , and Σ .

In the course of this thesis, several numerical approaches to the calculation of Fourier transforms in the GW approximation have been developed and implemented in FHI-aims. A brief review of these methods will be given in the following. For sake of conciseness, the methods will be presented only for the Green function, although they have been applied to other dynamic quantities, too.

The imaginary time and frequency representations of G are related by FTs:

$$G(i\tau) = \int_{-\infty}^{+\infty} \frac{d\omega}{2\pi} G(i\omega) e^{-i\omega\tau} \quad , \quad (6.2)$$

$$G(i\omega) = \int_{-\infty}^{+\infty} d\tau G(i\tau) e^{i\omega\tau} \quad . \quad (6.3)$$

On a discrete frequency grid the FT can be rewritten as:

$$G(i\tau_{k'}) = \sum_{k=1}^{N_\omega} \frac{w(\omega_k)}{2\pi} G(i\omega_k) e^{-i\omega_k\tau_{k'}} \quad . \quad (6.4)$$

The evaluation of FTs of this type is numerically cumbersome, despite the simplicity of the expression. The difficulty arises from the fast oscillations of the integrand $G(i\omega_k) e^{-i\omega_k\tau_{k'}}$ for large values of ω_k which ultimately leads to a slow convergence with the number of frequency points. As an example, Fig. 6.2 reports the FT – evaluated from Eq. 6.4 – of the first diagonal matrix element of the Green function of water, using

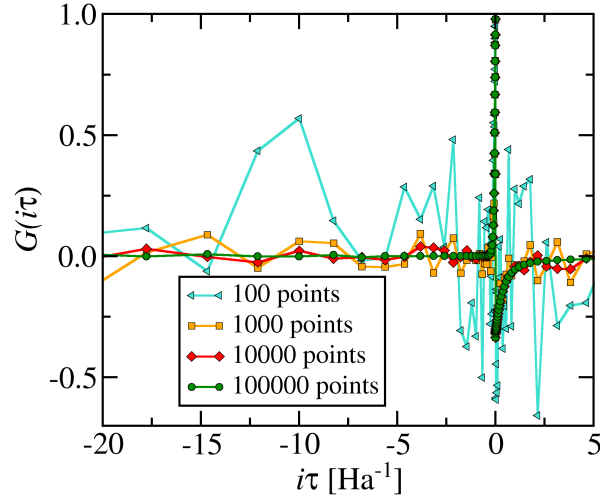


Figure 6.2: FT – evaluated from Eq. 6.4 – of the first diagonal matrix element of the Green function for the water molecule in a Tier 2 basis set. The different lines refer to different numbers of frequency points ($N_\omega = 10^n$ with $n = 2, 3, 4, 5$).

different values of N_ω . The number of frequency points N_ω must be increased up to approximately 10^5 , in order to converge the FT of G in the interval shown. Moreover, the larger the time interval, the larger the value of N_ω needed to converge the calculation. The application of Eq. 6.4 is clearly impractical for numerical calculations and motivates the development of more elaborate schemes for the computation of FTs in sc-GW.

TAIL-FITTING SCHEME

To reduce the number of frequency points in the evaluation of Fourier integrals, Steinbeck *et al.* proposed to fit the high frequency part of dynamic quantities using analytic functions with a known FT [209]. This principle is illustrated in Fig. 6.3. If the slow-decaying part of G can be accounted for analytically, only a small part of G needs to be transformed numerically.

At large frequencies the Green function decays as $1/i\omega$. Therefore, Lorentzian functions of the form $f(i\omega) = a/(b + i\omega)$ are an appropriate choice to represent the analytic behaviour of G at large values of $i\omega$. In practice, a frequency window is defined – typically including the last ten points of the frequency mesh – and the coefficients a and b are determined by means of non-linear least square fits solved with a Levenberg-Marquardt algorithm. The FT of $f(i\omega)$ can be evaluated analytically and yields $f(i\tau) = ae^{b\tau}[\theta(-\tau)\theta(b) - \theta(\tau)\theta(-b)]$. Therefore, the FT of the Green function can be rewritten as:

$$G(i\tau_{k'}) = f(i\tau_{k'}) + \sum_{k=1}^{N_\omega} \frac{w(\omega_k)}{2\pi} [G(i\omega_k) - f(i\omega_k)] e^{-i\omega_k \tau_{k'}} \quad (6.5)$$

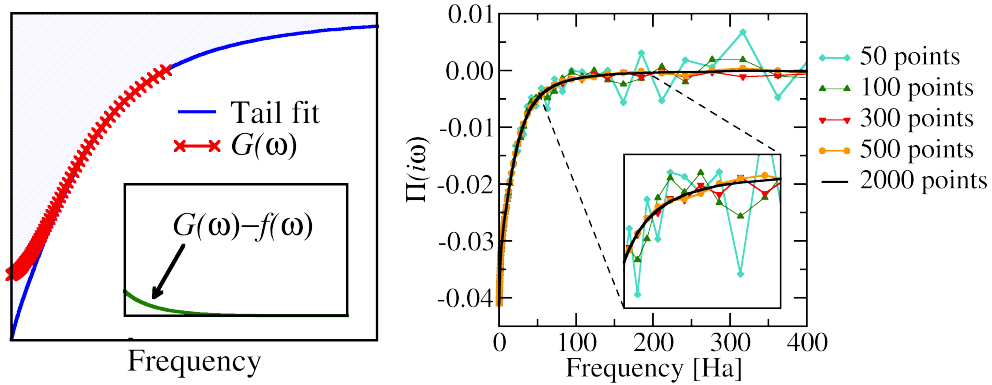


Figure 6.3: Left: Schematic representation of the tail-fitting scheme. The inset shows the function that eventually needs to be integrated numerically. Right: FT of the polarizability of water in a Tier 2 basis set evaluated with Eq. 6.5. Only the first diagonal matrix element was considered here.

Since the term $[G(i\omega_k) - f(i\omega_k)]$ is expected to vanish faster than $G(i\omega_k)$ for increasing $i\omega$, Fourier integrals evaluated from Eq. 6.5 converge faster with the frequency grid size.

This scheme is very accurate for the FT of the Green function, since the $f(i\omega)$ capture most of the analytic behaviour of $G(i\omega)$. For instance for the H_2O molecule, a few tens of grid points are sufficient to evaluate the FT of $G(i\omega)$ with an average accuracy of 10^{-9} (not shown).

More points are required for the FT of $\Pi(i\tau)$ to the frequency domain, as illustrated in Fig. 6.3, for H_2O . Nonetheless, due to the exponential decay of $\Pi(i\tau)$, the FT can be converged systematically simply by increasing the grid size. On the other hand, as discussed in Ref. [209] in detail, problems may arise in the computation of the FT of W since, for certain matrix elements, negative values of the fitted parameter b may be obtained. This in turn introduces singularities in the function $W(i\omega) - f(i\omega)$, leading to numerical noise in the FT.

Due to these instabilities, the method turned out to be inapplicable to large systems – where many $b < 0$ coefficients arise – and was eventually rejected.

POLE-EXPANSION METHOD

To obviate the problems discussed above, one can introduce a fully analytical representation for the frequency dependence of the Green function. This would enable a completely analytic representation of the FT, thus reducing the grid size considerably. In practice, one has to expand each matrix element of G in a set of basis functions, for which the FT is known analytically. In this way, the problem of evaluating the sum in Eq. 6.2 numerically is reduced to the construction of an optimal basis for the representation of the time and frequency dependence of G .

In short, the Green function is expanded in a set of poles of the form $f_k(i\omega) =$

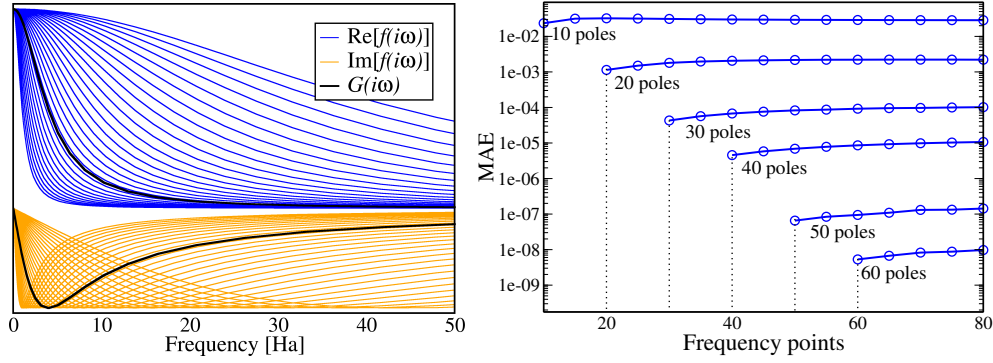


Figure 6.4: Left: Comparison of the analytic structure of the real (in blue, above) and of the imaginary part (in orange, below) of $f_k(i\omega)$ for different values of b_k , and a matrix element of the Green function of the Neon atom (black). Right: Mean absolute error (MAE) introduced by Fourier transforming the Green function of N_2 for different numbers of poles and frequency points.

$1/(b_k + i\omega)$, with corresponding FT $f_k(i\tau) = e^{b_k\tau}[\theta(-\tau)\theta(b_k) - \theta(\tau)\theta(-b_k)]$. The index k runs over the total number of poles N_{poles} . The parameters b_k are fixed at the beginning of the calculation and are distributed logarithmically in the energy range covered by the eigenvalues ϵ_n^σ . Although in principle other functions could be used, the functions $f_k(i\omega)$ constitute a natural choice for the expansion of the Green function, as the frequency dependence of $f_k(i\omega)$ closely resembles the analytic structure of G and captures the large frequency $1/i\omega$ behaviour. This is illustrated in Fig. 6.4, where the real and imaginary parts of $f_k(i\omega)$ – with different values of b_k – are compared to the first diagonal matrix element of the Green function of Ne.

The Green function can be expanded in the pole basis as:

$$G_{ij}^\sigma(i\omega) = \sum_{k=1}^{N_{\text{poles}}} [\alpha_{ij}^k f_k^{\text{Re}}(i\omega) + \beta_{ij}^k f_k^{\text{Im}}(i\omega)], \quad (6.6)$$

where $f_k^{\text{Re(Im)}}(i\omega)$ denotes the real (imaginary) part of $f_k(i\omega)$. The real and imaginary part of the Green function have been treated separately to maintain a real-valued linear-least square problem, leading in turn to real-valued coefficients α_k and β_k . Since the FT of the basis functions $f_k(i\omega)$ is known, the coefficients α_k and β_k also determine the expansion of the transformed Green function. Expansions similar to Eq. 6.6 were employed also for the FT of χ , W and Σ .

The error introduced by the FT can be quantified for functions known analytically on both the (imaginary) frequency and time axes as, for instance, the non-interacting Green function (for which the time and frequency representation are given in Eqs. 5.8 and 5.9). In Fig. 6.4, I report the mean absolute error (MAE) in the FT of the non-interacting Green function $G_0^\sigma(i\omega)$ of the nitrogen dimer N_2 , averaged over all matrix elements. The MAE drops exponentially when increasing the number of functions f_k , showing that a few

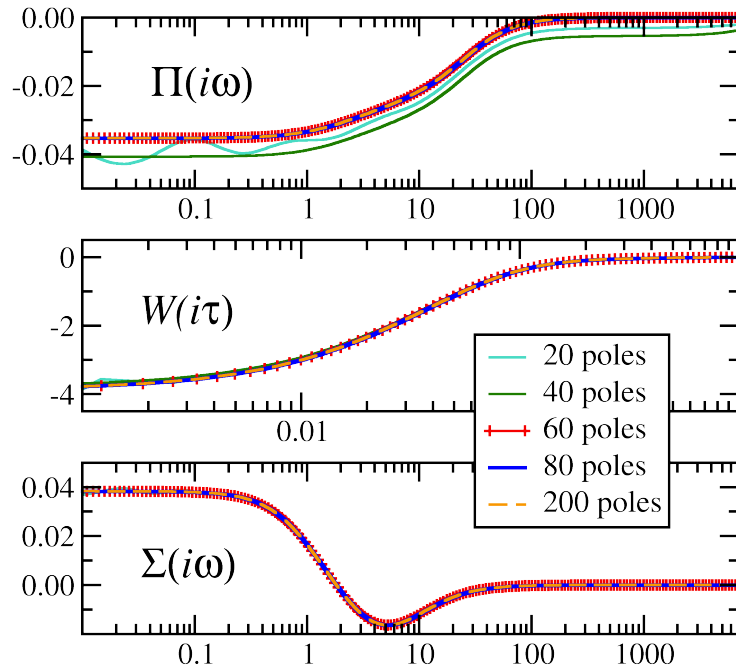


Figure 6.5: Polarizability Π , screened interaction \bar{W} , and self-energy Σ for different number of poles in the evaluation of the Fourier transform. For Π and \bar{W} the $\mu = \nu = 1$ matrix element was considered, whereas for Σ_{KS} the curves refer to the highest occupied molecular orbital. All plots are for the H_2O molecule evaluated with a Tier 2 basis set and $N_\tau = N_\omega = 200$.

tens of frequency points suffice to converge the Fourier integrals with an accuracy of the order of 10^{-8} .

Figure 6.5 illustrates the effect of the number of poles on the Fourier transformed quantities. The FT of Π , \bar{W} and Σ was evaluated using N_{poles} ranging from 20 to 200 in Eq. 6.6. As illustrated in Fig. 6.5, the number of poles only slightly affects the quantities. For $N_{\text{poles}} = 20-40$, small oscillations are observed in the polarizability and the screened Coulomb interaction at small values of ω and τ , respectively. Nevertheless, these errors do not affect visibly the structure of Σ at low frequency. For $N_{\text{poles}} = 60$ all quantities are converged. In the following, the default values adopted in all calculations, unless otherwise stated, are $N_\omega = N_\tau = 60$.

7 NUMERICAL EVALUATION OF PHYSICAL QUANTITIES

In previous Chapters I proposed a scheme to solve Hedin's GW approximation numerically without resorting to first-order perturbation theory (G_0W_0). Differently from G_0W_0 – and other partially self-consistent schemes based on perturbation theory – in sc- GW all physical quantities have to be extracted from the self-consistent Green function. The basic connection between the Green function, observables and the physical properties of a systems, has been outlined in Sec. 3.3. In this Chapter, it is addressed how these relations may be translated into a concrete recipe. In particular, I will focus on the evaluation of (charged) excitation energies and total energies.

7.1 SPECTRAL FUNCTION

In sc- GW , excitation energies are encoded in the spectral function, which is related to the Green function through Eq. 3.34:

$$A^\sigma(\omega) = \frac{1}{\pi} |\text{Tr}[\text{Im}G^\sigma(\omega)]| \quad ,$$

where the Green function is expressed on the real frequency axis. To bring the Green function from the imaginary to the real axis one has to perform the analytic continuation, a well established procedure not only for the GW approximation [163, 209, 211, 212, 215, 216], but also in Dynamical Mean Field Theory [217], and Quantum Monte Carlo [218–220].

This procedure is in principle exact, due to the one-to-one correspondence between the real and imaginary axis representation of holomorphic functions. In practice, the analytic continuation is performed by fitting the Green function or the self-energy with polynomials on the imaginary axis and the form of the chosen polynomial may affect the accuracy of the analytic continuation.

To evaluate the spectral function, minimizing the impact of the analytic continuation on the reliability of the quasi-particle energies, the following approach has been developed. The self-energy is first obtained in real frequency by means of the analytic continuation based on a two-pole fitting scheme [215]. In this approach, the matrix

elements of the self-energy in the imaginary frequency are fitted by polynomials of the form:

$$\Sigma_{ij}^{\sigma}(i\omega) \simeq \sum_{\alpha=1}^2 \frac{a_{\alpha,ij}^{\sigma}}{i\omega + b_{\alpha,ij}^{\sigma}} \quad (7.1)$$

Here, the coefficients $a_{\alpha,ij}^{\sigma}$ and $b_{\alpha,ij}^{\sigma}$ are determined by means of a non-linear least-square fit, solved with a Levenberg-Marquardt algorithm. The expression above fully defines Σ^{σ} also on the real axis – which is obtained from Eq. 7.1 by replacing $i\omega$ by ω . Once the real-frequency self-energy is obtained, the Dyson equation is solved directly in real frequency on a fine, equally spaced grid. The resulting Green function is used to determine the *sc-GW* spectral function $A(\omega)$. In this scheme, only the self-energy is subjected to the analytic continuation, whereas the remaining terms in the Dyson equation are unaffected. Alternatively, one can apply the analytic continuation directly to the Green function. However, this approach introduces a considerable numerical noise as compared to the scheme presented above and, consequently, the quasi-particle peaks appear unphysically broadened.

For the spectral properties, the analytic continuation constitutes the only approximation of the present implementation. Previous works [215] have indicated that the two-pole model for the analytic continuation (Eq. 7.1) reliably reproduce quasi-particle energies with an average relative error of the 0.2% for solids. More recently, it was shown for molecules that the two-poles fit provides results within a few meV compared to real-frequency *GW* calculations [221]. The parameter η in the denominator of the real-frequency G_0 (see Eq. 3.14), necessary to avoid the numerical divergence of G_0 , is set to $\eta = 10^{-4}$. This parameter contributes negligibly to the broadening of the spectral function and has no effect on the position of the quasi-particle peaks.

As an example, I report the *sc-GW* spectral functions of H_2O , NH_3 , and N_2 in Fig. 7.1 calculated using basis sets of increasing size. The *sc-GW* spectral function shows sharp δ -function like peaks at the quasi-particle energies. In panels a), b), and c) in Fig. 7.1, I report the spectral function corresponding to the highest occupied quasi-particle states evaluated with a Tier 1, Tier 2, and Tier 3 basis; panels d), e), and f) show the peaks corresponding to the lowest unoccupied quasi-particle states. The G_0W_0 @HF and *sc-GW* ionization energies are reported in panels g), h), and i) of Fig. 7.1 as a function of the basis set size. The G_0W_0 ionization energy is calculated from the linearized quasi-particle equation (Eq. 4.18), whereas in *sc-GW* it is extracted from the highest (valence) peak of the spectra shown in panels a), b), and c).

For the quasi-particle energies corresponding to occupied states, the largest change is observed going from Tier 1 to Tier 2. For N_2 for example, the HOMO changes by approximately 0.2 eV going from Tier 1 (which consists of 14 NAO basis functions per atom) to Tier 2 (39 NAO per atom). A further increase of the basis set from Tier 2 to Tier 3 (55 NAO per atom) leads to changes of the order of 5 meV in the HOMO – as illustrated in the right panels of Fig. 7.1. Lower lying quasi-particle peaks show

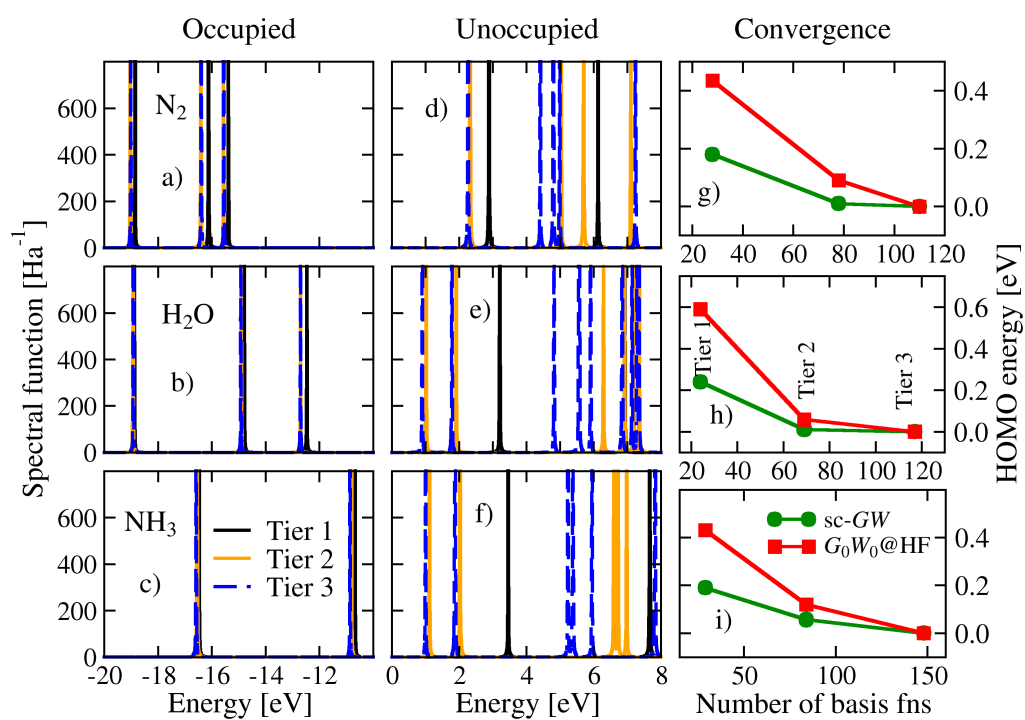


Figure 7.1: Self-consistent GW spectral function for H_2O , NH_3 , and N_2 with Tier 1, Tier 2 and Tier 3 NAO basis sets. Panels a), b), and c) show the peaks corresponding to the first valence states, peaks relative to unoccupied states are reported in panels d), e), and f). Finally, panels g), h), and i) report the convergence of the HOMO level as a function of the number of numerical orbitals used in the basis set.

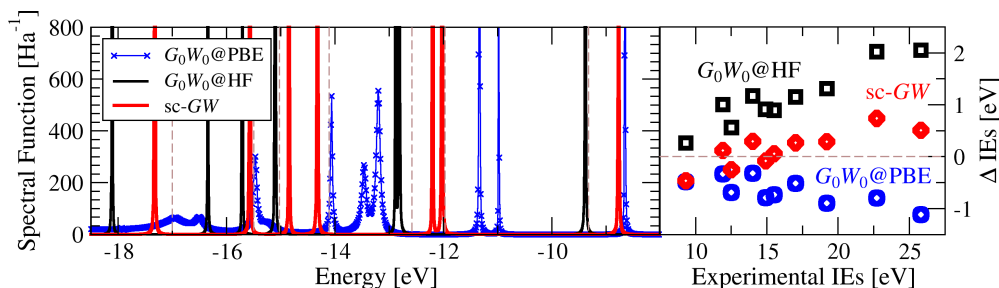


Figure 7.2: Left panel: The spectral function of benzene calculated with a Tier 2 basis set. Vertical dashed lines are located at experimental vertical ionization energies (VIEs) from Ref. [222]. Right panel: comparison of experimental [222] and theoretical VIEs extracted from the spectral function of benzene for $sc-GW$, $G_0W_0@HF$, and $G_0W_0@PBE$.

a similar convergence behavior as the HOMO. H_2O and NH_3 exhibit a qualitatively similar behavior. Surprisingly, for all systems considered here, $sc-GW$ converges faster with the basis set size than perturbative G_0W_0 calculations. Compared to the occupied states, the convergence of the empty states is considerably slower and larger basis sets are required for the calculation of quasi-particle states above the Fermi energy.

To test the quality of the $sc-GW$ spectra the benzene molecule was chosen as a benchmark, for which the $sc-GW$ spectral function in Fig. 7.2 is compared to the $G_0W_0@HF$ and $G_0W_0@PBE$ ones calculated using Eq. 3.34. The VIEs shown in the right panel of Fig. 7.2 correspond to the peak positions in the spectral function. All peaks reported in the left panel of Fig. 7.2 correspond to occupied quasi-particle states and the associated energy can be directly related to ionization energies as measured in photoemission spectroscopy. The G_0W_0 quasi-particle energies – reported in the right panel of Fig. 7.2 – depend strongly on the starting point: HF-(PBE)-based G_0W_0 has a tendency to overestimate (underestimate) VIEs. The deviation between $G_0W_0@HF$ and $G_0W_0@PBE$ is $\simeq 0.5$ eV for the first ionization energy and can be as large as $\simeq 3$ eV for lower lying quasi-particle states. Furthermore, due to overscreening $G_0W_0@PBE$ yields a large broadening (i.e., short lifetimes) for quasi-particle peaks below -12 eV. Those peaks are not plasmon satellites, but quasi-particle states with a short lifetime. The short lifetime arises from the small HOMO-LUMO gap in PBE that allows quasi-particle states to decay through the creation of electron-hole pairs [223], as it will be discussed in detail in the following. At self-consistency, the quasi-particle energies are uniquely defined, the systematic (over)underestimation of G_0W_0 calculations is considerably reduced and the resulting quasi-particle energies are in better agreement with photoemission data [222]. A more extended assessment of the overall accuracy of $sc-GW$ for the description of photoemission processes is deferred to Chap. 10.

7.2 GALITSKII-MIGDAL TOTAL ENERGY

The method of choice here for total-energy calculations is based on the Galitskii-Migdal (GM) formula:¹

$$E_{\text{GM}} = -i \sum_{\sigma} \int d1 \lim_{2 \rightarrow 1^+} \left[i \frac{\partial}{\partial t_1} - \frac{\nabla_1^2}{2} + v_{\text{ext}}(1) \right] G^{\sigma}(1, 2) \quad .$$

In the following, I derive an expression for the numerical evaluation of the GM total energy in a basis, with a discrete frequency grid. As a first step, one has to rewrite the GM total energy without the partial derivative with respect to time. This term may lead to numerical instabilities or – if Fourier transformed to frequency – to slow convergence with the grid size, due to the slow decaying behavior with frequency. This can be done inserting the equation of motion for the single-particle Green function (Eq. 3.7) in the GM formula, leading to:

$$E_{\text{GM}} = -i \sum_{\sigma} \int d1 d2 \lim_{3 \rightarrow 1^+} [(-\nabla_1^2 + 2v_{\text{ext}}(1) + v_{\text{H}}(1)) \delta(1 - 2) + \Sigma^{\sigma}(1, 2)] G^{\sigma}(2, 3) \quad . \quad (7.2)$$

Now Eq. 7.2 has to be recast into a matrix form. Making use of the matrix representation of the Green function in a basis:

$$\begin{aligned} G^{\sigma}(\mathbf{r}, \mathbf{r}', \tau) &= \sum_{ijklm} \varphi_i(\mathbf{r}) s_{ij}^{-1} G_{jl}^{\sigma}(\tau) s_{lm}^{-1} \varphi_m(\mathbf{r}') \\ &= \sum_{ij} \varphi_i(\mathbf{r}) \bar{G}_{ij}^{\sigma}(\tau) \varphi_j(\mathbf{r}') \end{aligned}$$

– with $\bar{G}_{ij}^{\sigma}(\tau)$ defined according to Eq. 5.10 – the first three terms in Eq. 7.2 can be rewritten as:

$$\begin{aligned} &-i \sum_{\sigma} \int d1 \lim_{2 \rightarrow 1^+} [-\nabla_1^2 + 2v_{\text{ext}}(1) + v_{\text{H}}(1)] G^{\sigma}(1, 2) = \\ &-i \sum_{\sigma} \int d^3\mathbf{r} \lim_{\mathbf{r}' \rightarrow \mathbf{r}} [-\nabla_{\mathbf{r}}^2 + 2v_{\text{ext}}(\mathbf{r}) + v_{\text{H}}(\mathbf{r})] \sum_{ij} \varphi_i(\mathbf{r}) \bar{G}_{ij}^{\sigma}(\tau = 0^-) \varphi_j(\mathbf{r}') = \\ &-i \sum_{\sigma} \sum_{ij} \bar{G}_{ij}^{\sigma}(\tau = 0^-) [2t_{ji} + 2v_{\text{ext},ji} + v_{\text{H},ji}] \end{aligned} \quad (7.3)$$

where the Green function depends only on the difference of time variables $\tau \equiv t - t'$, and the Hamiltonian is assumed to be time-independent. In the last step of Eq. 7.3, I defined the matrix representation of the kinetic energy operator as $t_{ij} = \int d^3\mathbf{r} \varphi_i(\mathbf{r}) \left[-\frac{\nabla_{\mathbf{r}}^2}{2} \right] \varphi_j(\mathbf{r})$, and used similar expressions for $v_{\text{ext},ji}$ and $v_{\text{H},ji}$. Finally, the last term in Eq. 7.2 can be rearranged by using the Fourier transform of the Green function and the self-

¹As discussed in Sec. 3.3, the total energy is independent of the total-energy functional if the Dyson equation is solved self-consistently, therefore this choice has no impact on the sc-*GW* total energies.

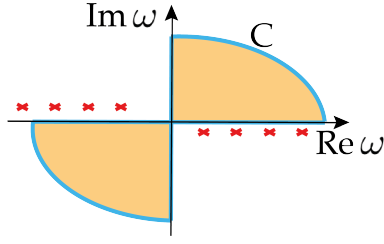


Figure 7.3: Contour C for the integration of Eq. 7.4 (blue solid line) and position of the poles of the integrand (red crosses).

energy $G(t, t') = \int_{-\infty}^{+\infty} \frac{d\omega}{2\pi} e^{-i\omega(t-t')} G(\omega)$. Replacing G with its matrix representation and carrying out the integrals over the real-space variables, yields:

$$-i \sum_{\sigma} \int d1d2 \lim_{3 \rightarrow 1^+} \Sigma^{\sigma}(1, 2) G^{\sigma}(2, 3) = -i \sum_{\sigma} \sum_{ij} \int \frac{d\omega}{2\pi} \Sigma_{ji}^{\sigma}(\omega) \bar{G}_{ij}^{\sigma}(\omega) e^{i\omega\eta} \quad (7.4)$$

It remains to demonstrate that the integral in Eq. 7.4 can be evaluated on the imaginary axis. By the residual theorem of complex analysis, the integral over a closed contour C that does not include poles is zero. The integrand of Eq. 7.4 has poles only on the upper-left and lower-right quadrant in the complex plane, as illustrated in Fig. 7.3. Therefore, one can always define the contour C that does not include poles, as depicted in Fig. 7.3, so that the integral on C is zero. Since the integrand vanishes on the closure (i.e., the curve part) of the contour for $|\omega| \rightarrow \infty$, the imaginary axis integral is equal and opposite in sign to the integral on the real axis. Therefore, the frequency integral in Eq. 7.4 can be evaluated directly on the imaginary axis without resorting to any analytic continuation. The integral in Eq. 7.4 can be rewritten on an imaginary frequency grid as:

$$-i \sum_{\sigma} \int d1d2 \lim_{3 \rightarrow 1^+} \Sigma^{\sigma}(1, 2) G^{\sigma}(2, 3) = \frac{i}{2\pi} \sum_{\sigma} \sum_{ij} \sum_k w(\omega_k) \Sigma_{ji}^{\sigma}(\omega_k) \bar{G}_{ij}^{\sigma}(\omega_k) \quad (7.5)$$

Finally, the sum of Eqs. 7.3 and 7.5 yields the desired expression for the total energy:

$$E_{\text{GM}} = -i \sum_{\sigma} \sum_{ij} [2t_{ji} + 2v_{\text{ext},ji} + v_{\text{H},ji} + \Sigma_{x,ji}^{\sigma}] \bar{G}_{ij}^{\sigma}(\tau = 0^-) + \frac{i}{2\pi} \sum_{\sigma} \sum_{ij} \sum_k w(\omega_k) \Sigma_{c,ji}^{\sigma}(\omega_k) \bar{G}_{ij}^{\sigma}(\omega_k) \quad (7.6)$$

where the self-energy was separated into its exchange and correlation components $\Sigma^{\sigma}(\omega) = \Sigma_x^{\sigma} + \Sigma_c^{\sigma}(\omega)$. In summary, I derived an exact reformulation of the Galitskii-Migdal formula in a basis, within a discrete frequency mesh. Although implemented for the evaluation of sc- GW total energies, Eq. 7.6 is not restricted to GW and is generally applicable to other self-energy approximations, or in the framework of perturbation theory. As an example choosing $\Sigma_c = 0$, Eq. 7.6 coincides with the Hartree-Fock total energy if G is the Hartree-Fock Green function.²

If evaluated with a non-interacting Green function G_0 obtained, e.g., from a PBE

²This identity served as a consistency check for the numerical implementation of Eq. 7.6.

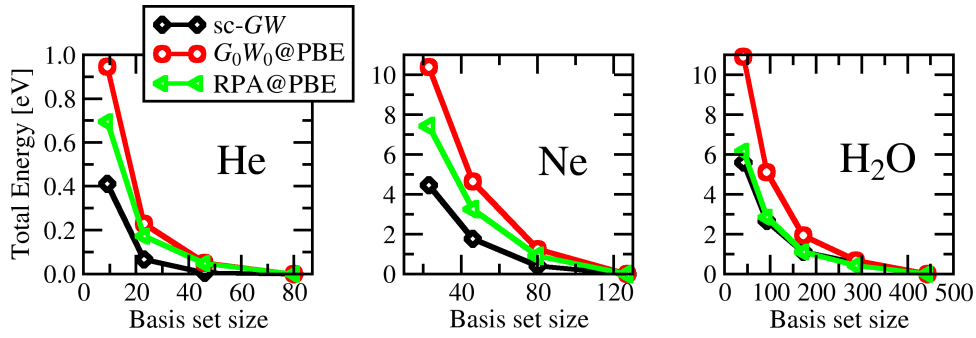


Figure 7.4: Total energy of He and Ne evaluated with *sc-GW*, $G_0W_0@PBE$ and $RPA@PBE$ with the Gaussian basis sets aug-cc-pVNZ with $N = D, T, Q, 5$. All total energies are referenced to the aug-cc-pV5Z value (see Table 7.1).

calculation, Eq. 7.6 provides the first-order perturbative correction to the PBE ground-state total energy due to the perturbing potential $\Sigma - v_{xc}$. Due to the analogy with the perturbative calculation of excitation energies in G_0W_0 , the total energy evaluated in this way is referred to as G_0W_0 total energy. As for spectral properties, perturbative total energies depend on the starting point. Therefore, I adopt the notation $G_0W_0@starting\ point$ to denote the corresponding starting point.

To validate the implementation of Eq. 7.6, the *sc-GW* total energies are compared with literature values from Ref. [104] in Table 7.1. The values obtained from the two implementations are in excellent agreement. The residual numerical differences are attributed to the different basis sets used in the two calculations.

CONVERGENCE WITH THE BASIS SET

To illustrate the convergence with the basis set, I report in Fig. 7.4 the total energy of He, Ne and H_2O as function of the basis set size using Dunning’s augmented correlation consistent polarized valence N zeta (aug-cc-pVNZ) basis sets [205], with $N = D, T, Q, 5$. Figure 7.4 indicates that *sc-GW* total energies converge faster with the basis set size, compared to perturbative G_0W_0 and RPA. Tentatively, one can attribute the origin of this behavior to the optimization of the empty state due to the self-consistency. Unfortunately, an unquestionable explanation still remains elusive.

In Fig. 7.5, I compare the total-energy convergence of He, Ne and H_2O evaluated with the aug-cc-pVNZ basis sets and FHI-aims Tiers. As discussed in Section 5.1, the Tiers

Table 7.1: *sc-GW* total energy calculated from Eq. 7.6 and literature values from [104]. For He, H_2 , and Ne the calculation were done with the aug-cc-pV5Z basis set. For LiH and Be with the aug-cc-pVQZ basis – which is the largest available for those elements. All values are in Hartree.

	He	Be	Ne	H_2	LiH
<i>sc-GW</i> [104]	-2.9278	-14.7024	-129.0499	-1.1887	-8.0995
<i>sc-GW</i>	-2.9252	-14.6534	-128.9796	-1.1898	-8.0678

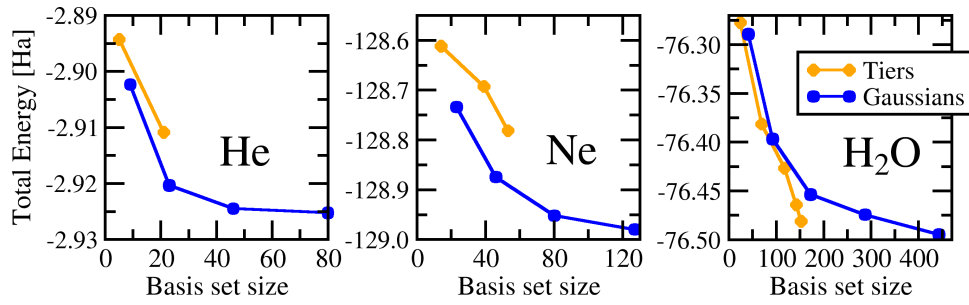


Figure 7.5: Self-consistent GW total energy of He and Ne evaluated with FHI-aims Tiers and with the Gaussian basis sets aug-cc-p VN Z with $N = D, T, Q, 5$.

basis sets are constructed and optimized for the minimization of the DFT total energy (of a given optimization target) within a local approximation for the exchange-correlation functional. However, this procedure does not guarantee full transferability of the Tier basis sets for total energy approaches which explicitly depend on the unoccupied states, as GW and RPA. For sc- GW , the right panel of Fig. 7.5 illustrates that for water the Tier basis outperforms Gaussians, although the latter are optimized for explicitly correlated methods. This indicates that the NAO basis functions potentially provide an optimal framework for the evaluation of *absolute* total energies. On the other hand, the Tier basis sets are insufficient for the sc- GW total energy of He and Ne. These arguments motivate the choice of using Gaussian basis sets for the evaluation of absolute total energies.

Total-energy differences are by far more important than absolute total energies, as they provide information on structural properties and on the strength of chemical bonds. From a technical perspective, energy differences are easier to compute as a faster convergence with the basis set size arises due to cancellation effects. This is illustrated in Fig. 7.6 where the binding energy of the carbon monoxide dimer is evaluated with sc- GW , RPA@PBE and G_0W_0 @PBE with increasingly larger basis sets (Tier 1-4). Also in this case, the convergence of the sc- GW total energy is faster as compared to perturbative total energy methods (G_0W_0 and RPA).

For completeness, I report the convergence of the sc- GW total energy as a function of several integration grid parameters in Appendix B.

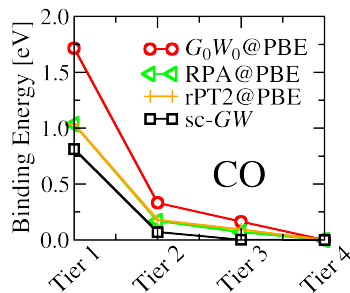


Figure 7.6: Self-consistent GW binding energy of the carbon monoxide dimer evaluated with different FHI-aims Tiers. For sc- GW , convergence is clearly achieved with Tier 3.

Part III

Applications to atoms and molecules

8 UNIFIED DESCRIPTION OF GROUND AND EXCITED STATES

In this Chapter, I demonstrate certain key aspects of the *sc-GW* approach for closed-shell molecules, that make *sc-GW* attractive as a general purpose electronic-structure method. First, the iteration of the Dyson equation produces a self-consistent Green function that is independent of the starting point, and determines both the ground- and excited-state properties (quasi-particle spectra) of a given system on the same quantum-mechanical level. These aspects distinguish *sc-GW* from other (partially) self-consistent *GW* schemes [174, 177, 178], which do not lend themselves to total-energy or ionic-force calculations, and depends on the starting point (i.e., the initial reference calculation). Moreover the uniqueness of the *sc-GW* Green function facilitates an unprecedented and unbiased assessment of the *GW* approach, which previously was masked by the starting-point dependence of G_0W_0 . Second, self-consistency improves total energies compared to G_0W_0 based on HF or DFT in (semi)local approximations and yields better agreement with high level quantum-chemical calculations. Third, unlike G_0W_0 , *sc-GW* yields an associated ground-state electron density, whose quality is e.g. reflected in the improved description of dipole moments. This is an essential feature for the reliable prediction of the electronic structure of charge-transfer compounds, as exemplified for the TTF-TCNQ molecular interface. All these points taken together are essential for future developments in electronic-structure theory such as vertex functions, beyond *GW* approaches, and new Green-function-based non-perturbative methods for the evaluation of ground and excited states.

8.1 INDEPENDENCE OF THE STARTING POINT AND CONSERVATION LAWS

The dependence on the starting point is a major shortcoming of perturbative (and partially self-consistent) *GW* methods, which makes G_0W_0 quasi-particle energies dependent on the choice of the input orbitals. This effect may lead to uncertainties of several eV in the quasi-particle spectra and it considerably limits the predictive power of *GW* calculations. In the following, a numerical proof of the independence of the starting point of *sc-GW* is reported for finite systems. This is crucial for establishing

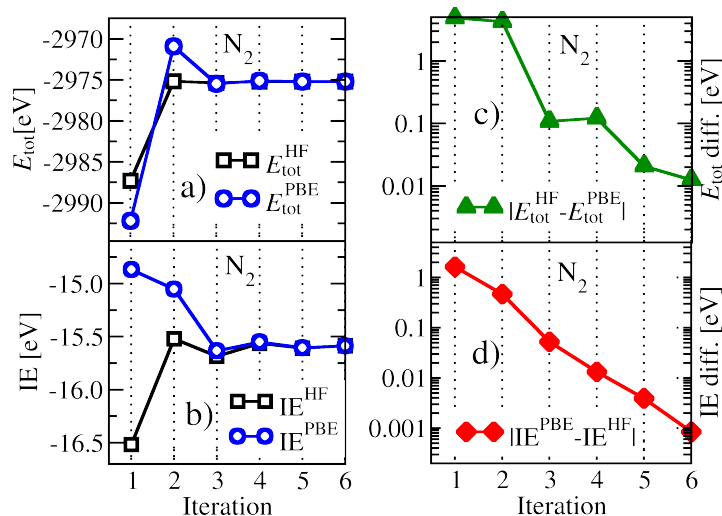


Figure 8.1: Total energy (a) and ionization energy (b) of N₂ at each iteration of the sc-GW loop for a HF and PBE input Green function, for the aug-cc-pVQZ basis set [205]. The absolute values of the differences arising from HF and PBE initializations vanish exponentially for both total energy (c) and ionization energy (d).

sc-GW as a reference method for perturbative G_0W_0 calculations.

In Fig. 8.1, I demonstrate for N₂ that the sc-GW Green function provides total energies (a) and vertical ionization energies (VIEs) (b) that are independent of the starting point. The self-consistency cycle is initialized with either HF or DFT in the Perdew-Burke-Ernzerhof (PBE) generalized gradient approximation [41], but other initializations like the local-density approximation (LDA) or the simple Hartree approximation produce the same final sc-GW Green function. The deviation in the Green function, exemplified by the absolute value of the total-energy difference (Fig. 8.1(c)) and the ionization-energy difference (Fig. 8.1(d)), converges exponentially fast with the number of iterations, canceling the starting-point dependence. Further tests performed on a set of 30 closed-shell molecules (see Fig. 10.8 and Appendix C) confirm this fact and demonstrate that sc-GW provides a recipe for linking different reference systems of independent electrons (or non-interacting Kohn-Sham particles) to a unified interacting many-body state.

The spectral function of N₂ is reported in Fig. 8.2 for the first six iterations of the Dyson equation, using HF and PBE as starting points. Figure 8.2 demonstrates that already a few iterations of the Dyson equation suffice to obtain both quasi-particle energies and peak broadenings (i.e., lifetimes of the quasi-particle states) which do not depend on the initial reference state. The reader is referred to Chap. 10 for a more detailed discussion of the broadening of low-energy quasi-particle peaks.

As mentioned in Sec. 4.3, the satisfaction of the particle-number-conservation law is reformulated in Green function theory in terms of the continuity equation. As demonstrated by Baym and Kadanoff, the continuity equation in turn requires the self-energy to obey certain symmetry properties which – in the GW approximation – are only

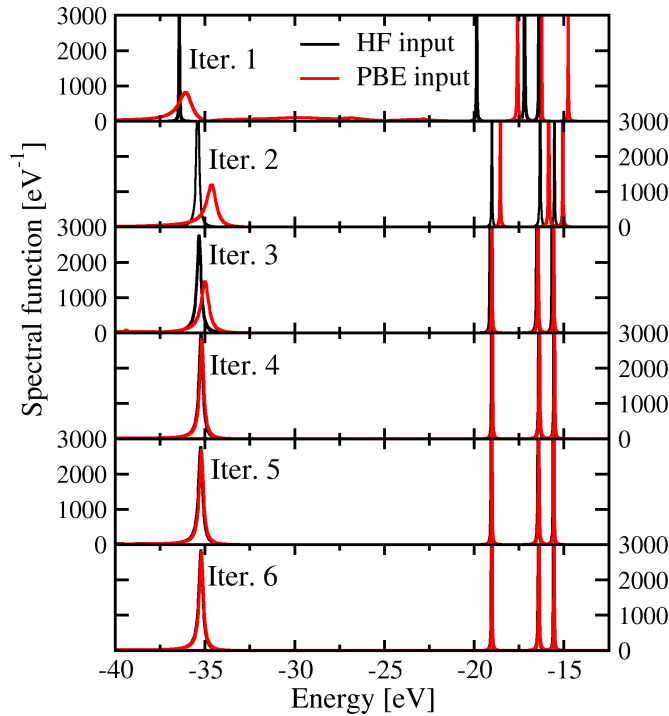


Figure 8.2: Spectral function of the N_2 dimer evaluated for the first six iterations of the Dyson equation using a HF and PBE initialization of the sc-GW loop.

satisfied at self-consistency [102, 169]. Similar arguments also hold for the momentum- and energy-conservation laws.

The satisfaction of the particle-number-conservation law was first demonstrated numerically in Ref. [196] for H_2 , for self-consistent and partially self-consistent approaches based on the solution of the Dyson equation. As a consistency check, the satisfaction of the particle-number-conservation law has been verified also for the sc-GW implementation developed in this work. In Fig. 8.3, the electron number of the hydrogen dimer (extracted from the Green function by taking the trace of the density matrix defined in Eq. 3.39) is shown for different interatomic distances. For G_0W_0 , I considered the Green function obtained solving the Dyson equation once. The violation of conservation laws is manifested in G_0W_0 by the deviation from the correct particle number, which increases for larger bond lengths. On the other hand, the sc-GW Green function satisfies the Baym-Kadanoff conservation laws and the corrected particle number is retrieved at all bond lengths.

Having established the important point that the sc-GW solution is independent of the starting point and having verified the satisfaction of conservation laws at self-consistency, I now turn to an assessment of the performance of the GW approach for the ground-state properties of atoms and molecules.

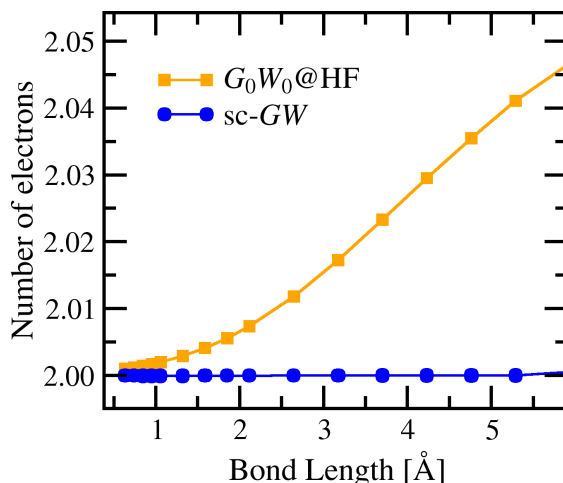


Figure 8.3: Number of electrons in the H_2 dimer extracted from the Green function at different internuclear separations. The G_0W_0 values are obtained solving the Dyson equation once.

8.2 TOTAL ENERGIES

Total-energy calculations in the GW approximation have previously been reported in the literature [104, 193, 196, 199–202, 224–226], however only a few studies have been devoted to finite systems at self-consistency [104, 196]. In this Section, I provide an assessment of self-consistent and G_0W_0 total energies evaluated with the Galitskii-Migdal (GM) formula. As alluded to in Sec. 3.3, the total energy is independent of the choice of the total energy functional if the Dyson equation is solved self-consistently, therefore the sc- GW results are not affected by this choice. On the other hand, in perturbative and partially self-consistent calculations the total energy may differ if one uses a different total energy functional [104].

For the atoms in the first two rows of the periodic table (i.e., $Z = 1 - 10$) accurate reference data from full configuration-interaction (full-CI) calculations are available [227–229]. Figure 8.4 (upper panel) reports the difference to full-CI for basis set converged sc- GW , G_0W_0 , and sc- GW_0 total energies based on HF and PBE. A subset of these systems has previously been calculated using sc- GW [104] and the results of the present work are in good agreement with the published results, as the comparison reported in Table 7.1 illustrates. The error of the EX+cRPA and rPT2 total energies based on HF and PBE are reported in the lower panel of Fig. 8.4 for comparison. In line with previous calculations for the electron gas [201, 226], solids [199, 200], atoms and small molecules [104], G_0W_0 total energies (in various flavors) tend to be too negative. The self-consistent treatment largely (but not fully) corrects this overestimation and provides total energies in more satisfying agreement with full-CI. The remaining overestimation provides a clear and unbiased quantification of the required vertex corrections in a beyond GW treatment. The numerical values of the total energies of atoms evaluated

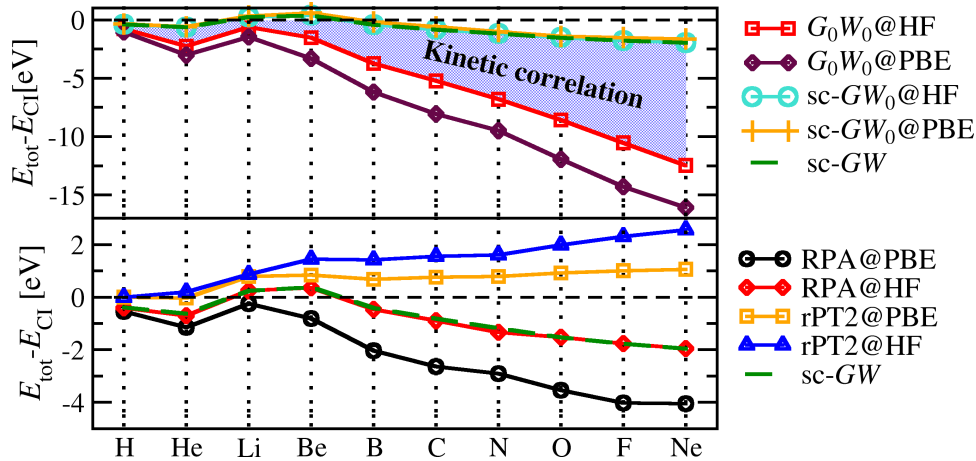


Figure 8.4: Difference between GW total energies at different level of self-consistency and full configuration interaction values (E_{CI}) from Refs. [227–229] (upper panel) for atoms from H to Ne. The EX+cRPA and rPT2 total energy differences to full-CI are reported in the lower panel. The differences between the self-consistent and $G_0W_0@HF$ total energies (shaded in light blue) are attributed to the kinetic correlation energy, as discussed below. The calculations were performed using the aug-cc-pV5Z basis set [205].

with G_0W_0 , EX+cRPA (equivalent to the perturbative evaluation of the Klein functional in the GW approximation), partially self-consistent sc- GW_0 , and sc- GW , are reported in Appendix D, whereby PBE, Hartree-Fock, and rPT2 are included for comparison. Interestingly, sc- GW_0 and sc- GW total energies show very small numerical differences, indicating that the quality of the screened Coulomb interaction contributes negligibly to the total energy, as shown in Table D.1. On the other hand, as demonstrated in Chap. 10, the dependence of the spectral properties on the choice of W is substantially more pronounced. For the total energy, rPT2 gives the best agreement with full-CI, although its performance is contingent on the choice of a good starting point. EX+cRPA@PBE considerably overestimates the reference data, whereas EX+cRPA@HF provides similar total energies to sc- GW . This similarity is expected for two reasons: First, in atoms screening is small, thus the sc- GW Green function resembles the Hartree-Fock one (since in the absence of polarization W reduces to the bare Coulomb interaction). Second, the EX+cRPA total energy is a variational functional of the Green function, and it therefore provides total energies close to sc- GW , if the input Green function is *close enough* to the sc- GW Green function [101]. Larger discrepancies between EX+cRPA and sc- GW are to be expected for systems for which sc- GW provides a substantially different density as compared to HF or semi-local DFT. Example of these material are molecular interfaces and charge-transfer compounds – as demonstrated below for the TTF-TCNQ dimer – where the ground-state density (and the charge transfer) depends strongly on the level alignment between the individual components of the system. This will be addressed below for the representative case of the TTF-TCNQ dimer.

The differences between self-consistent and perturbative total energies – highlighted

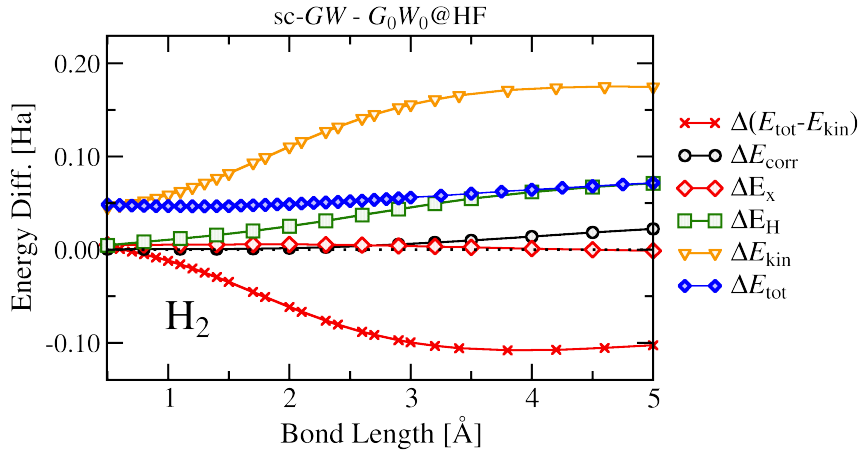


Figure 8.5: Difference between the sc-*GW* and G_0W_0 @HF total (ΔE_{tot}), kinetic (ΔE_{kin}), Hartree (ΔE_{H}), and correlation energy (ΔE_{c}) of the hydrogen dimer at several bond lengths.

in Fig. 8.4 – show that sc-*GW* total energies are systematically smaller (i.e., less negative) than the G_0W_0 ones. To understand the origin of this qualitative difference, it is useful to look at the changes between the individual contributions to the total energy. In Fig. 8.5, I report the differences between the sc-*GW* and G_0W_0 @HF total (ΔE_{tot}), kinetic (ΔE_{kin}), Hartree (ΔE_{H}), and correlation energies (ΔE_{c}) of the hydrogen dimer at several values of the bond length. Figure 8.5 demonstrates that, for H_2 close to its equilibrium bond length (0.7414 Å), the Hartree, exchange and correlation energies do not change substantially at self-consistency. The differences of the total energy at self-consistency can therefore be attributed to an increase of the kinetic energy term. This is a consequence of the structure of the Galitskii-Migdal total energy functional E_{GM} : When evaluated with a non-interacting Green function, the E_{GM} functional does not account for kinetic correlation energy contributions (defined as the difference between the kinetic energy of the interacting system and the non-interacting total energy). In contrast, the Klein and Luttinger-Ward functionals include kinetic correlation through the coupling constant integration as discussed in more details in the following Chapter. Differently to G_0W_0 , the Green function obtained from sc-*GW* corresponds to an interacting many-body state, and therefore the kinetic correlation energy is correctly accounted for. In other words, the improvement of the sc-*GW* total energy at self-consistency arises from the inclusion of kinetic correlation energy contributions. These are absent in a perturbative total energy calculation based on the Galitskii-Migdal functional, but they are fully taken into account when the self-consistent Green function is used. Obviously, at self-consistency, the GM and Klein total energies are identical.

For larger interatomic distances the total energy differences between self-consistent and perturbative *GW* calculations cannot be attributed to the kinetic term alone. The dissociation regime is characterized by a strong multi-reference character (i.e., its wave function is not representable in terms of a single Slater determinant). This is a challeng-

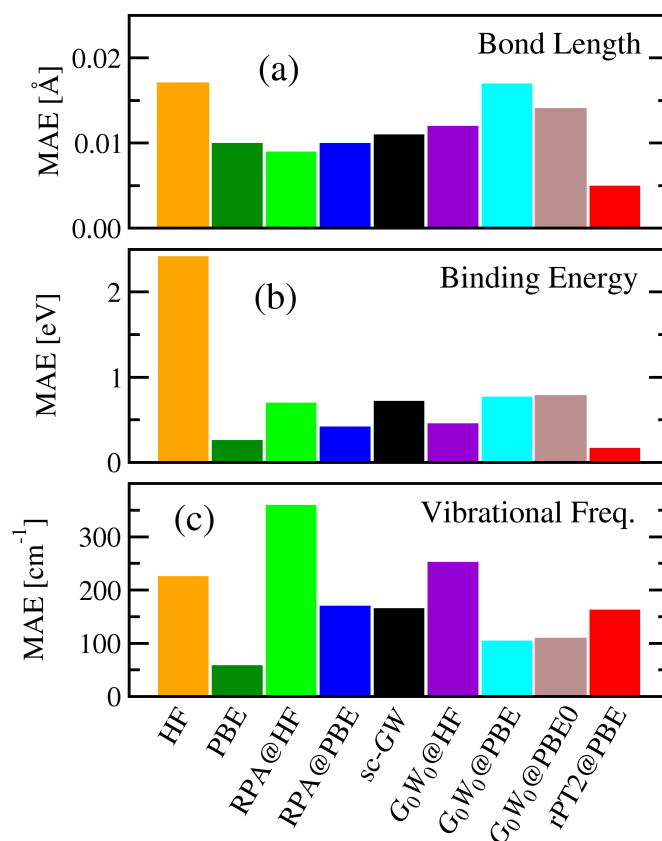


Figure 8.6: Mean absolute error (MAE) of bond lengths (a), binding energies (b), and vibrational frequencies (c) of LiH, LiF, HF, CO, H₂, and N₂ evaluated at different levels of theory. The estimated zero-point motion correction has been subtracted from the experimental binding energies (from Ref. [230]). Numerical values are reported in Tables 8.1, 8.2, and 8.3.

ing test case for which many electronic-structure approaches fail. The dissociation of diatomic molecules will be addressed in detail in the following Chapter.

STRUCTURAL PROPERTIES OF DIATOMIC MOLECULES

In this Section, the accuracy of the *sc-GW* method is benchmarked for bond lengths, binding energies, and vibrational frequencies based on the calculations of the potential-energy curve of LiH, LiF, HF, CO, H₂, and N₂. I emphasize that the focus of this Section is on ground-state properties of diatomic molecules at their equilibrium geometry. The dissociation of diatomic molecules, due to the predominance of static correlation, also presents a challenging and interesting case, that will be discussed in Chap. 9. Calculations were done with a Tier 3 basis set (the largest basis set available) for H₂, LiH, LiF, and HF, whereas a Tier 4 basis was used for N₂ and CO. The results of this study are summarized in Fig. 8.6, whereas the corresponding numerical values are reported in Tables 8.1, 8.2, and 8.3.

Panel (a) of Fig. 8.6 reports the mean absolute error (MAE) of the *sc-GW* bond

Table 8.1: *sc-GW* and G_0W_0 binding energies for diatomic molecules compared to (zero point motion corrected) experimental reference data taken from Ref. [230]. Perturbative EX+cRPA, HF, PBE, and renormalized second-order perturbation theory (rPT2) are included for comparison. Calculations were done with a Tier 3 basis set for H₂, LiH, LiF, and HF, whereas a Tier 4 basis was used for N₂ and CO. All values are in eV.

	H ₂	LiH	HF	LiF	N ₂	CO	ME	MAE
Exp (no ZPM)	-4.48	-2.41	-5.87	-5.97	-9.76	-11.11		
Exp	-4.75	-2.52	-6.12	-6.02	-9.91	-11.24		
<i>sc-GW</i>	-4.41	-2.16	-5.55	-5.50	-8.42	-10.19	-0.72	0.72
G_0W_0 @HF	-5.05	-2.72	-6.45	-6.60	-10.61	-11.88	0.46	0.46
G_0W_0 @PBE	-5.44	-2.94	-6.46	-6.37	-11.82	-12.16	0.77	0.77
G_0W_0 @PBE0	-5.32	-2.90	-6.49	-6.67	-11.50	-12.34	0.78	0.78
(EX+cRPA)@HF	-4.41	-2.17	-5.54	-5.52	-8.51	-10.19	-0.70	0.70
(EX+cRPA)@PBE	-4.68	-2.32	-5.60	-5.43	-9.54	-10.48	-0.42	0.42
rPT2@PBE	-4.71	-2.49	-5.93	-5.90	-9.42	-11.06	-0.17	0.17
HF	-3.64	-1.49	-4.22	-3.95	-5.10	-7.62	-2.42	2.42
PBE	-4.54	-2.32	-6.17	-6.03	-10.58	-11.67	0.13	0.26

Table 8.2: *sc-GW* and G_0W_0 bond lengths for diatomic molecules compared to experimental reference data taken from Ref. [128]. Perturbative EX+cRPA, HF, PBE, and PBE-based renormalized second-order perturbation theory (rPT2@PBE) are included for comparison. All values are in Å.

	H ₂	LiH	HF	LiF	N ₂	CO	ME	MAE
Exp.	0.741	1.595	0.917	1.564	1.098	1.128		
<i>sc-GW</i>	0.735	1.579	0.919	1.586	1.085	1.118	0.003	0.011
G_0W_0 @HF	0.733	1.560	0.919	1.579	1.093	1.119	0.007	0.012
G_0W_0 @PBE	0.746	1.582	0.938	1.593	1.116	1.143	-0.013	0.017
G_0W_0 @PBE0	0.741	1.564	0.932	1.590	1.100	1.136	0.003	0.014
(EX+cRPA)@HF	0.734	1.587	0.914	1.576	1.087	1.117	0.005	0.009
(EX+cRPA)@PBE	0.745	1.597	0.927	1.589	1.107	1.137	-0.010	0.010
rPT2@PBE	0.739	1.597	0.914	1.578	1.091	1.125	0.000	0.005
HF	0.734	1.606	0.898	1.560	1.066	1.102	0.013	0.017
PBE	0.751	1.605	0.930	1.575	1.104	1.136	-0.010	0.010

lengths as compared to experiment [128]. Binding energies are reported in the panel (b), whereas vibrational frequencies in panel (c). Several perturbative approaches based on MBPT, namely G_0W_0 , EX+cRPA, and PBE-based renormalized second-order perturbation theory [77, 231] (rPT2@PBE), are included for comparison.

Self-consistency provides better bond lengths than G_0W_0 , that gives too large distances. However, the accuracy achieved by *sc-GW* for the bond lengths is still comparable to EX+cRPA@HF and not as good as rPT2@PBE, which includes higher-order exchange and correlation diagrams.

The binding energies obtained from G_0W_0 based on HF and PBE are systematically overestimated. Self-consistent *GW* overcorrects this trend and provides binding energies

Table 8.3: *sc-GW*, and perturbative G_0W_0 vibrational frequencies of diatomic molecules compared to experimental reference data taken from Ref. [128]. EX+cRPA, HF, PBE, and renormalized second-order perturbation theory (rPT2) are included for comparison. All values are in cm^{-1} .

	H ₂	LiH	HF	LiF	N ₂	CO	ME	MAE
Exp.	4401	1405	4138	911	2359	2170		
<i>sc-GW</i>	4533	1743	4266	971	2543	2322	-166	166
G_0W_0 @HF	4585	1827	4341	1010	2490	2647	-252	252
G_0W_0 @PBE	4341	1743	4130	971	2346	2322	-78	105
G_0W_0 @PBE0	4425	1813	4273	922	2386	2222	-109	109
EX+cRPA@HF	4533	1685	5512	952	2544	2321	-360	360
EX+cRPA@PBE	4357	1691	4757	933	2354	2115	-137	172
HF	4567	1473	4569	949	2736	2448	-226	226
PBE	4320	1364	3991	899	2328	2128	59	59
rPT2@PBE	4460	1605	4620	922	2507	2251	-163	163

that slightly underestimate experiment. As for the total energy, EX+cRPA@HF and *sc-GW* give a very similar description of the binding energy, the deviation between the two methods being approximately 10 – 20 meV.

Also for the binding energies, *sc-GW* is outperformed by rPT2@PBE, which illustrates the importance of including exchange and correlation diagrams beyond the *GW* approximation for a systematic improvement of the ground-state properties of finite systems.

For vibrational frequencies, the dependence on the starting point is larger than for binding energies or bond lengths. In this case, the best agreement with experiment is achieved with the PBE functional, whereas for HF the errors are substantially larger. Similarly, PBE-based G_0W_0 and EX+cRPA deviate less from experiment than HF-based schemes. For instance, the mean absolute error of EX+cRPA@HF is approximately a factor of two larger than EX+cRPA@PBE, and the same is observed for G_0W_0 . Consequently, *sc-GW* gives smaller MAEs compared to HF-based schemes, but does not improve over PBE-based perturbative schemes.

8.3 ELECTRON DENSITY AND DIPOLE MOMENT

In perturbative approaches, such as G_0W_0 , EX+cRPA, and rPT2, the electron density of a system is defined by the eigenstates of the unperturbed reference Hamiltonian – although in principle perturbative corrections to the eigenstates of the unperturbed Hamiltonian could be calculated. This constitutes a major drawback, which is in part responsible for the well-known starting-point dependence of perturbative schemes. On the other hand, a self-consistent theory provides a natural framework for incorporating exact-exchange and dynamical-correlation effects in the electron density. To illustrate this aspect within *sc-GW*, I discuss in the following the effects of self-consistency on the density and the dipole moment of diatomic molecules.

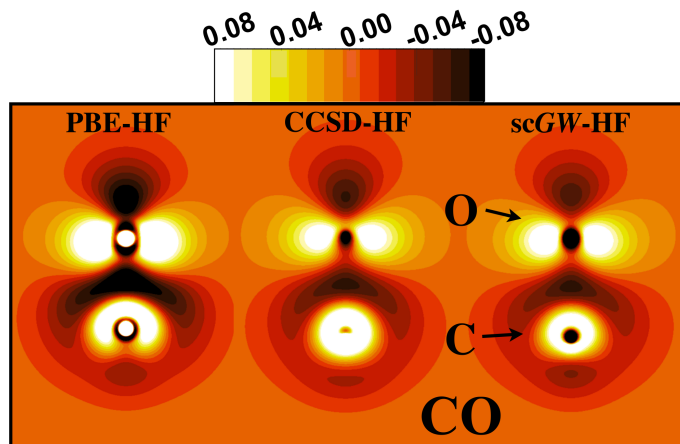


Figure 8.7: Difference $\Delta n(\text{sc-GW}-\text{HF}) = n^{\text{scGW}} - n^{\text{HF}}$ between the *sc-GW* and Hartree-Fock densities (right) for the CO dimer, the density differences $\Delta n(\text{CCSD}-\text{HF})$ (center) and $\Delta n(\text{PBE}-\text{HF})$ (left) are defined similarly in terms the CCSD and PBE densities. Dark regions correspond to negative values whereas positive regions are light. Units are \AA^{-3} and the calculation were performed using an aug-cc-pVTZ basis set.

Figure 8.7 illustrates the effect of many-body correlations in the CO dimer by comparing coupled cluster singles doubles (CCSD) calculations, PBE and *sc-GW* with HF which was obtained using the aug-cc-pVTZ basis set. CCSD and *sc-GW* both exhibit left-right correlation (density is shifted from the bonding region to the individual atoms) and angular correlation (the angular distribution of charge becomes more pronounced). The similarity between the CCSD and *sc-GW* density reflects the good agreement of the *sc-GW* dipole moment with the experimental one (Table 8.4). In PBE, on the other hand, electron density drifts out of the bond region as a result of the delocalization error, which ultimately leads to an overestimation of the dipole moment (Fig. 8.7, left).

The dipole moment provides a systematic way to quantify the quality of the electron density of a system, as it is directly comparable with experimental data. I report in Table 8.4 the dipole moments of LiH, LiF, HF, and CO evaluated with *sc-GW*, PBE, PBE0

Table 8.4: Comparison between experimental [128] and theoretical dipole moments evaluated with *sc-GW*, PBE, PBE0, and HF at their corresponding equilibrium bond lengths. All values are in Debye.

	LiH	HF	LiF	CO	MAE
Exp.	5.88	1.82	6.28	0.11	-
<i>sc-GW</i>	5.90	1.85	6.48	0.07	0.07
PBE	5.63	1.77	6.12	0.20	0.14
PBE0	5.77	1.81	6.20	0.13	0.06
HF	6.04	1.89	6.46	-0.13	0.17

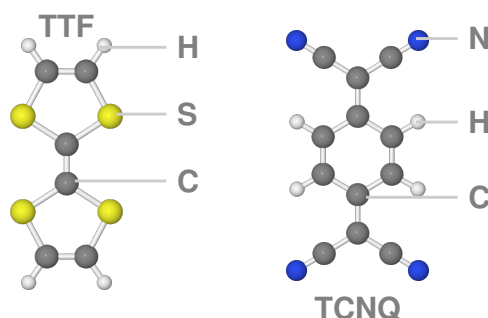


Figure 8.8: Equilibrium geometries of the isolated TTF and TCNQ molecules.

and HF. *sc-GW* and PBE0 dipole moments are in good agreement with experiments and, with an average error of 0.06-0.07 Debye, reduce the deviation from experiment by approximately a factor of two as compared to HF and PBE, that tend to under and overestimate, respectively. The good agreement with experimental data, indicates that *sc-GW* is a promising method for the description of charge-transfer compounds, such as molecular interfaces and hetero-structures.

CHARGE TRANSFER IN MOLECULAR INTERFACES: THE TTF-TCNQ DIMER

To illustrate the advantage of describing both ground and excited states at the same level of theory, I present in the following the example of the tetracyanoquinodimethane (TCNQ) and tetrathiafulvalene (TTF) molecular dimer, a prototypical charge transfer system of interest for applications in organic electronics. This system is particularly interesting for its peculiar conducting properties[232]. Molecular crystals composed of either TTF or TCNQ behave as large-gap undoped semiconductors, and are therefore insulating. However, it has recently been shown that interfaces of the TTF- and TCNQ-based molecular crystals give rise to highly-conducting behavior [233]. This phenomena – which is fundamentally different from the conductivity induced by the Peierls transition in 1D stacked TTF-TCNQ chains – is due to the formation of a two-dimensional electron gas at the interface, arising from the charge transfer between two well-separated TTF and TCNQ crystals. However, it is not clear whether charge transfer would occur at the interface between the molecules. In the following, I address the problem of the charge transfer occurring between the TTF and TCNQ molecules in the gas phase. The ground-state geometries of TTF and TCNQ are illustrated in Fig. 8.8. The geometry of the TTF-TCNQ compound has been obtained by cutting out a dimer of an interface of TTF and TCNQ crystals along the [001] surface of TCNQ, as described in more details in Ref. [67]. This simplified model allows to investigate the charge transfer which arises exclusively from the relative alignment of the frontier orbitals of TTF and TCNQ.

TCNQ has a large electronic affinity (3.22 eV, according to coupled cluster singles

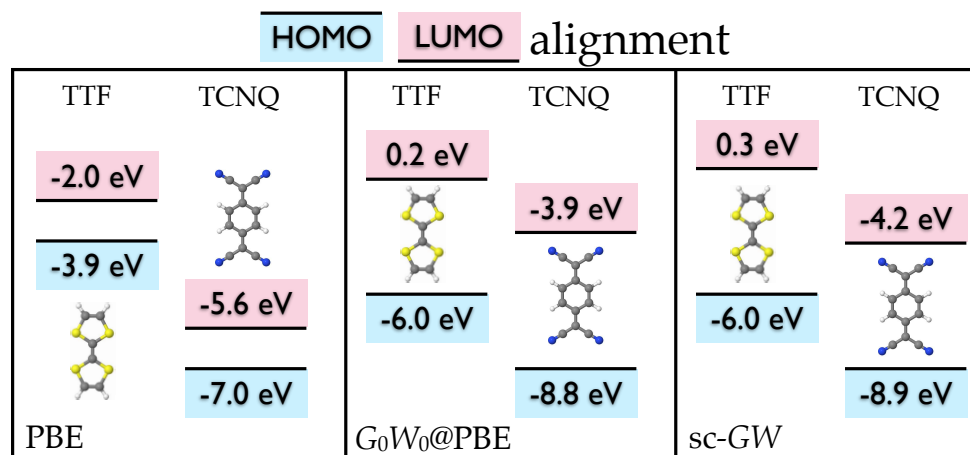


Figure 8.9: Representation of the relative alignment of the HOMO and LUMO of (isolated) TTF and TCNQ, as given in PBE (left), $G_0W_0@PBE$ (center), and sc-GW (right) for the isolated molecules with the Tier 2 basis set.

doubles with perturbative triples calculations from Ref. [234]) and is an acceptor commonly employed in charge transfer molecular crystals. TTF on the other hand, due to its small ionization energy (6.70 eV, based on photoemission experiment from Ref. [235]), is a donor-type molecule. The *ab initio* description of the ground-state electronic structure of the TTF-TCNQ interface is particularly challenging, due to the importance of properly accounting for the relative alignment of the highest occupied molecular orbital (HOMO) and the lowest unoccupied molecular orbital (LUMO) of the two components of the dimer. The PBE approximation to DFT places the LUMO of TCNQ below the HOMO of TTF. The PBE level alignment at the interface is schematically depicted in the left panel of Fig. 8.9. Since the Fermi energy should be equal in the entire system, this alignment of the frontier orbitals leads to a charge transfer of approximately 0.24 electrons from TTF to TCNQ. This spurious charge transfer is present also at infinite separation between the two molecules, as demonstrated by the non-vanishing dipole moment at large intermolecular separation [67]. The charge transfer in the TTF-TCNQ dimer is illustrated in the left side of Fig. 8.10. This picture is clearly in contrast with what one would expect based on the existing reference data reported above for the ionization energy and the electron affinity of TCNQ and TTF, respectively. In fact, based on CCSD(T) calculations and experiment for the isolated molecules, no electron transfer between TTF and TCNQ should occur, since the TCNQ LUMO should lie at higher energy than the TTF HOMO. On the other hand, this order is reversed in PBE. This suggests that the spurious charge transfer reported above is an artifact of the wrong level alignment provided by the PBE exchange-correlation functional.

Perturbative G_0W_0 calculations based on PBE improve the energy of the frontier

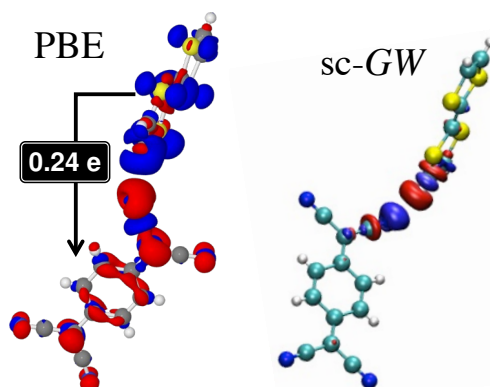


Figure 8.10: Charge transfer at the TTF-TCNQ interface. Red surfaces indicate additional electronic charge, whereas blue indicates charge depletion.

orbitals of TTF and TCNQ, and consequently restores the proper energy hierarchy, i.e., no charge transfer would be expected based on $G_0W_0@PBE$. However, since the density is not updated in the G_0W_0 approach, the underlying electronic structure is still wrong. Self-consistent GW yields orbital energies in qualitative agreement with perturbative $G_0W_0@PBE$ and locates the HOMO of TCNQ at a lower energy compared to the LUMO of TTF, as illustrated in the right panel of Fig. 8.9. Moreover, since the Green function is updated iteratively, the correct ordering of the orbital energies does not lead to charge transfer (see Fig. 8.10), but rather to a small rearrangement of the electron density at the interface.

Due to the numerical cost of $sc-GW$ for systems of this size, the calculations for the TTF-TCNQ dimer were performed with a Tier 1 basis set. This is not enough to obtain converged quasi-particle energies. However, according to the convergence tests reported in Fig. 7.1, one may expect deviations smaller than 0.3-0.5 eV between Tier 1 values for the $sc-GW$ ionization energy and the corresponding converged value. These differences would not affect the amount of charge transfer for this system.

8.4 SUMMARY

In summary, for the systems considered here the total energy and the spectral function are independent of the starting point, and conservation laws are satisfied at self-consistency. Therefore, $sc-GW$ total energies based on the Galitskii-Migdal formula facilitate an unbiased assessment of ground-state and structural properties of molecules.

For the first ten atoms in the periodic table and for a couple of light dimers, the total energy agrees better with full-CI calculations at self-consistency, as compared to G_0W_0 calculations. This is attributed to the inclusion of kinetic correlation energy, absent

in G_0W_0 . For a small set of diatomic molecules, binding energies, bond lengths, and vibrational frequencies have been investigated to benchmark the accuracy of the *sc-GW* ground state. The bond lengths improve at self-consistency, but still have an accuracy comparable to other perturbative methods such as EX+cRPA. *sc-GW* binding energies typically underestimate the experimental reference data and do not substantially improve over G_0W_0 . Vibrational frequencies evaluated from perturbative methods are very sensitive to the choice of the starting point. Self-consistent *GW* improves over G_0W_0 @HF, but is not as accurate as G_0W_0 @PBE and G_0W_0 @PBE0. These results are somehow in contrast with the common belief – based on previous studies for the homogeneous electron gas [193, 201, 202] – that *sc-GW* total energies should have an accuracy comparable to quantum Monte Carlo calculations. The deviation from the experimental reference data permits us to quantify the importance of including higher-order correlation and exchange diagrams to achieve an accurate description of the structural properties of molecules.

The dipole moment for a set of hetero-atomic dimers was investigated to quantify the accuracy of the *sc-GW* density. Compared to HF and PBE, the *sc-GW* dipole moments are found in better agreement with experiment, similarly to PBE0. As prototypical charge-transfer compound, I considered the TTF-TCNQ dimer, relevant for organic electronics applications. For the TTF-TCNQ dimer, *sc-GW* provides no charge transfer between the two molecules, in agreement with expectations based on CCSD(T), whereas in PBE a spurious charge transfer occurs due to the misalignment of the frontier orbitals of TTF and TCNQ. This suggests that *sc-GW* might be an accurate method to describe charge-transfer compounds and hetero-junctions, where the relative ordering of the frontier orbitals influences the charge transfer at the interface.

9 THE BOND-BREAKING PUZZLE: MANY-BODY VERSUS DENSITY-FUNCTIONAL THEORY

In this Chapter, I extend the study of the ground-state properties of molecules in the *GW* approach by considering dimers in the dissociation limit. Due to the strong multi-reference character of the many-body wave function at large interatomic separation, a quantitative description of the dissociation of covalently-bonded molecules remains a challenge for most electronic-structure approaches. The correlation energy arising from the multi-Slater-determinant character of the wave function – generally referred to as “static correlation” in quantum chemistry – dominates the dissociation regime. The capability of a method to capture static correlation is, therefore, crucial for achieving a proper description of the dissociation of covalently bonded systems. In the following, I address the difference between density-functional theory (DFT) and many-body perturbation theory (MBPT) for the dissociation energy of diatomic molecules and ask the questions: Given a fixed set of diagrams for the electron-electron interaction, will the DFT and the MBPT framework give the same result? And if not, which one is better? To answer these questions the paradigmatic case of H_2 dissociation is considered.

In the past, DFT and MBPT have been compared directly in the exchange-only case [91]. In MBPT this corresponds to the Hartree-Fock approach, whereas in DFT a multiplicative Kohn-Sham (KS) potential is constructed by means of the optimized effective potential approach (OEP) [30]. However, this comparison is mostly of academic interest, because electron correlation is not included. As it will be demonstrated in the following, the comparison between DFT and MBPT can be extended to encompass correlation using exact-exchange plus correlation in the random-phase approximation to DFT [70, 77, 236, 237], and the *GW* approach to MBPT [14, 121]. The exchange-correlation diagrams in both approaches are topologically identical (see Fig. 4.5), but in RPA they are evaluated with a non-interacting KS and in *GW* with an interacting Green function. The implications of this similarity between RPA and the *GW* approximation have been presented in Sec. 4.6. To illustrate the impact of these differences, the bond-breaking/formation regimes in the binding curves of H_2 will be discussed. To avoid starting-point effects both approaches are iterated to self-consistency.

9.1 EVALUATION OF THE SC-RPA TOTAL ENERGY

The RPA correlation potential was determined following the direct minimization scheme of Yang *et al.* [53]. The basic idea of this approach consists in introducing a basis for the representation of the KS potential, to simplify the numerical treatment of the OEP problem. The introduction of a set of Gaussian basis functions $\{g_i(\mathbf{r})\}$ permits one to expand the KS exchange-correlation potential as [53]:

$$v_{xc}(\mathbf{r}) = v_0(\mathbf{r}) + \sum_i b_i g_i(\mathbf{r}) \quad , \quad (9.1)$$

where v_0 is a fixed reference potential, and b_i are real coefficients. By virtue of the Hohenberg-Kohn theorem, the coefficients b_i can in turn be obtained by a direct unconstrained minimization of the total energy functional, i.e.:

$$\frac{\partial E_{xc}[\{\phi_i\}]}{\partial b_i} = 0 \quad . \quad (9.2)$$

The resulting coefficients determine the exchange-correlation potential corresponding to the energy functional E_{xc} . The orbitals and eigenvalues obtained from this procedure were used to evaluate the sc-RPA total energy from Eq. 4.23. The reader is referred to a previous publication for details of the sc-RPA implementation [238].

To facilitate a term-by-term comparison between sc-*GW* and sc-RPA total energies, one may separate E_c^{RPA} into the Coulomb correlation energy U_c^{RPA} and the kinetic correlation energy T_c^{RPA} . U_c^{RPA} is given by the $\lambda = 1$ part of the RPA correlation energy, i.e.:

$$U_c^{\text{RPA}} = - \int_0^\infty \frac{d\omega}{2\pi} \text{Tr} \left[\sum_{n=2}^\infty (\chi_s(i\omega)v)^n \right] = E_c^{\text{GW}}[G_s] \quad , \quad (9.3)$$

where E_c^{GW} is the last term of Eq. 7.6. The kinetic correlation energy can thus be expressed as $T_c^{\text{RPA}} = E_c^{\text{RPA}} - U_c^{\text{RPA}}$. The total kinetic energy in sc-RPA is then given by:

$$T^{\text{RPA}} = T_s + T_c^{\text{RPA}} \quad . \quad (9.4)$$

With this reorganization of terms, the kinetic energy in sc-*GW* can be directly compared to T^{RPA} , and similarly E_c^{GW} to U_c^{RPA} . Now the only factor responsible for the difference in these different pairs of terms arises from the difference in the input Green functions used to evaluate them.

9.2 POTENTIAL-ENERGY CURVE OF H₂: SC-RPA AND SC-GW

I now turn to an assessment of sc-RPA and sc-GW for the potential-energy curve of H₂. Figure 9.1 reports the total energy of H₂ for different flavors of GW and RPA. For comparison, the full configuration interaction (full-CI) potential-energy curve of H₂ [229] – that provides an exact reference for this system – is reported. I also report the total energy of H₂ evaluated from renormalized second-order perturbation theory (rPT2) [77, 85]. As reported previously [47, 77, 93, 239], non-self-consistent RPA overestimates the total energy of H₂ at the equilibrium bond length. Around the equilibrium distance, the RPA total energy based on exact exchange (OEPx) and sc-RPA are almost identical and overestimate by approximately 0.8 eV, compared to full-CI. At intermediate bond distances and in the dissociation region a lowering of the sc-RPA energy compared to RPA@OEPx is observed. The spurious “bump” [77, 93], present in all RPA calculations for H₂ and other covalently bonded molecules, is reduced in sc-RPA but is still present. The total energy stays below the full-CI energy throughout, indicating a general overestimation of the bonding and dissociation regions.

In agreement with Stan *et al.* [104], sc-GW provides an accurate total energy for H₂ close to equilibrium. For the Galitskii-Migdal framework, self-consistency is crucial as G_0W_0 @HF and G_0W_0 @PBE largely overestimate the total energy. In contrast, the Klein functional evaluated with the HF Green function (RPA@HF) provides similar results to sc-GW. sc-RPA and sc-GW thus provide a qualitatively similar description of the energetics of the covalent bond of H₂, which results in a slight overestimation of the total energy. However, sc-GW is in better agreement with full-CI. The inclusion of higher-order exchange-correlation diagrams in the PBE-based rPT2 potential-energy curve, improves the description of the total energy at the equilibrium bond lengths which are found in excellent agreement with full-CI. Most interestingly, the sc-GW energy is higher than the sc-RPA one. This is in contrast to the exchange only case, in which the HF total energy is always lower than (or equal for a two electron system) the OEPx energy [30]. This is expected, as HF is variational and the local potential in OEPx provides an additional constraint that increases the energy. Conversely, the total energy in sc-GW has to be higher than in sc-RPA, because the variational procedure yields a maximum at the self-consistent Green function [99, 100].

In the dissociation region, sc-RPA and sc-GW deviate markedly. For sc-RPA the dissociation energy is lightly too negative, but in rather good agreement with the full-CI energy. sc-GW, on the other hand, fails dramatically in the dissociation limit and with 24.5 eV underestimates the total energy considerably. The inclusion of more diagrams does not help in this case, and rPT2@PBE and rPT2@PBE0 also underestimate the dissociation energy. On the plus side, sc-GW dissociates monotonically and therefore does not show the unphysical “bump” present in all RPA-based approaches. Again, both non-self-consistent G_0W_0 @HF and G_0W_0 @PBE energies give better agreement

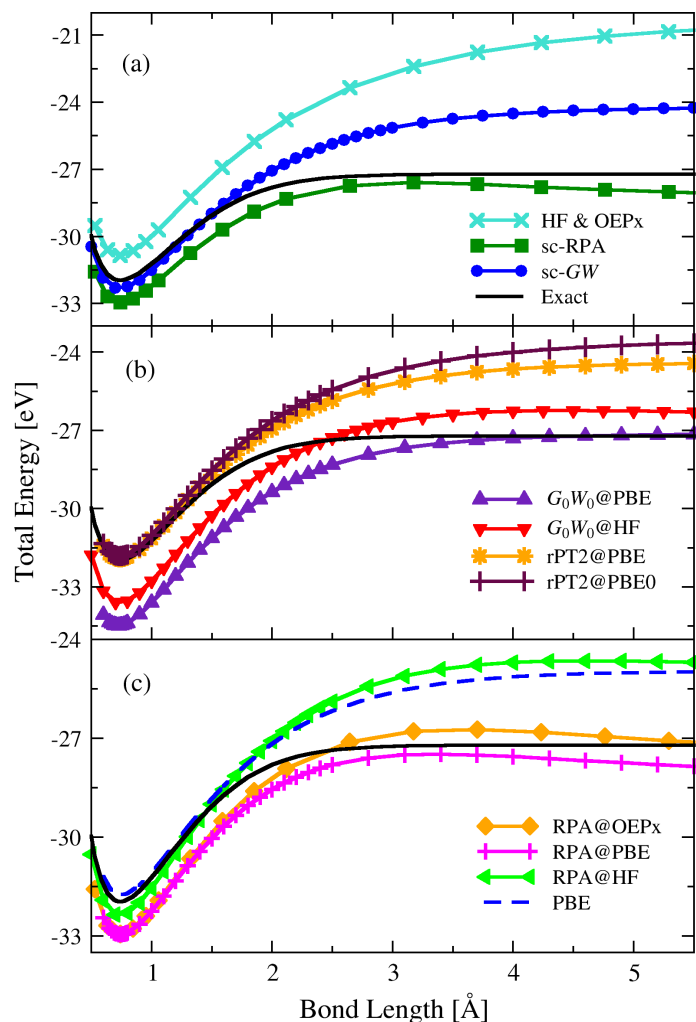


Figure 9.1: Total energy (eV) of the H_2 molecule as a function of bond length (\AA). Different flavors of GW and RPA are shown compared to PBE, rPT2 and accurate full configuration interaction (full-CI) calculations taken from Ref. [229]. Hartree-Fock (HF) and exact-exchange OEP (OEPx) are identical for H_2 and are included for comparison. All calculations were performed using a Gaussian cc-pVQZ basis set [205].

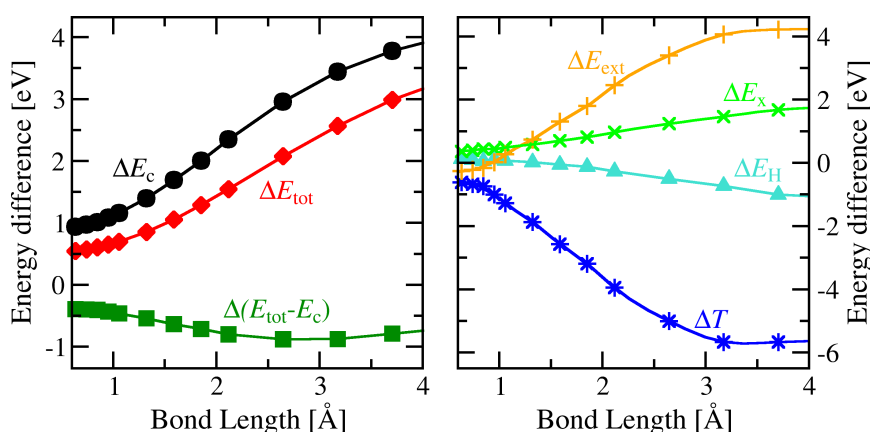


Figure 9.2: Left panel: difference between the sc-GW and sc-RPA total energy (ΔE_{tot}), the correlation energy ($\Delta E_c = E_c^{GW} - U_c^{RPA}$) and the remaining terms ($\Delta(E_{tot} - E_c)$). Right panel: breakdown of the remaining term into the difference of the Hartree (ΔE_H), the external (ΔE_{ext}), the exchange (ΔE_x), and the kinetic energy (ΔT).

with the reference curve than sc-GW.

One could surmise that this qualitatively different behavior originates from the different treatment of the kinetic energies discussed earlier. Figure 9.2, however, shows that this is not the case. At equilibrium the kinetic energy in sc-GW differs only slightly from the sc-RPA kinetic energy defined in Eq. 9.4. This indicates that in the bonding regime the AC framework correctly reproduces the kinetic energy of an interacting system. At larger bond distances, the kinetic energy differs increasingly in the two approaches. However, this effect is compensated by an opposing change in the external energy that arises from an increasing deviation in the electron densities. The same is observed for the Hartree and the exchange energy, although the absolute magnitude of the effect is smaller. The total-energy difference between sc-GW and sc-RPA can be finally ascribed to the Coulomb correlation energy $\Delta E_c = E_c^{GW} - U_c^{RPA} = E_c^{GW}[G] - E_c^{GW}[G_s]$, as the left panel of Fig. 9.2 demonstrates. Close to equilibrium ΔE_c is of the order of 1 eV, but increases to approximately 4 eV at larger bond lengths. This illustrates that it matters decisively whether the correlation energy is evaluated with the interacting sc-GW or the non-interacting sc-RPA Green function.

Why the difference is so pronounced at dissociation is still an open question. A potential explanation can be found in the inverse dependence of the RPA Coulomb correlation energy on the gap between the highest occupied and the lowest unoccupied molecular orbital (HOMO and LUMO, respectively). This is exemplified by the right panel of Fig. 9.3, which shows the inverse of U_c as a function of the gap for a simplified two level system. The large value of U_c obtained from sc-RPA for H₂ at dissociation can therefore be traced back to the small HOMO-LUMO gap (left panel of Fig. 9.3) of the RPA Green function. In contrast, due to the spatial non-locality of the self-energy, the HOMO-LUMO gap of the HF and GW Green functions is much larger at every given

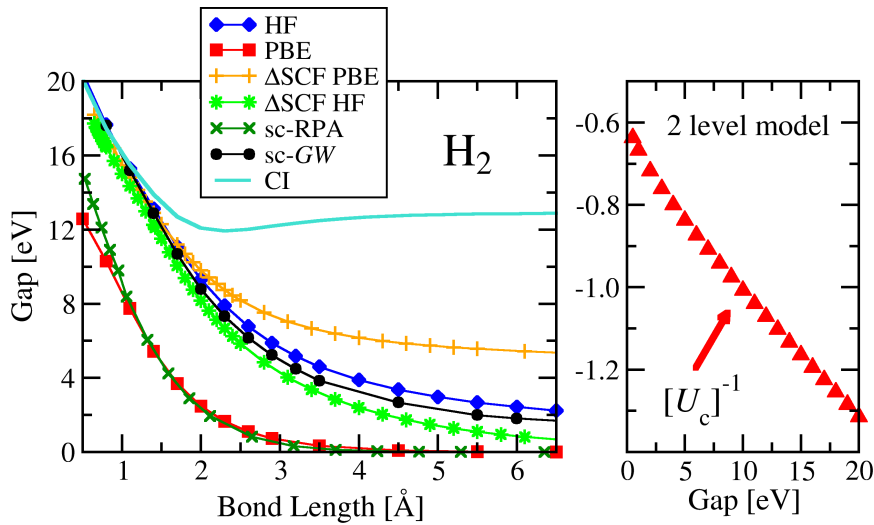


Figure 9.3: Left panel: HOMO-LUMO gap extracted from the *sc-GW* spectral function and from HF, PBE, and *sc-RPA* eigenvalues. The HOMO-LUMO gap evaluated from PBE and HF total-energy differences (Δ SCF) is included for comparison. Full configuration interaction (CI) calculation were done with a aug-cc-pVDZ basis set. Right panel: Inverse of the RPA Coulomb correlation energy U_c^{RPA} for a two-level model as a function of the HOMO-LUMO gap.

bond distance. This leads in turn to a smaller Coulomb correlation energy for *sc-GW* and HF-based perturbative methods.

9.3 NATURAL OCCUPATIONS AND THE ROLE OF SPIN-SYMMETRY

As discussed in Sec. 3.3, the density matrix may provide insightful information on the nature of electronic correlation and on the dissociation of diatomic molecules. For H₂, the natural orbitals and the corresponding occupation numbers – i.e., the eigenvectors and eigenvalues derived from the diagonalization of the reduced single-particle density matrix – can be derived from full-CI, which provides an exact reference for this system in the complete basis set limit.

In the left panel of Fig. 9.4, the first two natural occupations obtained from *sc-GW* ($n_1^{\text{sc-GW}}$ and $n_2^{\text{sc-GW}}$) and full-CI (n_1^{CI} and n_2^{CI}) are reported for several values of the H₂ bond length. The full-CI occupations deviate from unity at all bond lengths, reflecting the multi-Slater-determinant nature of the many-body wave function. For bond lengths far from the equilibrium geometry, the deviation from integer occupation increases and, at dissociation, the first two natural occupation numbers become degenerate. As in full-CI, the *sc-GW* natural occupations are always fractional and deviate increasingly from integer values for larger bond lengths. However, the degeneracy of the natural occupations is never achieved. This suggests that *sc-GW* describes the static correlation characteristic of the dissociation limit of covalent bonds poorly.

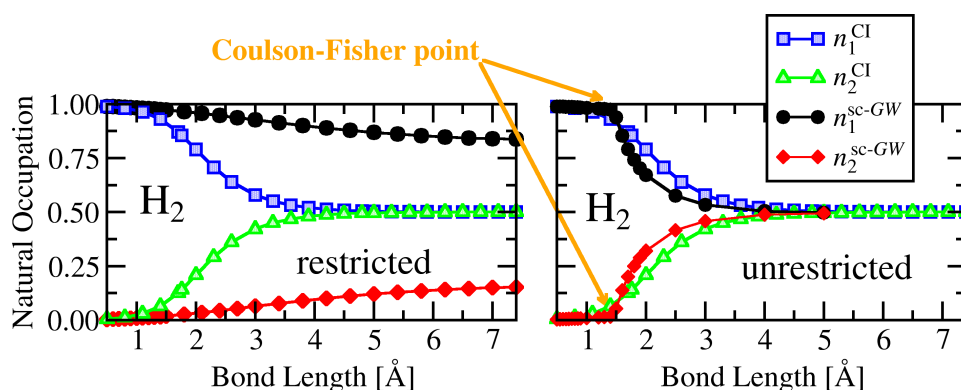


Figure 9.4: Natural occupation numbers of the first two natural orbitals (n_1 and n_2) of H_2 evaluated from full configuration interaction (full-CI), spin-restricted *sc-GW* (left) and spin-unrestricted *sc-GW* (right).

To achieve an improved description of the dissociation limit, one can proceed analogously to the unrestricted-Hartree-Fock case (UHF) [7]. In UHF, different spin-orbitals (corresponding to spin-up and spin-down electrons) do not necessarily have the same spatial distribution. A drawback of UHF method is that the resulting wave function localizes the spin-up and spin-down electrons on different atoms (e.g., spin-up on the right atom, and spin-down on the left atom). In other words, the wave function is not anti-symmetric upon exchange of two electrons, i.e., it is not fermionic. The unrestricted solution most often coincides with the restricted-Hartree-Fock (RHF, or simply HF) one – in which spin-up and spin-down orbitals have the same spatial distribution. For H_2 , the restricted- and unrestricted-HF solutions coincide for bond lengths shorter than 1.2 Å, often denoted as Coulson-Fisher (CF) point [240]. At distances larger than the CF point, UHF starts to differ from RHF and provides a larger (i.e., more negative) total energy, and a correct description of the dissociation energy. In other words, at bond lengths larger than the Coulson-Fisher point, it is energetically more favorable to break the spin symmetry and localize the spin-up and spin-down electrons on different atoms.

The UHF dissociation energy equals twice the energy of the free atom (0.5 Ha, or ~ 13.60 eV), as illustrated in panels (b) and (d) of Fig. 9.5. Therefore for H_2 , and similarly for all σ -bonded systems, UHF gives the correct dissociation energy, whereas RHF underestimates the dissociation limit.

In analogy to UHF, a spin-dependent formulation of *sc-GW* allows the Green function to assume different spatial distributions for the spin-up and spin-down components. This procedure will be denoted in the following as unrestricted *sc-GW* (U*sc-GW*). The behavior of the U*sc-GW* total energy is qualitatively similar to the UHF case, as illustrated in panels (a) and (b) of Fig. 9.5: for bond lengths close to equilibrium, the *sc-GW* and U*sc-GW* total energies are identical. At larger distances, on the other hand, the unrestricted calculation provides a qualitatively different behavior at dissociation. As in UHF, the dissociation energy of U*sc-GW* is twice the *sc-GW* energy of a free H atom (\sim

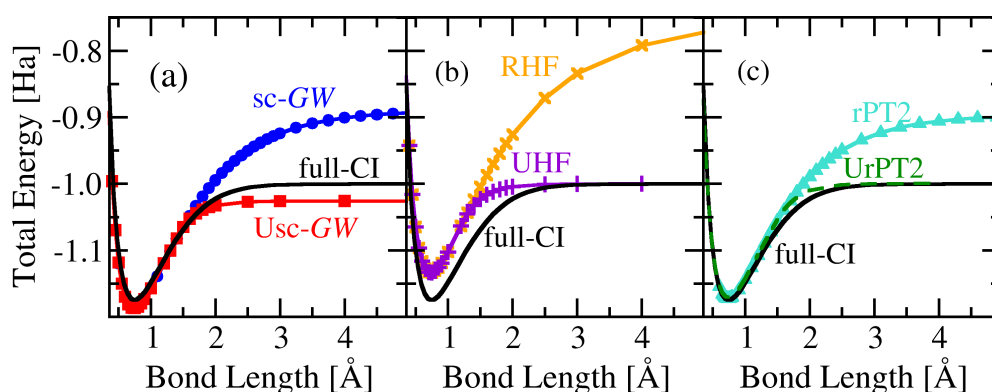


Figure 9.5: Binding energy (eV) of the H₂ molecule as a function of bond length (Å) evaluated from spin-restricted and unrestricted sc-GW (a), Hartree-Fock (b), and PBE-based rPT2 (c). The corresponding sc-GW and Hartree-Fock *total* energies curves are reported in panels (c) and (d), respectively. The full configuration interaction (full-CI) potential-energy curve (reproduced from Ref. [229]) is included for comparison.

0.514 Ha, or ~ 13.987 eV), as illustrated in Fig. 9.5. Therefore, also Usc-GW dissociates correctly, as demonstrated by the degeneracy of the first two natural occupation numbers (see Fig. 9.4). The total energy of the individual H (panel (c) of Fig. 9.5) atoms however is slightly overestimated as compared to the exact reference due to the well known self-screening (or self-correlation) error of sc-GW [81, 241, 242], and is responsible for the overestimation of the total energy in Usc-GW at large interatomic separations. The right panel of Fig. 9.4 shows that in the unrestricted case, the sc-GW natural occupation numbers correctly reach degeneracy at dissociation. A discontinuity in the first derivative of the natural occupations is observed at the Coulson-Fisher point and marks the transition to the spin-symmetry broken ground state. Similar improvement are also observed for rPT2 based on unrestricted PBE (panel (c) in Fig. 9.5). In this case, however, the (partial) removal of the self-screening error through the inclusion of SOSEX diagrams improves the free-atom total energy. The resulting unrestricted rPT2 potential-energy curve is in good agreement with full-CI over the whole range of bond lengths considered.

9.4 SUMMARY

In summary, I have compared MBPT in the *GW* approximation to DFT in the RPA. The density-functional description was found superior at dissociation, yielding a total energy in qualitative agreement with the exact energy along the entire dissociation curve. These results illustrate how MBPT and DFT based approaches deal with multi-reference ground-states. In a DFT-based framework the closure of the (KS) HOMO-LUMO gap is in part responsible for the improved description at dissociation, i.e., static correlation is better accounted for in sc-RPA, than in sc-GW. The same effect in Green function theory has to be achieved by the right (potentially infinite) set of diagrams. The inclusion

of higher-order exchange-correlation diagrams through the rPT2 approach led to an excellent total energy at equilibrium geometries, but it did not improve the description at dissociation for restricted calculations. *A priori*, it is not known which set of Feynman diagrams may improve the description of static correlation. In conclusion, static and local approximations of exchange-correlation potentials – as opposed to non-local, frequency dependent self-energy approximations – are more effective in describing the dissociation regime of covalently bonded molecules.

How to properly describe the dissociation regime – or alternatively, electronic configurations characterized by a multi-Slater-determinant wave function – in Green function based approaches remains an open question. The dissociation energy H_2 is strongly improved for spin-symmetry-broken calculations based on HF, sc-*GW*, and rPT2. On the other hand, the resulting ground-state wave function is not of fermionic character. Therefore, future efforts should be focused on the development of the beyond-*GW* schemes (e.g., vertex corrections) capable of capturing the static correlations that dominates the dissociation regime, without resorting to spin-symmetry-broken calculations.

10 ASSESSMENT OF GW METHODS FOR PHOTOEMISSION PROCESSES IN MOLECULES

In this Chapter, the performance of GW methods for the description of excitation energies is investigated for a set of molecules, at different levels of self-consistency. The non-self-consistent GW method (G_0W_0), simple self-consistency in the eigenvalues (ev-sc GW), partial self-consistency with fixed screened Coulomb interaction (sc- GW_0), full self-consistency in both G and W (sc- GW) and – as an attempt to go beyond GW – G_0W_0 plus second-order exchange (G_0W_0+2OX) are considered for benzene, pyridine, and the diazines: pyridazine, pyrimidine, and pyrazine. The ground-state geometries of all molecules are illustrated in Fig. 10.1.¹ Benchmark studies of GW methods have typically focused only on the values of the ionization potentials (IP) and/or fundamental gaps of the systems of interest. In contrast, here it will be examined the whole spectrum as well as the predicted character of the frontier orbitals.

To extend this benchmark to a larger set of molecules, I will report calculations of the first ionization energy for a set of 30 closed-shell molecules, and of the full excitation spectrum of five molecules relevant for photo-voltaic applications: thiophene, naphthalene, benzothiazole, 1,2,5-thiadiazole, and tetrathiafulvalene.

10.1 A HIERARCHY OF THEORETICAL CONSISTENCY

Owing to the computational cost of sc- GW calculations, a range of GW schemes, from non-self-consistent to partially self-consistent, have emerged. These constitute a hierarchy of theoretical consistency, in terms of properties that are considered desirable for a generally applicable electronic-structure approach, including: (i) independence of the starting point; (ii) satisfaction of conservation laws for the number of particles, momentum and total energy [102, 169]; (iii) inclusion of exact-exchange and dynamical-correlation effects consistently in the ground state.

Perturbative, self-consistent, and partially self-consistent GW methods have been

¹Here and in the rest of this Chapter all geometries are relaxed with the PBE exchange-correlation functional with a Tier 2 basis set.

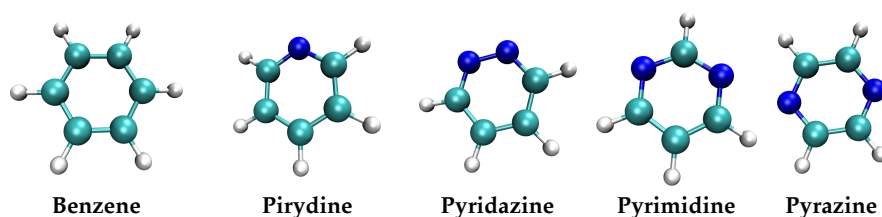


Figure 10.1: Geometries of benzene, pirydine, pyridazine, pyrimidine and pyrazine, optimized at the DFT level with a PBE exchange-correlation functional in a Tier 2 basis set.

introduced in Chap. 4. In the following, their classification in terms of points (i)-(iii) will be recalled for the reader's convenience. The lowest rung in this hierarchy is the widely used G_0W_0 approach, which does not satisfy points (i)-(iii). In this approach, the quasi-particle (QP) excitation energies are obtained from first-order perturbation theory as corrections to the eigenvalues from density-functional theory (DFT). Despite the limited validity of the first-order perturbative treatment, G_0W_0 often yields excellent agreement with experiment. However, the non-self-consistency gives rise to a dependence of the G_0W_0 results on the DFT starting point and to other undesirable shortcomings that have been discussed in detail in Sec. 4.2.

The second rung in the hierarchy are partially self-consistent GW schemes, in which the quasi-particle energies are updated in the construction of the self-energy operator [57]. The *ev-scGW* scheme has been shown to yield better results than G_0W_0 calculations based on a semi-local starting point for the first ionization energy of molecules [124, 175, 243, 244]. In the quasi-particle self-consistent GW (QP-sc GW) method – that will not be considered here – proposed by Faleev, van Schilfgaarde, and Kotani, the single-particle wave functions are updated by optimizing the starting point with respect to the GW perturbation [177, 178]. In this scheme the orbitals are updated by solving the quasi-particle equation with a Hermitian approximation to the GW self-energy. This procedure has been applied successfully to a variety of systems, including *d*- and *f*-electron systems [177–179, 186]. However, both *ev-scGW* and QP-sc GW may still have a considerable starting-point dependence [192]. They also do not satisfy points (ii) and (iii).

The third rung in the hierarchy is a partially self-consistent scheme, obtained by combining a self-consistent G with a non-self-consistent W , *sc-GW*₀ [245]. This scheme incorporates GW exchange and dynamical-correlation effects in the ground state because the Green function is updated (point iii) and satisfies the particle-number-conservation law (point ii). However, some starting-point dependence is still expected, owing to the non-self-consistent W_0 .

The fourth and highest rung in the hierarchy is *sc-GW*, in which the Dyson equation is iterated. This is the only GW method that satisfies properties (i)-(iii). Full self-consistency is the only way to eliminate the starting-point dependence completely, and to describe excited- and ground-state properties at the same level of theory. In the

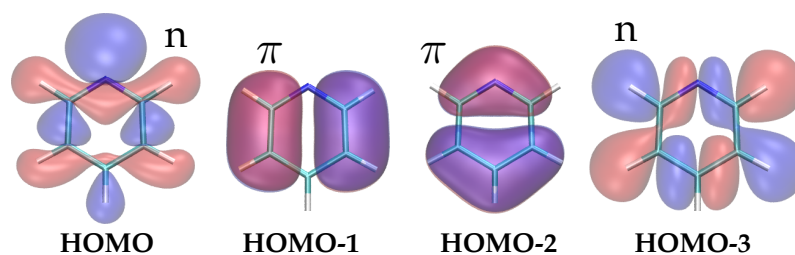


Figure 10.2: Orbital character of the four highest occupied molecular orbitals of pyridine.

following, each rung of the hierarchy will be investigated and benchmarked for benzene and the azabenzenes.

10.2 THE AZABENZENES

Benzene and the azabenzenes are the basic building blocks of polycyclic aromatic hydrocarbons (PAHs), π -conjugated oligomers, and many organic semiconductors and dyes. They embody the basic physics of such systems including the strong correlation effects in aromatic π -systems [246–248] and the self-interaction effects introduced by localized nitrogen lone pairs [175, 249]. The four highest occupied molecular orbitals of pyridine, illustrated in Fig. 10.2, exemplify the alternation of π -orbitals and n-lone pairs characteristic of the azabenzenes set. The symmetry and spatial distribution of the frontier orbitals affect the formation of chemical bonds, photoexcitation, and charge transfer processes. Therefore, in the context of photovoltaics, it is important not only to predict the IP correctly but also to reproduce the character of the highest occupied molecular orbital (HOMO) and the lowest unoccupied molecular orbital (LUMO).

Additionally, another advantage of these systems is that they are well-characterized experimentally [250–265] and well-studied theoretically by multi-reference configuration interaction [266–270], outer-valence Green function methods [271–273], and coupled cluster [274]. For an unbiased assessment, it would be desirable to benchmark *GW* against higher level theories for the entire excitation spectrum, since in experiment the distinction between vertical and adiabatic ionization energies is difficult and vibrational effects are always present. However, the scarcity of theoretical benchmarks for the the ionization energies of molecules makes comparison to experiment unavoidable. For benzene and the azabenzenes, however, the effects of zero-point motion on the ionization energies is small. As an example, for Benzene the zero-point motion should not affect the first ionization energy by more than 70 meV based on recent CCSD(T) calculations at basis set extrapolation [6].

In the following the electronic structure of benzene, pyridine, and the diazines are evaluated with: (i) semi-local and hybrid DFT (ii) G_0W_0 , (iii) *ev-scGW*, (iv) *sc-GW*₀, (v) *sc-GW*. The results are compared to gas phase photoemission spectroscopy (PES) experiments and to reference calculations. Surprisingly, the accuracy of the spectral

Table 10.1: Character of the highest occupied states of the azabenzenes evaluated from HF, PBE, PBE0, and different levels of GW . Results in agreement with experiment are shaded. Experimental references are taken from: (a) Ref. [253, 254, 257–259, 270, 271, 275], (b) Ref. [254, 257, 271, 272], (c) Ref. [255, 257, 258, 260, 261, 265, 268, 271, 272], (d) Ref. [250, 257, 258, 260, 269, 271].

	Pyridine	Pyridazine	Pyrimidine	Pyrazine
Reference	n- π - π^a	n- π - π -n b	n- π -n- π^c	n- π -n- π^d
PBE	n- π - π	n-n- π - π	n-n- π - π	n- π -n- π
PBE0	n- π - π	n- π - π -n	n- π -n- π	n- π -n- π
HF	π - π -n	π - π -n-n	π -n- π -n	π -n- π -n
G_0W_0 @PBE	n- π - π	n- π - π -n	n- π -n- π	n- π -n- π
G_0W_0 @PBE0	π -n- π	n- π - π -n	n- π -n- π	n- π -n- π
G_0W_0 @HF	π - π -n	n- π - π -n	n- π - π -n	π -n- π -n
ev-scGW@PBE	π -n- π	n- π - π -n	n- π - π -n	n- π -n- π
ev-scGW@HF	π -n- π	n- π - π -n	n- π - π -n	π -n- π -n
scGW $_0$ @PBE	π -n- π	n- π - π -n	n- π -n- π	n- π -n- π
scGW $_0$ @HF	π -n- π	n- π - π -n	n- π - π -n	π -n- π -n
sc- GW	π -n- π	n- π - π -n	n- π - π -n	π -n- π -n
G_0W_0 @PBE+2OX	π -n- π	n- π - π -n	n- π - π -n	π -n- π -n
G_0W_0 @PBE0+2OX	π -n- π	n- π - π -n	n- π - π -n	π -n- π -n
G_0W_0 @HF+2OX	π -n- π	n- π - π -n	π -n- π -n	π -n- π -n

properties of benzene and the azabenzenes does not match the expectations based on the hierarchy established above. In particular, for certain starting points G_0W_0 and sc- GW_0 outperform sc- GW , providing spectra in better agreement with PES.

NON-SELF-CONSISTENT G_0W_0

Within G_0W_0 , the self-energy and the quasi-particle energies are evaluated non-self-consistently, as described in Sec. 4.3, based on KS or HF eigenvalues and orbitals. To estimate the accuracy of the QP energies, the mean absolute error (MAE) is defined as:

$$\text{MAE} = \frac{1}{N} \sum_{n=1}^N |\epsilon_n^{\text{exp}} - \epsilon_n^{\text{QP}}| \quad (10.1)$$

with N being the number of distinct peaks in the experimental spectra, i.e., the HOMO to HOMO-9 peaks for benzene and the azabenzenes.

The starting-point dependence for all approaches is quantified estimating the mean difference in the n -th QP energy obtained from the two extreme starting points in terms of the amount of exact-exchange, i.e., PBE and HF:

$$\Delta_{\text{SPD}} = \frac{1}{N} \sum_{n=1}^N |\epsilon_{n,\text{HF}}^{\text{QP}} - \epsilon_{n,\text{PBE}}^{\text{QP}}| \quad (10.2)$$

The results are given in Tables 10.2 and 10.3. Figure 10.3 shows the results of G_0W_0 calculations based on PBE, PBE0, and HF starting points for pyridine. The spectra of benzene, pyridazine, pyrimidine, and pyrazine, are reported in Figs. E.1-E.4 in Appendix

Table 10.2: Mean absolute error (MAE, obtained from Eq. 10.1) in eV for the QP energies of benzene and the azabenzenes obtained with different DFT and *GW* methods, as compared to experiment (Ref. [253, 257]). All values are in eV.

	Benzene	Pyridine	Pyridazine	Pyrim.	Pyraz.	Average
PBE	3.75	3.80	3.82	3.76	3.73	3.77
PBE (shifted)	0.80	0.40	0.38	0.51	0.56	0.53
PBE0	2.17	2.21	2.20	2.18	2.32	2.22
PBE0 (shifted)	0.21	0.18	0.08	0.06	0.17	0.14
HF	1.85	1.93	1.68	1.63	1.70	1.76
G_0W_0 @PBE	0.39	0.34	0.36	0.40	0.40	0.38
G_0W_0 @PBE0	0.18	0.19	0.16	0.12	0.22	0.17
G_0W_0 @HF	1.07	1.11	1.06	0.99	1.01	1.05
sc- <i>GW</i>	0.45	0.31	0.25	0.25	0.28	0.31
sc- GW_0 @HF	0.92	0.95	0.93	0.88	0.88	0.91
sc- GW_0 @PBE	0.35	0.27	0.27	0.22	0.24	0.27
ev-sc <i>GW</i> @HF	0.99	1.00	1.12	0.91	0.91	0.99
ev-sc <i>GW</i> @PBE	0.53	0.57	0.58	0.66	0.52	0.57

E. The orbital ordering predicted by G_0W_0 is fairly robust to the mean-field starting point, although considerable differences in the QP energies are observed for different starting points. One discrepancy with experiment that particularly stands out in all G_0W_0 spectra is that the HOMO-2/HOMO-3 (degenerate for benzene) are too close to the HOMO-4 (see Fig. E.1 in Appendix E), possibly due to the missing higher-order exchange diagrams. It should also be noted that the amount of EX required for obtaining the best agreement with PES for the IP is about 40% (not shown for brevity). However, with this amount of EX the QP energies of most orbitals, other than the HOMO, are too low compared to the PES.

For the azabenzenes the QP corrections to the GKS eigenvalues, $\epsilon_n^{\text{QP}} - \epsilon_n^{\text{GKS}}$, are generally more negative for n-orbitals than for π -orbitals when starting from PBE or PBE0, due to the effect of the self-interaction error for the localized n-type orbitals. On the other hand, the trend is inverted for the HF starting point, that is not affected by the self-interaction. This leads to a reshuffling of the energy positions of these orbitals in the G_0W_0 calculation, as compared to their ordering in the underlying mean-field calculation. For all azabenzenes, changes in orbital ordering are observed as a function

Table 10.3: Dependence on the starting point for different *GW* methods. All values are in eV.

	G_0W_0	ev-sc <i>GW</i>	sc- GW_0	sc- <i>GW</i>	$G_0W_0+2\text{OX}$
Benzene	1.32	0.41	0.87	0.0	0.72
Pyridine	1.37	0.41	0.64	0.0	0.75
Pyridazine	1.42	0.42	0.66	0.0	0.77
Pyrimidine	1.40	0.40	0.66	0.0	0.94
Pyrazine	1.38	0.40	0.70	0.0	0.80
Average	1.38	0.40	0.70	0.0	0.80

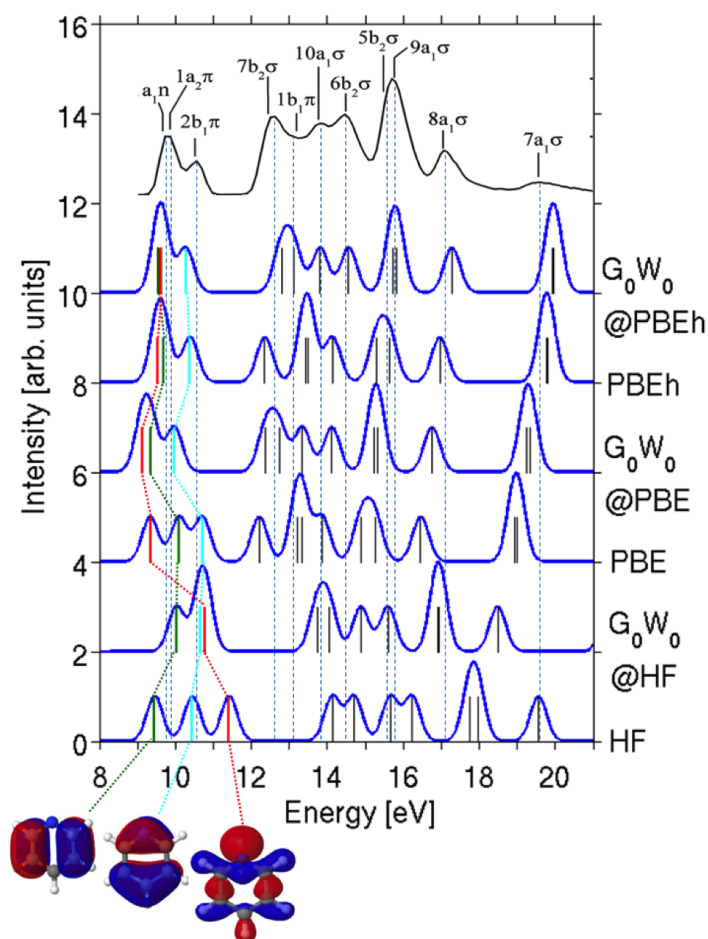


Figure 10.3: Spectra of pyridine calculated with DFT, Hartree-Fock, and G_0W_0 based on different starting points, (Gaussian broadened by 0.4 eV), compared to gas phase PES (Ref. [253]). Illustration of the frontier orbital character is also shown.

of the fraction of EX included in the calculation, as reported in Table 10.1.

For pyridine, both the G_0W_0 @PBE and the G_0W_0 @PBE0 spectra are in agreement with experiment in terms of the spectral shape. In both, the n-orbital is shifted down in energy with respect to the π -orbitals, as compared to the underlying DFT calculation. Although the spectral shape of the G_0W_0 @HF spectrum is improved compared HF itself, a visible distortion is caused by the HOMO-1 and HOMO-2 being nearly degenerate instead of the HOMO and HOMO-1. Only G_0W_0 @PBE reproduces the reference orbital ordering of n- π -n.

For pyridazine and pyrazine, the G_0W_0 @PBE spectra are qualitatively more similar to the PES in terms of the spectral shape (i.e., the positions of the peaks relative to each other) than the G_0W_0 @PBE0 spectra. However, the G_0W_0 @PBE0 spectra are still in better quantitative agreement with the PES with respect to the peak positions. For pyrimidine, only the G_0W_0 @PBE0 spectrum is qualitatively similar to the PES. In terms of orbital

ordering (see Table 10.1), for pyridazine, G_0W_0 based on all starting points reproduces the reference orbital ordering of $n-\pi-\pi-n$. For pyrimidine and pyrazine, $G_0W_0@PBE$ and $G_0W_0@PBE0$ reproduce the reference orbital ordering of $n-\pi-n-\pi$, whereas $G_0W_0@HF$ does not.

Generally, as shown in Table 10.2, the best agreement with experimental ionization energies is obtained with $G_0W_0@PBE0$, which also yields the experimental energy hierarchy for all molecules, as shown in Table 10.1. Table 10.3 shows that G_0W_0 suffers from a severe starting-point sensitivity for all azabenzenes, with an average difference of approximately 1.38 eV, between HF- and PBE- based G_0W_0 ionization energies. The origin of the starting-point dependence in G_0W_0 can be traced back to differences in the orbitals and orbital energies, used as input for the self-energy calculation. The screening of W , being roughly inversely proportional to the occupied-unoccupied transition energies, is severely affected by the (over-) under-estimation of the HOMO-LUMO gap, which generally results in the (under-) over-estimation of screening. For instance, in G_0W_0 based on a PBE starting point (smaller gaps) the interaction W is typically “over-screened” whereas, for similar reasons, W is “under-screened” in $G_0W_0@HF$ (too large gaps). The (over-) under-screening in turn leads to a systematic error in the description of the excitation spectrum, as exemplified by the overestimation of the QP energies in the $G_0W_0@HF$ spectra reported in Figs. 10.3 and E.1-E.4. As a result, a G_0W_0 calculation based on a DFT starting point with the “right amount” of screening may yield valence spectra in excellent agreement with experiment, as is the case for $G_0W_0@PBE0$. I now proceed to examine to what extent partial self-consistency can alleviate the starting-point dependence.

PARTIAL SELF-CONSISTENCY IN THE EIGENVALUES

It has been suggested that the starting-point dependence of the G_0W_0 QP energies may be reduced by partial self-consistency in the eigenvalues [57, 174]. In the *ev-scGW* scheme, the QP equation (Eq. 4.18) is solved iteratively, recalculating the self-energy with QP energies obtained from the previous iteration of the self-consistency loop. The *ev-scGW* scheme is expected to reduce the overestimation of the screening typically observed in G_0W_0 based on semi-local DFT (or the underestimation in the case of HF), as the screened interaction W is now evaluated with occupied-unoccupied transition energies obtained from a *GW* calculation. However, since the orbitals are not updated self-consistently, the starting-point dependence cannot be eliminated entirely. As shown in Table 10.3, self-consistency in the eigenvalues succeeds in significantly reducing the starting-point dependence as compared to G_0W_0 , resulting in an average difference of 0.4 eV between the QP energies based on HF vs. PBE. The *ev-scGW* spectra of pyridine is reported in Fig. 10.4, whereas the spectra of benzene, pyridazine, pyrimidine, and pyrazine are shown in Figs. E.5-E.8, respectively, in Appendix E.

Generally, *ev-scGW@PBE* yields improved IPs, as compared to $G_0W_0@PBE$, whereas *ev-scGW@HF* yields IPs with similar accuracy to $G_0W_0@HF$. It should be noted, how-

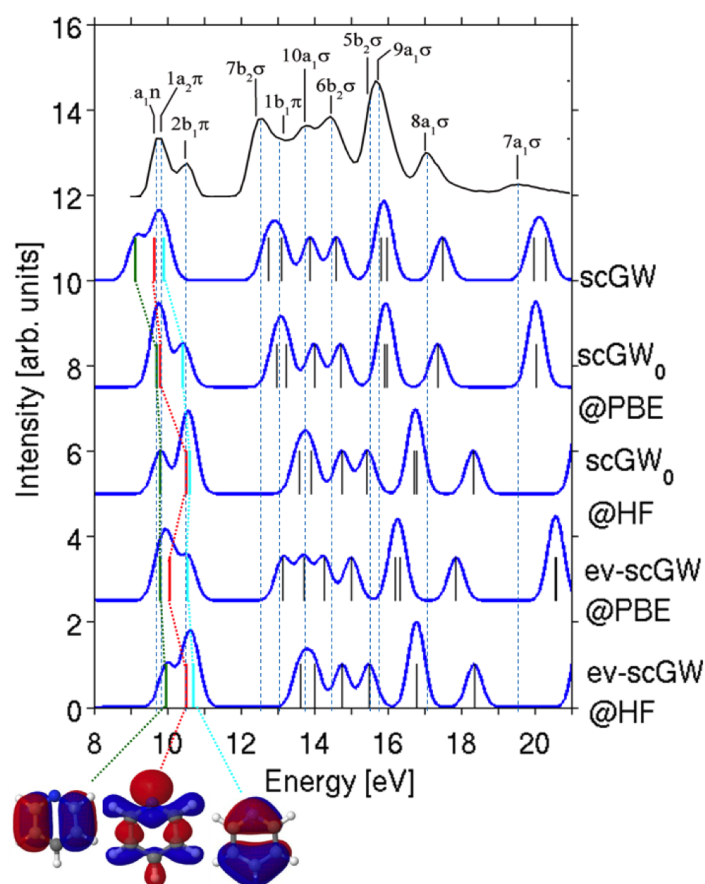


Figure 10.4: Spectra of pyridine calculated from *sc-GW*, *sc-GW*₀ and *ev-scGW* based on different starting points, (Gaussian broadened by 0.4 eV) compared to gas phase PES (from Ref. [253]). Illustration of the frontier orbital character is also shown.

ever, that evaluating the performance of *ev-scGW* based only on the IP and/or HOMO-LUMO gap may give a false impression of an improvement over *G*₀*W*₀. Examining the entire spectrum reveals that the partial self-consistency in the eigenvalues does not, in fact, lead to a consistent improvement over *G*₀*W*₀ for benzene and the azabenzenes. As shown in Table 10.2, the MAE of *ev-scGW*@HF is similar to that of *G*₀*W*₀@HF and the MAE of *ev-scGW*@PBE is worse than that of *G*₀*W*₀@PBE. For all molecules, the *ev-scGW* spectra appear overly stretched with respect to the PES, such that large deviations (on the order of 1 eV) from experiment occur for deeper QP states. Moreover, for most systems the orbital ordering deviates from experimental observations (Table 10.1).

The systematic overestimation of the *ev-scGW* QP energies can be understood as a manifestation of the under-screening of the Coulomb interaction *W*, which now resembles that of *G*₀*W*₀@HF. Interestingly, the so called, *G*₁*W*₁ scheme, in which only one eigenvalue update is performed, has been shown to reduce the PBE overscreening and give comparable results to *G*₀*W*₀ based on a hybrid functional [276]. However,

self-consistency ultimately leads to a systematic under-screening in W , as manifested by the overall overestimation of the QP energies. Therefore, based on this analysis, partial self-consistency in the eigenvalues cannot be considered as a way to improve the molecular excitation spectrum over G_0W_0 . The disappointing performance of *ev-scGW* emphasizes the importance of updating both eigenvalues and eigenfunctions self-consistently. I therefore proceed to evaluate the performance of the *sc-GW₀* scheme, in which G is computed self-consistently while W remains non-self-consistent.

PARTIALLY SELF-CONSISTENT *sc-GW₀*

Within the *sc-GW₀* scheme, G is calculated by iteratively solving the Dyson equation (Eq. 5.26), whereas W_0 is kept fixed at the first iteration and used to evaluate the self-energy throughout the iterative procedure. The QP energies are then extracted directly from the poles of the self-consistent Green function through the (integrated) spectral function in Eq. 3.34.

The spectra of benzene and the azabenzenes, obtained with this *sc-GW₀* scheme, based on PBE and HF starting points, are shown in Figs. 10.4 and E.5-E.8. It is clear from a visual inspection of the spectra, as well as from the MAEs in Table 10.2, that *sc-GW₀@PBE* generally yields QP spectra in better agreement with experiment than *G₀W₀@PBE*. In addition, as shown in Table 10.1, *sc-GW₀@PBE* correctly predicts the character of the frontier orbitals of the diazines (though not of pyridine). In contrast to *sc-GW₀@PBE*, *sc-GW₀@HF* yields overly stretched spectra, similar to *ev-scGW@HF*. The QP energies are mostly overestimated and considerable deviations from experiment are observed in the whole spectral region for all molecules. The MAE of *sc-GW₀@HF*, though somewhat smaller than that of *G₀W₀@HF* and *ev-scGW@HF*, is considerably larger than that of *sc-GW₀@PBE*.

The significant differences between *sc-GW₀@PBE* and *sc-GW₀@HF* spectra are reflected in the average starting-point dependence of 0.70 eV, which is greater than the starting-point dependence of *ev-scGW*. This indicates that the eigenvalues used in the calculation of the screened Coulomb interaction, W , are largely responsible for the starting-point dependence of *G₀W₀*. The update of the wave functions (through the iterative calculation of G) reduces the starting-point dependence to a lesser extent if the screening is not updated. This means that although the self-consistency in G incorporates many-body (dynamic) correlation effects and exact-exchange in the ground state, leading to a consistent description of excitations and ground state, a judicious choice of the DFT starting point is still necessary for W_0 . Starting from HF leads to underscreening of the Coulomb interaction and to a deterioration of the QP spectra, similarly to *G₀W₀@HF* and *ev-scGW@HF*. In contrast, *sc-GW₀@PBE* can be said to “enjoy the best of both worlds” in the sense that it benefits from an improved treatment of the ground-state electronic structure through the self-consistency in G , while preserving the PBE screening in the non-self-consistent W_0 . Due to the underestimation of the HOMO-LUMO gap in PBE-based calculations, the resulting screened Coulomb interaction is

slightly overscreened. It has been argued that this effect might mimic the missing vertex corrections (i.e., the electron-hole contribution to the dielectric function), which explains the success of $sc-GW_0@PBE$ [173, 277]. One may expect other partially self-consistent approaches in which the single-particle wave functions are updated through the approximate solution of the QP equation (e.g. the quasi-particle self-consistent GW approach [178, 278], or G_0W_0 based on the Coulomb-hole plus screened exchange (COHSEX) approximation [279]) to yield QP spectra of similar quality to $sc-GW_0@PBE$. I now turn to self-consistent GW to evaluate the effects of the self-consistent computation of the screening on the spectral properties of benzene and the azabenzenes.

FULLY SELF-CONSISTENT GW

As demonstrated above, the performance of non-self-consistent and partially self-consistent GW schemes is contingent on choosing a good starting point. Therefore, the only way to eliminate the starting-point dependence completely and to truly evaluate the quality and validity of the GW approximation itself is self-consistency [56].

The $sc-GW$ spectra of benzene and the azabenzenes are shown in Figs. 10.3 and E.1-E.4. The $sc-GW$ results are insensitive to the starting point and the same final spectrum is obtained regardless of whether the calculation is started from PBE or from HF. Overall, $sc-GW$ provides a better description of the QP energies than $G_0W_0@PBE$, $G_0W_0@HF$, $ev-scGW$, and $sc-GW_0@HF$ for the systems considered here. However, its performance is not as good as one might expect, as it fails to reproduce some important qualitative features of the spectra, such the spectral shape and the ordering of the frontier orbitals of pyridine, pyrimidine, and pyrazine (see Table 10.1). An appropriate choice of the starting point for G_0W_0 or $sc-GW_0$, may correctly reproduce these features, outperforming $sc-GW$. This is reflected by the lower MAE (Table 10.2) of $G_0W_0@PBE0$ and $sc-GW_0@PBE$. Interestingly, the $sc-GW$ spectra resemble those of the HF-based schemes with respect to the orbital ordering in the frontier region. In this respect, the non-self-consistent $G_0W_0@PBE0$ and partially self-consistent $sc-GW_0@PBE$ seem to capture or otherwise compensate for vertex corrections beyond $sc-GW$. This is possibly due to a fortunate error cancellation, whereby the overscreening in the PBE based W_0 compensates for neglecting the vertex function.

Now, one may ask whether including additional Feynman diagrams would lead to an improved description of the correlation energy, resulting in better agreement with the PES. In the following such a way of going beyond the GW approximation is examined by introducing second-order exchange diagrams.

G_0W_0 WITH SECOND-ORDER EXCHANGE

In physical terms, the correlation part of the GW self-energy corresponds to higher-order direct scattering processes. Higher-order exchange processes, however, are neglected. The simplest correlation method that treats direct and exchange interactions on an equal footing is second-order Møller-Plesset perturbation theory (MP2), where both



Figure 10.5: Second-order exchange diagrams. Dashed lines denote the Coulomb interaction v , whereas arrows indicates the non-interacting Green function G_0 .

direct and exchange processes are taken into account up to second-order. It has been suggested that adding the second-order exchange (2OX) diagram to the self-energy may correct the self-screening errors in GW , whose effect, like that of SIE, is more significant for localized states [241]. For the direct term, it is essential to sum over the so-called ring diagrams to infinite order to avoid divergence for systems with zero gaps. In contrast, for exchange-type interactions, the second-order exchange diagram, illustrated in Fig. 10.5 is the dominant contribution to the self-energy and neglecting the higher-order diagrams does not lead to a divergence. Thus, the G_0W_0+2OX scheme, suggested here, is a simple practical correction to the GW approximation. Within this scheme, the self-energy is written as:

$$\Sigma^{GW+2OX} = \Sigma^{GW} + \Sigma^{2OX} \quad , \quad (10.3)$$

where Σ^{2OX} is given in terms of the Green function and the bare Coulomb interaction, v , as [7]:

$$\Sigma^{2OX} = i \int d3d4 G(1,3)G(3,4)v(1,4)v(3,2) \quad . \quad (10.4)$$

The single-particle Green function, G_0 , is used to evaluate the 2OX self-energy, which reduces Eq. 10.4 to an expression involving only single-particle orbitals and eigenvalues:

$$\begin{aligned} \Sigma_{n,\sigma}^{2OX}(\omega) &= (np, \sigma | la, \sigma)(pl, \sigma | an, \sigma) \times \\ &\times \left[\frac{\theta(\mu - \epsilon_p^\sigma)}{\omega + \epsilon_a^\sigma - \epsilon_i^\sigma - \epsilon_p^\sigma - i\eta} + \frac{\theta(\epsilon_p^\sigma - \mu)}{\omega + \epsilon_l^\sigma - \epsilon_a^\sigma - \epsilon_p^\sigma + i\eta} \right] \quad , \quad (10.5) \end{aligned}$$

where $(np, \sigma | la, \sigma)$ is the two-electron Coulomb repulsion integral over single-particle orbitals:

$$(np, \sigma | la, \sigma') \equiv \int d\mathbf{r}d\mathbf{r}' \frac{\psi_n^{\sigma*}(\mathbf{r})\psi_p^{\sigma*}(\mathbf{r}')\psi_l^{\sigma'}(\mathbf{r})\psi_a^{\sigma'}(\mathbf{r}')}{|\mathbf{r} - \mathbf{r}'|} \quad . \quad (10.6)$$

While the G_0W_0+2OX scheme is physically motivated and conceptually appealing, its usefulness can only be judged *a posteriori*, based on its performance, which is here assessed at the G_0W_0 level. Figure 10.6 show the G_0W_0+2OX spectra of pyridine based on different starting points, compared to the PES experiments. The G_0W_0+2OX spectra for the remaining molecules is reported in Figs. E.9-E.12 in Appendix E. Because the

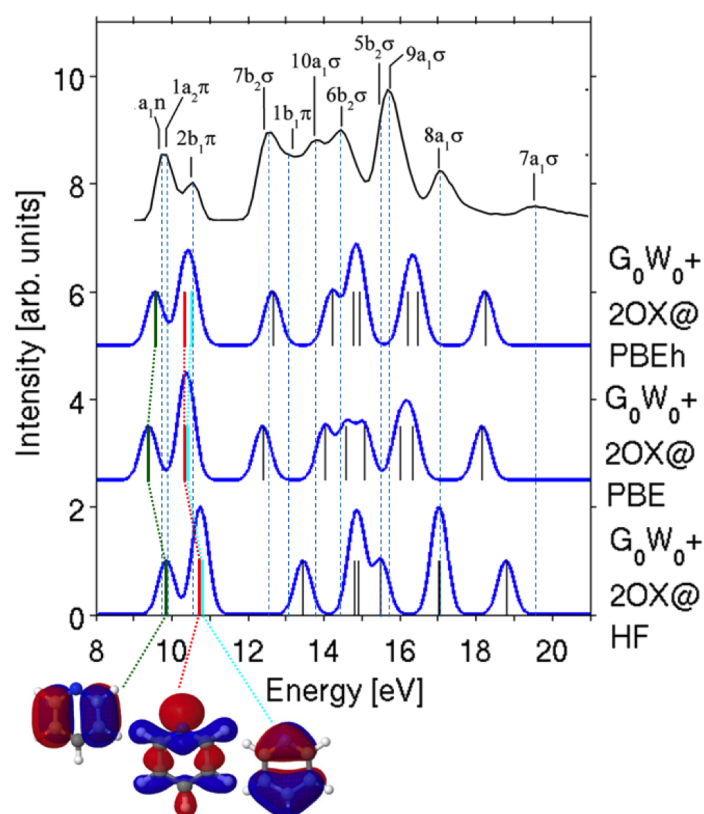


Figure 10.6: Spectra of pyridine calculated with G_0W_0 plus second-order exchange based on HF, and different DFT starting points, Gaussian broadened by 0.3 eV. The experimental PES spectrum is reproduced from Ref. [253]. Illustration of the frontier orbital character is also shown.

G_0W_0+2OX scheme is non-self-consistent, a significant starting-point dependence of 0.8 eV on average is observed (Table 10.3). This starting-point dependence is smaller than that of G_0W_0 but larger than that of the partially self-consistent schemes. Overall, adding the second-order exchange at the G_0W_0 level is not worthwhile. It does not alleviate the starting-point dependence and yields worse agreement with experiment in terms of the spectral shape (for all molecules) and the ordering of the frontier orbitals of pyridine, pyrimidine, and pyrazine. To illustrate the effect of the $2OX$ correction, I compare in Fig. 10.7 the $G_0W_0@PBE$ and $G_0W_0@PBE+2OX$ spectra of benzene. For benzene, the $2OX$ correction splits the quasi-particle energies of the HOMO-1 and HOMO-2 levels, which are separated by approximately 0.5 eV in experiment and almost degenerate in $G_0W_0@PBE$. $G_0W_0@PBE+2OX$ however overestimates the splitting by a factor of 4. This is possibly a result of using the bare, rather than the screened, Coulomb interaction in the $2OX$ self-energy. Second-order screened exchange (SOSEX), in which one of the bare Coulomb line is replaced by a dressed line (i.e., v is replaced by W), was proposed as a possible correction of the self-screening error that affects the GW self-energy, and is therefore expected to improve the spectral properties of molecules and solids – at the

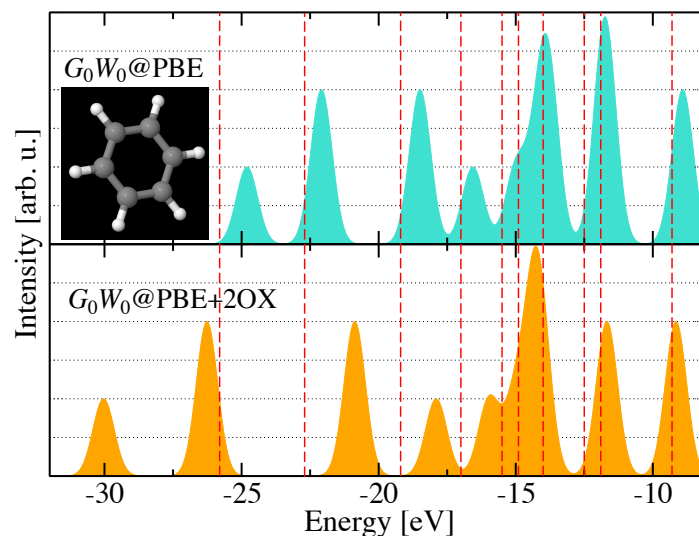


Figure 10.7: Comparison between the $G_0W_0@PBE$ and $G_0W_0@PBE+2OX$ spectra of benzene Gaussian broadened by 0.3 eV. The experimental vertical ionization energies from Ref. [253] are shown as vertical dashed lines.

price of a considerably higher computational cost. This calls for further investigation of vertex correction, which will be pursued in the future.

10.3 IONIZATION ENERGIES OF CLOSED-SHELL MOLECULES

The accuracy of the *sc-GW* quasi-particle HOMO was further assessed for a set of 30 closed-shell molecules first put forward by Rostgaard *et al.* [58]. For brevity the results are summarized in Fig. 10.8 and in Table 10.4. The reader is referred to the Appendix C for the actual numerical values. In Ref. [58], *sc-GW* was based on the

Table 10.4: Mean error (ME), mean absolute error (MAE), and percentage error (PE) of the ionization energies for the 30 closed-shell molecules shown in Fig. 10.8.

	ME	MAE	PE
<i>sc-GW</i>	-0.03	0.31	2.6 %
<i>sc-GW</i> ₀ @HF	0.30	0.37	3.0 %
<i>sc-GW</i> ₀ @PBE	-0.14	0.28	2.4 %
G_0W_0 @HF	0.53	0.54	4.4 %
G_0W_0 @PBE	-0.57	0.63	5.6 %
G_0W_0 @PBE0	-0.18	0.34	2.9 %
HF	0.75	0.87	6.9 %
PBE	-4.46	4.46	60.1 %
PBE0	-2.96	2.96	33.2 %

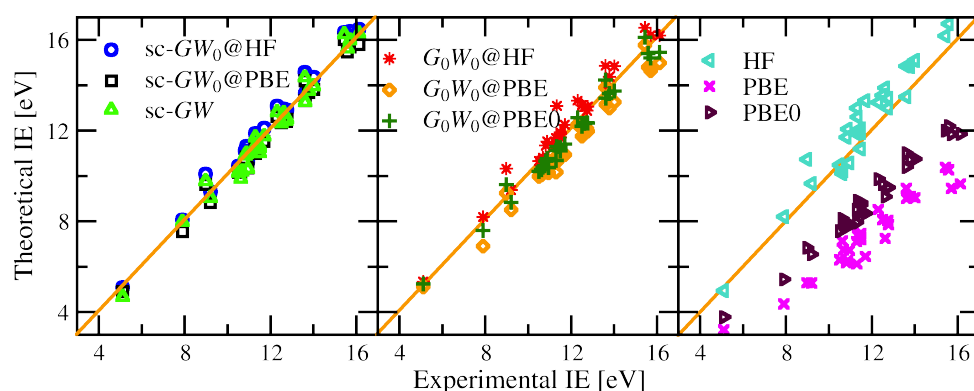


Figure 10.8: First vertical ionization energy (VIE) for 30 closed-shell molecules composed of 2 to 6 atoms evaluated from different perturbative and self-consistent approaches. Experimental values are taken from Ref. [128]. All calculations are performed with a Tier 4 basis set.

frozen-core approximation, whereas in this work core electrons are also treated fully self-consistently. As for benzene, G_0W_0 @HF tends to overestimate VIEs, while G_0W_0 @PBE underestimates. sc -GW also slightly underestimates the VIEs, but gives an average deviation of only 2.6% compared to 5.6% in G_0W_0 @PBE and 4.4% in G_0W_0 @HF. PBE and HF present two extreme starting points. In PBE the gap between the HOMO and the LUMO is severely underestimated, while in HF it is considerably overestimated. This in part explains the behavior of G_0W_0 @PBE and G_0W_0 @HF. Since the screening strength is inversely proportional to the HOMO-LUMO gap, G_0W_0 @PBE overscreens and G_0W_0 @HF underscreens, as mentioned before. G_0W_0 @PBE0 reduces the over- and under-screening error, and produces ionization energies in better agreement with experiment, with a percentage error of 2.9% which is comparable to sc -GW. These results lead me to conclude that sc -GW systematically improves the first ionization energy of the systems considered here as compared to G_0W_0 based on PBE and HF. On the other hand, through an appropriate choice of the G_0W_0 starting point, it is possible to obtain ionization energies with an accuracy comparable to sc -GW, as reported in the previous Section for benzene and the azabenzenes. In addition, when G_0W_0 @PBE and G_0W_0 @HF bracket experimental values, there exists at least one hybrid starting point that matches the first experimental ionization energy. As compared to perturbative G_0W_0 calculations, partially self-consistent sc -GW also improves the agreement with the experimental first VIE, and yields percentage errors of 3% and 2.4% for sc -GW@HF and sc -GW@PBE, respectively.

To demonstrate the general validity of the findings reported in the previous Section for benzene and the azabenzenes, I now move on to discuss the performance of sc -GW for the description of the *full* excitation spectrum for a set of molecules relevant for organic photo-voltaic applications: thiophene, benzothiazole, naphthalene, tetrathiafulvalene, and 1, 2, 5-thiadiazole. The molecular geometries – illustrated in Fig. 10.9 – are obtained from a DFT structural optimization performed with the PBE functional in a Tier 2 basis

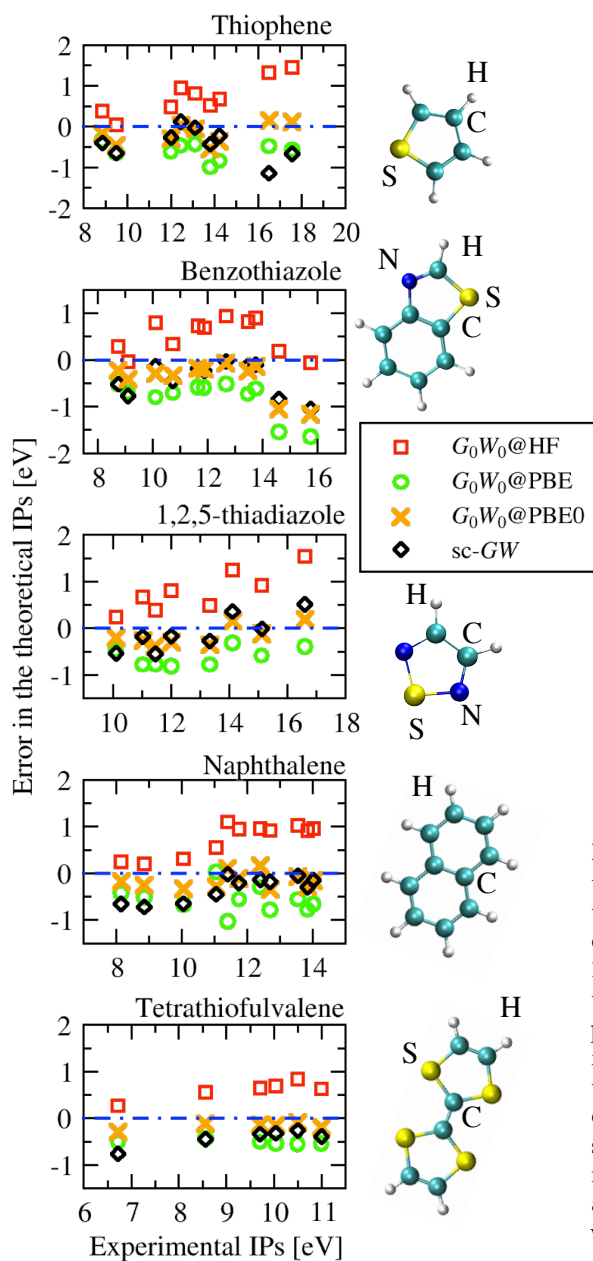


Figure 10.9: Comparison between theoretical and experimental vertical ionization energies (VIEs) of thiophene, benzothiazole, 1, 2, 5–thiadiazole, naphthalene, and tetrathiofulvalene. Experimental photo-emission data are reproduced from Refs. [108, 280–283], respectively. The molecular geometries – optimized with PBE in a Tier 2 basis set – are reported on the right. G_0W_0 ionization energies are obtained with a Tier 4 basis set, the $sc-GW$ ones with a Tier 2 basis.

set.

For naphthalene the coupled cluster singles doubles with perturbative triples (CCSD(T)) method gives a vertical ionization potential of 8.241 eV [6], which $sc-GW$ underestimates significantly (7.48 eV). For this molecule, the difference between the vertical and the adiabatic ionization potential is only 0.1 eV in CCSD(T). For thiophene, CCSD(T) calculations of the adiabatic ionization energy obtain 8.888 eV [284], in good agreement with experiment, whereas $sc-GW$ yields 8.45 eV. As for the azabenzenes, zero-point vibration effects are small and compensate with relativistic corrections. However, in Ref. [284] the

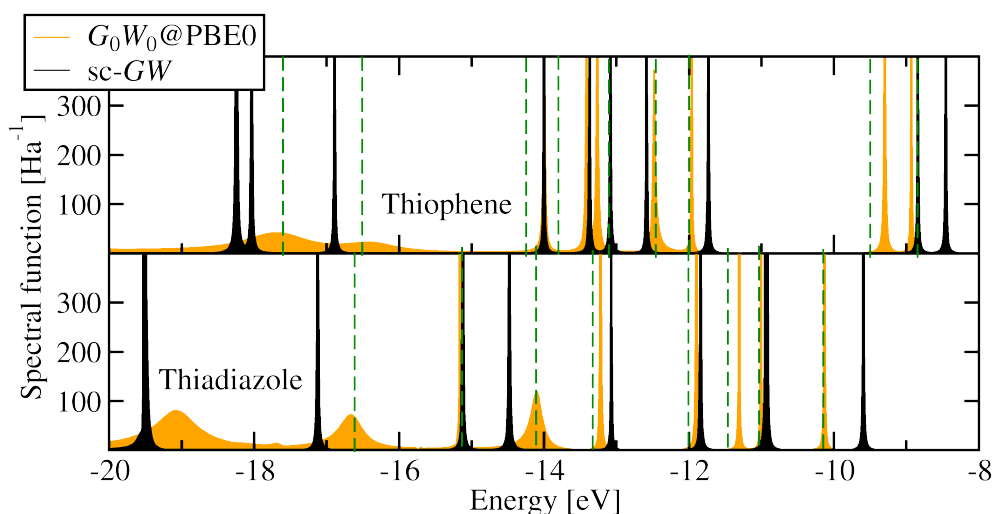


Figure 10.10: Comparison between *sc-GW* and $G_0W_0@PBE0$ spectral functions for thiophene, and 1,2,5-thiadiazole. Vertical dashed lines denote experimental photo-emission data from Refs. [108] and [280], respectively.

authors reported that the geometry of the cation differs considerably from that of the molecule, but did not give values for the vertical ionization energy. It therefore remains an open question, by how much vertical and adiabatic ionization potentials differ for thiophene. For benzothiazole, 1,2,5-thiadiazole, and tetrathiafulvalene we were not able to find CCSD(T) calculations for the vertical ionization potential.

Figure 10.9 depicts the comparison between experimental [108, 280–283] and theoretical ionization energies evaluated with *sc-GW* and G_0W_0 based on the HF, PBE, and PBE0 starting points. For all molecules, self-consistency provides ionization energies in agreement with experiment, and a good overall description of the excitation spectrum: *sc-GW* leads to an average error of 0.4 eV between the experimental and theoretical ionization energies, whereas HF- and PBE-based G_0W_0 differ on average by 0.7 eV. Interestingly, $G_0W_0@PBE0$ provides ionization energies close to *sc-GW*. Moreover, the $G_0W_0@PBE0$ spectrum is in slightly better agreement with experiment with an average deviation of 0.3 eV – as recently reported for benzene and the azabenzene in Ref. [176].

LIFETIMES OF QUASI-PARTICLE STATES

To facilitate the comparison of $G_0W_0@PBE0$ and *sc-GW*, I report in Fig. 10.10 the *sc-GW* and $G_0W_0@PBE0$ spectral functions of thiophene, and 1,2,5-thiadiazole. As discussed above, *sc-GW* and $G_0W_0@PBE0$ provide a similar description of the VIEs, which in both cases agrees well with the experimental references. Nevertheless, the corresponding spectral functions differ substantially for what concerns the broadening of the quasi-particle excitations. The quasi-particle peaks in the *sc-GW* spectral function have a δ -function-like character in this energy range, which reflects the infinite lifetime of the

quasi-particle states. On the other hand, in $G_0W_0@PBE0$ the lower lying peaks are more broadened than the corresponding *sc-GW* peaks, which can be attributed to a finite quasi-particle lifetime. Similar features are also observed in the $G_0W_0@PBE$ spectrum of the benzene molecule reported in Fig. 7.2.

A careful quantitative evaluation of lifetimes would require to properly account for effects beyond the *GW* approximation (such as the coupling between electrons and vibrational modes and the satisfaction of selection rules in the decay process) and goes beyond the purpose of the present work. Therefore, the following discussion will not address a quantitative comparison with experimental lifetimes, but will be limited to explain why even the quasi-particle excitations of small molecules have finite lifetimes and I will briefly characterize their starting-point dependence.

The physical origin of the lifetime is simple. The hole created in a lower valence (or core) state by the photoemission process can in principle decay to the HOMO, or to states energetically close to the Fermi energy. The energy released in this process has to be converted into an internal excitation of the system, since isolated molecules cannot dissipate energy. If the released energy is larger than the HOMO-LUMO gap, a particle-hole pair can be created. This opens up a scattering or decay channel for the hole, which therefore acquires a lifetime. The energy threshold for electron-hole formation is then given by $\Delta \equiv E_{\text{HOMO}}^{\text{GS}} - E_{\text{gap}}^{\text{GS}}$, with $E_{\text{HOMO}}^{\text{GS}}$ and $E_{\text{gap}}^{\text{GS}}$ the HOMO level and the HOMO-LUMO gap of the starting point, respectively. In other words, only quasi-particle states with an energy below Δ may decay, and acquire a finite broadening. On the other hand, if the hole is close to the Fermi energy – as, e.g., in case the HOMO level is depleted – no decay channel is allowed. Correspondingly, the quasiparticle lifetime is infinite. This argument is general and does not only apply to *GW*. What is particular to G_0W_0 is that the relevant gap for this process is determined by the starting point; in this case the DFT functional for the ground state.

To illustrate this effect on the broadening of the quasi-particle peaks, I report in Fig. 10.11 the spectrum of benzene evaluated with G_0W_0 based on HF, PBE, PBE-hybrid (PBEh) with different fraction of exact exchange, and at self-consistency. Values of Δ for the different exchange-correlation functionals are reported as vertical dashed lines (in green). PBE has the smallest HOMO-LUMO gap (~ 5.2 eV) and a noticeable peak broadening (i.e., short lifetime) is observed at ~ 14 eV in the $G_0W_0@PBE$ spectrum. For peaks above Δ , the residual broadening stems from the parameter $\eta = 10^{-4}$ discussed in Sec. 7.1. A systematic increase of the broadening is then observed the further a state lies below Δ . This is consistent with Landau’s Fermi-liquid theory, which predicts an inverse proportionality between the quasi-particle lifetime τ and the squared of the quasi-particle energy relative to the Fermi energy μ , i.e., $\tau^{-1} \propto (\epsilon^{\text{QP}} - \mu)^2$ [86, 285]. Adding exact exchange to the DFT functional and increasing its admixture opens the HOMO-LUMO gap. The onset of the finite lifetime subsequently moves to lower energies.

In *sc-GW*, the broadening of the quasi-particle peaks is consistent with the HOMO-LUMO gap at the *GW* level, and the ambiguity of the starting-point dependence is lifted.

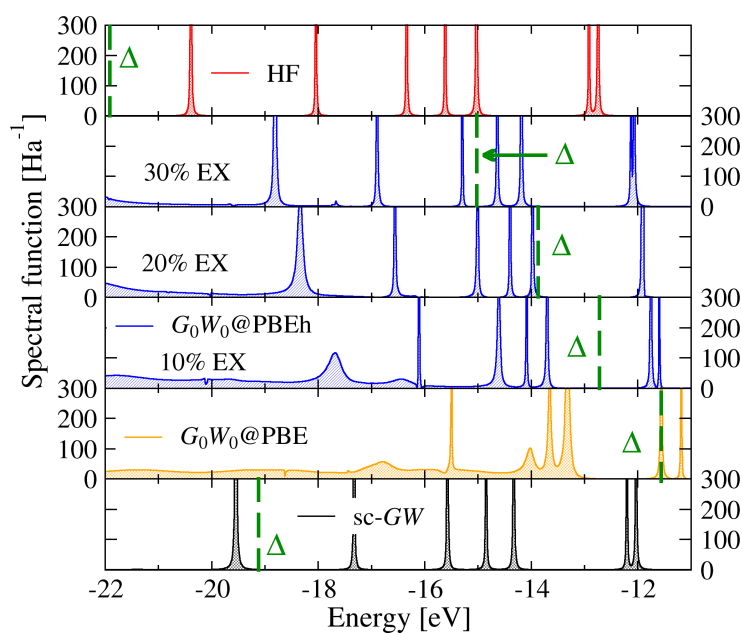


Figure 10.11: Spectral function of benzene on a logarithmic scale evaluated with *sc-GW* and G_0W_0 based on PBE, PBEh with different mixture of exact exchange (EX), and HF. Vertical dashed lines (in green) denote the energy threshold Δ for the formation of an electron-hole pair, which depends explicitly on the HOMO and LUMO levels of the underlying DFT/HF calculation. The quasi-particle peaks acquire a finite broadening only for states below Δ .

Consequently, for benzene only peaks below -19 eV acquire a small finite broadening. Based on the *sc-GW* results, the large broadening observed in the G_0W_0 @PBEh spectrum can be attributed to the small HOMO-LUMO gap of the underlying PBEh calculation. The inclusion of a fraction of exact exchange partially ameliorates this problem, but not fully. This shows that the calculation of lifetimes presents an additional situation in which – due to the severe dependence on the starting point – resorting to self-consistency is essential.

10.4 SUMMARY

A benchmark study of the performance of *GW* methods at different levels of self-consistency has been conducted for benzene and azabenzenes, as a set of representative organic molecules. The quality of the calculated spectra was evaluated based on a comparison to PES experiments, in terms of all valence peak positions, as well as the frontier orbital character. The accuracy of *sc-GW* for excited-state properties has further been assessed for a set of 30 small closed-shell molecules, and 5 molecules relevant for photo-voltaic applications: thiophene, 1,2,5-thiadiazole, benzothiazole, naphthalene, and tetrathiafulvalene. For the azabenzenes, which are characterized by localized nitrogen lone-pair orbitals, the effects of the self-interaction error and of the addition of EX are considerably more dramatic than for benzene with respect to the ordering of the

frontier orbitals.

A significant starting-point dependence was found for all non-self-consistent and partially self-consistent GW schemes. The best agreement with the PES was obtained with $G_0W_0@PBE0$ and $sc-GW_0@PBE$. Unlike partial self-consistency in G , partial self-consistency in the eigenvalues was found to cause underscreening and deterioration of the spectra, regardless of the starting point. Although in some cases $ev-scGW$ improved the IP with respect to G_0W_0 , the $ev-scGW$ spectra generally appeared overstretched as compared to experiment.

Due to underscreening, the spectra obtained from Hartree-Fock based calculations are distorted, and systematically overestimate the QP energies for all perturbative and partially self-consistent schemes analyzed in the present work. One can therefore conclude that HF is generally inadequate as starting point for the computation of spectral properties of molecules. Interestingly, no type of partial self-consistency improves on $G_0W_0@HF$ for lower lying excitation energies.

Full-self consistency succeeded in eliminating the starting-point dependence, providing an unbiased reference for the performance of the GW approximation for the molecules considered in this study. The $sc-GW$ spectra improve the quasi-particle energies as compared to PBE and HF based G_0W_0 , all $ev-scGW$ calculations, and $sc-GW_0@HF$. However, $G_0W_0@PBE0$ and $sc-GW_0@PBE$ provided excitation energies with an accuracy comparable to $sc-GW$. In this respect, the success of $G_0W_0@PBE0$ may be explained by a fortunate error cancellation, whereby the “right amount” of DFT overscreening compensates for neglecting the vertex function. Applying similar considerations, $sc-GW_0@PBE$ may be said to “enjoy the best of both worlds”, as it benefits from an improved treatment of the correlation through the self-consistency in G , while preserving the PBE overscreening in the non-self-consistent W_0 .

As an initial foray into the land beyond GW , the effect of adding the second-order exchange contribution to the self-energy at the G_0W_0 level has been investigated. The resulting G_0W_0+2OX spectra were in worse agreement with experiment than the corresponding G_0W_0 spectra and seemed overstretched to an even greater extent than the $ev-scGW$ spectra. This may be a result of using the bare, rather than the screened, Coulomb interaction in the 2OX self-energy. This and the effect of adding the 2OX self-energy to $sc-GW$ will be investigated in future work.

11 CONCLUSIONS AND OUTLOOK

In this doctoral work, I developed a numerical implementation of the self-consistent GW (sc- GW) approach to many-body perturbation theory (MBPT) and employed it for the description of excited- and ground-state properties of atoms and molecules.

The self-consistent procedure introduces a noticeably higher computational cost, as compared to conventional non-self-consistent perturbative GW (G_0W_0) calculations. Therefore, part of my work has been devoted to the development of numerical techniques adequate to the computational complexity of the problem. The sc- GW method has been implemented in the FHI-aims code in an all-electron numeric atom-centered orbital basis-set framework. The central ingredients of this implementation have been: (i) the resolution-of-identity formalism for the representation of two-particle operators in an atom-centered basis set; (ii) an imaginary time/frequency framework for the representation of the dynamical (i.e., frequency/time dependent) quantities; (iii) an optimized scheme for the evaluation of Fourier integrals. Through points (i-iii), the applicability of the sc- GW method could be extended to molecules up to 20-30 atoms, facilitating a systematic assessment of the accuracy of the GW approach for finite systems.

To further improve the efficiency of this implementation two ways can be undertaken: the first one involves the separation of core and valence electronic degrees of freedom, and the restriction of the self-consistent procedure to the valence states. However, the core-valence separation neglects the contribution of the core to the screening of the valence electrons, and it therefore introduces an additional error that, for finite systems, still has to be quantified. The second way, currently under investigation in the theory department of the Fritz Haber Institute, involves the development of approaches to the resolution-of-identity technique which would reduce the size of the auxiliary basis set, needed for the matrix representation of all two-particle operators. This can be achieved, for instance, by defining auxiliary basis functions that span the Hilbert space of a subset of numeric orbitals pairs (as, e.g., only neighbouring pairs), rather than for all possible pairs. The reduction of the auxiliary-basis size is the key for the optimization of the linear algebra operations that presently constitute the main bottleneck of the implementation presented in this thesis.

At self-consistency, GW has several properties that make it desirable as a general purpose electronic-structure approach: i) Excited- and ground-state properties are described at the same level of theory. ii) Ground and excited states are independent

of the initial reference state. iii) Conservation laws for total energy, momentum, and particle number are satisfied. Points i)-iii) define a hierarchy of theoretical consistency for different levels of self-consistency of the GW approximation. $sc-GW$ occupies the highest place in this hierarchy (all points are satisfied), whereas G_0W_0 lies at the bottom since all points are violated. Partial self-consistent approaches, such as eigenvalue self-consistent GW and $sc-GW_0$ (with fixed screened Coulomb interaction), occupy intermediate levels. Whether this hierarchy of GW methods also reflects an actual accuracy hierarchy – defined more empirically based on the agreement with experiment – has been investigated for benzene and the azabenzenes. Self-consistent GW was found to not necessarily provide the best agreement with the reference data. In fact, the comparison with photoemission spectroscopy reveals that, for certain starting points, G_0W_0 and partial self-consistent schemes ($sc-GW_0$) may outperform $sc-GW$. Hybrid functionals, in particular, have been shown to provide an optimal reference state for the perturbative calculations of spectral properties, yielding comparable to (or better than) $sc-GW$.

I have further benchmarked the accuracy of the GW approximation for bond lengths, vibrational frequencies, binding energies, and dipole moments for a set of diatomic molecules. The results illustrate that, on the whole, $sc-GW$ is not worthwhile for the ground-state properties of systems of this size, as its accuracy is comparable to computationally cheaper perturbative approaches, such as EX+cRPA. For larger systems, however, the combined description of ground and excited states at the same level of theory, might be desirable. For describing the electron density in charge-transfer compounds, for example, it is necessary to reproduce correctly the relative alignment of the HOMO and LUMO levels for the different components of the system, and the electron density must be updated accordingly. Therefore – as exemplified by the TTF-TCNQ dimer – self-consistency is essential to describe the charge transfer, since methods based on perturbation theory do not introduce changes in the electron density.

For comparing how electronic correlation is captured in DFT and MBPT, I considered the dissociation of covalently bonded dimers as a test case. The GW series of Feynman diagrams was used to define the total energy in the many-body framework (corresponding to $sc-GW$, in practice) and in a DFT context, through the solution of the optimized effective potential equations (leading to the self-consistent random-phase approximation, or $sc-RPA$). For the hydrogen molecule, the potential-energy curve evaluated in $sc-GW$ and $sc-RPA$ show large differences. The analysis of the sources of such differences demonstrates that a DFT-based framework ($sc-RPA$) is more effective in describing dissociation as it mimics the static correlation that dominates the dissociation regime. In $sc-GW$, on the other hand, the dissociation limit is severely underestimated due to the wrong spatial distribution of the bonding orbitals. Nevertheless, considerable improvements in the dissociation energy may be achieved by resorting to spin-symmetry broken calculations, which enforce the localization of each spin-orbital on a different atom of the dimer.

Finally, this doctoral work allowed to identify some characteristics that an ideal

electronic-structure scheme for the computation of electronic excitation should encompass. The most prominent is the combination of MBPT-based description of electronic excitations with some form of self-consistency – which ultimately permits to incorporate dynamical many-body correlation effects in the ground state. This consideration, however, is not specific to GW , but embraces also other methods and is important for the future development of approximate numerical approaches. As an example, the inclusion of dynamical correlation in the ground state is expected to be relevant for materials in which the ground-state electronic structure depends on the alignment of energy levels between different components of the system. The class of systems that corresponds to this description is broad and includes molecular interfaces, hetero-junctions, molecules absorbed on surfaces, transport devices *et cetera*.

Among the available methods for the computation of electronic excitations, the GW approximation offers probably the best compromise between computational cost and accuracy. However, GW calculations are still too demanding (with current computational resources) to compute the photoemission spectra of many systems of interest for technological applications, such as large molecules absorbed on a substrate, or molecules in solution. Future studies should therefore aspire to extend the applicability of GW methods to systems composed by thousands of atoms (and beyond) through the development of new algorithms, the optimization of existing ones, and the introduction of well-controlled approximations. Moreover, it is desirable to go beyond the state-of-the-art accuracy achievable within the GW approach, that currently allows to determine excitation energies with an average percentage error of 3 – 5%. A better agreement with experimental references is, in fact, achievable by resorting to a beyond- GW description of exchange and correlation, e.g., through the inclusion of self-screening corrections or higher-order exchange-correlation diagrams. Unfortunately, beyond- GW approaches often involve a higher numerical cost. One of the great challenges that was not considered in this thesis is how the interplay of electronic excitations and other environmental and/or nuclear effects (e.g., vibrations and phonons) may affect experimental measurements. The interplay of these effects has been quantified only for the simplest cases. This is an area where quantitative understanding must be acquired for realistic systems, and the development of new *ab-initio* techniques that properly account for these processes is a necessary requirement for future advances in this field.

In summary, three complementary aspects should be addressed by future developments in the field: (i) the extension of the applicability of GW approaches to large systems (e.g., solid-molecules interfaces); (ii) the realization of beyond- GW schemes, for a more accurate prediction of excitation energies in an *ab-initio* framework; (iii) a quantitative characterization of the influence of nuclear vibrations on excitation spectra. The results presented in this doctoral work have shown that sc- GW constitutes an indispensable tool for the achievement of points (i)-(iii), as it provides an unbiased assessment of the accuracy of the GW approximation, and therefore quantifies the importance of a beyond- GW description of electronic excitations.

Part IV

Backmatter

Appendices

A FUNCTIONAL IDENTITIES

Being $A[\varphi]$ a functional of the function φ , the inverse of A is implicitly defined through the relation:

$$\int d3A(1,3)A^{-1}(3,2) = \int d3A^{-1}(1,3)A(3,2) = \delta(1,2) \quad . \quad (\text{A.1})$$

Due to basic rules of functional derivatives, differentiation of Eq. A.1 by $\varphi(4)$ yields:

$$\int d3 \frac{\delta A(1,3)}{\delta \varphi(4)} A^{-1}(3,2) = - \int d3A(1,3) \frac{\delta A^{-1}(3,2)}{\delta \varphi(4)} \quad . \quad (\text{A.2})$$

Multiplying A.2 on the right by $A(2,5)$ and integrating of 2 leads to:

$$\frac{\delta A(1,3)}{\delta \varphi(4)} = - \int d23A(1,3) \frac{\delta A^{-1}(3,2)}{\delta \varphi(4)} A(2,5) \quad , \quad (\text{A.3})$$

and similarly

$$\frac{\delta A^{-1}(1,3)}{\delta \varphi(4)} = - \int d23A^{-1}(1,3) \frac{\delta A(3,2)}{\delta \varphi(4)} A^{-1}(2,5) \quad . \quad (\text{A.4})$$

If A depends on φ , through a local functional B , i.e. $A[B[\varphi]]$, then the chain rule for functional differentiation applies:

$$\frac{\delta A(1,2)}{\delta \varphi(3)} = \int d4 \frac{\delta A(1,2)}{\delta B(4)} \frac{\delta B(4)}{\delta \varphi(3)} \quad . \quad (\text{A.5})$$

If the operator B is non-local, then:

$$\frac{\delta A(1,2)}{\delta \varphi(3)} = \int d45 \frac{\delta A(1,2)}{\delta B(4,5)} \frac{\delta B(4,5)}{\delta \varphi(3)} \quad . \quad (\text{A.6})$$

B CONVERGENCE WITH THE GRID PARAMETERS

Figure B.1 illustrates the effect of integration grid parameter values on the total energy of H_2O , with a Tier 2 basis settings. For a detailed discussion about each of the convergence parameters reported in Fig. B.1 the reader is referred to the main paper describing the FHI-aims implementation [204]. Briefly:

- The “cutoff potential” indicates the radius (in \AA) of the confinement potential used to set the tails of all numerical orbital basis functions to zero;
- “Hartree multipole expansion” specifies the angular momentum expansion of the atom-centered charge density multipole for the electrostatic potential;
- “Radial multiplier” systematically increases the density of the integration grid points;
- “Angular division” denotes the maximum number of angular integration grid points;
- “Radial base 1” is the total number of radial integration grids;
- “Radial base 2” is the position (in \AA) of the outermost radial integration grid.

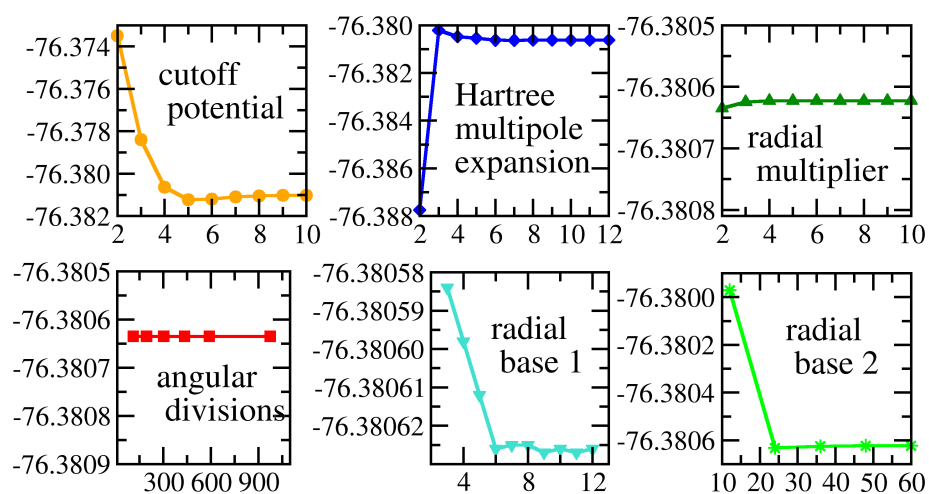


Figure B.1: Total energy of H₂O in a Tier 2 basis set as a function of the integration grid parameters. All values are in Hartree.

C IONIZATION ENERGIES OF CLOSED-SHELL MOLECULES

In this Appendix, I report the theoretical ionization energies obtained from G_0W_0 , $sc-GW_0$, and $sc-GW$ based on different starting points for a set of 30 closed-shell molecules. All ionization energies were obtained with the FHI-aims code using a Tier 4 numeric atom-centered orbital basis set [204]. The experimental values are taken from the photoemission data compiled in Ref. [128].

Table C.1: Ionization energy for 30 closed-shell molecules evaluated with G_0W_0 , $sc\text{-}GW_0$, and $sc\text{-}GW$ based on different starting points (in parenthesis) with a Tier 4 basis set. The mean error (ME), mean absolute error (MAE), and mean absolute percentage error (MAPE) are relative to the experimental values from [128] (reported in Table C.2).

	$scGW$	$scGW_0(\text{HF})$	$scGW_0(\text{PBE})$	$G_0W_0(\text{HF})$	$G_0W_0(\text{PBE})$	$G_0W_0(\text{PBE0})$
Cl ₂	-11.24	-11.66	-11.32	-11.84	-10.92	-11.24
ClF	-12.51	-12.91	-12.49	-13.06	-11.98	-12.34
CS	-11.36	-11.87	-11.34	-13.09	-10.62	-11.30
F ₂	-15.97	-16.38	-15.68	-16.21	-14.64	-15.20
HCl	-12.43	-12.73	-12.41	-12.88	-12.09	-12.35
Li ₂	-4.67	-5.08	-4.91	-5.34	-5.11	-5.24
LiF	-11.69	-11.87	-10.99	-11.43	-10.17	-10.69
LiH	-7.97	-8.06	-7.55	-8.19	-6.90	-7.60
N ₂	-15.61	-16.02	-15.47	-17.20	-14.79	-15.40
NaCl	-9.03	-9.30	-8.83	-9.38	-8.51	-8.84
SiO	-11.30	-11.67	-11.31	-11.92	-10.79	-11.11
CO ₂	-13.75	-14.17	-13.68	-14.38	-12.99	-13.63
H ₂ O	-12.76	-12.96	-12.41	-13.04	-11.89	-12.32
HCN	-13.26	-13.64	-13.32	-13.94	-13.15	-13.43
SH ₂	-10.14	-10.43	-10.17	-10.66	-9.98	-10.20
SO ₂	-12.32	-12.83	-12.34	-13.12	-11.76	-12.20
C ₂ H ₄	-10.19	-10.49	-10.26	-10.81	-10.18	-10.39
H ₂ CO	-10.97	-11.31	-10.83	-11.52	-10.35	-10.76
H ₂ O ₂	-11.74	-12.11	-11.53	-12.26	-10.94	-11.41
NH ₃	-10.89	-11.11	-10.66	-11.34	-10.26	-10.65
CO	-13.96	-14.36	-13.82	-14.84	-13.26	-13.75
HF	-16.28	-16.47	-15.80	-16.19	-14.99	-15.45
H ₂	-16.24	-16.34	-16.02	-16.53	-15.77	-16.11
P ₂	-9.88	-10.35	-10.16	-10.68	-10.04	-10.28
C ₂ H ₂	-11.00	-11.34	-11.08	-11.70	-10.95	-11.25
CH ₃ Cl	-11.17	-11.54	-11.18	-11.67	-10.82	-11.13
CH ₄	-14.34	-14.58	-14.20	-14.86	-13.90	-14.23
PH ₃	-10.32	-10.62	-10.35	-10.81	-10.14	-10.38
SiH ₄	-12.81	-13.08	-12.62	-13.32	-12.27	-12.57
N ₂ H ₄	-9.77	-10.09	-9.63	-10.32	-9.25	-9.62
ME	-0.03	0.30	-0.14	0.53	-0.57	-0.18
MAE	0.31	0.37	0.28	0.54	0.63	0.34
MAPE	2.58	3.00	2.41	4.37	5.57	2.88

Table C.2: HF, PBE, and PBE0 HOMO eigenvalue for 30 closed-shell molecules evaluated with the Tier 4 basis set. PBE-based Slater-transition-state (PBE-STs) ionization energies are included for comparison. The mean error (ME), mean absolute error (MAE), and mean absolute percentage error (MAPE) are relative to the experimental values. Experimental ionization energies are reported from [128].

	Exp.	HF	PBE	PBE0	PBE-STs
Cl ₂	-11.49	-12.08	-7.30	-8.72	-11.34
ClF	-12.77	-13.43	-7.85	-9.49	-12.65
CS	-11.33	-12.60	-7.38	-8.91	-11.96
F ₂	-15.70	-18.19	-9.45	-11.84	-15.68
HCl	-12.74	-12.99	-8.04	-9.51	-13.09
Li ₂	-5.11	-4.94	-3.22	-3.78	-5.61
LiF	-11.30	-13.00	-6.12	-7.95	-12.43
LiH	-7.90	-8.21	-4.36	-5.44	-9.00
N ₂	-15.58	-16.71	-10.27	-12.20	-15.87
NaCl	-9.20	-9.67	-5.28	-6.55	-9.64
SiO	-11.49	-11.91	-7.47	-8.83	-11.66
CO ₂	-13.78	-14.83	-9.09	-10.72	-14.02
H ₂ O	-12.62	-13.89	-7.25	-9.09	-13.65
HCN	-13.61	-13.50	-9.02	-10.40	-14.12
SH ₂	-10.50	-10.49	-6.30	-7.57	-10.91
SO ₂	-12.50	-13.55	-8.07	-9.64	-12.41
C ₂ H ₄	-10.68	-10.23	-6.74	-7.86	-11.07
H ₂ CO	-10.88	-12.06	-6.26	-7.88	-11.24
H ₂ O ₂	-11.70	-13.32	-6.45	-8.35	-11.69
NH ₃	-10.82	-11.70	-6.18	-7.74	-11.75
CO	-14.01	-15.10	-9.04	-10.75	-14.65
HF	-16.12	-17.72	-9.65	-11.85	-17.03
H ₂	-15.43	-16.18	-10.38	-12.00	-17.60
P ₂	-10.62	-10.10	-7.13	-8.11	-10.71
C ₂ H ₂	-11.49	-11.19	-7.20	-8.44	-11.79
CH ₃ Cl	-11.29	-11.88	-7.11	-8.52	-11.32
CH ₄	-13.60	-14.84	-9.46	-11.00	-14.29
PH ₃	-10.95	-10.58	-6.72	-7.88	-10.97
SiH ₄	-12.30	-13.24	-8.52	-9.87	-12.36
N ₂ H ₄	-8.98	-10.73	-5.29	-6.83	-9.75
ME		0.75	-4.46	-2.96	0.46
MAE		0.87	4.46	2.96	0.48
MAPE		6.92	60.15	33.16	3.92

D TOTAL ENERGY OF ATOMS

In Tables D.1 and D.2 are reported the total energies of atoms evaluated with perturbative G_0W_0 and different total energy functionals (GM, referred to as G_0W_0 and Klein, denoted as EX+cRPA), partially self-consistent sc- GW_0 and sc- GW . PBE, Hartree-Fock and renormalized second-order perturbation theory (rPT2) are included for comparison.

Table D.1: Total energies of the free atoms in the first two rows in the periodic table evaluated with sc- GW , partially self-consistent sc- GW_0 and G_0W_0 based on HF and PBE and full configuration interaction (full-CI). The aug-cc-pVQZ basis set was used for Li and Be (i.e. the largest aug-cc-pVNZ basis available for those elements) whereas the remaining elements were computed with the aug-cc-pV6Z basis set. All values are in Ha.

	full-CI	sc- GW	sc- GW_0 @PBE	sc- GW_0 @HF	G_0W_0 @PBE	G_0W_0 @HF
H	-0.500	-0.514	-0.513	-0.514	-0.538	-0.528
He	-2.902	-2.924	-2.923	-2.924	-3.013	-2.984
Li	-7.478	-7.469	-7.467	-7.469	-7.533	-7.501
Be	-14.667	-14.653	-14.646	-14.653	-14.790	-14.724
B	-24.654	-24.669	-24.661	-24.669	-24.881	-24.791
C	-37.845	-37.875	-37.867	-37.875	-38.141	-38.037
N	-54.589	-54.632	-54.626	-54.632	-54.938	-54.839
O	-75.067	-75.124	-75.119	-75.124	-75.507	-75.383
F	-99.734	-99.799	-99.790	-99.799	-100.259	-100.121
Ne	-128.938	-129.010	-128.998	-129.010	-129.528	-129.396
ME		0.034	0.030	0.034	0.275	0.193
MAE		-0.029	-0.023	-0.029	-0.275	-0.193

Table D.2: Total energies of the free atoms in the first two rows in the periodic table evaluated with perturbative RPA (equivalent to the Klein functional), rPT2, HF and PBE. The aug-cc-pVQZ basis set was used for Li and Be (i.e. the largest aug-cc-pVNZ basis available for those elements) whereas the remaining elements were computed with the aug-cc-pV6Z basis set. All values are in Ha.

	full-CI	RPA@PBE	RPA@HF	rPT2@PBE	rPT2@HF	PBE	HF
H	-0.500	-0.520	-0.515	-0.500	-0.500	-0.500	-0.500
He	-2.902	-2.943	-2.928	-2.903	-2.895	-2.893	-2.862
Li	-7.478	-7.487	-7.469	-7.449	-7.446	-7.461	-7.433
Be	-14.667	-14.697	-14.654	-14.637	-14.614	-14.629	-14.573
B	-24.654	-24.728	-24.671	-24.628	-24.602	-24.612	-24.533
C	-37.845	-37.942	-37.878	-37.817	-37.788	-37.799	-37.694
N	-54.589	-54.696	-54.638	-54.560	-54.531	-54.536	-54.405
O	-75.067	-75.197	-75.124	-75.033	-74.994	-75.015	-74.819
F	-99.734	-99.881	-99.799	-99.697	-99.649	-99.676	-99.416
Ne	-128.938	-129.087	-129.010	-128.899	-128.844	-128.866	-128.547
ME		-0.081	-0.031	0.025	0.051	0.039	0.159
MAE		0.081	0.036	0.025	0.051	0.039	0.159

E SPECTRA OF BENZENE, PYRAZINE,
PYRIDAZINE, AND PYRIMIDINE

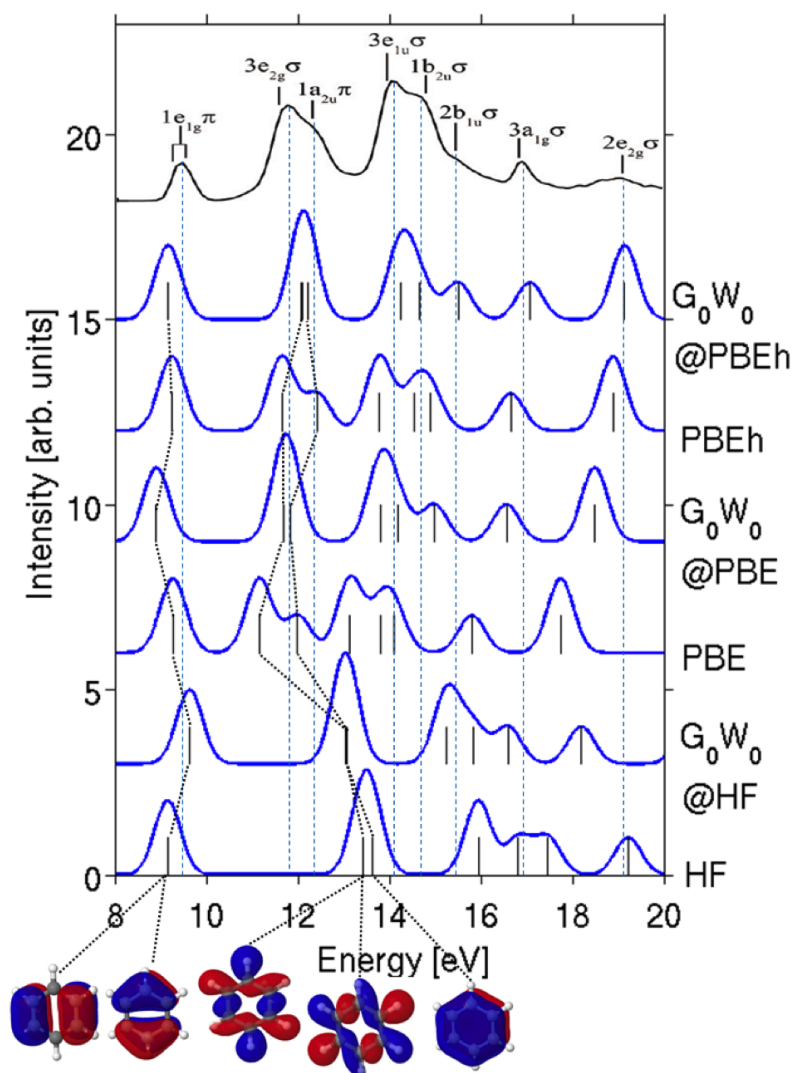


Figure E.1: Spectra of benzene calculated with DFT, Hartree-Fock, and G_0W_0 based on different starting points, Gaussian broadened by 0.4 eV. The experimental photo-emission spectrum is reproduced from Ref. [253]. Illustration of the frontier orbital character is also shown.

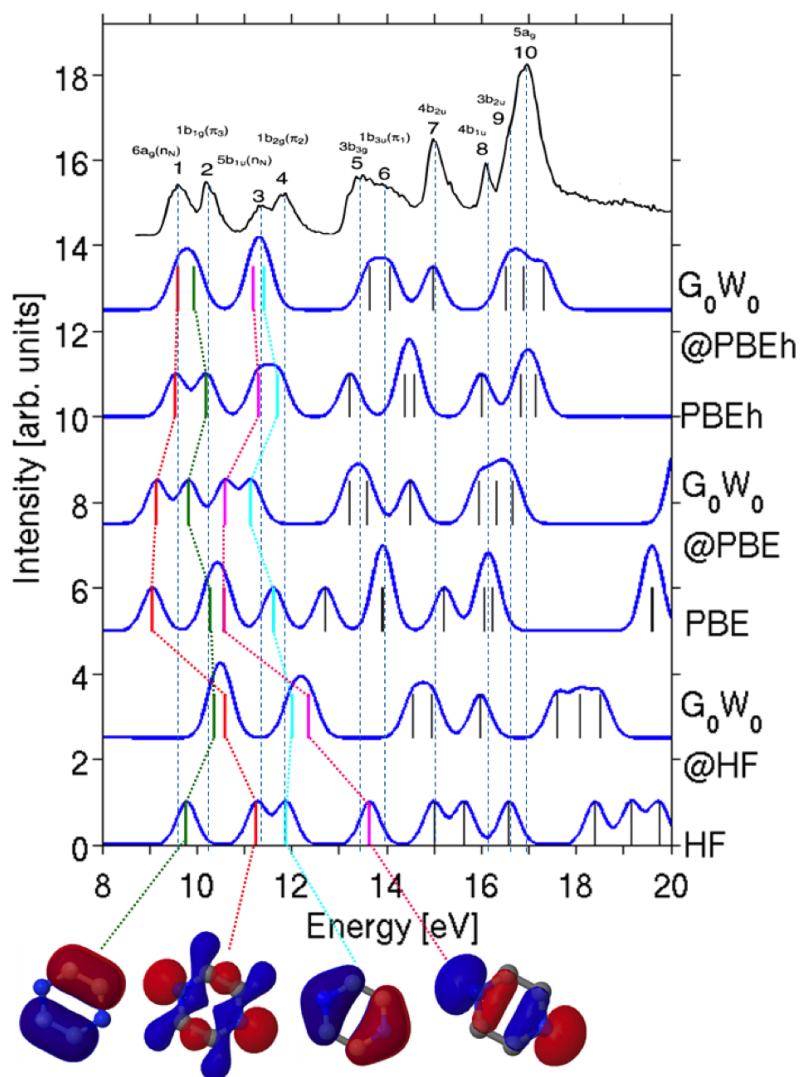


Figure E.2: Spectra of pyrazine calculated with DFT, Hartree-Fock, and G_0W_0 based on different starting points, Gaussian broadened by 0.4 eV. The experimental photo-emission spectrum is reproduced from Ref. [257]. Illustration of the frontier orbital character is also shown.

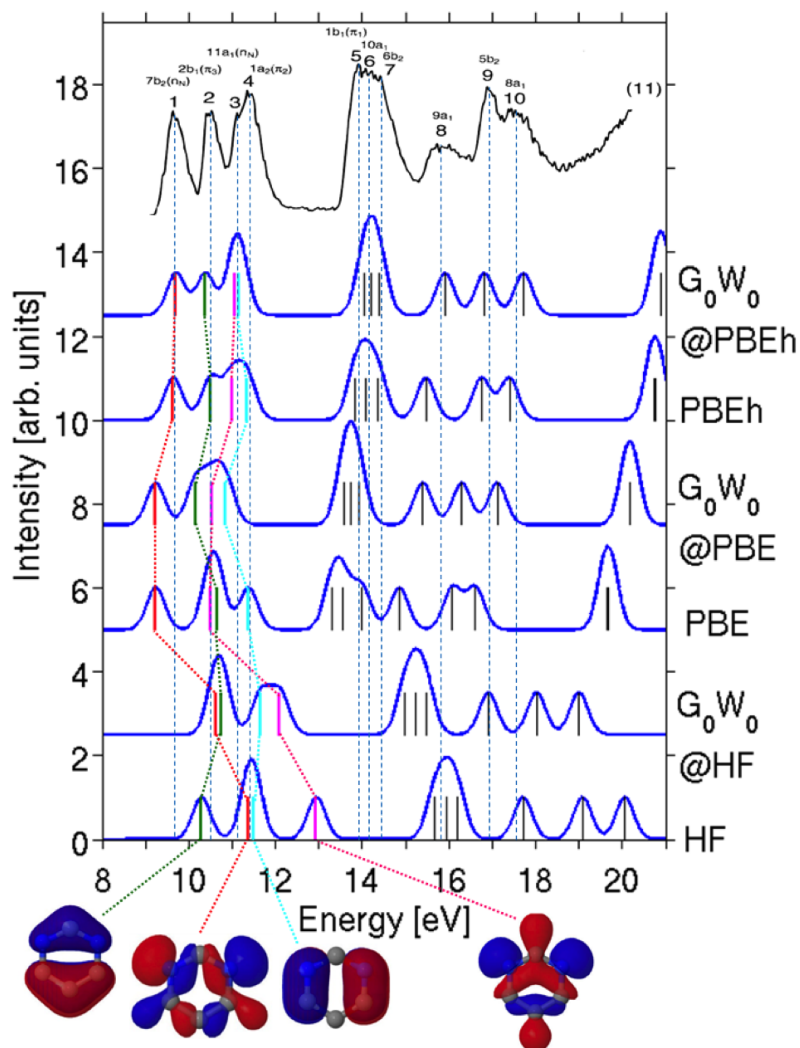


Figure E.3: Spectra of pyrimidine calculated with DFT, Hartree-Fock, and G_0W_0 based on different starting points, Gaussian broadened by 0.4 eV. The experimental photo-emission spectrum is reproduced from Ref. [257]. Illustration of the frontier orbital character is also shown.

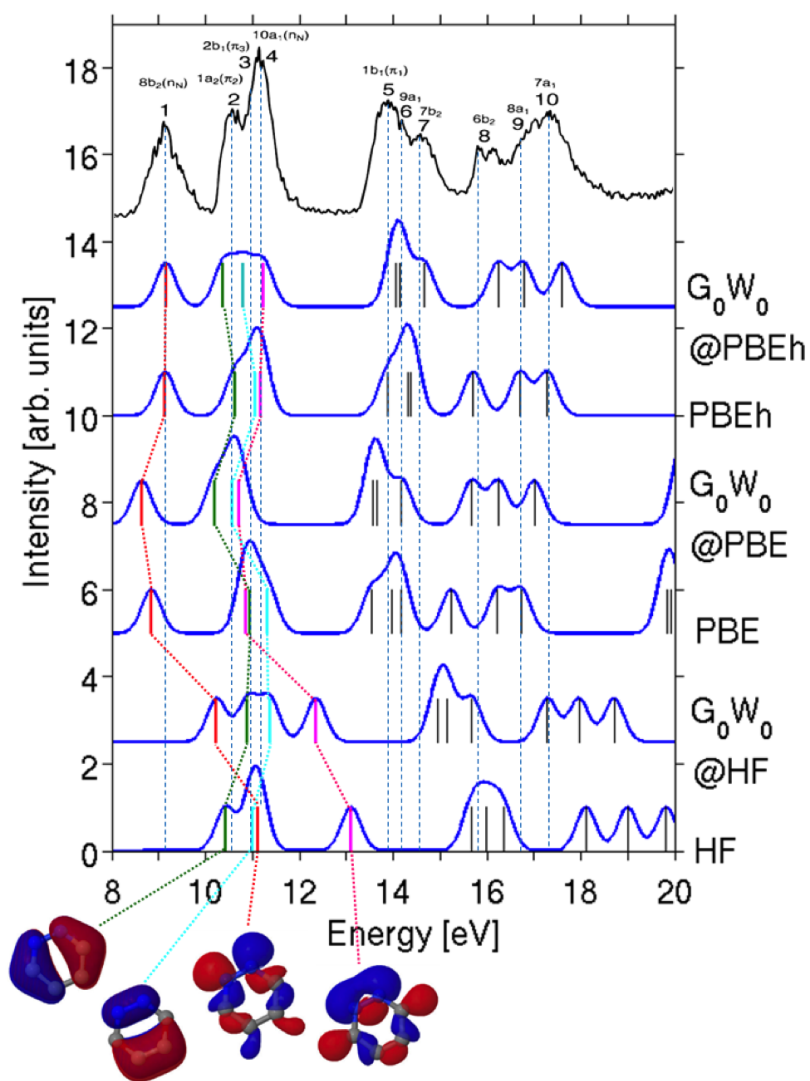


Figure E.4: Spectra of pyridazine calculated with DFT, Hartree-Fock, and G_0W_0 based on different starting points, Gaussian broadened by 0.4 eV. The experimental photo-emission spectrum is reproduced from Ref. [257]. Illustration of the frontier orbital character is also shown.

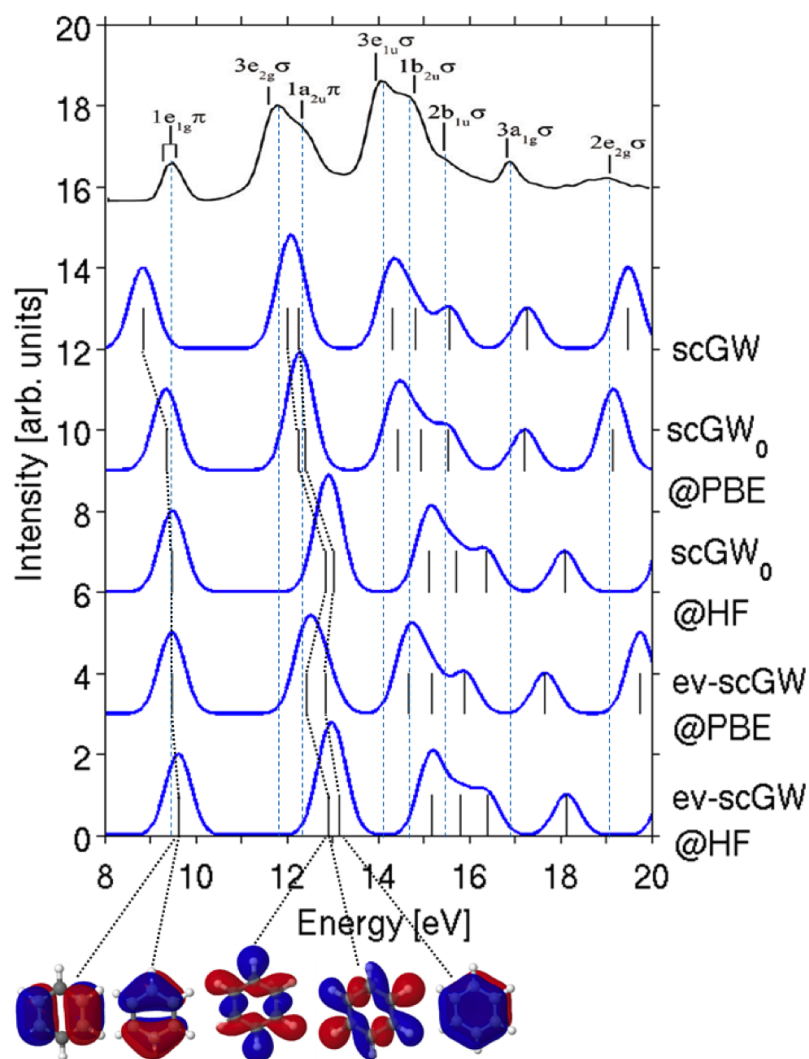


Figure E.5: Spectra of benzene calculated from $sc-GW$, $sc-GW_0$ and $ev-scGW$ based on different starting points, Gaussian broadened by 0.4 eV. The experimental photo-emission spectrum is reproduced from Ref. [253]. Illustration of the frontier orbital character is also shown.

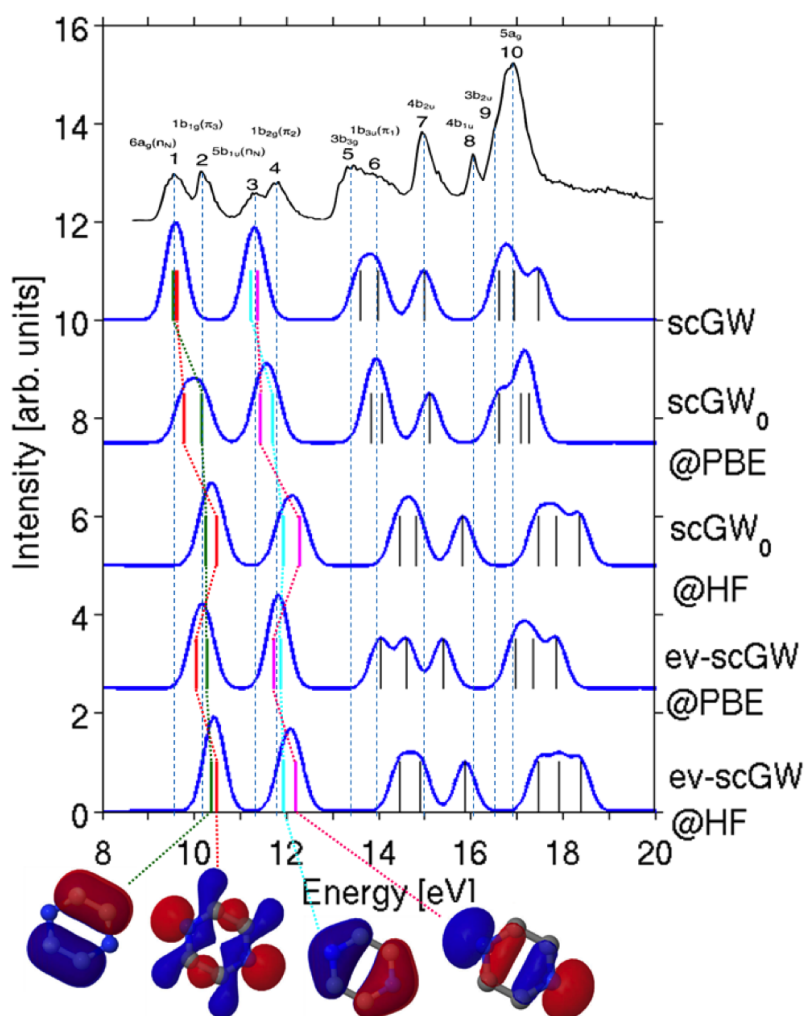


Figure E.6: Spectra of pyrazine calculated from *sc-GW*, *sc-GW*₀ and *ev-scGW* based on different starting points, Gaussian broadened by 0.4 eV. The experimental photo-emission spectrum is reproduced from Ref. [257]. Illustration of the frontier orbital character is also shown.

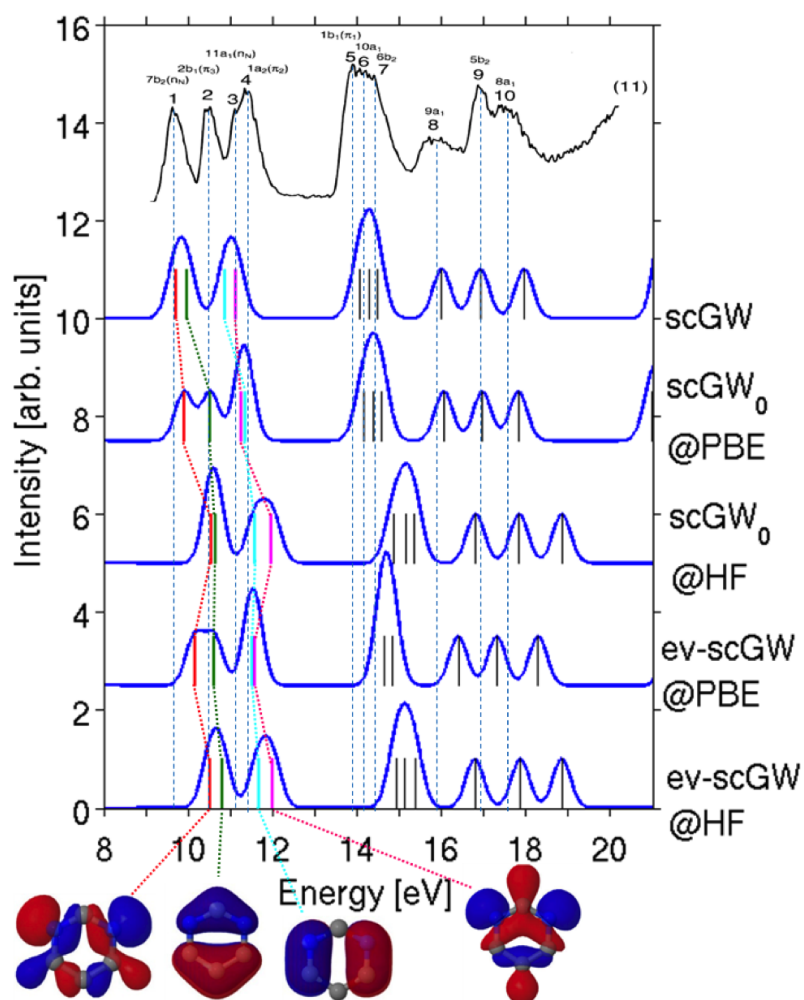


Figure E.7: Spectra of pyrimidine calculated from *sc-GW*, *sc-GW*₀ and *ev-scGW* based on different starting points, Gaussian broadened by 0.4 eV. The experimental photo-emission spectrum is reproduced from Ref. [257]. Illustration of the frontier orbital character is also shown.

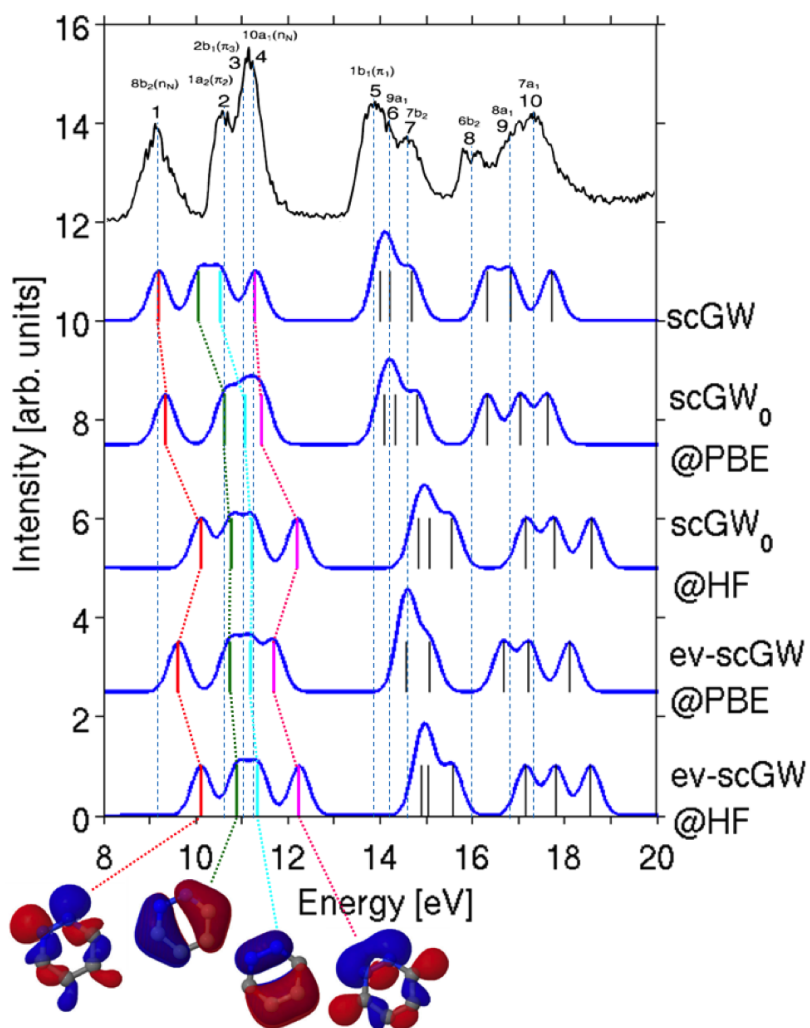


Figure E.8: Spectra of pyridazine calculated from *sc-GW*, *sc-GW*₀ and *ev-scGW* based on different starting points, Gaussian broadened by 0.4 eV. The experimental photo-emission spectrum is reproduced from Ref. [257]. Illustration of the frontier orbital character is also shown.

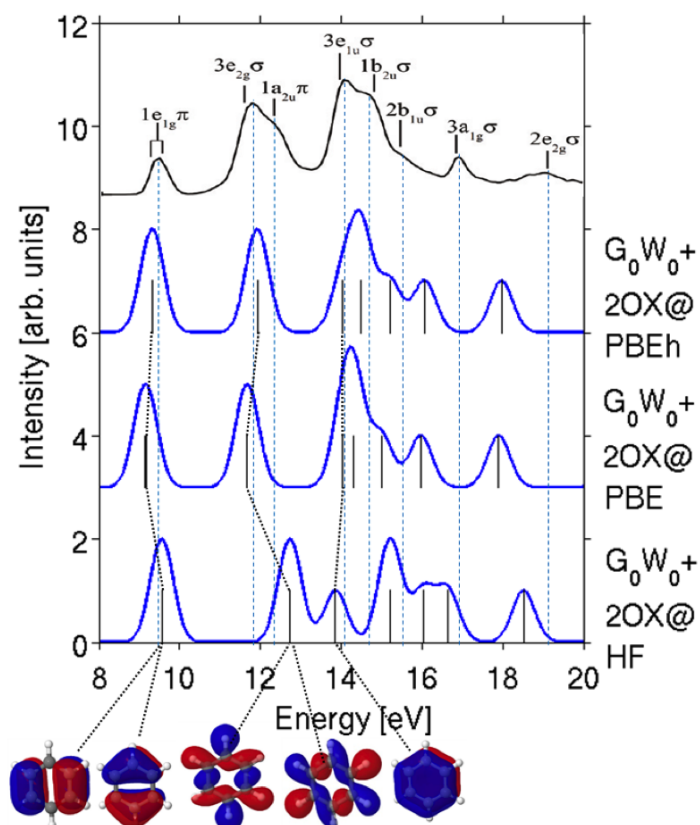


Figure E.9: Spectra of benzene calculated with G_0W_0 plus second-order exchange based on HF, and different DFT starting points, Gaussian broadened by 0.3 eV. The experimental photoemission spectrum is reproduced from Ref. [253]. Illustration of the frontier orbital character is also shown.

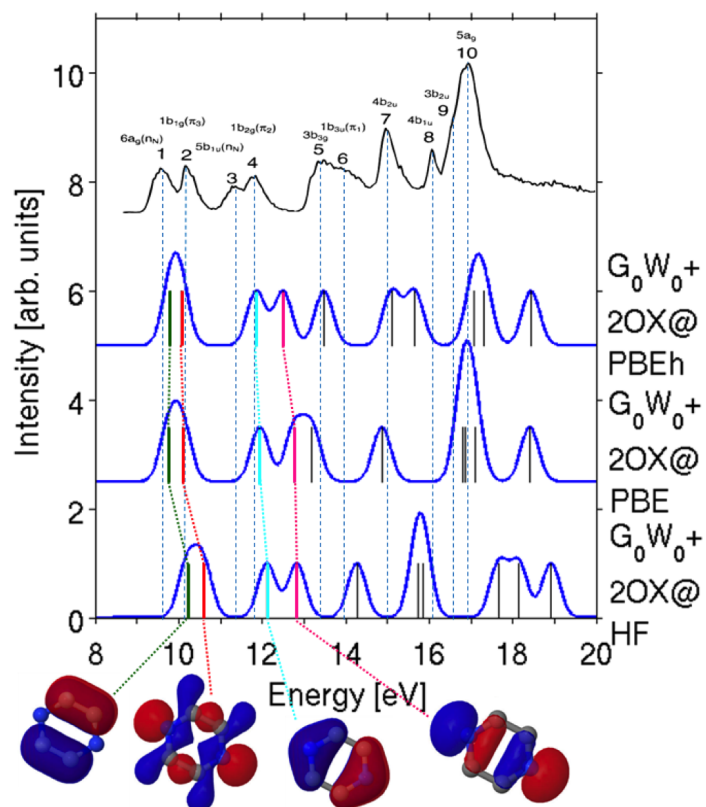


Figure E.10: Spectra of pyrazine calculated with G_0W_0 plus second-order exchange based on HF, and different DFT starting points. Gaussian broadened by 0.3 eV. The experimental photoemission spectrum is reproduced from Ref. [257]. Illustration of the frontier orbital character is also shown.

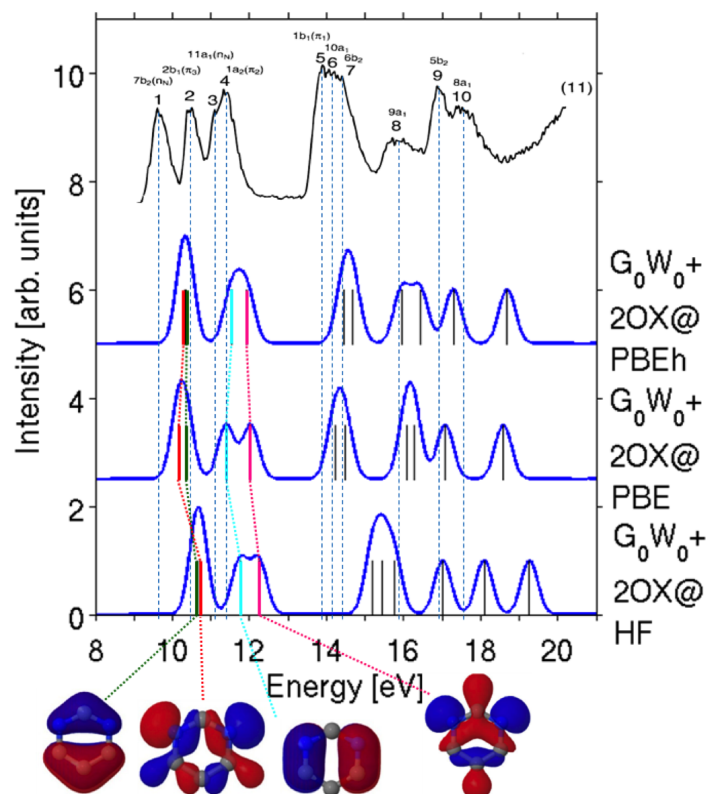


Figure E.11: Spectra of pyrimidine calculated with G_0W_0 plus second-order exchange based on HF, and different DFT starting points, Gaussian broadened by 0.3 eV. The experimental photoemission spectrum is reproduced from Ref. [257]. Illustration of the frontier orbital character is also shown.

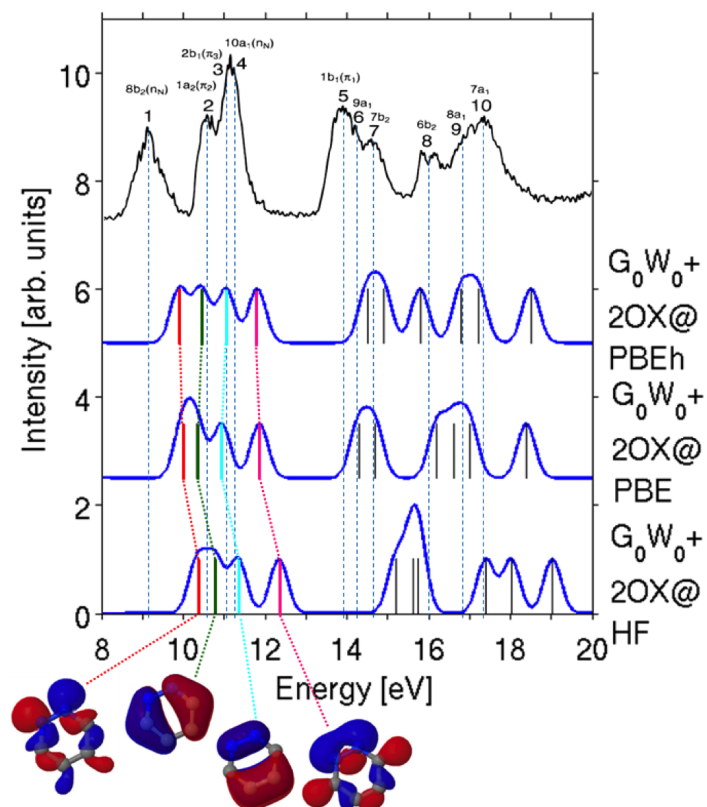


Figure E.12: Spectra of pyridazine calculated with G_0W_0 plus second-order exchange based on HF, and different DFT starting points, Gaussian broadened by 0.3 eV. The experimental photo-emission spectrum is reproduced from Ref. [257]. Illustration of the frontier orbital character is also shown.

F DERIVATION OF THE KLEIN AND LUTTINGER-WARD FUNCTIONALS

The ground-state total-energy expression for an interacting electron system can be obtained using the adiabatic-connection (AC) technique

$$E = T_s + \int d\mathbf{r} n(\mathbf{r}) (v_{\text{ext}}(\mathbf{r}) + \frac{1}{2} v_{\text{H}}(\mathbf{r})) + \int_0^1 \frac{d\lambda}{2\lambda} \text{Tr} [\Sigma_\lambda G_\lambda], \quad (\text{F.1})$$

where

$$\text{Tr} [AB] = \frac{1}{2\pi} \int_{-\infty}^{\infty} d\omega e^{i\omega\eta} \int d\mathbf{r} d\mathbf{r}' A(\mathbf{r}, \mathbf{r}', i\omega) B(\mathbf{r}', \mathbf{r}, i\omega), \quad (\text{F.2})$$

and $n(\mathbf{r})$ is the electron density which is fixed at its physical value along the AC path. Here G_λ and Σ_λ are respectively the interacting single-particle Green function and the self-energy for the “intermediate” system where the electrons interact with scaled Coulomb interaction $v_\lambda(\mathbf{r} - \mathbf{r}') = \lambda v(\mathbf{r} - \mathbf{r}') = \lambda/|\mathbf{r} - \mathbf{r}'|$.

The key question now is how to integrate the coupling constant λ out. To this end, it is customary to introduce the so-called Φ functional, defined in Eq. 3.31. It should be kept in mind that $\Sigma_\lambda^{(n)}$ (see Eq. 3.31) depends on λ in two ways: explicitly via the scaled Coulomb lines (there are n of them) and implicitly via G_λ (there are $2n - 1$ of them). The multiplication of G_λ with $\Sigma_\lambda^{(n)}$ in $\text{Tr} [\Sigma_\lambda^{(n)} G_\lambda]$ closes the self-energy diagrams, yielding the n -th order Φ -digrams which contain $2n$ Green-function lines. A key property of Φ_λ is therefore

$$\delta\Phi_\lambda / \delta G_\lambda = \sum_{n=1}^{\infty} \Sigma_\lambda^{(n)} = \Sigma_\lambda. \quad (\text{F.3})$$

The derivative of Φ_λ with respect to λ is given by

$$\begin{aligned} \frac{d\Phi_\lambda}{d\lambda} &= \sum_{n=1}^{\infty} \frac{1}{2n} \text{Tr} \left[\frac{n}{\lambda} \Sigma_\lambda^{(n)} G_\lambda \right] + \text{Tr} \left[\frac{\delta\Phi_\lambda}{\delta G_\lambda} \frac{dG_\lambda}{d\lambda} \right] \\ &= \frac{1}{2\lambda} \text{Tr} [\Sigma_\lambda G_\lambda] + \text{Tr} \left[\Sigma_\lambda \frac{dG_\lambda}{d\lambda} \right]. \end{aligned} \quad (\text{F.4})$$

Making use of Eq. F.4, Eq. F.1 becomes

$$\begin{aligned}
E &= T_s + \int d\mathbf{r} n(\mathbf{r}) v_{\text{ext}}(\mathbf{r}) + E_{\text{H}}[G] + \\
&\quad \int_0^1 d\lambda \left\{ \frac{d\Phi_\lambda}{d\lambda} - \text{Tr} \left[\Sigma_\lambda \frac{dG_\lambda}{d\lambda} \right] \right\} \\
&= T_s + \int d\mathbf{r} n(\mathbf{r}) v_{\text{ext}}(\mathbf{r}) + E_{\text{H}} + \Phi_{\lambda=1}[G_{\lambda=1}] \\
&\quad - \text{Tr} [\Sigma_{\lambda=1} G_{\lambda=1}] + \int_0^1 d\lambda \text{Tr} \left[G_\lambda \frac{d\Sigma_\lambda}{d\lambda} \right], \tag{F.5}
\end{aligned}$$

where $\Sigma_{\lambda=0} = 0$ and $\Phi_{\lambda=0} = 0$ have been used, and $E_{\text{H}}[G] = 1/2 \int d\mathbf{r} v_{\text{H}}(\mathbf{r}) n(\mathbf{r})$ is the Hartree energy.

To proceed, the Dyson equation linking G_λ and Σ_λ has to be invoked, which in the current context reads

$$G_\lambda^{-1} = G_s^{-1} - \Sigma_\lambda[G_\lambda] - v_{\text{ext}}^\lambda - \lambda v_{\text{H}} + v_s \tag{F.6}$$

where v_{ext}^λ is the external potential of the λ -dependent system (with $v_{\text{ext}}^{\lambda=1} = v_{\text{ext}}$) to keep the density unchanged, and $v_s = v_{\text{ext}} + v_{\text{H}} + v_{\text{xc}}$ is the effective single-particle potential of the KS reference system. From Eq. F.6, one gets

$$\begin{aligned}
-\frac{d}{d\lambda} \ln G_\lambda^{-1} &= -\frac{d}{d\lambda} \ln [G_s^{-1} - \Sigma_\lambda - v_{\text{ext}}^\lambda - \lambda v_{\text{H}} + v_s] \\
&= G_\lambda \left[\frac{d}{d\lambda} \Sigma_\lambda + \frac{d}{d\lambda} v_{\text{ext}}^\lambda + V_{\text{H}} \right]. \tag{F.7}
\end{aligned}$$

Using Eq. F.7, and denoting $G_{\lambda=1} = G$, $\Sigma_{\lambda=1} = \Sigma$, and $\Phi_{\lambda=1} = \Phi$, one obtains

$$\begin{aligned}
E &= T_s + \int d\mathbf{r} n(\mathbf{r}) v_{\text{ext}}(\mathbf{r}) + E_{\text{H}}[G] + \Phi[G] - \text{Tr} [\Sigma G] \\
&\quad - \int_0^1 d\lambda \text{Tr} \left[\frac{d}{d\lambda} \ln G_\lambda^{-1} + G_\lambda \frac{d}{d\lambda} v_{\text{ext}}^\lambda + G_\lambda V_{\text{H}} \right] \\
&= T_s + \int d\mathbf{r} n(\mathbf{r}) v_{\text{ext}}(\mathbf{r}) - E_{\text{H}}[G] + \Phi[G] - \text{Tr} [\Sigma G] \\
&\quad - \text{Tr} [\ln G^{-1}] + \text{Tr} [\ln G_s^{-1}] - \int d\mathbf{r} n(\mathbf{r}) \frac{d}{d\lambda} v_{\text{ext}}^\lambda(\mathbf{r}) \\
&= T_s + \int d\mathbf{r} n(\mathbf{r}) v_s(\mathbf{r}) - E_{\text{H}}[G] + \Phi[G] - \text{Tr} [\Sigma G] \\
&\quad - \text{Tr} [\ln G^{-1}] + \text{Tr} [\ln G_s^{-1}] \\
&= -E_{\text{H}}[G] + \Phi[G] - \text{Tr} [\Sigma G] - \text{Tr} [\ln G^{-1}], \tag{F.8}
\end{aligned}$$

where $G_s = G_{\lambda=0}$ is the reference KS Green function, and

$$\text{Tr} [\ln G_s^{-1}] = -\sum_i^{\text{occ}} \epsilon_i = -T_s - \int d\mathbf{r} n(\mathbf{r}) v_s(\mathbf{r}), \tag{F.9}$$

with ϵ_i being the KS eigenvalues. To derive Eq. F.8, I have also used

$$\begin{aligned} & \int_0^1 d\lambda \text{Tr} [G_\lambda v_H] \\ &= \int_0^1 d\lambda \int_{-\infty}^{\infty} \frac{d\omega}{2\pi} \int d\mathbf{r} d\mathbf{r}' G_\lambda(\mathbf{r}, \mathbf{r}', i\omega) V_H(\mathbf{r}) \delta(\mathbf{r} - \mathbf{r}') \\ &= \int d\mathbf{r} n(\mathbf{r}) v_H(\mathbf{r}) = 2E_H \end{aligned} \quad (\text{F.10})$$

and similarly

$$\begin{aligned} \int_0^1 d\lambda \text{Tr} \left[G_\lambda \frac{dv_{\text{ext}}^\lambda}{d\lambda} \right] &= \int_0^1 d\lambda \int d\mathbf{r} n(\mathbf{r}) \frac{dv_{\text{ext}}^\lambda(\mathbf{r})}{d\lambda} \\ &= \int d\mathbf{r} (v_{\text{ext}}(\mathbf{r}) - v_s(\mathbf{r})) n(\mathbf{r}) d\mathbf{r}, \end{aligned} \quad (\text{F.11})$$

noting that $v_{\text{ext}}(\mathbf{r}) = v_{\text{ext}}^{\lambda=1}$ and $v_s(\mathbf{r}) = v_{\text{ext}}^{\lambda=0}$.

Equation F.8 clearly indicates the resultant interacting ground-state energy does not depend on the reference state. Making use of the Dyson Eq. F.6 at $\lambda = 1$, Equivalent expressions to Eq. F.8 can be obtained,

$$E = -E_H[G] + \Phi[G] - \text{Tr} [\Sigma G] - \text{Tr} [\ln (G_s^{-1} + v_{\text{xc}} - \Sigma)] \quad (\text{F.12})$$

$$= -E_H[G] + \Phi[G] - \text{Tr} [(G_s^{-1} + v_{\text{xc}})G - 1] - \text{Tr} [\ln G^{-1}]. \quad (\text{F.13})$$

Equations F.8, F.12, and F.13 are all equivalent when G is a self-consistent solution of the Dyson Eq. 4.24. Regarding the energy E as a functional of G , Eq. F.12 is known as the Luttinger-Ward functional [99] and Eq. F.13 the Klein functional [100]. the form of the Klein functional is thus derived.

As discussed in Refs. [101, 203], evaluating the Klein functional under the GW approximation with the noninteracting Green function G_s one obtains the RPA total energy

$$\begin{aligned} E^{\text{RPA}} &= -E_H[G_s] + \Phi^{GW}[G_s] - \text{Tr} [v_{\text{xc}} G_s] - \text{Tr} [\ln G_s^{-1}] \\ &= T_s + \int d\mathbf{r} n(\mathbf{r}) v_{\text{ext}}(\mathbf{r}) + E_H[G_s] + E_x[G_s] + E_c^{\text{RPA}}[G_s], \end{aligned} \quad (\text{F.14})$$

where I have used:

$$- \text{Tr} [v_{\text{xc}} G_s] - \text{Tr} [\ln G_s^{-1}] = T_s + \int d\mathbf{r} n(\mathbf{r}) v_{\text{ext}}(\mathbf{r}) + 2E_H \quad (\text{F.15})$$

and

$$\begin{aligned}
 \Phi^{GW}[G_s] &= \sum_{n=1}^{\infty} \frac{1}{2n} \text{Tr} \left[\Sigma^{(n)}[G_s] G_s \right] \\
 &= \frac{1}{2} \text{Tr} [\Sigma_x G_s] - \sum_{n=2}^{\infty} \frac{1}{2n} \text{Tr} [(v\chi_s)^n] \\
 &= E_x + E_c^{\text{RPA}}
 \end{aligned} \tag{F.16}$$

with the Σ_x being the exact-exchange self-energy.

CURRICULUM VITÆ

For reasons of data protection, the curriculum vitæ is not included in the online version.

PUBLICATIONS

JOURNAL ARTICLES

1. V. Atalla, M. Yoon, **F. Caruso**, P. Rinke, and M. Scheffler, *Hybrid density functional theory meets quasiparticle calculations: a consistent electronic structure approach*, submitted.
2. **F. Caruso**, P. Rinke, X. Ren, A. Rubio, and M. Scheffler, *Self-consistent GW: All-electron implementation with localized basis functions*, Phys. Rev. B **88**, 075105 (2013), [DOI](#)
3. **F. Caruso**, D. R. Rohr, M. Hellgren, X. Ren, P. Rinke, A. Rubio, and M. Scheffler, *Bond Breaking and Bond Formation: How Electron Correlation is Captured in Many-Body Perturbation Theory and Density-Functional Theory*, Phys. Rev. Lett. **110**, 146403 (2013), [DOI](#).
4. N. Marom, **F. Caruso**, X. Ren, O. T. Hofmann, T. Körzdörfer, J. R. Chelikowsky, A. Rubio, M. Scheffler, and P. Rinke, *A Benchmark of GW Methods for Azabenzenes*, Phys. Rev. B **86**, 245127 (2012), [DOI](#).
5. **F. Caruso**, P. Rinke, X. Ren, M. Scheffler, and A. Rubio, *Unified description of ground and excited states of finite systems: the self-consistent GW approach*, Phys. Rev. B **86**, 081102(R) (2012), [DOI](#).
6. A. Vanossi, N. Manini, **F. Caruso**, G. E. Santoro, and E. Tosatti, *Static friction on the fly: velocity depinning transitions of lubricants in motion*, Phys. Rev. Lett. **99**, 206101 (2007), [DOI](#).

TALKS AT CONFERENCES

1. (INVITED) *ETSF Young Researchers Meeting*, University of Budapest, Hungary, May 2013
2. *March Meeting of the American Physical Society*, Baltimore, Maryland, United States, March 2013

3. *Spring Meeting of the German Physical Society*,
Regensburg, Germany, March 2013
4. (INVITED) *Recent progress in Dynamical Mean-Field Theory and GW calculations, and hands-on school on full-potential LMTO method*,
IPCMS, Strasbourg, France, December 2012
5. *17th ETSF Workshop on Electronic Excitations: Advanced Green function methods*,
University of Coimbra, Portugal, October 2012
6. (INVITED) *Density Functional Theory and Beyond with Numeric Atom-Centered Orbitals. FHI-aims Developers' and Users' Meeting*,
Freie Universität zu Berlin, Germany, August 2012
7. (INVITED) *International Workshop on "Frontiers in Computational Material Science"*,
Ringberg Castle, Rottach-Egern, Germany, July 2012
8. (INVITED) *GW quasiparticle calculations in condensed matter physics and nanoscience*,
CECAM Headquarter, Lausanne, Switzerland, April 2012
9. *March Meeting of the American Physical Society*,
Boston, Massachusetts, United States, March 2012
10. *Spring Meeting of the German Physical Society*,
Technische Universität zu Berlin, Germany, March 2012
11. (INVITED) *Computational Surface Science*,
University of California Santa Barbara, August 2011
12. (INVITED) *Hands-On Tutorial: Density Functional Theory and Beyond, Concepts and Applications*,
Fritz Haber Institut, Berlin, Germany, July 2011
13. *16th ETSF Workshop on Electronic Excitations: Bridging theory and experiment*,
Torino, Italy, September 2011
14. (INVITED) *ETSF Young Researchers Meeting*,
Università Federico II, Napoli, Italy, May 2011
15. *Spring Meeting of the German Physical Society*,
University of Dresden, Germany, March 2011

POSTER

1. *Perspectives and Challenges of Many-Particle Methods: Efficient Strategies and Tools for the Description of Complex Systems*,
University of Bremen, September 2011

2. *Strong Correlation from First Principles*,
Monastery Seeon, Bavaria, Germany, September 2011
3. *Challenges and Solutions in GW Calculations for Complex Systems*,
CECAM Headquarter, Lausanne, Switzerland, June 2011
4. *15th ETSF Workshop on Electronic Excitations*,
Seminaris Campus Hotel, Berlin, Germany, October 2010
5. Ψ_k conference 2010,
Henri-Ford Bau, Berlin, Germany, September 2010
6. *ETSF Young Researchers Meeting*,
University of Jyvaskyla, Finland, June 2010
7. *Density Functional Theory and Beyond with Numeric Atom-Centered Orbitals FHI-aims
Developers' and Users' Meeting*,
Fritz Haber Institute, Berlin, Germany, May 2010

BIBLIOGRAPHY

- [1] E. SCHRÖDINGER, An Undulatory Theory of the Mechanics of Atoms and Molecules, *Phys. Rev.* **28**, 1049 (1926), [DOI](#).
- [2] S. LOGOTHETIDIS, J. PETALAS, H. M. POLATOGLU, and D. FUCHS, Origin and temperature dependence of the first direct gap of diamond, *Phys. Rev. B* **46**, 4483 (1992), [DOI](#).
- [3] F. GIUSTINO, S. G. LOUIE, and M. L. COHEN, Electron-Phonon Renormalization of the Direct Band Gap of Diamond, *Phys. Rev. Lett.* **105**, 265501 (2010), [DOI](#).
- [4] S. HÜFNER, *Photoelectron Spectroscopy: Principles and Applications*, Advanced Texts in Physics, Springer, 2003.
- [5] M. CARDONA and M. L. W. THEWALT, Isotope effects on the optical spectra of semiconductors, *Rev. Mod. Phys.* **77**, 1173 (2005), [DOI](#).
- [6] M. S. DELEUZE, L. CLAES, E. S. KRYACHKO, and J.-P. FRANCOIS, Benchmark theoretical study of the ionization threshold of benzene and oligoacenes, *J. Chem. Phys.* **119**, 3106 (2003), [DOI](#).
- [7] A. SZABO and N. S. OSTLUND, *Modern Quantum Chemistry: Introduction to Advanced Electronic Structure Theory*, Dover Publications, 1996.
- [8] G. SENATORE and N. H. MARCH, Recent progress in the field of electron correlation, *Rev. Mod. Phys.* **66**, 445 (1994), [DOI](#).
- [9] W. M. C. FOULKES, L. MITAS, R. J. NEEDS, and G. RAJAGOPAL, Quantum Monte Carlo simulations of solids, *Rev. Mod. Phys.* **73**, 33 (2001), [DOI](#).
- [10] P. HOHENBERG and W. KOHN, Inhomogeneous Electron Gas, *Phys. Rev.* **136**, B864 (1964), [DOI](#).
- [11] W. KOHN and L. J. SHAM, Self-Consistent Equations Including Exchange and Correlation Effects, *Phys. Rev.* **140**, A1133 (1965), [DOI](#).
- [12] R. M. DREIZLER and E. K. U. GROSS, *Density Functional Theory*, Springer, Berlin, 1990.
- [13] A. L. FETTER and J. D. WALECKA, *Quantum Theory of Many-Particle Systems*, Dover Publications, 2003.
- [14] L. HEDIN, New Method for Calculating the One-Particle Green's Function with Application to the Electron-Gas Problem, *Phys. Rev.* **139**, A796 (1965), [DOI](#).
- [15] R. J. BARTLETT and M. MUSIAL, Coupled-cluster theory in quantum chemistry, *Rev. Mod. Phys.* **79**, 291 (2007), [DOI](#).
- [16] J. C. SLATER, The Theory of Complex Spectra, *Phys. Rev.* **34**, 1293 (1929), [DOI](#).
- [17] G. H. BOOTH, A. J. W. THOM, and A. ALAVI, Fermion Monte Carlo without fixed nodes: A game of life, death, and annihilation in Slater determinant space, *J. Chem. Phys.* **131**, 054106 (2009), [DOI](#).

- [18] J. J. SHEPHERD, G. BOOTH, A. GRÜNEIS, and A. ALAVI, Full configuration interaction perspective on the homogeneous electron gas, *Phys. Rev. B* **85**, 081103 (2012), [DOI](#).
- [19] F. COESTER and H. KÜMMEL, Short-range correlations in nuclear wave functions, *Nuclear Physics* **17**, 477 (1960), [DOI](#).
- [20] J. CIZEK, On the Correlation Problem in Atomic and Molecular Systems. Calculation of Wavefunction Components in Ursell-Type Expansion Using Quantum-Field Theoretical Methods, *J. Chem. Phys.* **45**, 4256 (1966), [DOI](#).
- [21] K. E. RILEY, M. PITOK, P. JUREKA, and P. HOBZA, Stabilization and Structure Calculations for Noncovalent Interactions in Extended Molecular Systems Based on Wave Function and Density Functional Theories, *Chem. Rev.* **110**, 5023 (2010), [DOI](#).
- [22] L. H. THOMAS, The calculation of atomic fields, *Math. Proc. Cambridge* **23**, 542 (1927), [DOI](#).
- [23] E. FERMI, Un metodo statistico per la determinazione di alcune proprietà dell'atomo, *Rend. Accad. Naz. Lincei* **6**, 602 (1927).
- [24] J. C. SLATER, A Simplification of the Hartree-Fock Method, *Phys. Rev.* **81**, 385 (1951), [DOI](#).
- [25] W. KOHN, *Highlights in Condensed Matter Theory*, North-Holland, Amsterdam, 1985.
- [26] U. VON BARTH and L. HEDIN, A local exchange-correlation potential for the spin polarized case, *J. Phys. C-Solid State* **5**, 1629 (1972), [DOI](#).
- [27] N. D. MERMIN, Thermal Properties of the Inhomogeneous Electron Gas, *Phys. Rev.* **137**, A1441 (1965), [DOI](#).
- [28] E. RUNGE and E. K. U. GROSS, Density-Functional Theory for Time-Dependent Systems, *Phys. Rev. Lett.* **52**, 997 (1984), [DOI](#).
- [29] R. G. PARR, *Density-Functional Theory of Atoms and Molecules*, Oxford University Press, USA, 1994.
- [30] S. KÜMMEL and L. KRONIK, Orbital-dependent density functionals: Theory and applications, *Rev. Mod. Phys.* **80**, 3 (2008), [DOI](#).
- [31] L. J. SHAM and W. KOHN, One-Particle Properties of an Inhomogeneous Interacting Electron Gas, *Phys. Rev.* **145**, 561 (1966), [DOI](#).
- [32] A. K. THEOPHILOU, The energy density functional formalism for excited states, *J. Phys. C-Solid State* **12**, 5419 (1979), [DOI](#).
- [33] M. A. L. MARQUES, M. J. T. OLIVEIRA, and T. BURNUS, Libxc: A library of exchange and correlation functionals for density functional theory, *Comput. Phys. Commun.* **183**, 2272 (2012), [DOI](#).
- [34] J. P. PERDEW and Y. WANG, Accurate and simple analytic representation of the electron-gas correlation energy, *Phys. Rev. B* **45**, 13244 (1992), [DOI](#).
- [35] D. C. LANGRETH and M. J. MEHL, Beyond the local-density approximation in calculations of ground-state electronic properties, *Phys. Rev. B* **28**, 1809 (1983), [DOI](#).

- [36] A. D. BECKE, A new inhomogeneity parameter in density-functional theory, *J. Chem. Phys.* **109**, 2092 (1998), [DOI](#).
- [37] A. D. BECKE, A new mixing of Hartree–Fock and local density-functional theories, *J. Chem. Phys.* **98**, 1372 (1993), [DOI](#).
- [38] J. P. PERDEW and A. ZUNGER, Self-interaction correction to density-functional approximations for many-electron systems, *Phys. Rev. B* **23**, 5048 (1981), [DOI](#).
- [39] R. O. JONES and O. GUNNARSSON, The density functional formalism, its applications and prospects, *Rev. Mod. Phys.* **61**, 689 (1989), [DOI](#).
- [40] M. ERNZERHOF and G. E. SCUSERIA, Assessment of the Perdew–Burke–Ernzerhof exchange–correlation functional, *J. Chem. Phys.* **110**, 5029 (1999), [DOI](#).
- [41] J. P. PERDEW, K. BURKE, and M. ERNZERHOF, Generalized Gradient Approximation Made Simple, *Phys. Rev. Lett.* **77**, 3865 (1996), [DOI](#).
- [42] A. TKATCHENKO and M. SCHEFFLER, Accurate Molecular Van Der Waals Interactions from Ground-State Electron Density and Free-Atom Reference Data, *Phys. Rev. Lett.* **102**, 073005 (2009), [DOI](#).
- [43] A. J. COHEN, P. MORI-SANCHEZ, and W. YANG, Insights into Current Limitations of Density Functional Theory, *Science* **321**, 792 (2008), [DOI](#).
- [44] E. R. JOHNSON, P. MORI-SANCHEZ, A. J. COHEN, and W. YANG, Delocalization errors in density functionals and implications for main-group thermochemistry, *J. Chem. Phys.* **129**, 204112 (2008), [DOI](#).
- [45] P. MORI-SÁNCHEZ, A. J. COHEN, and W. YANG, Localization and Delocalization Errors in Density Functional Theory and Implications for Band-Gap Prediction, *Phys. Rev. Lett.* **100**, 146401 (2008), [DOI](#).
- [46] V. POLO, J. GRAFENSTEIN, E. KRAKA, and D. CREMER, Influence of the self-interaction error on the structure of the DFT exchange hole, *Chem. Phys. Lett.* **352**, 469 (2002), [DOI](#).
- [47] T. M. HENDERSON and G. E. SCUSERIA, The connection between self-interaction and static correlation: a random phase approximation perspective, *Mol. Phys.* **108**, 2511 (2010), [DOI](#).
- [48] J. P. PERDEW, M. ERNZERHOF, and K. BURKE, Rationale for mixing exact exchange with density functional approximations, *J. Chem. Phys.* **105**, 9982 (1996), [DOI](#).
- [49] T. KÖRZDÖRFER and N. MAROM, Strategy for finding a reliable starting point for G_0W_0 demonstrated for molecules, *Phys. Rev. B* **86**, 041110 (2012), [DOI](#).
- [50] A. GÖRLING and M. LEVY, Exact Kohn–Sham scheme based on perturbation theory, *Phys. Rev. A* **50**, 196 (1994), [DOI](#).
- [51] T. GRABO and E. K. U. GROSS, Density-functional theory using an optimized exchange–correlation potential, *Chem. Phys. Lett.* **240**, 141 (1995), [DOI](#).
- [52] L. J. SHAM and M. SCHLÜTER, Density-Functional Theory of the Energy Gap, *Phys. Rev. Lett.* **51**, 1888 (1983), [DOI](#).

- [53] W. YANG and Q. WU, Direct Method for Optimized Effective Potentials in Density-Functional Theory, *Phys. Rev. Lett.* **89**, 143002 (2002), [DOI](#).
- [54] M. STÄDELE, M. MOUKARA, J. A. MAJEWSKI, P. VOGL, and A. GÖRLING, Exact exchange Kohn-Sham formalism applied to semiconductors, *Phys. Rev. B* **59**, 10031 (1999), [DOI](#).
- [55] Y. M. NIQUET, M. FUCHS, and X. GONZE, Avoiding asymptotic divergence of the potential from orbital- and energy-dependent exchange-correlation functionals, *Int. J. Quantum Chem.* **101**, 635 (2005), [DOI](#).
- [56] F. CARUSO, P. RINKE, X. REN, M. SCHEFFLER, and A. RUBIO, Unified description of ground and excited states of finite systems: The self-consistent GW approach, *Phys. Rev. B* **86**, 081102(R) (2012), [DOI](#).
- [57] M. S. HYBERTSEN and S. G. LOUIE, Electron correlation in semiconductors and insulators: Band gaps and quasiparticle energies, *Phys. Rev. B* **34**, 5390 (1986), [DOI](#).
- [58] C. ROSTGAARD, K. W. JACOBSEN, and K. S. THYGESEN, Fully self-consistent GW calculations for molecules, *Phys. Rev. B* **81**, 085103 (2010), [DOI](#).
- [59] S. REFAELY-ABRAMSON, R. BAER, and L. KRONIK, Fundamental and excitation gaps in molecules of relevance for organic photovoltaics from an optimally tuned range-separated hybrid functional, *Phys. Rev. B* **84**, 075144 (2011), [DOI](#).
- [60] J. F. JANAK, Proof that $\frac{\partial E}{\partial n_i} = \epsilon$ in density-functional theory, *Phys. Rev. B* **18**, 7165 (1978), [DOI](#).
- [61] J. P. PERDEW, R. G. PARR, M. LEVY, and J. L. BALDUZ, Density-Functional Theory for Fractional Particle Number: Derivative Discontinuities of the Energy, *Phys. Rev. Lett.* **49**, 1691 (1982), [DOI](#).
- [62] M. LEVY, J. P. PERDEW, and V. SAHNI, Exact differential equation for the density and ionization energy of a many-particle system, *Phys. Rev. A* **30**, 2745 (1984), [DOI](#).
- [63] O. V. GRITSENKO, B. BRAIDA, and E. J. BAERENDS, Physical interpretation and evaluation of the Kohn-Sham and Dyson components of the ϵ -I relations between the Kohn-Sham orbital energies and the ionization potentials, *J. Chem. Phys.* **119**, 1937 (2003), [DOI](#).
- [64] D. P. CHONG, O. V. GRITSENKO, and E. J. BAERENDS, Interpretation of the Kohn-Sham orbital energies as approximate vertical ionization potentials, *J. Chem. Phys.* **116**, 1760 (2002), [DOI](#).
- [65] J. C. SLATER and J. H. WOOD, Statistical exchange and the total energy of a crystal, *Int. J. Quantum Chem.* **5**, 3 (1970), [DOI](#).
- [66] J. C. SLATER, J. B. MANN, T. M. WILSON, and J. H. WOOD, Nonintegral Occupation Numbers in Transition Atoms in Crystals, *Phys. Rev.* **184**, 672 (1969), [DOI](#).
- [67] V. ATALLA, M. YOON, F. CARUSO, P. RINKE, and M. SCHEFFLER, Hybrid density functional theory meets quasiparticle calculations: a consistent electronic structure approach, *Submitted*

- [68] D. BOHM and D. PINES, A Collective Description of Electron Interactions. I. Magnetic Interactions, *Phys. Rev.* **82**, 625 (1951), [DOI](#).
- [69] D. PINES and D. BOHM, A Collective Description of Electron Interactions: II. Collective vs Individual Particle Aspects of the Interactions, *Phys. Rev.* **85**, 338 (1952), [DOI](#).
- [70] D. BOHM and D. PINES, A Collective Description of Electron Interactions: III. Coulomb Interactions in a Degenerate Electron Gas, *Phys. Rev.* **92**, 609 (1953), [DOI](#).
- [71] A. MARINI, P. GARCÍA-GONZÁLEZ, and A. RUBIO, First-Principles Description of Correlation Effects in Layered Materials, *Phys. Rev. Lett.* **96**, 136404 (2006), [DOI](#).
- [72] J. HARL and G. KRESSE, Cohesive energy curves for noble gas solids calculated by adiabatic connection fluctuation-dissipation theory, *Phys. Rev. B* **77**, 045136 (2008), [DOI](#).
- [73] J. HARL and G. KRESSE, Accurate Bulk Properties from Approximate Many-Body Techniques, *Phys. Rev. Lett.* **103**, 056401 (2009), [DOI](#).
- [74] F. FURCHE, Molecular tests of the random phase approximation to the exchange-correlation energy functional, *Phys. Rev. B* **64**, 195120 (2001), [DOI](#).
- [75] M. FUCHS and X. GONZE, Accurate density functionals: *hskip0.3emhskip0.3em* Approaches using the adiabatic-connection fluctuation-dissipation theorem, *Phys. Rev. B* **65**, 235109 (2002), [DOI](#).
- [76] H. JIANG and E. ENGEL, Random-phase-approximation-based correlation energy functionals: Benchmark results for atoms, *J. Chem. Phys.* **127**, 184108 (2007), [DOI](#).
- [77] X. REN, P. RINKE, C. JOAS, and M. SCHEFFLER, Random-phase approximation and its applications in computational chemistry and materials science, *J. of Mat. Sc.* **47**, 7447 (2012), [DOI](#).
- [78] F. FURCHE, Developing the random phase approximation into a practical post-Kohn–Sham correlation model, *J. Chem. Phys.* **129**, 114105 (2008), [DOI](#).
- [79] A. HESSELMANN and A. GÖRLING, Random-phase approximation correlation methods for molecules and solids, *Mol. Phys.* **109**, 2473 (2011), [DOI](#).
- [80] X. REN, A. TKATCHENKO, P. RINKE, and M. SCHEFFLER, Beyond the Random-Phase Approximation for the Electron Correlation Energy: The Importance of Single Excitations, *Phys. Rev. Lett.* **106**, 153003 (2011), [DOI](#).
- [81] P. ROMANIELLO, F. BECHSTEDT, and L. REINING, Beyond the GW approximation: Combining correlation channels, *Phys. Rev. B* **85**, 155131 (2012), [DOI](#).
- [82] J. PAIER, X. REN, P. RINKE, G. E. SCUSERIA, A. GRÜNEIS, G. KRESSE, and M. SCHEFFLER, Assessment of correlation energies based on the random-phase approximation, *New J. Phys.* **14**, 043002 (2012), [DOI](#).
- [83] J. PAIER, B. G. JANESKO, T. M. HENDERSON, G. E. SCUSERIA, A. GRÜNEIS, and G. KRESSE, Hybrid functionals including random phase approximation correlation and second-order screened exchange, *J. Chem. Phys.* **132**, 094103 (2010), [DOI](#).

- [84] P. JURECKA, J. SPONER, J. CERNY, and P. HOBZA, Benchmark database of accurate (MP2 and CCSD(T) complete basis set limit) interaction energies of small model complexes, DNA base pairs, and amino acid pairs, *Phys. Chem. Chem. Phys.* **8**, 1985 (2006), DOI.
- [85] X. REN, P. RINKE, G. E. SCUSERIA, and M. SCHEFFLER, *in preparation*.
- [86] A. A. ABRIKOSOV, L. P. GOR'KOV, and I. Y. DZIALOSHINSKII, *Quantum Field Theoretical Methods in Statistical Physics*, 1965.
- [87] G. STRINATI, Application of the Greens functions method to the study of the optical properties of semiconductors, *Riv. Nuovo Cimento* **11**, 1 (1988), DOI.
- [88] L. HEDIN and S. LUNDQVIST, Effects of Electron-Electron and Electron-Phonon Interactions on the One-Electron States of Solids, *Solid State Phys.* **23**, 1 (1969), DOI.
- [89] R. P. FEYNMAN, Space-Time Approach to Quantum Electrodynamics, *Phys. Rev.* **76**, 769 (1949), DOI.
- [90] H. LEHMANN, Über Eigenschaften von Ausbreitungsfunktionen und Renormierungskonstanten quantisierter Felder, *Nuovo Cimento* **11**, 342 (1954), DOI.
- [91] A. GÖRLING and M. ERNZERHOF, Energy differences between Kohn-Sham and Hartree-Fock wave functions yielding the same electron density, *Phys. Rev. A* **51**, 4501 (1995), DOI.
- [92] Y. M. NIQUET, M. FUCHS, and X. GONZE, Exchange-correlation potentials in the adiabatic connection fluctuation-dissipation framework, *Phys. Rev. A* **68**, 032507 (2003), DOI.
- [93] M. FUCHS, Y.-M. NIQUET, X. GONZE, and K. BURKE, Describing static correlation in bond dissociation by Kohn-Sham density functional theory, *J. Chem. Phys.* **122**, 094116 (2005), DOI.
- [94] M. HELLGREN and U. VON BARTH, Correlation potential in density functional theory at the GWA level: Spherical atoms, *Phys. Rev. B* **76**, 075107 (2007), DOI.
- [95] R. W. GODBY, M. SCHLÜTER, and L. J. SHAM, Self-energy operators and exchange-correlation potentials in semiconductors, *Phys. Rev. B* **37**, 10159 (1988), DOI.
- [96] M. GRUNING, A. MARINI, and A. RUBIO, Density functionals from many-body perturbation theory: The band gap for semiconductors and insulators, *J. Chem. Phys.* **124**, 154108 (2006), DOI.
- [97] V. GALITSKII and A. MIGDAL, *Sov. Phys. JETP* **7**, 96 (1958).
- [98] R. VAN LEEUWEN, N. E. DAHLEN, and A. STAN, Total energies from variational functionals of the Green function and the renormalized four-point vertex, *Phys. Rev. B* **74**, 195105 (2006), DOI.
- [99] J. M. LUTTINGER and J. C. WARD, Ground-State Energy of a Many-Fermion System. II, *Phys. Rev.* **118**, 1417 (1960), DOI.
- [100] A. KLEIN, Perturbation Theory for an Infinite Medium of Fermions. II, *Phys. Rev.* **121**, 950 (1961), DOI.

- [101] N. E. DAHLEN, R. VAN LEEUWEN, and U. VON BARTH, Variational energy functionals of the Green function and of the density tested on molecules, *Phys. Rev. A* **73**, 012511 (2006), DOI.
- [102] G. BAYM, Self-Consistent Approximations in Many-Body Systems, *Phys. Rev.* **127**, 1391 (1962), DOI.
- [103] N. E. DAHLEN, R. VAN LEEUWEN, and U. VON BARTH, Variational energy functionals of the Green function tested on molecules, *Int. J. Quantum Chem.* **101**, 512 (2005), DOI.
- [104] A. STAN, N. E. DAHLEN, and R. VAN LEEUWEN, Fully self-consistent GW calculations for atoms and molecules, *Europhys. Lett.* **76**, 298 (2006), DOI.
- [105] C. J. VESELY, D. L. KINGSTON, and D. W. LANGER, X-ray photoemission studies of silicon and germanium, *Phys. Status Solidi B* **59**, 121 (1973), DOI.
- [106] E. PEHLKE and M. SCHEFFLER, Evidence for site-sensitive screening of core holes at the Si and Ge (001) surface, *Phys. Rev. Lett.* **71**, 2338 (1993), DOI.
- [107] J. N. ANDERSEN, D. HENNIG, E. LUNDGREN, M. METHFESSEL, R. NYHOLM, and M. SCHEFFLER, Surface core-level shifts of some 4d-metal single-crystal surfaces: Experiments and *ab initio* calculations, *Phys. Rev. B* **50**, 17525 (1994), DOI.
- [108] L. KLASINC, A. SABLJIC, G. KLUGE, J. RIEGER, and M. SCHOLZ, Chemistry of excited states. Part 13. Assignment of lowest π -ionizations in photoelectron spectra of thiophen, furan, and pyrrole, *J. Chem. Soc., Perkin Trans. 2*, 539 (1982), DOI.
- [109] M. GUZZO, G. LANI, F. SOTTILE, P. ROMANIELLO, M. GATTI, J. J. KAS, J. J. REHR, M. G. SILLY, F. SIROTTI, and L. REINING, Valence Electron Photoemission Spectrum of Semiconductors: *Ab Initio* Description of Multiple Satellites, *Phys. Rev. Lett.* **107**, 166401 (2011), DOI.
- [110] F. ARYASETIAWAN, L. HEDIN, and K. KARLSSON, Multiple Plasmon Satellites in Na and Al Spectral Functions from *Ab Initio* Cumulant Expansion, *Phys. Rev. Lett.* **77**, 2268 (1996), DOI.
- [111] B. HOLM and F. ARYASETIAWAN, Self-consistent cumulant expansion for the electron gas, *Phys. Rev. B* **56**, 12825 (1997), DOI.
- [112] A. FUJIMORI, I. HASE, H. NAMATAME, Y. FUJISHIMA, Y. TOKURA, H. EISAKI, S. UCHIDA, K. TAKEGAHARA, and F. M. F. DE GROOT, Evolution of the spectral function in Mott-Hubbard systems with d^1 configuration, *Phys. Rev. Lett.* **69**, 1796 (1992), DOI.
- [113] F. J. GARCÍA DE ABAJO, Optical excitations in electron microscopy, *Rev. Mod. Phys.* **82**, 209 (2010), DOI.
- [114] S. PEREDKOV, G. ÖHRWALL, J. SCHULZ, M. LUNDWALL, T. RANER, A. LINDBLAD, H. BERGERSEN, A. ROSSO, W. POKAPANICH, N. MAARTENSSON, S. SVENSSON, S. L. SORENSEN, O. BJÖRNEHOLM, and M. TCHAPLYGUINE, Free nanoscale sodium clusters studied by core-level photoelectron spectroscopy, *Phys. Rev. B* **75**, 235407 (2007), DOI.
- [115] M. JURVANSUU, A. KIVIMÄKI, and S. AKSELA, Inherent lifetime widths of Ar $2p^{-1}$, Kr $3d^{-1}$, Xe $3d^{-1}$, and Xe $4d^{-1}$ states, *Phys. Rev. A* **64**, 012502 (2001), DOI.

- [116] M. DRESCHER, M. HENTSCHEL, R. KIENBERGER, M. UIBERACKER, V. YAKOVLEV, A. SCRINZI, T. WESTERWALBESLOH, U. KLEINEBERG, U. HEINZMANN, and F. KRAUSZ, Time-resolved atomic inner-shell spectroscopy, *Nature* **419**, 803 (2002), DOI.
- [117] J. HUBBARD, The Description of Collective Motions in Terms of Many-Body Perturbation Theory, *Proc. R. Soc. Lon. Ser.-A* **240**, 539 (1957), DOI.
- [118] J. SCHWINGER, On the Green's functions of quantized fields. I, *Proc. Nat. Acad. Sci.* **37**, 452 (1951), DOI.
- [119] D. R. HARTREE, The Wave Mechanics of an Atom with a Non-Coulomb Central Field. Part I. Theory and Methods, *Math. Proc. Cambridge* **24**, 89 (1928), DOI.
- [120] M. S. HYBERTSEN and S. G. LOUIE, First-Principles Theory of Quasiparticles: Calculation of Band Gaps in Semiconductors and Insulators, *Phys. Rev. Lett.* **55**, 1418 (1985), DOI.
- [121] F. ARYASETIAWAN and O. GUNNARSSON, The GW method, *Rep. Prog. Phys.* **61**, 237 (1998), DOI.
- [122] G. ONIDA, L. REINING, and A. RUBIO, Electronic excitations: density-functional versus many-body Green's-function approaches, *Rev. Mod. Phys.* **74**, 601 (2002), DOI.
- [123] W. G. AULBUR, L. JANSSON, and J. W. WILKINS, Quasiparticle Calculations in Solids, volume 54 of *Solid State Physics*, pp. 1 – 218, Academic Press, 1999.
- [124] X. BLASE, C. ATTACCALITE, and V. OLEVANO, First-principles GW calculations for fullerenes, porphyrins, phtalocyanine, and other molecules of interest for organic photovoltaic applications, *Phys. Rev. B* **83**, 115103 (2011), DOI.
- [125] S. L. ADLER, Quantum Theory of the Dielectric Constant in Real Solids, *Phys. Rev.* **126**, 413 (1962), DOI.
- [126] N. WISER, Dielectric Constant with Local Field Effects Included, *Phys. Rev.* **129**, 62 (1963), DOI.
- [127] P. RINKE, A. QTEISH, J. NEUGEBAUER, and M. SCHEFFLER, Exciting prospects for solids: Exact-exchange based functionals meet quasiparticle energy calculations, *Phys. Status Solidi B* **245**, 929 (2008), DOI.
- [128] <http://cccbdb.nist.gov/>.
- [129] J. E. NORTHRUP, M. S. HYBERTSEN, and S. G. LOUIE, Theory of quasiparticle energies in alkali metals, *Phys. Rev. Lett.* **59**, 819 (1987), DOI.
- [130] M. P. SURH, J. E. NORTHRUP, and S. G. LOUIE, Occupied quasiparticle bandwidth of potassium, *Phys. Rev. B* **38**, 5976 (1988), DOI.
- [131] R. W. GODBY, M. SCHLÜTER, and L. J. SHAM, Quasiparticle energies in GaAs and AlAs, *Phys. Rev. B* **35**, 4170 (1987), DOI.
- [132] M. ROHLFING, P. KRÜGER, and J. POLLMANN, Quasiparticle band-structure calculations for C, Si, Ge, GaAs, and SiC using Gaussian-orbital basis sets, *Phys. Rev. B* **48**, 17791 (1993), DOI.

- [133] M. ROHLFING, P. KRÜGER, and J. POLLMANN, Quasiparticle Band Structure of CdS, *Phys. Rev. Lett.* **75**, 3489 (1995), [DOI](#).
- [134] M. ROHLFING and S. G. LOUIE, Quasiparticle band structure of HgSe, *Phys. Rev. B* **57**, R9392 (1998), [DOI](#).
- [135] A. QTEISH, P. RINKE, M. SCHEFFLER, and J. NEUGEBAUER, Exact-exchange-based quasiparticle energy calculations for the band gap, effective masses, and deformation potentials of ScN, *Phys. Rev. B* **74**, 245208 (2006), [DOI](#).
- [136] H. JIANG, R. I. GOMEZ-ABAL, P. RINKE, and M. SCHEFFLER, First-principles modeling of localized *d* states with the $GW@LDA + U$ approach, *Phys. Rev. B* **82**, 045108 (2010), [DOI](#).
- [137] H. JIANG, R. I. GOMEZ-ABAL, P. RINKE, and M. SCHEFFLER, Electronic band structure of zirconia and hafnia polymorphs from the GW perspective, *Phys. Rev. B* **81**, 085119 (2010), [DOI](#).
- [138] R. SAKUMA, C. FRIEDRICH, T. MIYAKE, S. BLÜGEL, and F. ARYASETIAWAN, GW calculations including spin-orbit coupling: Application to Hg chalcogenides, *Phys. Rev. B* **84**, 085144 (2011), [DOI](#).
- [139] H. JIANG, R. I. GOMEZ-ABAL, P. RINKE, and M. SCHEFFLER, Localized and Itinerant States in Lanthanide Oxides United by $GWtext,@,LDA + U$, *Phys. Rev. Lett.* **102**, 126403 (2009), [DOI](#).
- [140] H. JIANG, P. RINKE, and M. SCHEFFLER, Electronic properties of lanthanide oxides from the GW perspective, *Phys. Rev. B* **86**, 125115 (2012), [DOI](#).
- [141] M. ROHLFING, P. KRÜGER, and J. POLLMANN, Quasiparticle calculations of surface core-level shifts, *Phys. Rev. B* **56**, 2191 (1997), [DOI](#).
- [142] G. FRATESI, G. P. BRIVIO, P. RINKE, and R. W. GODBY, Image resonance in the many-body density of states at a metal surface, *Phys. Rev. B* **68**, 195404 (2003), [DOI](#).
- [143] P. RINKE, K. DELANEY, P. GARCÍA-GONZÁLEZ, and R. W. GODBY, Image states in metal clusters, *Phys. Rev. A* **70**, 063201 (2004), [DOI](#).
- [144] J. E. NORTHRUP, Electronic structure of Si(100) $c(4\times 2)$ calculated within the GW approximation, *Phys. Rev. B* **47**, 10032 (1993), [DOI](#).
- [145] M. SABISCH, P. KRÜGER, A. MAZUR, M. ROHLFING, and J. POLLMANN, First-principles calculations of β -SiC(001) surfaces, *Phys. Rev. B* **53**, 13121 (1996), [DOI](#).
- [146] J. E. NORTHRUP, M. S. HYBERTSEN, and S. G. LOUIE, Many-body calculation of the surface-state energies for Si(111) 2×1 , *Phys. Rev. Lett.* **66**, 500 (1991), [DOI](#).
- [147] J. B. NEATON, M. S. HYBERTSEN, and S. G. LOUIE, Renormalization of Molecular Electronic Levels at Metal-Molecule Interfaces, *Phys. Rev. Lett.* **97**, 216405 (2006), [DOI](#).
- [148] C. E. PATRICK and F. GIUSTINO, Quantitative Analysis of Valence Photoemission Spectra and Quasiparticle Excitations at Chromophore-Semiconductor Interfaces, *Phys. Rev. Lett.* **109**, 116801 (2012), [DOI](#).

- [149] P. RINKE, A. JANOTTI, M. SCHEFFLER, and C. G. VAN DE WALLE, Defect Formation Energies without the Band-Gap Problem: Combining Density-Functional Theory and the GW Approach for the Silicon Self-Interstitial, *Phys. Rev. Lett.* **102**, 026402 (2009), DOI.
- [150] L. MARTIN-SAMOS, G. ROMA, P. RINKE, and Y. LIMOGÉ, Charged Oxygen Defects in SiO₂: Going beyond Local and Semilocal Approximations to Density Functional Theory, *Phys. Rev. Lett.* **104**, 075502 (2010), DOI.
- [151] R. RAMPRASAD, H. ZHU, P. RINKE, and M. SCHEFFLER, New Perspective on Formation Energies and Energy Levels of Point Defects in Nonmetals, *Phys. Rev. Lett.* **108**, 066404 (2012), DOI.
- [152] P. RINKE, A. SCHLEIFE, E. KIOUPAKIS, A. JANOTTI, C. RÖDL, F. BECHSTEDT, M. SCHEFFLER, and C. G. VAN DE WALLE, First-Principles Optical Spectra for *F* Centers in MgO, *Phys. Rev. Lett.* **108**, 126404 (2012), DOI.
- [153] X. QIAN, P. UMARI, and N. MARZARI, Photoelectron properties of DNA and RNA bases from many-body perturbation theory, *Phys. Rev. B* **84**, 075103 (2011), DOI.
- [154] S. SHARIFZADEH, A. BILLER, L. KRONIK, and J. B. NEATON, Quasiparticle and optical spectroscopy of the organic semiconductors pentacene and PTCDA from first principles, *Phys. Rev. B* **85**, 125307 (2012), DOI.
- [155] F. BRUNÉVAL, Ionization energy of atoms obtained from GW self-energy or from random phase approximation total energies, *J. Chem. Phys.* **136**, 194107 (2012), DOI.
- [156] S. REFAELY-ABRAMSON, R. BAER, and L. KRONIK, Fundamental and excitation gaps in molecules of relevance for organic photovoltaics from an optimally tuned range-separated hybrid functional, *Phys. Rev. B* **84**, 075144 (2011), DOI.
- [157] N. MAROM, X. REN, J. E. MOUSSA, J. R. CHELIKOWSKY, and L. KRONIK, Electronic structure of copper phthalocyanine from G_0W_0 calculations, *Phys. Rev. B* **84**, 195143 (2011), DOI.
- [158] X. REN, P. RINKE, V. BLUM, J. WIEFERINK, A. TKATCHENKO, A. SANFILIPPO, K. REUTER, and M. SCHEFFLER, Resolution-of-identity approach to Hartree-Fock, hybrid density functionals, RPA, MP2 and GW with numeric atom-centered orbital basis functions, *New J. Phys.* **14**, 053020 (2012), DOI.
- [159] D. FOERSTER, P. KOVAL, and D. SANCHEZ-PORTAL, An $O(N^3)$ implementation of Hedin's GW approximation for molecules, *J. Chem. Phys.* **135**, 074105 (2011), DOI.
- [160] J. DESLIPPE, G. SAMSONIDZE, D. A. STRUBBE, M. JAIN, M. L. COHEN, and S. G. LOUIE, BerkeleyGW: A massively parallel computer package for the calculation of the quasiparticle and optical properties of materials and nanostructures, *Comput. Phys. Commun.* **183**, 1269 (2012), DOI.
- [161] A. MARINI, C. HOGAN, M. GRUNING, and D. VARSANO, Yambo: An ab initio tool for excited state calculations, *Comput. Phys. Commun.* **180**, 1392 (2009), DOI.

- [162] X. GONZE, B. AMADON, P.-M. ANGLADE, J.-M. BEUKEN, F. BOTTIN, P. BOULANGER, F. BRUNEVAL, D. CALISTE, R. CARACAS, M. CÔTÉ, T. DEUTSCH, L. GENOVESE, P. GHOSSEZ, M. GIANTOMASSI, S. GOEDECKER, D. R. HAMANN, P. HERMET, F. JOLLET, G. JOMARD, S. LEROUX, M. MANCINI, S. MAZEVET, M. J. T. OLIVEIRA, G. ONIDA, Y. POUILLON, T. RANGEL, G.-M. RIGNANESE, D. SANGALLI, R. SHALTAF, M. TORRENT, M. J. VERSTRAETE, G. ZERAH, and J. W. ZWANZIGER, ABINIT: First-principles approach to material and nanosystem properties, *Comput. Phys. Commun.* **180**, 2582 (2009), DOI.
- [163] C. FRIEDRICH, S. BLÜGEL, and A. SCHINDLMAYR, Efficient implementation of the GW approximation within the all-electron FLAPW method, *Phys. Rev. B* **81**, 125102 (2010), DOI.
- [164] H. JIANG, R. I. GOMEZ-ABAL, X.-Z. LI, C. MEISENBICHLER, C. AMBROSCH-DRAXL, and M. SCHEFFLER, FHI-gap: A code based on the all-electron augmented plane wave method, *Comput. Phys. Commun.* **184**, 348 (2013), DOI.
- [165] M. J. VAN SETTEN, F. WEIGEND, and F. EVERS, The GW Method for Quantum Chemistry applications: Theory and Implementation, *J. Chem. Theory Comput.* **9**, 232 (2013), DOI.
- [166] T. RANGEL, D. KECIK, P. E. TREVISANUTTO, G.-M. RIGNANESE, H. VAN SWYGENHOVEN, and V. OLEVANO, Band structure of gold from many-body perturbation theory, *Phys. Rev. B* **86**, 125125 (2012), DOI.
- [167] W. LUO, S. ISMAIL-BEIGI, M. L. COHEN, and S. G. LOUIE, Quasiparticle band structure of ZnS and ZnSe, *Phys. Rev. B* **66**, 195215 (2002), DOI.
- [168] F. BRUNEVAL and M. A. L. MARQUES, Benchmarking the Starting Points of the GW Approximation for Molecules, *J. Chem. Theor. Comput.* **9**, 324 (2013), DOI.
- [169] G. BAYM and L. P. KADANOFF, Conservation Laws and Correlation Functions, *Phys. Rev.* **124**, 287 (1961), DOI.
- [170] L. P. KADANOFF and G. BAYM, *Quantum Statistical Mechanics; Green's Function Methods in Equilibrium and Non-equilibrium Problems*, Frontiers in physics, 1962.
- [171] G. SINI, J. S. SEARS, and J.-L. BREDAS, Evaluating the Performance of DFT Functionals in Assessing the Interaction Energy and Ground-State Charge Transfer of Donor/Acceptor Complexes: Tetrathiafulvalene-Tetracyanoquinodimethane (TTF-TCNQ) as a Model Case, *J. Chem. Theor. Comput.* **7**, 602 (2011), DOI.
- [172] F. FLORES, J. ORTEGA, and H. VAZQUEZ, Modelling energy level alignment at organic interfaces and density functional theory, *Phys. Chem. Chem. Phys.* **11**, 8658 (2009), DOI.
- [173] F. BRUNEVAL, F. SOTTILE, V. OLEVANO, R. DEL SOLE, and L. REINING, Many-Body Perturbation Theory Using the Density-Functional Concept: Beyond the GW Approximation, *Phys. Rev. Lett.* **94**, 186402 (2005), DOI.
- [174] M. SHISHKIN and G. KRESSE, Self-consistent GW calculations for semiconductors and insulators, *Phys. Rev. B* **75**, 235102 (2007), DOI.
- [175] C. FABER, C. ATTACALITE, V. OLEVANO, E. RUNGE, and X. BLASE, First-principles GW calculations for DNA and RNA nucleobases, *Phys. Rev. B* **83**, 115123 (2011), DOI.

- [176] N. MAROM, F. CARUSO, X. REN, O. T. HOFMANN, T. KÖRZDÖRFER, J. R. CHELIKOWSKY, A. RUBIO, M. SCHEFFLER, and P. RINKE, Benchmark of GW methods for azabenzene, *Phys. Rev. B* **86**, 245127 (2012), DOI.
- [177] S. V. FALEEV, M. VAN SCHILFGAARDE, and T. KOTANI, All-Electron Self-Consistent GW Approximation: Application to Si, MnO, and NiO, *Phys. Rev. Lett.* **93**, 126406 (2004), DOI.
- [178] M. VAN SCHILFGAARDE, T. KOTANI, and S. FALEEV, Quasiparticle Self-Consistent GW Theory, *Phys. Rev. Lett.* **96**, 226402 (2006), DOI.
- [179] A. SVANE, N. E. CHRISTENSEN, I. GORCZYCA, M. VAN SCHILFGAARDE, A. N. CHANTIS, and T. KOTANI, Quasiparticle self-consistent GW theory of III-V nitride semiconductors: Bands, gap bowing, and effective masses, *Phys. Rev. B* **82**, 115102 (2010), DOI.
- [180] J. M. TOMCZAK, M. VAN SCHILFGAARDE, and G. KOTLIAR, Many-Body Effects in Iron Pnictides and Chalcogenides: Nonlocal Versus Dynamic Origin of Effective Masses, *Phys. Rev. Lett.* **109**, 237010 (2012), DOI.
- [181] S. V. FALEEV, O. N. MRYASOV, and M. VAN SCHILFGAARDE, Effect of correlations on electronic structure and transport across (001) Fe/MgO/Fe junctions, *Phys. Rev. B* **85**, 174433 (2012), DOI.
- [182] A. SVANE, N. E. CHRISTENSEN, M. CARDONA, A. N. CHANTIS, M. VAN SCHILFGAARDE, and T. KOTANI, Quasiparticle band structures of β -HgS, HgSe, and HgTe, *Phys. Rev. B* **84**, 205205 (2011), DOI.
- [183] A. PUNYA, W. R. L. LAMBRECHT, and M. VAN SCHILFGAARDE, Quasiparticle band structure of Zn-IV-N₂ compounds, *Phys. Rev. B* **84**, 165204 (2011), DOI.
- [184] S. G. CHOI, M. VAN SCHILFGAARDE, D. E. ASPNES, A. G. NORMAN, J. M. OLSON, T. J. PESHEK, and D. H. LEVI, Above-band-gap dielectric functions of ZnGeAs₂: Ellipsometric measurements and quasiparticle self-consistent GW calculations, *Phys. Rev. B* **83**, 235210 (2011), DOI.
- [185] A. R. H. PRESTON, A. DEMASI, L. F. J. PIPER, K. E. SMITH, W. R. L. LAMBRECHT, A. BOONCHUN, T. CHEIWCHANHAMNANGIJ, J. ARNEMANN, M. VAN SCHILFGAARDE, and B. J. RUCK, First-principles calculation of resonant x-ray emission spectra applied to ZnO, *Phys. Rev. B* **83**, 205106 (2011), DOI.
- [186] A. SVANE, N. E. CHRISTENSEN, M. CARDONA, A. N. CHANTIS, M. VAN SCHILFGAARDE, and T. KOTANI, Quasiparticle self-consistent GW calculations for PbS, PbSe, and PbTe: Band structure and pressure coefficients, *Phys. Rev. B* **81**, 245120 (2010), DOI.
- [187] A. N. CHANTIS, M. VAN SCHILFGAARDE, and T. KOTANI, *Ab Initio* Prediction of Conduction Band Spin Splitting in Zinc Blende Semiconductors, *Phys. Rev. Lett.* **96**, 086405 (2006), DOI.
- [188] S. V. FALEEV, M. VAN SCHILFGAARDE, T. KOTANI, F. LÉONARD, and M. P. DESJARLAIS, Finite-temperature quasiparticle self-consistent GW approximation, *Phys. Rev. B* **74**, 033101 (2006), DOI.
- [189] M. VAN SCHILFGAARDE, T. KOTANI, and S. V. FALEEV, Adequacy of approximations in GW theory, *Phys. Rev. B* **74**, 245125 (2006), DOI.

- [190] T. KOTANI, M. VAN SCHILFGAARDE, and S. V. FALEEV, Quasiparticle self-consistent GW method: A basis for the independent-particle approximation, *Phys. Rev. B* **76**, 165106 (2007), DOI.
- [191] A. N. CHANTIS, M. VAN SCHILFGAARDE, and T. KOTANI, Quasiparticle self-consistent GW method applied to localized *4f*-electron systems, *Phys. Rev. B* **76**, 165126 (2007), DOI.
- [192] P. LIAO and E. A. CARTER, Testing variations of the GW approximation on strongly correlated transition metal oxides: hematite (α -Fe₂O₃) as a benchmark, *Phys. Chem. Chem. Phys.* **13**, 15189 (2011), DOI.
- [193] B. HOLM and U. VON BARTH, Fully self-consistent GW self-energy of the electron gas, *Phys. Rev. B* **57**, 2108 (1998), DOI.
- [194] W.-D. SCHÖNE and A. G. EGUILUZ, Self-Consistent Calculations of Quasiparticle States in Metals and Semiconductors, *Phys. Rev. Lett.* **81**, 1662 (1998), DOI.
- [195] W. KU and A. G. EGUILUZ, Band-Gap Problem in Semiconductors Revisited: Effects of Core States and Many-Body Self-Consistency, *Phys. Rev. Lett.* **89**, 126401 (2002), DOI.
- [196] A. STAN, N. E. DAHLEN, and R. VAN LEEUWEN, Levels of self-consistency in the GW approximation, *J. Chem. Phys.* **130**, 114105 (2009), DOI.
- [197] H. J. DE GROOT, P. A. BOBBERT, and W. VAN HAERINGEN, Self-consistent GW for a quasi-one-dimensional semiconductor, *Phys. Rev. B* **52**, 11000 (1995), DOI.
- [198] C. FRIEDRICH, A. SCHINDLMAYR, S. BLÜGEL, and T. KOTANI, Elimination of the linearization error in GW calculations based on the linearized augmented-plane-wave method, *Phys. Rev. B* **74**, 045104 (2006), DOI.
- [199] A. KUTEPOV, S. Y. SAVRASOV, and G. KOTLIAR, Ground-state properties of simple elements from GW calculations, *Phys. Rev. B* **80**, 041103 (2009), DOI.
- [200] A. KUTEPOV, K. HAULE, S. Y. SAVRASOV, and G. KOTLIAR, Electronic structure of Pu and Am metals by self-consistent relativistic GW method, *Phys. Rev. B* **85**, 155129 (2012), DOI.
- [201] B. HOLM, Total Energies from GW Calculations, *Phys. Rev. Lett.* **83**, 788 (1999), DOI.
- [202] P. GARCÍA-GONZÁLEZ and R. W. GODBY, Self-consistent calculation of total energies of the electron gas using many-body perturbation theory, *Phys. Rev. B* **63**, 075112 (2001), DOI.
- [203] M. E. CASIDA, Generalization of the optimized-effective-potential model to include electron correlation: A variational derivation of the Sham-Schlüter equation for the exact exchange-correlation potential, *Phys. Rev. A* **51**, 2005 (1995), DOI.
- [204] V. BLUM, R. GEHRKE, F. HANKE, P. HAVU, V. HAVU, X. REN, K. REUTER, and M. SCHEFFLER, Ab initio molecular simulations with numeric atom-centered orbitals, *Comp. Phys. Comm.* **180**, 2175 (2009), DOI.
- [205] T. H. DUNNING, Gaussian basis sets for use in correlated molecular calculations. I. The atoms boron through neon and hydrogen, *J. Chem. Phys.* **90**, 1007 (1989), DOI.

- [206] M. FEYEREISEN, G. FITZGERALD, and A. KOMORNICKI, Use of approximate integrals in ab initio theory. An application in MP2 energy calculations, *Chem. Phys. Lett.* **208**, 359 (1993), DOI.
- [207] F. WEIGEND, M. HÄSER, H. PATZELT, and R. AHLRICHS, RI-MP2: optimized auxiliary basis sets and demonstration of efficiency, *Chem. Phys. Lett.* **294**, 143 (1998), DOI.
- [208] F. WEIGEND, A fully direct RI-HF algorithm: Implementation, optimised auxiliary basis sets, demonstration of accuracy and efficiency, *Phys. Chem. Chem. Phys.* **4**, 4285 (2002), DOI.
- [209] L. STEINBECK, A. RUBIO, L. REINING, M. TORRENT, I. D. WHITE, and R. W. GODBY, Enhancements to the GW space-time method, *Comput. Phys. Commun.* **125**, 105 (2000), DOI.
- [210] S. LEBÈGUE, B. ARNAUD, M. ALOUANI, and P. E. BLOECHL, Implementation of an all-electron GW approximation based on the projector augmented wave method without plasmon pole approximation: Application to Si, SiC, AlAs, InAs, NaH, and KH, *Phys. Rev. B* **67**, 155208 (2003), DOI.
- [211] G. E. ENGEL, B. FARID, C. M. M. NEX, and N. H. MARCH, Calculation of the GW self-energy in semiconducting crystals, *Phys. Rev. B* **44**, 13356 (1991), DOI.
- [212] R. DALING, W. VAN HAERINGEN, and B. FARID, Plasmon dispersion in silicon obtained by analytic continuation of the random-phase-approximation dielectric matrix, *Phys. Rev. B* **44**, 2952 (1991), DOI.
- [213] B. FARID, R. DALING, D. LENSTRA, and W. VAN HAERINGEN, GW approach to the calculation of electron self-energies in semiconductors, *Phys. Rev. B* **38**, 7530 (1988), DOI.
- [214] T. MATSUBARA, A New Approach to Quantum-Statistical Mechanics, *Prog. Theor. Phys.* **14**, 351 (1955), DOI.
- [215] M. M. RIEGER, L. STEINBECK, I. D. WHITE, H. N. ROJAS, and R. W. GODBY, The GW space-time method for the self-energy of large systems, *Comput. Phys. Commun.* **117**, 211 (1999), DOI.
- [216] F. GIUSTINO, M. L. COHEN, and S. G. LOUIE, GW method with the self-consistent Sternheimer equation, *Phys. Rev. B* **81**, 115105 (2010), DOI.
- [217] A. GEORGES, G. KOTLIAR, W. KRAUTH, and M. J. ROZENBERG, Dynamical mean-field theory of strongly correlated fermion systems and the limit of infinite dimensions, *Rev. Mod. Phys.* **68**, 13 (1996), DOI.
- [218] R. N. SILVER, D. S. SIVIA, and J. E. GUBERNATIS, Maximum-entropy method for analytic continuation of quantum Monte Carlo data, *Phys. Rev. B* **41**, 2380 (1990), DOI.
- [219] M. JARRELL and O. BIHAM, Dynamical approach to analytic continuation of quantum Monte Carlo data, *Phys. Rev. Lett.* **63**, 2504 (1989), DOI.
- [220] A. W. SANDVIK, Stochastic method for analytic continuation of quantum Monte Carlo data, *Phys. Rev. B* **57**, 10287 (1998), DOI.
- [221] M. J. VAN SETTEN et al., *to be submitted* .

- [222] C. FRIDH, L. ASBRINK, and E. LINDHOLM, A modification of INDO for interpretation of photoelectron spectra, *Chem. Phys. Lett.* **15**, 282 (1972), [DOI](#).
- [223] A. MARINI and A. RUBIO, Electron linewidths of wide-gap insulators: Excitonic effects in LiF, *Phys. Rev. B* **70**, 081103 (2004), [DOI](#).
- [224] B. HOLM and F. ARYASETIAWAN, Total energy from the Galitskii-Migdal formula using realistic spectral functions, *Phys. Rev. B* **62**, 4858 (2000), [DOI](#).
- [225] T. MIYAKE, F. ARYASETIAWAN, H. KINO, and K. TERAURA, Total energy from the many-body perturbation approach with a model spectral function: An application to simple metals, *Phys. Rev. B* **64**, 233109 (2001), [DOI](#).
- [226] P. GARCÍA-GONZÁLEZ and R. W. GODBY, Many-Body *GW* Calculations of Ground-State Properties: Quasi-2D Electron Systems and van der Waals Forces, *Phys. Rev. Lett.* **88**, 056406 (2002), [DOI](#).
- [227] S. J. CHAKRAVORTY, S. R. GWALTNEY, E. R. DAVIDSON, F. A. PARPIA, and C. F. FISCHER, Ground-state correlation energies for atomic ions with 3 to 18 electrons, *Phys. Rev. A* **47**, 3649 (1993), [DOI](#).
- [228] X. LI and J. PALDUS, An accurate determination of rovibrational spectra using the externally corrected coupled-cluster approaches: LiH ground state, *J. Chem. Phys.* **118**, 2470 (2003), [DOI](#).
- [229] L. WOLNIEWICZ, Relativistic energies of the ground state of the hydrogen molecule, *J. Chem. Phys.* **99**, 1851 (1993), [DOI](#).
- [230] D. FELLER and K. A. PETERSON, Re-examination of atomization energies for the Gaussian-2 set of molecules, *J. Chem. Phys.* **110**, 8384 (1999), [DOI](#).
- [231] X. REN et al., *to be submitted* .
- [232] D. JÈROME, Organic Conductors: From Charge Density Wave TTFTCNQ to Superconducting (TMTSF)₂PF₆, *Chem. Rev.* **104**, 5565 (2004), [DOI](#).
- [233] H. ALVES, A. S. MOLINARI, H. XIE, and A. F. MORPURGO, Metallic conduction at organic charge-transfer interface, *Nature Mat.* **7**, 574 (2008), [DOI](#).
- [234] B. MILIÀN, R. POU-AMÈRIGO, R. VIRUELA, and E. ORTÍ, On the electron affinity of TCNQ, *Chem. Phys. Lett.* **391**, 148 (2004), [DOI](#).
- [235] D. L. LICHTENBERGER, R. L. JOHNSTON, K. HINKELMANN, T. SUZUKI, and F. WUDL, Relative electron donor strengths of tetrathiafulvene derivatives: effects of chemical substitutions and the molecular environment from a combined photoelectron and electrochemical study, *J. Am. Chem. Soc.* **112**, 3302 (1990), [DOI](#).
- [236] M. GELL-MANN and K. A. BRUECKNER, Correlation Energy of an Electron Gas at High Density, *Phys. Rev.* **106**, 364 (1957), [DOI](#).
- [237] D. C. LANGRETH and J. P. PERDEW, Exchange-correlation energy of a metal surface: Wave-vector analysis, *Phys. Rev. B* **15**, 2884 (1977), [DOI](#).

- [238] M. HELLGREN, D. R. ROHR, and E. K. U. GROSS, Correlation potentials for molecular bond dissociation within the self-consistent random phase approximation, *J. Chem. Phys.* **136**, 034106 (2012), [DOI](#).
- [239] A. HESSELMANN and A. GÖRLING, Correct Description of the Bond Dissociation Limit without Breaking Spin Symmetry by a Random-Phase-Approximation Correlation Functional, *Phys. Rev. Lett.* **106**, 093001 (2011), [DOI](#).
- [240] C. A. COULSON and I. FISCHER, XXXIV. Notes on the molecular orbital treatment of the hydrogen molecule, *Philos. Mag. Series 7* **40**, 386 (1949), [DOI](#).
- [241] F. ARYASETIAWAN, R. SAKUMA, and K. KARLSSON, GW approximation with self-screening correction, *Phys. Rev. B* **85**, 035106 (2012), [DOI](#).
- [242] Y.-W. CHANG and B.-Y. JIN, Self-interaction correction to GW approximation, *Phys. Scripta* **86**, 065301 (2012), [DOI](#).
- [243] X. BLASE and C. ATTACALITE, Charge-transfer excitations in molecular donor-acceptor complexes within the many-body Bethe-Salpeter approach, *Appl. Phys. Lett.* **99**, 171909 (2011), [DOI](#).
- [244] I. DUCHEMIN, T. DEUTSCH, and X. BLASE, Short-Range to Long-Range Charge-Transfer Excitations in the Zinbacteriochlorin-Bacteriochlorin Complex: A Bethe-Salpeter Study, *Phys. Rev. Lett.* **109**, 167801 (2012), [DOI](#).
- [245] U. VON BARTH and B. HOLM, Self-consistent GW_0 results for the electron gas: Fixed screened potential W_0 within the random-phase approximation, *Phys. Rev. B* **54**, 8411 (1996), [DOI](#).
- [246] K. KAASBJERG and K. S. THYGESEN, Benchmarking GW against exact diagonalization for semiempirical models, *Phys. Rev. B* **81**, 085102 (2010), [DOI](#).
- [247] Y.-W. CHANG and B.-Y. JIN, Correlation effects of π electrons on the band structures of conjugated polymers using the self-consistent GW approximation with vertex corrections, *J. Chem. Phys.* **136**, 024110 (2012), [DOI](#).
- [248] K. PELZER, L. GREENMAN, G. GIDOFALVI, and D. A. MAZZIOTTI, Strong Correlation in Acene Sheets from the Active-Space Variational Two-Electron Reduced Density Matrix Method: Effects of Symmetry and Size, *J. Phys. Chem. A* **115**, 5632 (2011), [DOI](#).
- [249] N. MAROM, J. E. MOUSSA, X. REN, A. TKATCHENKO, and J. R. CHELIKOWSKY, Electronic structure of dye-sensitized TiO_2 clusters from many-body perturbation theory, *Phys. Rev. B* **84**, 245115 (2011), [DOI](#).
- [250] P. BALTZER, L. KARLSSON, B. WANNBERG, G. AHRWALL, D. M. P. HOLLAND, M. A. MACDONALD, M. A. HAYES, and W. VON NIESSEN, An experimental and theoretical study of the valence shell photoelectron spectrum of the benzene molecule, *Chem. Phys.* **224**, 95 (1997), [DOI](#).
- [251] L. KARLSSON, L. MATTSSON, R. JADRNY, T. BERGMARK, and K. SIEGBAHN, Valence Electron Spectra of Benzene and the Hexafluorides of Sulphur, Molybdenum, Tungsten

- and Uranium. An Application of Multichannel Detector Technique to UV-Valence Electron Spectroscopy, *Phys. Scripta* **14**, 230 (1976), DOI.
- [252] J. A. SELL and A. KUPPERMANN, Angular distributions in the photoelectron spectra of benzene and its monohalogenated derivatives, *Chem. Phys.* **33**, 367 (1978), DOI.
- [253] S.-Y. LIU, K. ALNAMA, J. MATSUMOTO, K. NISHIZAWA, H. KOHGUCHI, Y.-P. LEE, and T. SUZUKI, He I Ultraviolet Photoelectron Spectroscopy of Benzene and Pyridine in Supersonic Molecular Beams Using Photoelectron Imaging, *J. Phys. Chem. A* **115**, 2953 (2011), DOI.
- [254] R. GLEITER, E. HEILBRONNER, and V. HORNING, Photoelectron Spectra of Azabenzene and Azanaphthalenes: I. Pyridine, diazines, s-triazine and s-tetrazine, *Helv. Chim. Acta* **55**, 255 (1972), DOI.
- [255] C. G. NING, K. LIU, Z. H. LUO, S. F. ZHANG, and J. K. DENG, Electron momentum spectroscopy study on valence electronic structures of pyrimidine, *Chem. Phys. Lett.* **476**, 157 (2009), DOI.
- [256] T. A. CARLSON, P. GERARD, M. O. KRAUSE, F. A. GRIMM, and B. P. PULLEN, Photoelectron dynamics of the valence shells of benzene as a function of photon energy, *J. Chem. Phys.* **86**, 6918 (1987), DOI.
- [257] N. KISHIMOTO and K. OHNO, Collision Energy Resolved Penning Ionization Electron Spectroscopy of Azines: Anisotropic Interaction of Azines with He*(23S) Atoms and Assignments of Ionic States, *J. Phys. Chem. A* **104**, 6940 (2000), DOI.
- [258] M. N. PIANCASTELLI, P. R. KELLER, and J. W. TAYLOR, Angular distribution parameter as a function of photon energy for some mono- and diazabenzene and its use for orbital assignment, *J. Am. Chem. Soc.* **105**, 4235 (1983), DOI.
- [259] C. UTSUNOMIYA, T. KOBAYASHI, and S. NAGAKURA, Photoelectron Angular Distribution Measurements for Some Pyridines, *Bull. Chem. Soc. Jpn.* **51**, 3482 (1978), DOI.
- [260] D. M. P. HOLLAND, A. W. POTTS, L. KARLSSON, M. STENER, and P. DECLEVA, A study of the valence shell photoionisation dynamics of pyrimidine and pyrazine, *Chem. Phys.* **390**, 25 (2011), DOI.
- [261] A. W. POTTS, D. M. P. HOLLAND, A. B. TROFIMOV, J. SCHIRMER, L. KARLSSON, and K. SIEGBAHN, An experimental and theoretical study of the valence shell photoelectron spectra of purine and pyrimidine molecules, *J. Phys. B-At. Mol. Opt.* **36**, 3129 (2003), DOI.
- [262] M. J. S. DEWAR and S. D. WORLEY, Photoelectron Spectra of Molecules. II. The Ionization Potentials of Azabenzene and Azanaphthalenes, *J. Chem. Phys.* **51**, 263 (1969), DOI.
- [263] I. FUSS, I. E. MCCARTHY, A. MINCHINTON, E. WEIGOLD, and F. P. LARKINS, Momentum distributions and ionization potentials for the valence orbitals of benzene, *Chem. Phys.* **63**, 19 (1981), DOI.
- [264] S. MASUDA, M. AOYAMA, K. OHNO, and Y. HARADA, Observation of unusually enhanced satellite band in Penning-ionization electron spectra of benzene and toluene, *Phys. Rev. Lett.* **65**, 3257 (1990), DOI.

- [265] J. D. BUILTH-WILLIAMS, S. M. BELLM, D. B. JONES, H. CHALUVADI, D. H. MADISON, C. G. NING, B. LOHMANN, and M. J. BRUNGER, Experimental and theoretical investigation of the triple differential cross section for electron impact ionization of pyrimidine molecules, *J. Chem. Phys.* **136**, 024304 (2012), [DOI](#).
- [266] M. H. PALMER and I. C. WALKER, The electronic states of benzene and the azines. I. The parent compound benzene. Correlation of vacuum UV and electron scattering data with ab initio CI studies, *Chem. Phys.* **133**, 113 (1989), [DOI](#).
- [267] M. H. PALMER and I. C. WALKER, The electronic states of the azines. V. Pyridazine, studied by VUV absorption, near threshold electron energy-loss spectroscopy and ab initio multi-reference configuration interaction calculations, *Chem. Phys.* **157**, 187 (1991), [DOI](#).
- [268] M. H. PALMER, I. C. WALKER, M. F. GUEST, and A. HOPKIRK, The electronic states of the azines. III. Pyrimidine, studied by VUV absorption, near-threshold electron energy-loss spectroscopy and ab initio multi-reference configuration calculations, *Chem. Phys.* **147**, 19 (1990), [DOI](#).
- [269] I. C. WALKER and M. H. PALMER, The electronic states of the azines. IV. Pyrazine, studied by VUV absorption, near-threshold electron energy-loss spectroscopy and ab initio multi-reference configuration interaction calculations, *Chem. Phys.* **153**, 169 (1991), [DOI](#).
- [270] I. C. WALKER, M. H. PALMER, and A. HOPKIRK, The electronic states of the azines. II. Pyridine, studied by VUV absorption, near-threshold electron energy loss spectroscopy and ab initio multi-reference configuration interaction calculations, *Chem. Phys.* **141**, 365 (1990), [DOI](#).
- [271] J. V. ORTIZ and V. G. ZAKRZEWSKI, A test of partial third order electron propagator theory: Vertical ionization energies of azabenzenes, *J. Chem. Phys.* **105**, 2762 (1996), [DOI](#).
- [272] W. V. NIESSSEN, W. P. KRAEMER, and G. H. F. DIERCKSEN, Interpretation of the photoelectron spectra of the azabenzenes by many-body calculations, *Chem. Phys.* **41**, 113 (1979), [DOI](#).
- [273] L. S. CEDERBAUM, W. DOMCKE, J. SCHIRMER, W. VON NIESSSEN, G. H. F. DIERCKSEN, and W. P. KRAEMER, Correlation effects in the ionization of hydrocarbons, *J. Chem. Phys.* **69**, 1591 (1978), [DOI](#).
- [274] M. S. DELEUZE, A. B. TROFIMOV, and L. S. CEDERBAUM, Valence one-electron and shake-up ionization bands of polycyclic aromatic hydrocarbons. I. Benzene, naphthalene, anthracene, naphthacene, and pentacene, *J. Chem. Phys.* **115**, 5859 (2001), [DOI](#).
- [275] J. WAN, M. HADA, M. EHARA, and H. NAKATSUJI, Electronic excitation and ionization spectra of azabenzenes: Pyridine revisited by the symmetry-adapted cluster configuration interaction method, *J. Chem. Phys.* **114**, 5117 (2001), [DOI](#).
- [276] S. SHARIFZADEH, A. BILLER, L. KRONIK, and J. B. NEATON, Quasiparticle and optical spectroscopy of the organic semiconductors pentacene and PTCDA from first principles, *Phys. Rev. B* **85**, 125307 (2012), [DOI](#).

- [277] M. SHISHKIN, M. MARSMAN, and G. KRESSE, Accurate Quasiparticle Spectra from Self-Consistent GW Calculations with Vertex Corrections, *Phys. Rev. Lett.* **99**, 246403 (2007), DOI.
- [278] F. FUCHS, J. FURTHMÜLLER, F. BECHSTEDT, M. SHISHKIN, and G. KRESSE, Quasiparticle band structure based on a generalized Kohn-Sham scheme, *Phys. Rev. B* **76**, 115109 (2007), DOI.
- [279] F. BRUNEVAL, N. VAST, and L. REINING, Effect of self-consistency on quasiparticles in solids, *Phys. Rev. B* **74**, 045102 (2006), DOI.
- [280] T. PASINSZKI, M. KREBSZ, and G. VASS, Ground and ionic states of 1,2,5-thiadiazoles: An UV-photoelectron spectroscopic and theoretical study, *J. Mol. Struct.* **966**, 85 (2010), DOI.
- [281] P. RADEMACHER, K. KOWSKI, A. MLLER, and G. BOHLMANN, Photoelectron spectra and electronic structures of some naphtho[1,2-d]thiazoles, *J. Mol. Struct.* **296**, 115 (1993), DOI.
- [282] P. M. MAYER, V. BLANCHET, and C. JOBLIN, Threshold photoelectron study of naphthalene, anthracene, pyrene, 1,2-dihydronaphthalene, and 9,10-dihydroanthracene, *J. Chem. Phys.* **134**, 244312 (2011), DOI.
- [283] T. KOBAYASHI, Z.-I. YOSHIDA, H. AWAJI, T. KAWASE, and S. YONEDA, Intramolecular Orbital Interactions in 6,6'-Bi(1,4-dithiafulvenyl) Studied by Photoelectron Spectroscopy, *Bull. Chem. Soc. Jpn.* **57**, 2591 (1984), DOI.
- [284] P.-K. LO and K.-C. LAU, High-Level ab Initio Predictions for the Ionization Energies and Heats of Formation of Five-Membered-Ring Molecules: Thiophene, Furan, Pyrrole, 1,3-Cyclopentadiene, and Borole, $C_4H_4X/C_4H_4X^+$ ($X = S, O, NH, CH_2,$ and BH), *J. Phys. Chem. A* **115**, 932 (2011), DOI.
- [285] N. W. ASHCROFT and N. D. MERMIN, *Solid State Physics*, 1976.

ACKNOWLEDGEMENTS

The first person the I have to thank for this thesis is Patrick Rinke, my supervisor, who helped me to get through each step of this work. Patrick, I really enjoyed to work in your group and I sincerely hope we'll keep in touch over the years. I am also very much indebted to Matthias Scheffler for giving me the possibility to work in a very stimulating environment, and for his constant support throughout the last four years. I am very thankful to Xinguo Ren, without whom this work could have hardly been possible. My sincere thanks go to Angel Rubio for his support and for many inspiring ideas.

Several other people have been essential for part of the work presented in this thesis. I owe gratitude to Noa Marom, Maria Hellgren, Viktor Atalla, and Daniel Rohr for very fruitful and enjoyable collaborations. Moreover, I would like to thank Pina Romaniello, Lucia Reining, and all the members of the ETSF collaboration team on electronic correlation, for many stimulating discussions that have been of inspiration for part of the work presented in this thesis. A special thank goes to all the members of the theory department of the Fritz Haber Institute that have been around over the last four years, and in particular to our secretaries Gaby, Julia, and Birgit for their great help.

Thanks to all the dear friends that were with me in these years, and for all the happy moments spent together. Grazie a Daniele, Laura, Francesca, e Rosaria, per la loro splendida e duratura amicizia. Many thanks to Sanfo, Eli, Hakim, Steffi, Anna, Victor, Wael, Matteo, and Alberto. Un ringraziamento speciale va a Marco Casadei – seduto alla mia sinistra mentre scrivo queste righe – per innumerevoli pillole di saggezza romagnola, e allo Svizzero per tutte le belle serate passate insieme. I want to thank Guo-xu, that has been a great office mate for a couple years, and Björn for helping me out with the German language. Ringrazio la Capy che, nonostante la distanza, ho sempre sentito vicina. Thanks to the Berlin Jammers – Bibi, Anton, Jan, Markus, Kolja, Marc, Woo, Philipp, and many others – for sharing with me the wind of Berlin over uncountable days of Jam.

Infine un ringraziamento alla mia famiglia per il supporto e la fiducia che mi hanno sempre trasmesso. A Maria Rosa, Alberto, e Silvia dedico questa tesi – a dimostrazione del fatto che ogni tanto a Berlino ho anche lavorato. Infine, grazie Mariana per avermi accompagnato in questo percorso fin dall'inizio. Senza di te questi anni non sarebbero stati così felici.